MEDNARODNA PODIPLOMSKA ŠOLA JOŽEFA STEFANA
JOŽEF STEFAN INTERNATIONAL POSTGRADUATE SCHOOL

JANA BEZJAK

THE SYNTHESIS AND CHARACTERIZATION OF BaO-RICH PHASES WITHIN THE $BaO–Nb_2O_5$ AND $BaO–WO_3–Nb_2O_5$ SYSTEM

DOCTORAL DISSERTATION

LJUBLJANA, JUNE 2009

THE SYNTHESIS AND CHARACTERIZATION OF BaO-RICH PHASES WITHIN THE $BaO–Nb_2O_5$ AND $BaO–WO_3–Nb_2O_5$ SYSTEM

Doctoral Dissertation
Jožef Stefan International Postgraduate School
Ljubljana, Slovenia, June 2009

Supervisor: *Prof. Dr. Danilo Suvorov*

Co-supervisor: *Assist. Prof. Boštjan Jančar*

Evaluation Board:

Prof. Dr. Albert Prodan, Chairman, Jožef Stefan Institute, Condensed Matter Physics department, Jamova cesta 39, 1000 Ljubljana, Slovenia

Assist. Prof. Goran Dražič, Member, Jožef Stefan Institute, Department for nanostructured materials, Jamova cesta 39, 1000 Ljubljana, Slovenia

Assist. Prof. Rick Ubic, Member, Boise State University, College of Engineering, 1910 University Drive, Boise, Idaho 83725-2100, USA

Jana Bezjak

THE SYNTHESIS AND CHARACTERIZATION OF BaO-RICH PHASES WITHIN THE $BaO–Nb_2O_5$ AND $BaO–WO_3–Nb_2O_5$ SYSTEM

Doctoral Dissertation

SINTEZA IN KARAKTERIZACIJA FAZ BOGATIH Z BaO V $BaO–Nb_2O_5$ IN $BaO–WO_3–Nb_2O_5$ SISTEMU

Doktorska disertacija

Supervisor: Prof. Dr. Danilo Suvorov

Co-Supervisor: Assist. Prof. Boštjan Jančar

June 2009

MEDNARODNA PODIPLOMSKA ŠOLA JOŽEFA STEFANA
JOŽEF STEFAN INTERNATIONAL POSTGRADUATE SCHOOL
Ljubljana, Slovenia

Index

Abstract

This PhD thesis presents experimental results from the synthesis, crystal structure and microwave dielectric characterization of BaO-rich phases within the BaO-Nb_2O_5 and BaO-Nb_2O_5-WO_3 system. I was primarily interested in two compounds with unknown crystal structure, *i.e.*, the binary $Ba_4Nb_2O_9$ and the ternary $Ba_6Nb_2WO_{14}$, which lie on a common virtual tie-line $Ba_4Nb_2O_9$–Ba_2WO_5. As such, the investigations presented in this PhD thesis were focused on:

(a) A detailed study of the formation conditions of $Ba_4Nb_2O_9$, the phase transitions in $Ba_4Nb_2O_9$ and the phase stability of the individual polymorph. These investigations were followed by decomposition studies of $Ba_4Nb_2O_9$, induced by various thermal and atmosphere treatments.

(b) The phase relations and the phase stability of the BaO-rich hexagonal phases within the BaO–Nb_2O_5–WO_3 ternary system. The first part of the ternary system investigation is dedicated to the phase formation and microstructure of the hexagonal-perovskite based ceramics, while the second part is related to the characterisation of the microwave dielectric properties of the ceramics and to the hexagonal-perovskite crystal structure of the high-temperature $Ba_6Nb_2WO_{14}$ polymorph.

(c) The crystal-structure characterization of the $Ba_4Nb_2O_9$ and $Ba_6Nb_2WO_{14}$ polymorphs. The structural characterizations are based on a special approach, *i.e.*, the TEM-tilting method in combination with a Rietveld refinement. The outcome of the applied methods is a space-group determination of the high-temperature γ-$Ba_4Nb_2O_9$ and $Ba_6Nb_2WO_{14}$, and the crystal structure of the low-temperature α-$Ba_4Nb_2O_9$. Therefore the presented tilting method represents a challenging starting point for the crystal-structure determination of inorganic ionic compounds.

Povzetek

Disertaciji se loteva študije sinteze, kristalne strukture in mikrovalovnih dielektričnih lastnosti z BaO-bogatih faz znotraj BaO-Nb_2O_5 in BaO-Nb_2O_5-WO_3 sistema. V glavnem sem študirala lastnosti dveh spojin z neznano kristalno strukturo, ki ležita na veznici $Ba_4Nb_2O_9$–Ba_2WO_5, ***t.j.***, binarna $Ba_4Nb_2O_9$ in ternarna $Ba_6Nb_2WO_{14}$. Zatorej disertacija povzema rezultate analiz:

a) pogojev sinteze $Ba_4Nb_2O_9$, faznih prehodov znotraj $Ba_4Nb_2O_9$ in stabilnost posameznih polimorfov. K temu sem dodala še študije razpada $Ba_4Nb_2O_9$ pri različnih temperaturnih in atmosferskih pogojih.

b) faznih relacij in stabilnost z BaO-bogatih heksagonalnih faz znotraj BaO–Nb_2O_5–WO_3 ternarnega sistema. Prvi del analiz ternarnega sistema predstavlja naravo formiranja posameznih ternarnih faz in mikrostrukturne lastnosti keramike na osnovi heksagonalnih perovskitov, med tem ko se rezultati drugega dela navezujejo na mikrovalovne dielektrične lastnosti keramike in na keksagonalno-perovskitno kristalno strukturo visoko-temperaturne modifikacije $Ba_6Nb_2WO_{14}$.

c) kristalne strukture posameznih polimorfov s sestavo $Ba_4Nb_2O_9$ in $Ba_6Nb_2WO_{14}$. Karakterizacija kristalne strukture temelji na presevni elektronski mikroskopiji in metodi vrtenja kristalov okrog conskih osi v kombinaciji z Rietveld refinement metodo. Na osnovi uporabljene kombinacije metod, sem določila prostorsko skupino in parametre osnovne celice visoko-temperaturne γ-$Ba_4Nb_2O_9$ in $Ba_6Nb_2WO_{14}$ ter kristalno strukturo nizko-temperaturne α-$Ba_4Nb_2O_9$. Kot taka, se je predvsem metoda vrtenja kristalov okrog conskih osi izkazala za optimalno pri določevanju kristalnih struktur anorganskih ionskih spojin.

Abbreviations

BE	=	Back-scattered Electrons
CBED	=	Convergent Beam Electron-Diffraction
ccp	=	cubic close-packed stacking sequence
c_P	=	crystallographic *c* parameter of cubic perovskite unit-cell
CSO	=	Corner-Sharing Octahedra
CTF	=	Contrast Transfer Function
DTA	=	Differential Thermal Analysis
DSC	=	Differential Scanning Calorimetry
ED	=	Electron Diffraction
EDP	=	Electron Diffraction Pattern
EDS	=	Energy Dispersive X-Ray Spectroscopy
FOLZ	=	First-Order Laue Zone
FSO	=	Face-Sharing Octahedra
hcp	=	hexagonal close-packed stacking sequence
HOLZ	=	High-Order Laue Zone
HRTEM	=	High-Resolution Transmission Electron Microscopy
HT-XRD	=	High-Temperature X-Ray Diffraction
MS	=	Mass Spectrometry
REE	=	Rare Earth Elements
SAED	=	Selected Area Electron Diffraction
SE	=	Secondary-electrons
SEM	=	Scanning Electron Microscope
SEM/EDS	=	Scanning Electron Microscope and Energy Dispersive X-Ray Spectroscopy
TEM	=	Transmission Electron Microscope
TEM/EDS	=	Transmission Electron Microscope and Energy Dispersive X-Ray Spectrometer
TG	=	Thermo-Gravimetry
ZAP	=	Zone-Axis Pattern
ZOLZ	=	Zero-Order Laue Zone
XRD	=	X-Ray Diffraction
$<111>_P$	=	crystallographic direction corresponding to one

		of four body diagonals in the cubic perovskite unit-cell, which is perpendicular to ***ccp*** stacking sequence.
$[001]_H$	=	crystallographic direction in hexagonal perovskite unit-cell perpendicular to ***hcp*** stacking sequence. $[001]_H$ is equivalent to $<111>_P$ of cubic perovskite unit-cell.
□	=	vacancy

1. THE PEROVSKITE CRYSTAL STRUCTURES

In the field of material science the term perovskite is reserved for a description of a class of compounds sharing the same general stoichiometry and similar relation between the atoms in the unit-cell as found in a naturally occurring archetypical $CaTiO_3$, which appears to crystallize within the cubic crystal system. Due to a slight lattice distortion, it adopts an orthorhombic-bipyramidal symmetry corresponding to *the* space group *Pnma*. On the other hand, the synthetic $CaTiO_3$ occurs in three different modifications with two subsequent phase transitions at 1230 and 1360 °C. These include orthorhombic, tetragonal and cubic polymorph [Ali *et al.*, 2005].

However, the ideal perovskites have a cubic *Pm-3m* space group symmetry [Yamanaka *et al*., 2002]. They are considered as an ionic compound with a general formula ABX_3, where A and B indicate cations and X is an anion. The A-cations are centrally located in the body center of the cube formed by eight corner-linked BX_6 octahedra having B-cations at their centers. Consequently, the B-cations are in octahedral coordination with atomic coordinates (0,0,0), whereas A cations with atomic coordinate (1/2,1/2,1/2) are surrounded by twelve anions at atomic coordinates (1/2,0,0). The type of the anion determines the type of cations, which could potentially occur in ABX_3 structure. For the monovalent anions [Luana *et al.*, 1997, Clearfield, 1963, Gingl *et al.*, 1999], the A-site cations must be monovalent and B-site cations divalent. For perovskites based on oxygen anions there is more flexibility in composition in that the sum of the A and B cations valences must be equal to six. Moreover, perovskite might also be based on hydroxyl anions [Roy, 2006]. These compounds have vacant A-sites positions. The B-sites are occupied by one trivalent or a combination of di- and tetravalent cations. Since the perovskite structures accommodate significant number of different anions and most of the metallic ions in the periodic table, perovskites with boron and beryllium have not been reported. Phosphorus and the noble gases are also not observed in the perovskite structure. Indeed, the crystal structure of an ideal perovskite (Fig.1a) can be considered either as a three-dimensional network of regular corner-linked BX_6 octahedra (Fig.1b) or as a cubic close-packed (*ccp*) stacking sequence of AX_3 layers along ⟨111⟩ direction according to the cubic unit-cell (Fig.1c) Megaw [1973]. One layer consists of a closest-packed array of anions where one quarter of them is replaced by A-cations in an ordered manner. The AX_3 layers are separated from one another by octahedrally coordinated B-site cations. Therefore, the ideal perovskite unit-cell is considered as a repeat sequence of cubic close-packed layers of octahedra in the unit cell (Fig.2d). Since three corner-linked octahedral layers describe the cubic perovskite unit-cell, it can be denoted as a 3C, where *C* describes a corner-sharing octahedral layer.

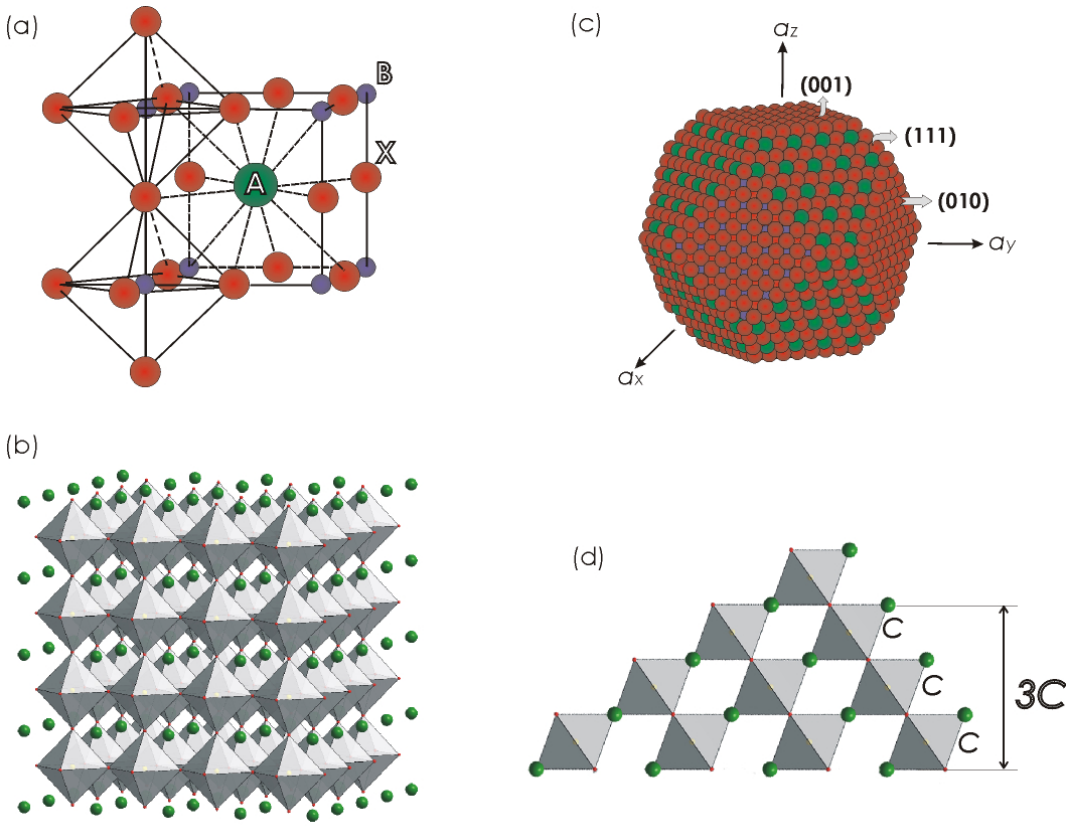

Figure 1: (**a)** The conventional representation of an ideal cubic perovskite crystal structure with B-cell setting unit-cell showing the octahedral coordination for B-cations and cubo-octahedral coordination A-cations. **(b)** The clinographic projection of a cubic perovskite in the view of a three dimensional network of corner-linked BX_6 octahedral. **(c)** The clinographic projection of a cubic perovskite in terms of the cubic close-packed layers. **(d)** The cubic close-packed layers of corner-linked octahedra in the cubic perovskite unit cell (3C) (by Mitchel *et al.*, 2002).

1.1. THE HEXAGONAL PEROVSKITES

Whether a given assemblage of ions will adopt the perovskite crystal structure depends on ionic radii and can be proposed from tolerance factor, $t = (R_X + R_A)/\left[\sqrt{2}(R_X + R_B)\right]$ given by Goldschmidt [1926]. However, for the perovskite crystal structures this structural parameter must be greater than 0.8 and lower than 1.11. The compounds with the value of *t* in the range of 0.9-1.05 can be described with the symmetry of ideal perovskite corresponding to space group *Pm-3m* [Goldschmidt, 1927]. In addition, the compounds with values of *t* lower than 0.8 adopt the ilmenite crystal structure [Goldschmidt, 1927] having a slightly disordered hexagonal close-packed arrangement of ions, while the compounds with *t*-values greater than 1.05 have a hexagonal perovskite crystal structure [Goldschmidt, 1927].

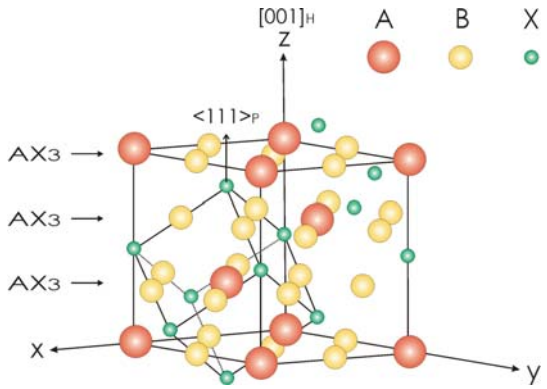

Figure 2: The relationship between the cubic and hexagonal perovskites unit-cells; $[001]_H$ crystallographic direction in hexagonal perovskite unit-cell is equivalent to the $\langle 111\rangle_P$ crystallographic direction off cubic perovskite unit-cell (by Mitchel *et al.*, 2002).

The structural relationship between an ideal cubic and an ideal hexagonal perovskite is represented in figure 2, which illustrates that the $\langle 111\rangle_P$ crystallographic direction of the cubic perovskite is identical to $[001]_H$ crystallographic direction of the hexagonal perovskite. Moreover, the figure reveals the geometrical relationship between the two crystal structures, *e.g.*, $a_{hex} \approx a_p\sqrt{2}$, $c_{hex} \approx c_p\sqrt{3}$ and $V_{hex} \approx 3 * V_p$.

Generally, the ideal hexagonal perovskite structures differ from the ideal cubic perovskites with exclusively cubic stacking sequence of AX_3 layers along $\langle 111\rangle_P$ axes (Fig. 1c), by the presence of exclusively hexagonal close-packed layers stacked perpendicular to $\langle 111\rangle_P$ or equivalent $[001]_H$ crystallographic direction (Fig. 3a). In the hexagonal-close packing the atoms of every second close-packed layer lie vertically above/below each other. The set of the identical atoms in two identical layers thus define the hexagonal lattice (Fig. 3a), which three-dimensional repetition results the ideal hexagonal perovskite crystal structure with the space group $P\frac{6_3}{m}\frac{2}{m}\frac{2}{m}$ ($P\frac{6_3}{m}mc = D_{6h}^{\ 4}$) (Fig. 3b). Additionally, one of the well-know structural correlation between these two crystal structures refers to the translation of AX_3 layers. In this respect the *ccp* stacking sequence undergoes into the hexagonal one when some of *ccp* layers are shifted by the vector (0,1,-1,0) along (111). This operation leads to the distortion-free rotation of BX_6 octahedra around pseudo-cubic axes. Therefore, BX_6 octahedra in hexagonal perovskite link up over common faces into chains parallel to the hexagonal *c*-axis. Since two face-sharing octahedral layers describe the unit-cell of an ideal hexagonal perovskite, where *h* denotes face-sharing octahedral layer these crystal structures are termed as 2H (Fig. 3b).

Regarding Pauling's third rule, perovskite structures with face-sharing BX_6 octahedra are innately less stable then those containing corner-sharing octahedra due to the repulsion forces between B-site cations.

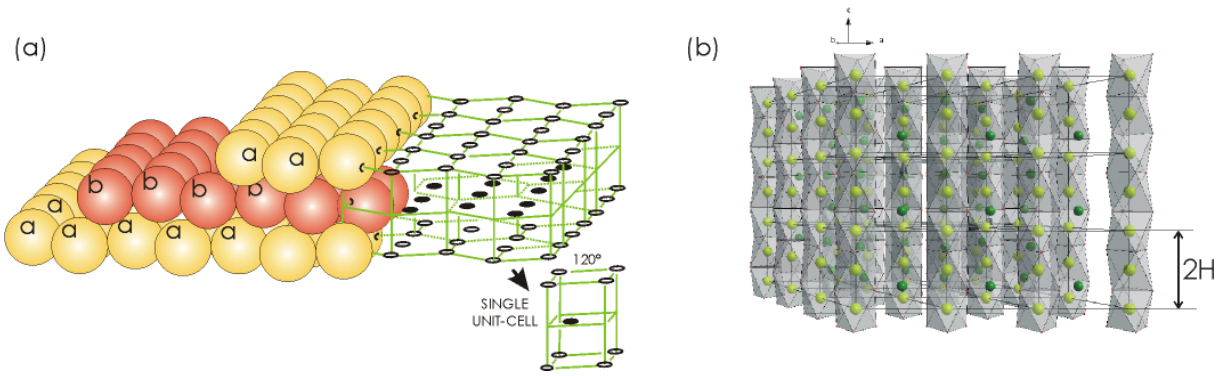

Figure 3: (a) Hexagonally stacked close packed AX_3 layers with stacking sequence ABABA… Identical spheres reveal the hexagonal unit-cell (by Bloss *et al.*, 1971). **(b)** The clinographic projection of an ideal hexagonal perovskite along $[210]_H$ crystallographic direction created by *hcp* stacking sequence of AX_3 layers along crystallographic c-axis according to the hexagonal unit-cell.

This is particularly true if the cation within each anion polyhedra: (a) is highly charged, (b) has a small coordination number and (c) has a radius ratio with respect to the anion (R_A/R_X) near the lowest limit tolerated by the anion polyhedron, *i.e.*, 0.414 for octahedrally coordinated B-site cations in hexagonal perovskites. This indicates that the stability of hexagonal perovskite crystal structures inherently depends on the size of B cations and on the possibility to compensate the electrostatic repulsion between octahedrally coordinated cations. These can be attained by: (a) the ordered substitution of B-site cations by the cations having lower charge in adjacent octahedra, (b) the B-site vacancies formation and (c) the formation of metal-metal bonds between B cation. This bond is not possible in the case of: (a) increased repulsion between B-site cations in face-sharing octahedral due to large cation charge, (b) the d^0 electronic configuration of B-site cations and (c) d-orbital contraction which occurs when B-cations change the oxidation state from higher to lower value, which decreases the d-d orbital contraction.

Nevertheless, the B-site cations in hexagonal perovskites fill up the octahedral interstices and are coordinated by six anions as it is the case in cubic perovskites. Comparable relationship was observed for the large A-site cations. These are coordinated by twelve anions in both, hexagonal and cubic perovskites. Nevertheless, the presence of face-sharing octahedra (FSO) in hexagonal perovskites results anti-cubo-octahedral coordination for A cations, while the same cations in cubic perovskite attain cubo-octahedral coordination (Fig. 4). This results in six shorter A–X bonds within AX_3 layer and in six longer A–X bonds between the layers; three in the layer below and three in the layer above A-site cation.

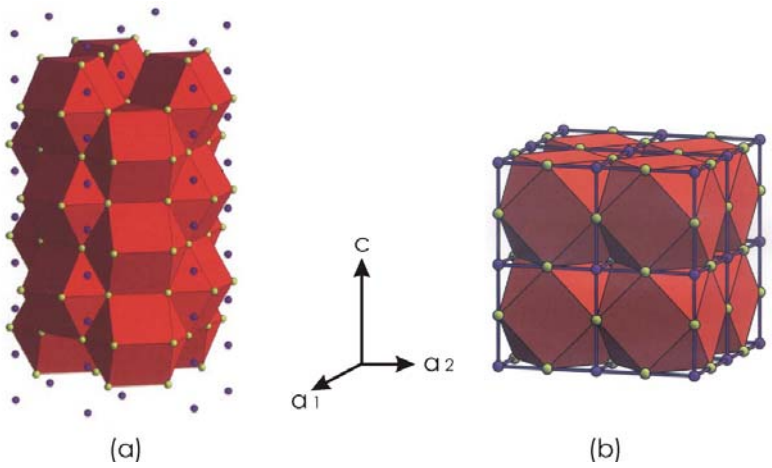

Figure 4: (a) The clinographic projection of hexagonal perovskite crystal structure based on AX_{12} polyhedra showing the anti-cubo-octahedral coordination for A-site cations. **(b)** The clinographic projection of cubic perovskite crystal structure in terms of AX_{12} polyhedra showing the cubo-octahedral coordination for A-site cations (by Mitchel *et al.*, 2002).

1.2. THE HEXAGONAL PEROVSKITE POLYTYPES

Hexagonal perovskite polytypes could be described in terms of intermediate structures between two end-members (Fig. 1b and Fig. 3b); an ideal cubic (3C) and an ideal hexagonal (2H) perovskite. They differ by the number of AX_3-layers along the c-crystallographic direction and in the way how these layers are stuck together. By introducing one cubic close-packed layer in between two hexagonal close-packed layers in 2H hexagonal perovskite structure (Fig. 5a) results the 4H polytype with *chch* stacking sequence (Fig. 5b). This *c-h* notation [Jagodzinski, 1949] considers the particular AX_3 layer in the unit-cell in terms of the orientation of the layer above and below the central one. Indeed, the central layer is denoted as "*h*" when it has hexagonal configuration, which means that it is packed in between two layers in similar orientation. In addition, the layer is said to be in a cubic configuration and is denoted as a "*c*" when it is stuck in between two layers in different orientation. The interstices between these layers are occupied by B-site cations, which are in octahedral coordination with anions. The distance between cations in neighboring face-sharing octahedra approximately correspond to the average thickness of close-packed layers, which varies in the range of 2.2– 2.4 Å. Increasing the number of *ccp* layers in between blocks of two *hcp* layers results the six layered crystal structure in which two face-sharing octahedral layers alternate with one corner-sharing octahedral layer. Therefore the structure is described as 6H polytype with stacking sequence *cchcch* (Fig. 5c). In the same way, the eight- and ten-layered crystal structure with $(cchc)_2$ and $(cchcc)_2$ stacking sequence can be

explained (Fig. 5d-5e). These hexagonal perovskite polytypes all adopt the hexagonal unit-cell with $P\frac{6_3}{m}mc$ space group symmetry. The same is true for an ideal hexagonal perovskite (2H) with exclusively *hcp* stacking sequence along $[001]_H$.

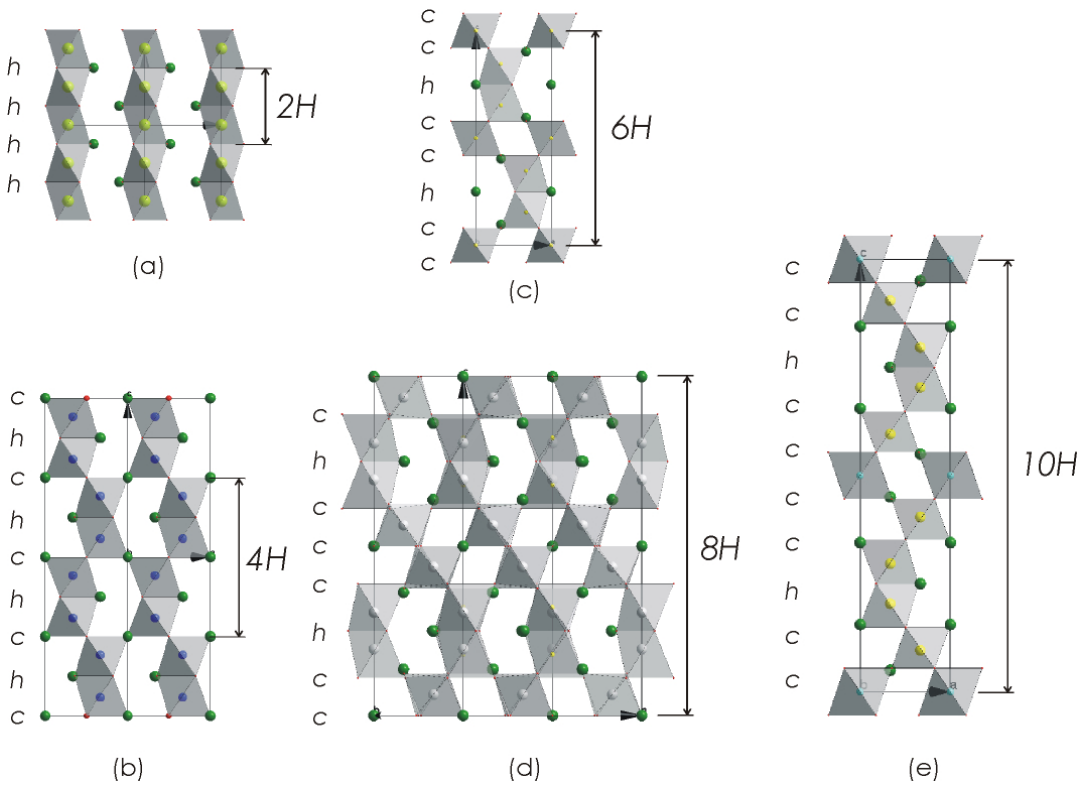

Figure 5: A schematic representation of crystal structure of hexagonal perovskite polytypes in $[110]_H$ orientation with corresponding Jagodzinski's notation: **(a)** the unit cell of deal hexagonal perovskite represented by two face-sharing octahedral layers, **(b)** four-layered polytype having four octahedral layers in the unit-cell, **(b)** six-layered polytype with six octahedral layers in the unit-cell, **(d)** eight-layered polytype represented by three CSO and one FSO layer, **(d)** ten-layered polytype with four CSO and one FSO layer and **(e)** ten-layered polytype.

Among these, many hexagonal perovskite polytypes have rhombohedral unit-cell (R) with the *R-3m* symmetry. The most predominant representatives contain five and nine close-packed layers in the unit-cell and are recognized by triplets of face-sharing octahedra along c-crystallographic direction. Considering the number of layers in the rhombohedral unit-cell, the two perovskites polytypes are known as 5R and 9R crystal structures (Fig. 6a-b). More complex *R-3m* polytypes correspond to 12R, 15R and 27R derivatives with $(cchh)_3$, $(cchch)_3$ and $(cchchchch)_3$ stacking sequence (Fig. 6c-e). According to Jagodzinski notation only 12-layered polytype contains chains of three face-sharing octahedra along $[001]_H$, whereas 15R and 27R polytypes have pairs of face-sharing octahedra in addition to corner-sharing octahedral layers. The particular crystal structures, especially those with block of three face-sharing octahedra, commonly contain B-site cation vacancies in order to reduce the

repulsion between the cations in face-sharing octahedra, excluding the hexagonal elapsolites with general formula $A_2BB'X_6$. In general, elapsolites are isostructural to 12R polytype but do not contain cation vacancies. The repulsion between the B-site cations within the face-sharing octahedra is reduced by the presence of low valence cations. Thus the central octahedron within the block of three face-sharing octahedra are fully occupied by trivalent cations (B' = Al, Ga, In), whereas the two adjacent octahedra in $(B_2B')X_{12}$ trimeric units are exclusively occupied by small monovalent cation (B = Li, Na). The trivalent cations are also positioned in corner-sharing octahedra. Moreover, the entire group of elapsolites also differs from 12R polytype by the presence of exclusively monovalent anions (X = F, Cl) and A-site cations (A = K, Rb, Cs).

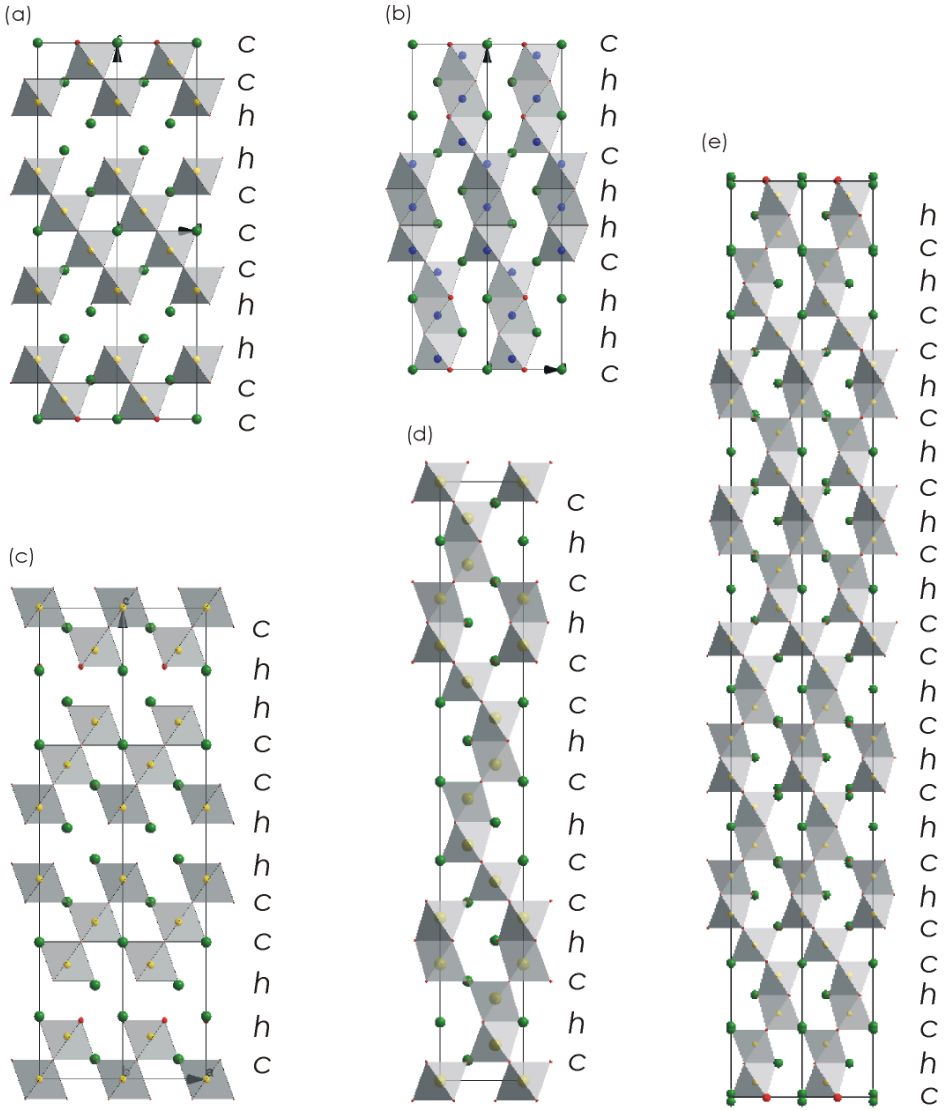

Figure 6: Clinographic projection of the hexagonal perovskite-based crystal structures in terms of coordination polyhedra of B-site cations viewed along $[010]_H$. *c* – indicates corner-sharing octahedra, *h* – indicates face-sharing octahedra, R – indicates rhombohedral unit-cell; the number in front of R denotes the number of layers in the unit-cell normal to c-axis.

1.3. THE B-site CATION-DEFICIENT HEXAGONAL PEROVSKITES

1.3.1. Classification of B-site cation-deficient hexagonal perovskites

The B-site cation deficient hexagonal perovskite with the general formula $A_nB_{n-1}O_{3n}$ can be generally divided into two groups including "shifted" and "twinned" members [Trolliard *et al.*, 2003, 2004]. Both "shifted" and "twined" type structures are associated with the distribution of planar defects such as shift planes and twin boundaries (Fig. 7). The "shifted" hexagonal perovskites (Fig. 7a) can be described as a fully ordered stacking block of n–1 corner-sharing octahedra separated by a vacant octahedral layer considering the periodic shift of $\frac{1}{3}\langle 120\rangle_H$ in the stacking of CSO blocks [Trolliard *et al.*, 2003]. In view of Jagodzinski's notation the "shifted" perovskite refers to (*hhc*…*c*)-type sequence implying two successive h-layers in the unit-cell. Furthermore, the "twinned" type structures can be described as being derived from the cubic perovskite structure by the periodic introduction of twin boundaries (Fig. 7b). The (*hc*…*c*)-type sequence representing this crystal structure corresponds to "perovskite-like block" linked together via octahedral faces (Fig. 7b). The B-site vacancies do not result in the existence of a fully vacant octahedral layer as it is the case in "shifted" perovskites but in a complex repetition of vacancies in pairs of face-sharing octahedra.

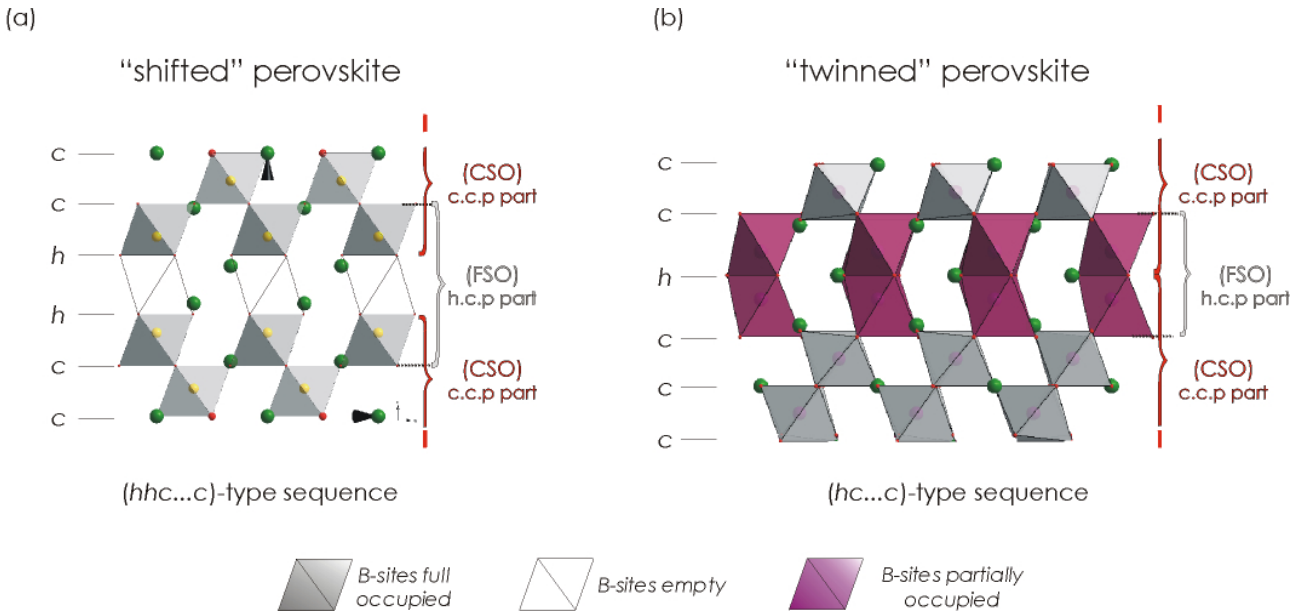

Figure 7: The clinographic projection of the two structural types of hexagonal perovskites; **(a)** "shifted" type structure and **(b)** "twinned" type structure (Trolliard *et al.*, 2003, 2004).

1.3.2. The stability of B-site cation-deficient hexagonal perovskite

The formation of "twinned" and "shifted" structural types mainly depends on the average size of the B-site cations [Trolliard *et al.*, 2003]. Therefore the stability of "twinned" and "shifted" domains can be interpreted in terms of Goldschmidt tolerance factor (*t*), which is classically used to state upon the stability of perovskite-related crystal structures, and as a function of the number of A-X layers (*n*) stack in the unit cell. The comprehensive study of cation-deficient hexagonal perovskites with general formula $A_nB_{n-1}O_{3n}$ (n ≥ 4) from various chemical systems [Trolliard *et al.*, 2003] revealed that the compounds with low n (n = 4, 5, 6) always display "shifted" crystal structure stabilized in a wide range of *t* values, typically $0.97 \leq t \leq 1.05$. In the "shifted" perovskites with general formula $A_nB_{n-1}O_{3n}$ and n > 4 vacancies on B-sublattice leads to a fully vacant octahedra layer located in the perovskite blocks (Fig. 6a). Therefore B-site cation vacancies are periodically ordered every *n* octahedral layers along the crystallographic c-axis. This long-range ordering becomes crucial for the stability of the "shift" type structure when the number of close-packed AX_3 layers between two vacant layers increases along crystallographic c-axis. As *n* increases the "shift" type structure turns to "twin" structure, which stability is assured on behalf of a drastic decrease of vacancies occurrence along c-axis (every n/2 of octahedra layers). However, the "twinned" structures can be stabilized only by simultaneous occupation of B-cations and vacancies on each side of the twinning plane in order to avoid the strong repulsive metal-metal forces. Nevertheless, the crystal structures of the "twinned" type are seldom observed and always correspond to compounds with high values of *n* (*n* > 7) and *t* (*t* > 1.05). If *t* is too small, the distance between FSO centers become too short to allow the simultaneous occupation of these two B-sites and the twin structure is no longer stable. For the whole $A_nB_{n-1}O_{3n}$ (n ≥ 4) the "twin" structure type has been stabilized only for n = 8 [Abakumov *et al.*, 1996, Shpanchenko et al., 1995, Trolliard et al., 2004].

1.4. THE B-site CATION ORDERING in HEXAGONAL PEROVSKITES

The B-site vacancies in cation-deficient hexagonal perovskite normally result in the B-site cation ordering, which is among octahedral distortion, rotation and tilting operation the main reason for lowering the symmetry of $P\frac{6_3}{m}mc$ and $R\bar{3}m$ perovskites. Moreover, the effect of ordering on B-sublattice is not strongly related to the hexagonal perovskites with empty octahedral positions but was also observed in the structures lacking B-site cation vacancies.

The representative of the simplest ordered structures without cation vacancies are 6H hexagonal perovskites with general formula $Ba_3B_2B'O_9$ [Ling *et al.*, 2007, Zandbergen *et al.*, 1983, Lightfoot *et al.*, 1990]. The corner-sharing octahedral positions in this crystal structure are exclusively occupied by divalent cations, whereas the pairs of face-sharing octahedra are occupied by isovalent large charged cations of the same type, which are not able to form metal-metal bond. This bonding is not possible since the B-site cations in $Ba_3B_2B'O_9$ lack electrons in d-shell, i.e., they have d^0 electronic configuration. The fact that low-charged cations can fill merely bridging corner-sharing octahedra and large-charged cations only the octahedra sharing faces indicates the way of cations ordering in $Ba_3B_2B'O_9$. Furthermore, the size of divalent cations in this structure regularly influence tilting the corner-sharing octahedra around their three-fold axis, which is ruled out by the volume difference between BO_6 and $B'O_6$ polyhedra. Since octahedral tilting creates too much space for A-site cations, the structure tends to compensate it by a distortion of AO_{12} polyhedra and by a decrease of coordination number for part of A-site cations from twelve to nine-fold as it is the case in $Ba_3Nb_2SrO_9$ [Zandbergen *et al.*, 1983]. Consequently, these particular changes in related compounds with large divalent cations in corner-sharing octahedra reduce the symmetry from $P\frac{6_3}{m}mc$ to $P\frac{6_3}{m}$. Moreover, the effective size of B-cations in particular those in face-sharing octahedra influence the off-centered displacement of the B-site cations, which was in detail studied by Megaw [1976]. Furthermore, some perovskites lacking B-cations with open d-shells as well B-cation vacancies can achieve the cation ordering and consequently the crystal structure stability by incorporation of cations of a small charge on the B-sites in adjacent face-sharing octahedra, *e.g.* $Ba_4Nb_3LiO_{12}$ [Jendrek *et al.*, 1974] and $Ba_5W_3Li_2O_{15}$ [Jacobson *et al.*, 1974 and Hutchison *et al.*, 1975]. Ordering occurs in such a way that large charged cations with d^0 electronic configuration and those of a low charge are brought to the nearest cation position trough a pair of face-sharing octahedra. The pairing with the low-charged small cations reduces the repulsion between the two highly charged cations, which would appear together in adjacent octahedra. This would additionally cause the considerable displacement of large-charged transition metal ions from the central position in both, corner-sharing and face-sharing octahedra. It is not necessarily true that related compounds, i.e., $Ba_4Sb_3LiO_{12}$ or $Ba_5Te_3Li_2O_{15}$ [Jacobson *et al.*, 1974] will adopt analogue crystal structure. The major difference between the structures arising from transition metals, *i.e.*, B-group elements is the extent to which π-bonding influence the crystal structure. Whether the bond is formed between the low-charged small cation and transition metal cations such as W^{6+} and Nb^{5+} the π-bonding involve relatively low-lying 5d orbitals, while bonding the low-charged small cation and metalloids cation, *i.e.*, Te^{6+} and Sb^{5+} involve electrons from d orbitals with much higher energy. Therefore the difference in covalency is the main reason for which $Ba_4Sb_3LiO_{12}$ or $Ba_5Te_3Li_2O_{15}$ appears in cubic crystal structure corresponding to space group *Fm3m* [Jacobson *et al.*, 1974]. Among these crystal structures, there exists a group of hexagonal perovskites having at least two different cations on B-site

sublattice in addition to B-site cation vacancies. Their combination affects the formation of two types of face-sharing octahedra occurring in pairs, which have consequently a direct bearing on B-site ordering. If pairs of face-sharing octahedra have similar occupancy it creates a possibility for disordered crystal structure. This is the case in 10H $Ba_{10}Ta_{7.04}Ti_{1.2}\square_{1.74}O_{30}$ polytype, where the occupancy in the first pair corresponds to 0.5 of Ta and 0.5 of vacancies, while the second pair is occupied by 0.44 of vacancies and 0.56 of Ta and Ti. If the occupancy in first and the second pair essentially differentiate the perovskite would have to adobe the ordered crystal structure, *e.g.* 8H $Ba_8Ta_4Ni_3\square O_{24}$. Alike in cubic perovskite, the B-site cation ordering in hexagonal perovskite crystal structures may be explained in terms of long- and short-range ordering. Generally, the perovskite will adopt the long-range ordered crystal structure when the B-site cations obviously differ in the size and the valence state. On principle, whether the charge difference between B and B' cations is greater than two, the cations will order. Indeed, the long-range ordering on the B-site is clearly evident from the super-structural X-ray diffraction peaks and weak super-structural reflection spots in selected area electron diffraction patterns. On the contrary the short-range ordering usually refers to the ordering on the local level of the crystal structure, *i.e.*, regular displacement of ions from the ideal position. This type of ordering is indirectly reflected with an unusual bond length between B-site ions, which obviously deviate from the calculated one.

1.5. THE A-site CATION-ORDERING in HEXAGONAL PEROVSKITES

An ordering in the perovskite crystal structure might not affect only B-site positions but also the A-site cations. The ordering on the A-sublattice is associated with the large discrepancy in the size and the valance of cations. In addition, the A-site cation ordering commonly affects dielectric properties of the material as it is the case in $(Ba,La)_5Ti_4O_{15}$ and $(Ca,La)_5Ti_4O_{15}$; where the barium modification exhibit higher dielectric constant due the larger size difference between barium and lanthanum ion, while calcium compound shows higher quality factor due to the lower size difference between the cations. Moreover, a partial replacement of lanthanum by barium or calcium in four and five layered $(A,La)_nTi_{n-1}O_{3n}$ additionally favors the rotation of TiO_6 octahedra. The majority of an A-site cation ordered hexagonal perovskite structures are found in oxygen-deficient hexagonal perovskites, where ordering of anion vacancies reduce the coordination number of A cations and enhance the driving force for chemical ordering. The anion vacancies are not exclusively accompanied with an A-site cation ordering but also with the partial substitution of B-site cations with lower valent cations as it the case in solid-solution with the composition of $BaTi^{4+}_{1-x}Ti^{3+}_xO_{3-x/2}$ [Sinclair *et al.*, 1999].

1.6. THE ANION-DEFICENT HEXAGONAL PEROVSKITES

Anion-deficient hexagonal perovskite with general formula $ABX_{3-\delta}$ ($0 < \delta < 0.5$) are characterized by the presence of anion vacancies. Within the particular crystal structure they can be concentrating exclusively in the h-stacked or c-stacked layer and in both "h"- and "c"- layers. Within these layers anion vacancies can be distributed in an ordered or a disordered manner. With this respect anion-deficient hexagonal perovskites are classified into two groups.

1.6.1. Hexagonal perovskite with disordered anion vacancies

Anion-deficient hexagonal perovskite-type with a disordered distribution of anion vacancies is commonly related to 6H-ABO_3 type crystal structure. These are mostly solid-solutions [Sinclair *et al.*, 1999] and compounds prone to the reduction during synthesis, in particular those prepared from Fe_2O_3 [Jacobson, 1975 and Grey *et al.*, 1997], V_2O_5 [Liu *et al.*, 1993] or Mn_2O_3 [Floros *et al.*, 2000].

The typical representative of an anion-deficient hexagonal perovskite with disordered distribution of anion vacancies exclusively within the "h"-layer is a six-layered $BaTi^{4+}_{1-x}Ti^{3+}_xO_{3-x/2}$ reported by Siclair *et al.* [1999]. In this compound the concentration of anion vacancies increases steeply with progressive substitution of Ti^{4+} by Ti^{3+}, which in turns separate pairs of occupied face-sharing octahedra and hence increase the Ti-Ti distances. In general, as oxygen are removed from the shared octahedral face of the B_2O_9 dimers, the B-site cations are less well shielded and move apart as a result of a greater Columbic repulsion between adjacent B-site cations in face-sharing octahedra. Although there are many structural studies reported in the literature on oxygen-deficient 6H-Ba*B*O_3 phases, there appears to be only one other well-documented example of a 6H structure in which the oxygen vacancies are confined to the h-layer. This occurs for Ba_2ScAlO_5 [Rath et al., 1992], in which bridging corner-sharing octahedra are occupied by Sc^{3+}, while pairs of face-sharing octahedra comprises 0.25 Sc^{3+} and 0.75 Al^{3+}.

Moreover, there are many reports of hexagonal perovskites with disordered distribution of anion vacancies located in both cubic- and hexagonal-stacked layers. The example is six-layered $BaFeO_{2.79}$ reported by Jacobson [1976] and distorted nine-layered $BaIrO_{3-\delta}$ reported by Powell et al. [1996]. The concentration of defect on oxygen sub-lattice in $BaIrO_{3-\delta}$, which is appears to be isostructural to the 9R hexagonal perovskite polytype

depends on the cooling conditions. Thus rapid cooling of the sample results in clearly oxygen deficient compound $BaIrO_{2.74}$ due to the substantial reduction of Ir^{4+} to Ir^{3+} during synthesis. Significant number of oxide ion vacancies occurs both at shared vertices and at sites in the shared faces. The presence of oxygen vacancies thus affects octahedral distortion, which in turns lower the space group of typical 9R polytype to monoclinic C2/m. On contrary slow cooling results a nearly stoichiometric $BaIrO_{2.94}$ phase. The few oxygen vacancies present in this compound are effectively confined to the shared vertices of corner-sharing octahedra. In addition, the concentration of anion vacancies in the c-layers was recently observed by Cussen *et al.,* [2009] in 15R $SrMn_{1-x}Fe_xO_{3-\delta}$ ($x \approx 0.1$).

1.6.2. Hexagonal perovskite with ordered anion vacancies

The hexagonal perovskite with an ordered distribution of anions vacancies exhibits the maximum possible number of onion vacancies located exclusively in *h*-AX_3 layers. Therefore the hexagonal perovskite with an ordered distribution of anion vacancies can be considered as $ABX_{3-\delta}$ ($\delta = 0.5$) structures derived by two types of stacking layers, *i.e.*, AX_3 and $AX\square_2$. The $AX\square_2$-layer is alike to AX_3 in which three oxygen are replaced by one vacancy.

There are only a few anion deficient hexagonal perovskites with uniform distribution of anion vacancies. On contrary with hexagonal perovskites having disordered distribution of defect on anion sublattice ordering of anion vacancies leads to the formation of coordination polyhedra for some B-site cations with coordination number less than six. The simple representative of this crystal structure; *e.g. 8H* Ba_2InAlO_5 [Müller *et al.*, 1990] can be derived from eight-layered hexagonal perovskite polytype having $(ccch)_2$ stacking sequence, after replacing *h*-AX_3 layers with $AX\square_2$-layers (Fig. 8a). Accordingly anion vacancies appear every fourth layer, which then leads to the formation of hexagonal perovskite being structurally related to the brownmillerites (Fig. 8b). However, the brownmillerite crystal structure can be derived from the ideal cubic perovskite (3C) by the ordering of oxygen vacancies in the form of rows parallel to $[10\text{-}1]_P$ direction [Colville, et al., 1971]. This leads to the formation of tetrahedral sites. Additionally, the Ba_2InAlO_5 crystal structure (Fig. 8c) can be derived from eight-layered hexagonal perovskite and described in terms of double layers of BX_4 tetrahedra having their common apices in the $AX\square_2$-layer and their parallel triangular basis in the two adjacent AX_3-layers with corner-sharing octahedra.

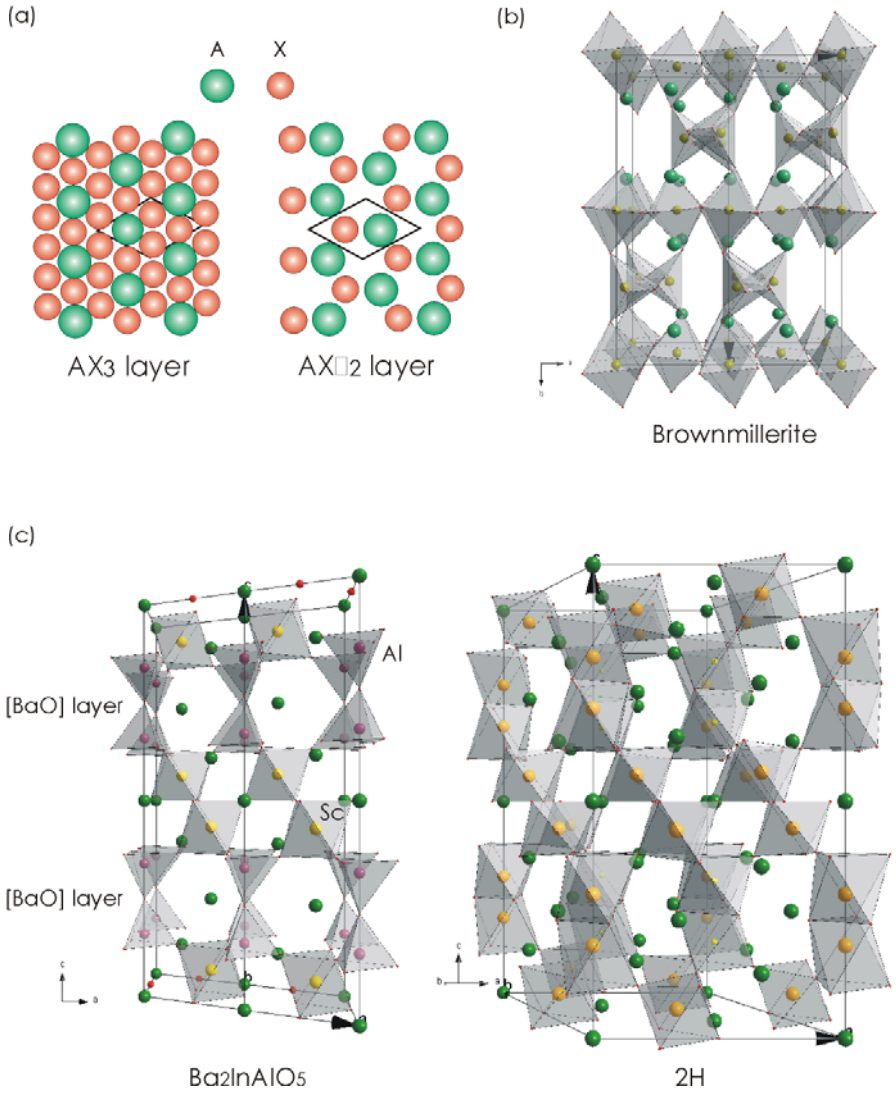

Figure 8: (a) The representation of AX_3 and $AX\square_2$ layer with two-dimensional unit-cells. **(b)** The clinographic projection of a brownmillerite crystal structure. **(c)** The clinographic projection of a Ba_2InAlO_5 crystal structure in comparison with 8H hexagonal perovskite polytype.

Furthermore, as there are many different possible stacking sequences of *ccp* and *hcp* layers, the unit-cell of many hexagonal-perovskite crystal structures having ordered vacancies on anion sublattice commonly represents at least two types of structural blocks (Fig. 9), which occur in periodic sequences along [001] hexagonal supercell; *e.g.* $Ba_5In_2Al_2ZrO_{13}$ [Shpanchenko *et al.*, 1994]. Additionally, these types of crystal structures are known as intergrowth structure. By definition this term refers to the phase, which is formed by stacking of at least two types of blocks *u* and *v*, where each type of block periodically repeated as (*uuu*…) or (*vvv*…) generates an existing simpler structure [Shpanchenko *et al.*, 1994]. The crystal structures u_n and v_n are the terminal members of the homologue series of intergrowth structures; e.g. $u_nv_mu_pv_q$ … u_rv_s. With this respect the $Ba_5In_2Al_2ZrO_{13}$ represent an intergrowth of two blocks; Ba_2AlO_5 and $BaZrO_3$, which alternate along $[001]_H$ crystallographic direction.

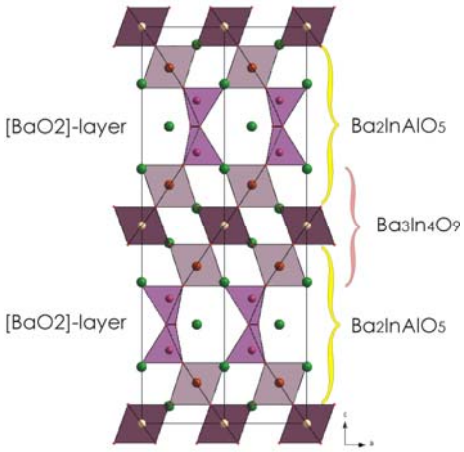

Figure 9: The clinographic projection of an intergrowth crystal structure with a composition $Ba_5M_2Al_2ZrO_{13}$ (M = In, Sc). The structure is composed of two blocks, *i.e,* Ba_2InAlO_5 and $Ba_3In_4O_9$.

The formation of intergrowth structure mainly depends on epitaxy along the contact plane between two different types of structural blocks, i.e., the lattice parameters of both blocks are of the same range. The epitaxy may be additionally promoted by the partial substitution of cations between the building blocks resulting into the structural disorder. Nevertheless, intergrowth structures usually contain long sequences, which are not strictly periodic; therefore their crystal structure study by means of X-ray powder diffraction can only provide average structural information. Since they require a detail analyses on the very local level the high-resolution transmission electron microscopy, which allows direct imaging of long even non-periodic sequence, provide enough data for exact crystal structure determination. However, hexagonal perovskites with an ordered distribution of anion vacancies belong to the special group of hexagonal perovskite, i.e., Derivatives of hexagonal perovskite crystal structures, which essentially differs by the number and types of A-X layers alternating along c-crystallographic axis in a hexagonal unit cell.

1.7. DERIVATIVES OF THE HEXAGONAL PEROVSKITE CRYSTAL STRUCTURE

The crystal structure of hexagonal perovskite derivatives can be described in terms of mixed stacking of AX_3 and A_nX_m layers along $[001]_H$ direction, where n and m define the fraction of A-cations (A = alkaline-earth metal ions) and anions (X = O^{2-}, Cl^-, Br^-) within the two-dimensional unit-mesh. Indexes n and m in A_nX_m notation refer to the natural numbers with the value of n+m ≤ 4. However, as n+m < 4 the A_nX_m notation describes layers with diverse concentration of uniformly distributed anion vacancies. This in general results six different A-X layers including AX_3-, AX_2-, A_2X-, AX-, A_3X_9- and $A_3A'X_6$-layer (Fig. 10). Numerous hexagonal perovskite-related crystal structures can arise from the alternation of A_3X_9-layer with any of AX_2-, A_2X-, AX- and $A_3A'X_6$-layer along crystallographic c-direction.

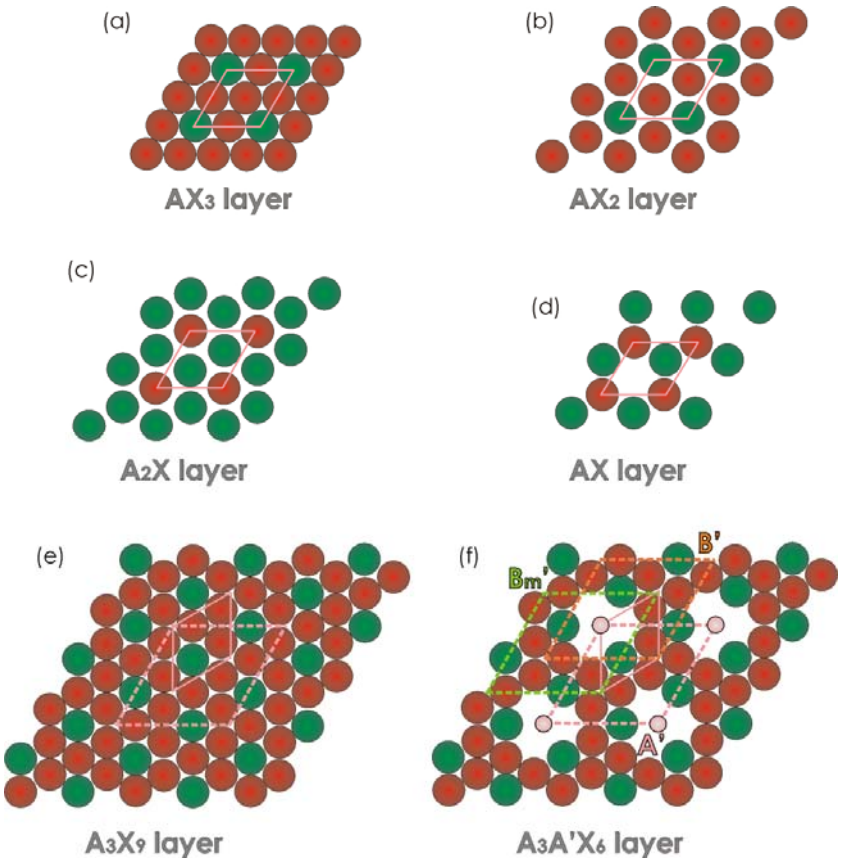

Figure 10: The relationship between A-X layers (after Darriet and Subramanian, 1995). **(a)** The close-packed AX_3 layer with hexagonal symmetry. **(b)** AX_2 layer. **(c)** A_2X layer. **(d)** AX layer. **(e)** The tripled AX_3 layer with hexagonal symmetry. Units mesh with composition AX_3 (pink full line) and A_3X_9 (pink dashed line) is outlined. **(f)** the $A_3A'X_6$ layer with threefold symmetry derives from the tripled AX_3 layer by substituting one A' ion by three oxygen in the center of the "hole" created. The schematic view of the A' (pink dashed line), B' (orange dashed line) and B'_m (green dashed line) layer; the composition of indicated unit mesh is the same for all three types of layers and corresponds to $A_3A'O_6$.

1.7.1. Derivatives of hexagonal perovskite crystal structure based on AX_3 and $A\square X_2$ layers

The crystal structure composed of AX_3 and $A\square X_2$ layers is known as palmierite described with general formula $A_3B_2O_8$, where A corresponds to alkaline earth ions, most commonly Sr or Ba, while B indicates P, V, As, Re, Ru or Nb ions. Palmierites crystallize as a nine-layered structure similar to 9R hexagonal perovskite polytype $BaRuO_3$ [Donohue *et al.*, 1965] having the rhombohedral cell symmetry (*R-3m*).

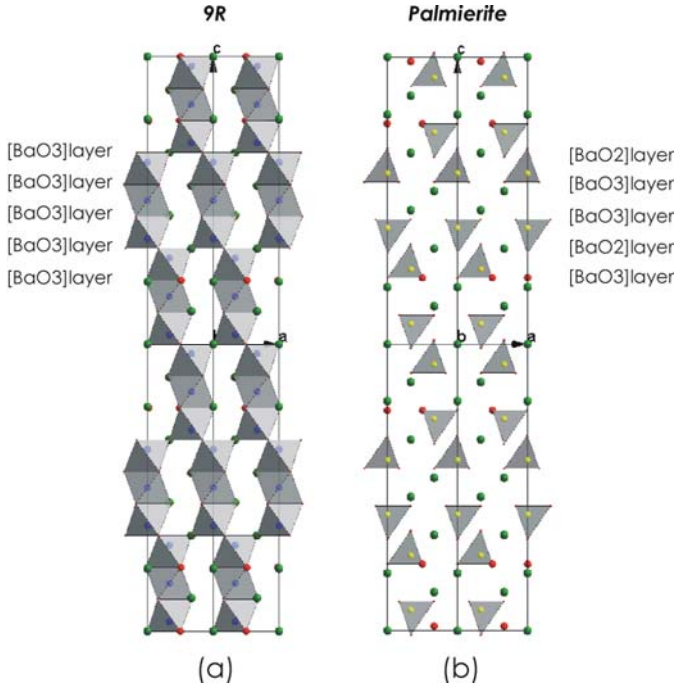

Figure 11: The clinographic projection along $[010]_H$ crystallographic orientation showing the relationship between the nine-layered hexagonal perovskite polytype$BaRuO_3$ **(a)** and palmierite crystal structure$Ba_3Nb_2O_8$ **(b)**.

The transformation from the 9R polytype with $(hhc)_3$ stacking sequence to palmierite crystal structure involve the replacement of the cubic AO_3 layer by the anion vacant $A\square X_2$ layer, which results the formation of tetrahedral sites separated by the vacant or partly occupied octahedral sites (Fig. 11a). Crystallographically, this transformation might be effected by shifting the oxygen at atomic positions (1/2, 0, 0) with a multiplicity 9e (Wyckoff positions) to the position of (0, 0, 1/3) with a multiplicity 6c; positions of the remaining atoms are unchanged (Fig. 11b). In addition, Mössner et al. [1985] reported the existence of nonstoichiometric isostructural phases with the composition $Ba_3B_{2-x}V_x\ O_{9-x/2}$ ($1 < x < 2$) and $Ba_3M_{2-x}Ti_x\ O_{9-x}$ ($3/4 < x < 1$) for B = Mo or W. In both cases the oxygen nonstoichiometry occurs in the cubic BaO_3 layers and strongly depends on incorporation of B^{6+}. Similar effect was

observed for $Ba_3MoNb_2O_{8.5}$ [Garcia-Gonzalez *et al.*, 1998], which has an oxygen stoichiometry between 9R cation-deficient hexagonal perovskite polytype ($A_3B_2O_9$) and the palmierite ($A_3B_2O_8$). The electron diffraction study of this phase revealed the existence of satellite reflections, which are not discrete spots but rather rods of diffuse intensity parallel to [1-1-1]* direction. The satellite reflections are associated with the replacement of BaO_3 layers by $BaO_{2.6}$ in an ordered way. This fact, together with the alternation of contrast in a 3:2 ratio observed in HRTEM recorded along [100] zone-axis, is in agreement with an ordered distribution of octahedra and tetrahedral in the ratio 3:2. The ordering is not well developed. It can be approximated by sinusoidal modulated model affecting the oxygen occupation factor in Ba-O layers. The ordering is probably also associated with a significant displacement of the surrounding barium atoms.

On principle, the palmierite structure can be also modified. Its transformation could extend to the other hexagonal perovskite polytypes, which form new phases with varying stacking sequence of octahedral and tetrahedral layers. The representative is 24-layered $Ba_8V_7O_{22}$ [Liu *et al.*, 1993] with *(hhcc'hhc'c)*$_3$ stacking sequence, where h and c denote hexagonal and cubic BaO_3 layers while c' indicates cubic anion-deficient $Ba\square X_2$ layer. Since the stacking sequence of $Ba_8V_7O_{22}$ is similar to that of 12R hexagonal perovskite polytype *(hhcc)*$_3$ this suggests that there is a link between these two structures (Fig. 12) related to the reorganization of oxygen. This results the change in B-site cation coordination. Therefore B-site cations in 12R crystal structures have octahedral coordination, while B-cations in 24-leyer "palmierite" structure occupy octahedral and tetrahedral sites. The BO_6 octahedra in both structures form linear B_3O_{12} trimmer units through face-sharing. The B_3O_{12} trimmers are connected to each other by corner-sharing bridging, i.e., by corner-sharing octahedra in 12R polytypes and via corner-sharing tetrahedral in 24R palmierite.

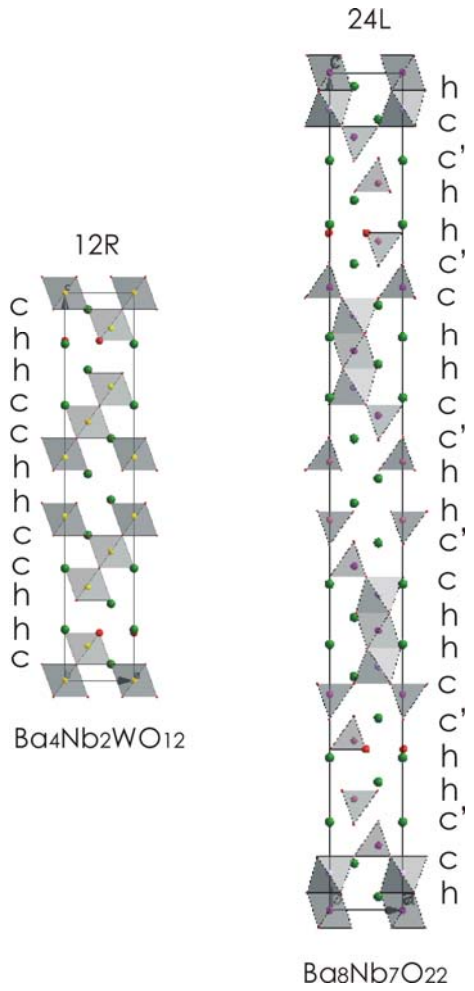

Figure 12: The comparison between 12R hexagonal perovskite polytype and 24-layered palmierite crystal structure of $Ba_8V_7O_{22}$. **(a)** The clinogryphic projection of an ideal 12R polytype. **(b)** Clinographic projection of 24R $Ba_8V_7O_{22}$ in which vanadium ions occupy the tetrahedral sites and ¾ of the octahedral sites in an ordered fashion.

In general, the majority of palmierite-type structures are formed by replacing cubic AO_3 layer by anion deficient $A\square X_2$ layer. However, Neubaher *et al*. [1992] described the only known palmierite-type structure, *i.e.*, $Ba_5IrIn_2Al_2O_{13}Cl$ (Fig. 13) formed by substitution of some hexagonal AO_3 layer by BaOCl layer. The structure is derived from the 10H hexagonal polytype with $(hhchc)_2$ stacking sequence by partial substitution of hexagonal BaO_3 layer with BaOCl layer, which results the stacking sequence of $(hhch_1c)_2$, where h_1 refers to the barium oxychloride layer. The particular stacking sequence thus results the crystal structure in which triplets of face-sharing octahedra are corner linked by double layers of corner-linked tetrahedra.

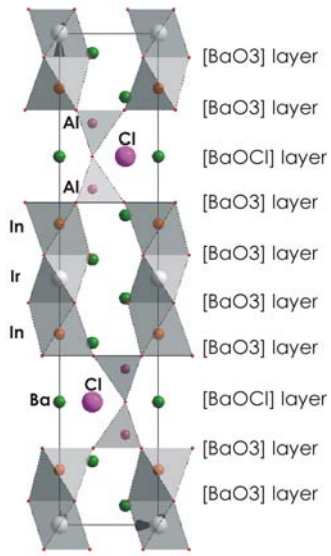

Figure 13: The clinographic projection of the palmierite-type crystal structure derivate from 10H hexagonal polytype by replacement of hexagonal AO_3 layers by anion-deficient $A\square X_2$ layers.

1.7.2. Derivatives of hexagonal perovskite crystal structure based on AX_3 and $AX\square_2$ layers

Structures composed of mixed BaO_3 and $BaX\square_2$ layers where X are monovalent anions such as Cl^- and Br^- can be generally formulated as $(Ba_2X_2)(Ba_{n+1}B_nO_{3n+3})$, n ≥ 1, where n is the number of AO_3 layers normal to the c-crystallographic axis. Generally, the crystal structure of these oxychloride can be described in terms of uniform stacking of one $(A_{n+1}B_nO_{3n+3})$ hexagonal perovskite-like block and double rock salt-type cationic layers (BaX) normal to the crystallographic c-axis. Hence, this type of intergrowth crystal structure is structurally related to Ruddlesden-Pooper [Ruddlesden *et al*., 1958] and Aurivillius phases [Aurivillius, 1949] (Fig. 14). The crystal structure of Ruddlesden-Pooper series of general formula AX + $nABX_3$ can be illustrated by double layers of corner-sharing octahedra in between the AX-layers having NaCl configuration. Similarly the crystal structure of Aurivillius phase with $(Bi_2O_2)^{2+}[A_{n-1}B_nO_{3n+1}]^{2-}$ stoichiometry results from alternation of two structural blocks along [001], *i.e.*, slabs of three corner-sharing octahedral and sheets of Bi_2O_2. The already known members of $(Ba_2X_2)(Ba_{n+1}B_nO_{3n+3})$ family contain from two to five BaO_3-layers in the hexagonal perovskite block; *e.g.* $Ba_5Ru_{1.6}W_{0.4}O_9Cl_2$ for n = 2 [Tancret *et al.*, 2004], $Ba_6Nb_2IrO_{12}Cl_2$ for n = 3 [Wilkens *et al.*, 1992], $Ba_7Ru_4O_{15}Cl_2$ for n = 4 [Wilkens *et al.*, 1991], and $Ba_8Ru_3Ta_2O_{18}Br_2$ for n = 5 [Wilkens *et al.*, 1992].

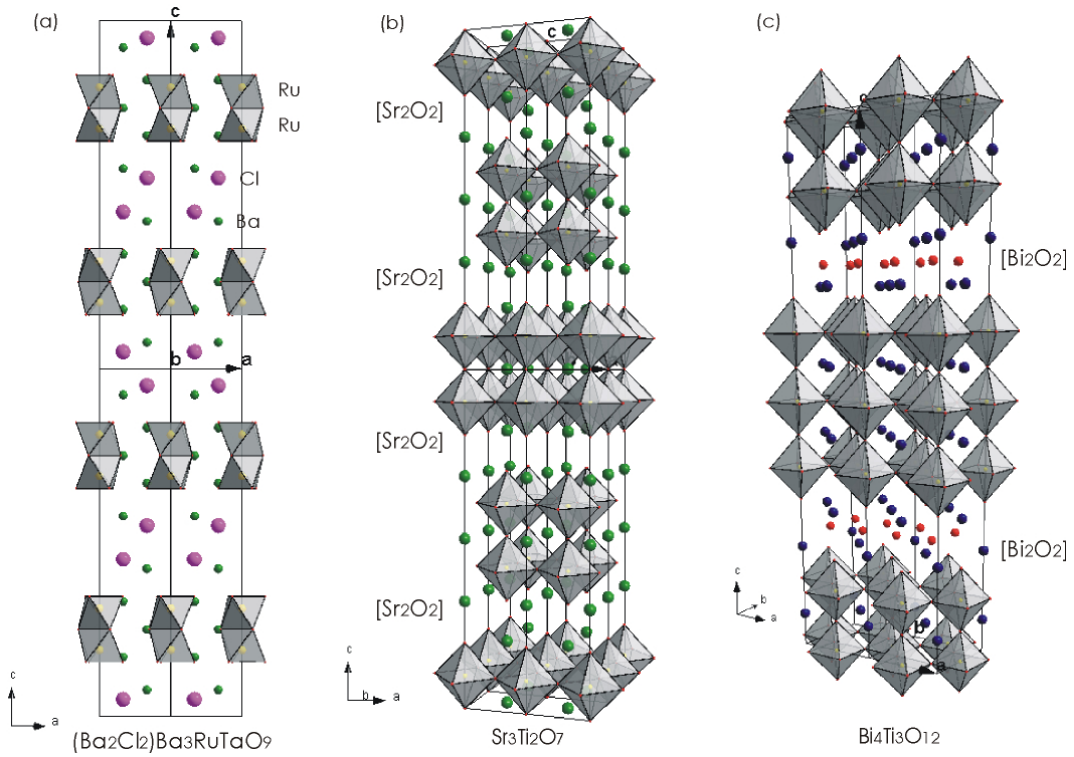

Figure 14: (a) Polyhedral representation of $(Ba_2X_2)(Ba_{n+1}B_nO_{3n+3})$ crystal structure with alternating sequence of two h-BaO_3 and two rock salt-type BaCl layers along $[001]_H$. **(b)** Polyhedral representation of an ideal Ruddlesden-Popper crystal structure-type with space group symmetry I4/mmm viewed along $[100]_H$; the two structural blocks, sheets with NaCl configuration and cubic perovskite-like slabs alternate along $[001]_H$. **(c)** The crystal structure of an ideal Aurivillius phase with space group symmetry Fmmm viewed along $[100]_H$; the two structural blocks, sheets of (Bi_2O_2) and cubic perovskite-like slabs alternate along $[001]_H$.

1.7.3. Derivatives of hexagonal perovskite crystal structure based on AX_3 and A_2X layers

The crystal structure comprises AX_3 and A_2X layers perpendicular to the c-crystallographic direction belong to the hexagonal-perovskite intergrowth family with the general formula $(A_2X)(A_{n+1}B_nO_{3n+3})$, where A is alkaline earth or rare earth ion and X may be oxygen or monovalent anion; *e.g.* Cl^-. These structures are recognized by hexagonal perovskite block and graphite-like sheet. The simple representatives; *e.g.* $Ba_5Ru_2O_{10}$ and $La_2Ba_{0.8}Sr_{0.6}Ca_{1.6}Mn_2O_{10}$ [Dussarrat *et al.*, 1994 and Bie, *et al.*, 2002], build up the periodic stacking of three hexagonal close packing AO_3 layers and one A_2X layer (Fig.15a). This stacking sequence results the formation of double face-sharing octahedral layer and one graphite-like A_2X layer, which alternate along the c-axis, and three type of coordination for A-site cations (Fig.15b).

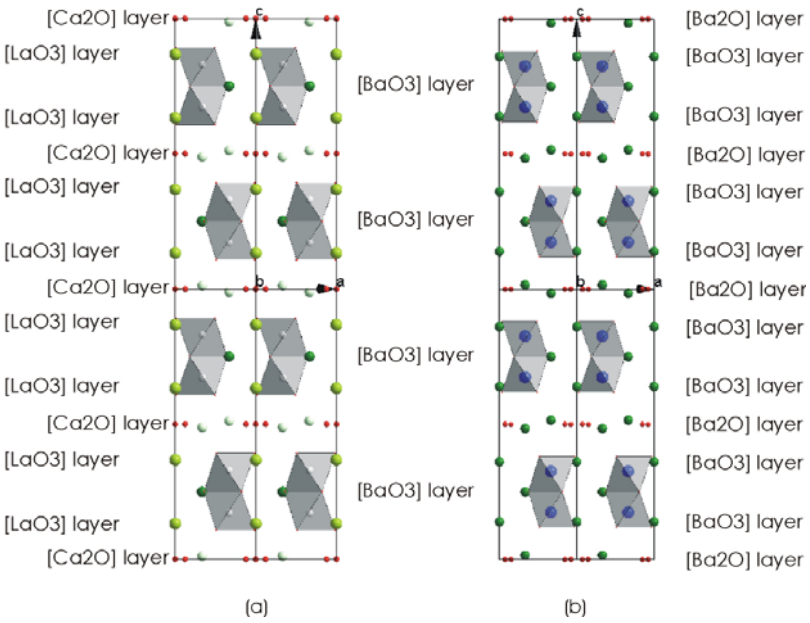

Figure 15: (a) The clinographic projection of $(A_2X)(A_{n+1}B_nO_{3n+3})$ for n = 1 **(b)** The environment of A-site cations in $Ba_5Ru_2O_{10}$.

1.7.4. Derivatives of hexagonal perovskite crystal structure based on A_3X_9 and $A_3A'X_6$ layers

Staking of mixed A_3X_9 and $A_3A'X_6$ layers along c-direction of hexagonal unit-cell creates prismatic sites with triangular bases and hence leads to a new family of phases with a general formula $A_{3n+3m}A'_nB_{3m+n}O_{9m+6n}$, where n/m is the ration between the number of A_3X_9 and $A_3A'X_6$ layers [Perez-Mato *et al.*, 1999]. The two successive h-A_3X_9 layers form the octahedral sites, while the introduction of one $A_3A'X_6$ layer, which is designed by dashed symbol such as A', B' and C', into the hexagonal stacking sequence of A_3X_9 layers denotes by undashed symbol leads to the formation of trigonal prismatic sites [Huve *et al.*, 1997].

The main feature of compounds from $A_{3n+3m}A'_nB_{3m+n}O_{9m+6n}$ series is the presence of $[A',B]O_3$ columns, which run along three-fold axis of hexagonal unit-cell. They consist of isolated trigonal prism separated by small number (*i.e.*, 1, 2, 3 or 4) of face-sharing octahedra. The size of all octahedra and prisms are in principle similar, which is forced by symmetry. Their distortion corresponds to minimum rotation of the O_3 triangles, while the heights of octahedra and prisms along c-axis may slightly fluctuate from their average value. From the ideal structural model it is expected that the average height of the prisms is significantly smaller then the heights of pairs of face-sharing octahedra. The $[A',B]O_3$ columns are shifted along their length axes over one or two structural units relative to adjacent column. As a result within the same layer trigonal prisms cannot occur in adjacent positions. Moreover, prisms are also never consecutive within the column. The octahedral O_6 units are occupied by B cations, whereas the A'-cations are located in the center of trigonal prisms or are displaced toward

their rectangular faces [Abraham *et al.*, 1994]. In addition, A-cations constitute chains in between the [A',B]O_3 columns. For the compounds with short period along the c-crystallographic direction, i.e., small n/m ratio, the A atoms in the chain are normally located either at the level of the center of a triangular prism or at the level of the O_3 triangles in neighboring columns.

However, the appearance of chains and columns in c-crystallographic direction make the crystal structures of $A_{3n+3m}A'_nB_{3m+n}O_{9m+6n}$ family related to the 2H hexagonal perovskite. The structure of all the phases belonging to this family are characterized by a parameter *a* ~10Å ($\sqrt{3}a_P$) and a parameter *c*, which is much larger than the perovskite lattice parameter c_P. In general, the c parameter is strongly related to the number of layers stacked along *c*-axis and depends on the manner to which the particular layers are stacked along *c*-crystallographic direction. Perez-Mato *et al.* [1999] observed an approximate relation of the unit-cell parameter c to the average thickness of a layer (*i.e.*, "e"). This can be deduced from two general considerations: *i.e.*, in order to obtain and $A_3A'O_6$ layer from an A_3O_9 layer there are three different possibilities of a substitution, hence there are three different types of $A_3A'O_6$ layers in the unit cell (Fig. 10e-f), including A', B' and B'$_m$. Therefore, the total number of $A_3A'O_6$ layers in the unit cell has to be multiple of three. Moreover, whether the stacking of $A_3A'O_6$ and A_3O_9 layers is absolutely hexagonal the total number of layers in the-unit cell is expected to be even. The unit-cell parameter *c* can be then calculated for four different cases:

a) When $n + m$ is even and n is a multiple of 3, then the $c = (n + m)e$

b) When $n + m$ is even and n is not a multiple of 3, then the $c = 3(n + m)e$

c) When $n + m$ is odd and n is a multiple of 3, then the $c = 2(n + m)e$

d) When $n + m$ is odd and n is not a multiple of 3, then the $c = 6(n + m)e$

Several groups of compounds have been reported within the $A_{3n+3m}A'_nB_{3m+n}O_{9m+6n}$ series (Fig. 16). All of them are structurally related to the 2H hexagonal perovskite-like crystal structure [Stitzer *et al.*, 2001]. Between the two end-members with general formula ABO_3 ($n = 0; m = 1$) and $A_3A'BO_6$ ($n = 1, m = 0$), the three additional members with the composition corresponding to $A_6A'B_4O_{15}$ ($n = 1; m = 1$), $A_9A'_2B_5O_{21}$ ($n = 2; m = 1$) and $A_4A'B_2O_9$ ($n = 3; m = 1$) were observed.

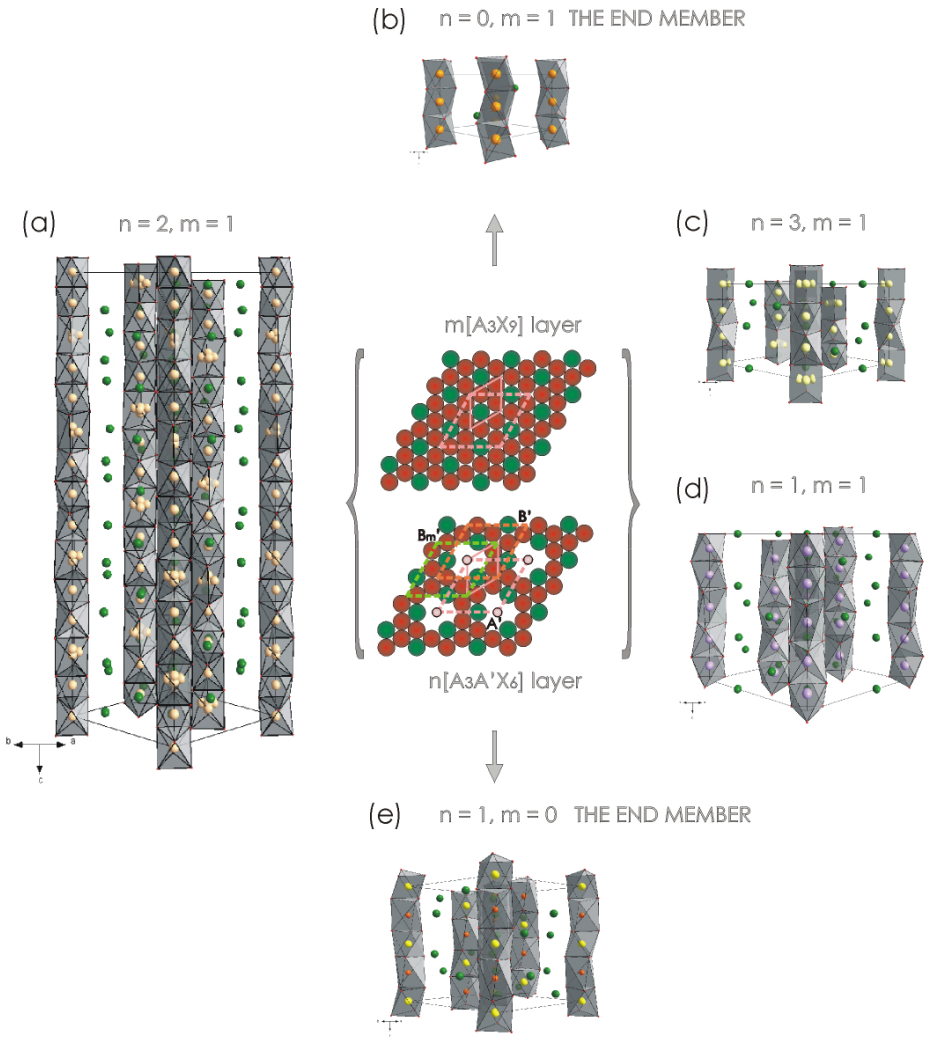

Figure 16: The clinographic projection of representative crystal structures that result from the stacking of the A_3O_9 and $A_3A'O_6$ layers (by Perez-Mato *et al.*, 1999).

The general formula of the whole family $A_{3n+3m}A'_nB_{3m+n}O_{9m+6n}$ can be expressed in an equivalent way as $A_{1+x}(A'_xB_{1-x})O_3$ with $x = n/(3m + 2n)$. In this formulation the x represents the variable in composition and can be any number between 0 and ½. It can be seen that similar compositions (*i.e.* similar value of x) in general correspond to quite different value of *n*/*m* and hence to very different unit-cell parameter c and space group symmetry. Despite of this the electron diffraction revealed similar diffraction patterns for the compounds with similar value of the composition misfit x. Moreover, electron diffraction patterns vary continuously with changing the value of x. Common patterns can be obtained if the compounds are modulated, either commensurately or incommensurately [Huvé *et al.*, 1998].

1.7.5. The modulated crystal structure of the $A_{3n+3m}A'_nB_{3m+n}O_{9m+6n}$ series

The modulated crystal structure can be considered as a periodic deformation of an average conventional structure with a space-group symmetry [Janssen *et al*, 2006]. Physically it means that neighboring unit cells are not alike. The deviation of each unit cell from an average structure can be described by periodic function with its own period. Thus the modulated crystal structures do not obey the classical requirements for crystals, *i.e.*, the lattice periodicity, but their long-range order is perfect as in ordinary crystals. The presence of such periodicity is proved by the observation of electron diffraction patterns, which exhibit two sets of reflections; the main reflections of predominately strong intensity and the additional reflection of weaker intensity called satellites. The main reflections are consistent with regular three-dimensional (R_3) reciprocal Bravais lattice, while the satellite reflections do not fit the same lattice. Therefore the whole pattern can be described in four-dimensional space [Mironov *et al*, 2003] in which the fourth basic vector a_4 is perpendicular to the a_1, a_2, and a_3 basic vectors of the R_3 direct space. Hence it can be imagined that the three-dimensional diffraction pattern is a projection of a 3+d-dimensional reciprocal lattice. Thus, the a_4 is defined through a projection of corresponding reciprocal vector a_4^*, called modulation vector q in R_3^* reciprocal space. This modulation wave-vector q represents an integral linear combination of some basic modulation wave vectors, *i.e.*, $q = \sum_{i=1}^{3} k_i a_i^* = \alpha a^* + \beta b^* + \gamma c^*$ [de Wolff *et al.*, 1974]. When at least one component of a basic modulation vector q (α, β or γ) with respect to the lattice of the main reflections has the irrational value the crystal phase is called the incommensurably modulated structure [Zakhour *et al.*, 2000]. In the case of commensurate crystal structures [Loye *et al.*, 2001] the ratio between the components of the modulation vector and cell parameters is rational and the structure can be described in terms of a superstructure. The modulated crystal structure of the $A_{3n+3m}A'_nB_{3m+n}O_{9m+6n}$ series are considered as two mutually interacting subsystems each with its own set of cell parameters and space group. The first subsystem is formed by the [A',B]O_3 columns and has an average *c*-lattice parameter c_1 close to $c_P/2$, while the second subsystem corresponds to chains of A-cations and has the average *c*-lattice parameter c_2 equal to c_P. Since the two subsystems share *a** and *b** of their reciprocal lattice basis and differ in periodicity along [001] they are considered to be one-dimensionally modulated. Hence an indexation of four indexes is used, *i.e.*, (*hklm*) and each Bragg reflection H can be expressed as $H = ha^*+kb^*+lc_1^*+mc_2^*$. The modulation of both systems due to their mutual interaction contributes to the both set of main reflections and leads to the appearance of the additional reflection of weaker intensity called satellite reflections [(*hklm*) for $l \neq 0$ and $m \neq 0$]. The intensity of the satellites fall off rapidly for large *m* so that the observed diffraction spots

remain separated, although vector *H* may come arbitrary close to each other. For small m the peaks of arbitrary small intensity form a dense set, because they may come arbitrary close to each other. Whether the modulation of both subsystems is neglected the main reflections (*hkl0*) with l ≠ 0 and (*hk0m*) m ≠ 0 situated on a reciprocal lattice could be interpreted in terms of Bragg reflections produced exclusively by subsystem A and [A',B]O_3. In this case the satellite reflections will not exist. The mutual interaction of the two subsystems is reflected in that the first subsystem is modulated with the modulation period given by the average c-parameter of the other subsystem, *e.g.* the modulation period of [A',B]O_3 subsystem is c_2* and *vice*. In direct space the two subsystems can be analyzed separately as two independently modulated structures, while in reciprocal space their diffraction diagrams superpose coherently. Nevertheless in Fourier space their diffraction diagrams superpose separately. Therefore each Bragg reflection H is expressed as $H = ha^*+kb^*+lc_1^*+mc_2^* = (hklm)$.

1.7.5.1. The layered structures with general formula ABO_3 based on A_3X_9 and $A_3A'X_6$ layers

The crystal structure of the compound with the general formula ABO_3 represents the end member of $A_{3n+3m}A'_nB_{3m+n}O_{9m+6n}$ series. Due to the absence of $A_3A'X_6$ layers (n = 0), the characteristic columns consist exclusively of BX_6 face-sharing octahedra running along the c-axis of the unit cell. Consequently, these phases are considered as the 2H hexagonal perovskite polytype.

1.7.5.2. The layered structures with general formula $A_6A'B_4O_{15}$ based on A_3X_9 and $A_3A'X_6$ layers

The ideal crystal structure of $A_6A'B_4O_{15}$ members (n = 1, m = 1) is characterized by the presence of B_4O_{15} octahedral tetramers, *i.e.* four face-sharing octahedra alternating with one $A'O_6$ trigonal prism along the *c*-axis of the hexagonal unit-cell (Fig. 17a). All $A_6A'B_4O_{15}$ phases crystallize with *R*32 symmetry and can be classified into two groups depending upon whether or not octahedra and the trigonal prisms are occupied by the same atom type. When A'-cations occupy also B sites [Bazuev *et al*, 2003], they are ordered within both, octahedral and prismatic sites, but appear in different oxidation state [Campa *et al.*, 1994 and Stitzer *et al.*, 2001].

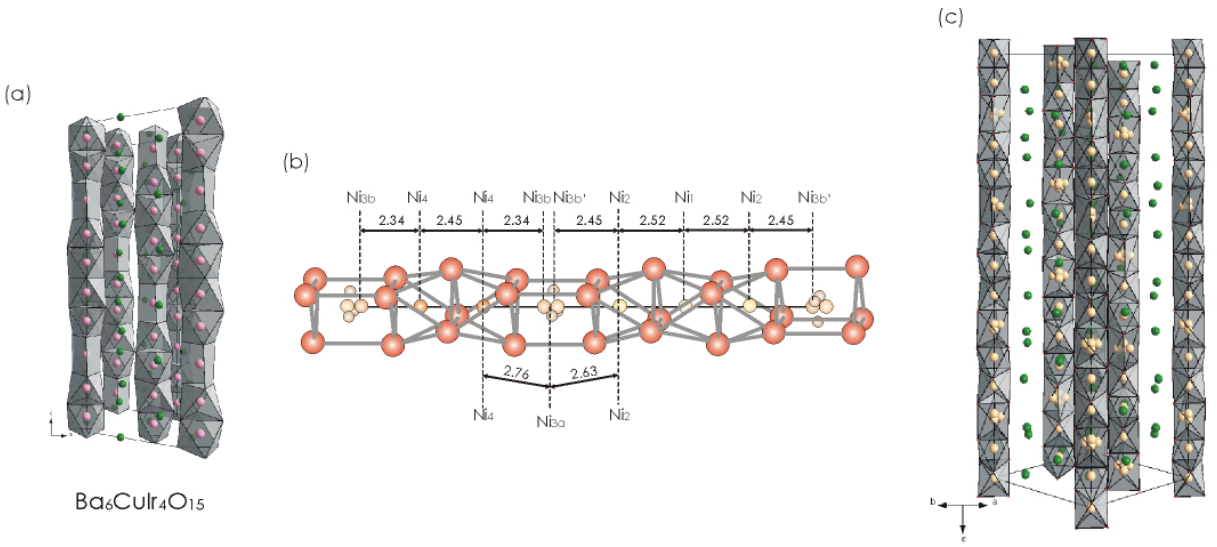

Figure 17: (a) The clinographic projection of $A_6A'B_4O_{15}$ along $[110]_H$; the columns consist of four face-sharing octahedra followed by one trigonal prism. **(b)** The NiO_6-polyhedral chain in the case of 3D commensurate approximation for $Sr_{1.2872}NiO_3$. (by Evain *et al.*, 1998). **(c)** The clinographic projection of the crystal structure of $Sr_9Nb_2O_{21}$ along $[110]_H$. The columns comprises block of two or three face-sharing octahedra occupied by Nb ions followed by one NbO_6 trigonal prism. The columns are separated by chains of Sr ions.

1.7.5.3. The layered structures with general formula $A_9A'_2B_5O_{21}$ based on A_3X_9 and $A_3A'X_6$ layers

This group of compounds is the most rare among $A_{3n+3m}A'_nB_{3m+n}O_{9m+6n}$ family. There are the only two known examples with the stoichiometry corresponding $A_9A'_2B_5O_{21}$, including $Sr_9Ni_7O_{21}$ [Evain *et al.*, 1998] and Ba_8CoRhO_{21} [Loye *et al.*, 2001]. In general, both structures consist of five $A_3A'O_6$ and three A_3O_9 layers in the unit-cell, but they differ in the stacking sequence. Hence the crystal structure of $Sr_9Ni_7O_{21}$ (Fig. 17b-c), which is a hypothetical commensurate counterpart of $Sr_{1.2872}NiO_3$, consist of two types of octahedral blocks, including Ni_3O_{12} trimeric unit and Ni_2O_9 dimeric group, connected to each other trough trigonal prism. In the NiO_6 polyhedral chains, three dickel environments can be distinguished octahedral (Ni1, Ni2, Ni4), square-like (Ni3a) and trigonal prismatic (Ni3b, Ni3b').Ni2 is displaced from the octahedron center toward trigonal prismatic sites. In trigonal prismatic sites the nickel atoms are distributed over five positions; three positions close to the center of square-like laces and two positions analogue to the off-center displacement along the trigonal axis. This structural model is reliable if considering two different types of Ni ions; Ni^{2+} in trigonal prisms and Ni^{4+} in octahedra, which then results in incommensurate character of $Sr_{1.2872}NiO_3$. Although not many compounds are found within $A_9A'_2B_5O_{21}$ group, the Ba_8CoRhO_{21} [Loye *et al.*, 2001] is the first known example of a structurally characterized m = 5, n = 3 member of the $A_{3n+3m}A'_nB_{3m+n}O_{9m+6n}$ family and one of only small number of compositions other than m = 0, n

=1 that remain in a commensurate form. Therefore the composite structure of Ba_8CoRhO_{21} consists of six consecutive RhO_6 octahedra followed by one disordered CoO_6 trigonal prism.

1.7.5.4. The layered structures with general formula $A_4A'B_2O_9$ based on A_3X_9 and $A_3A'X_6$ layers

The chain structures of compounds with general formula $A_4A'B_2O_9$ are formed by hexagonal stacking of one A_3O_9 and three $A_3A'O_6$ layers normal the c axis [Perez-Mato et al., 1999]. These infinite columns consist of two face-sharing octahedral block alternating with isolated trigonal prisms (see figure 16c). The columns are shifted along their length axes over either one or two structural units relative to adjacent one. Hence within the same layer trigonal prisms cannot occur in adjacent positions. However, there is evidence of a local diffusion of three oxygen atoms out of A_3O_9 layer into neighboring trigonal prism. This diffusion locally transforms A_3O_9 layer into $A_3A'O_6$ and change a trigonal prism in $A_3A'O_6$ layer into two octahedra. Trigonal prismatic interstices can thus migrate by an oxygen vacancy diffusion mechanism, without changing the layer stacking mode. In this case two trigonal prisms can occur at the same level in adjacent column.

All members of this series have fully occupied octahedral positions, while trigonal prismatic sites may remain vacant as in $Sr_4Ru_2O_9$ [Dussarrat *et al.*, 1995], partly occupied as in more complex $Sr_{12}NaNi_7O_{23}$ [Strunk *et al.*, 1994] or fully occupied as in $Sr_4Ni_3O_9$ [Huvé *et al.*, 1998] and $A_4A'Ir_2O_9$ (A = Sr, Ba; A' = Cu, Zn) [Battle *et al.*, 1998]. The $Sr_4Ni_3O_9$ and strontium homologue of $A_4A'Ir_2O_9$ members may appear in commensurate and incommensurate structural form (Fig. 18a-c).

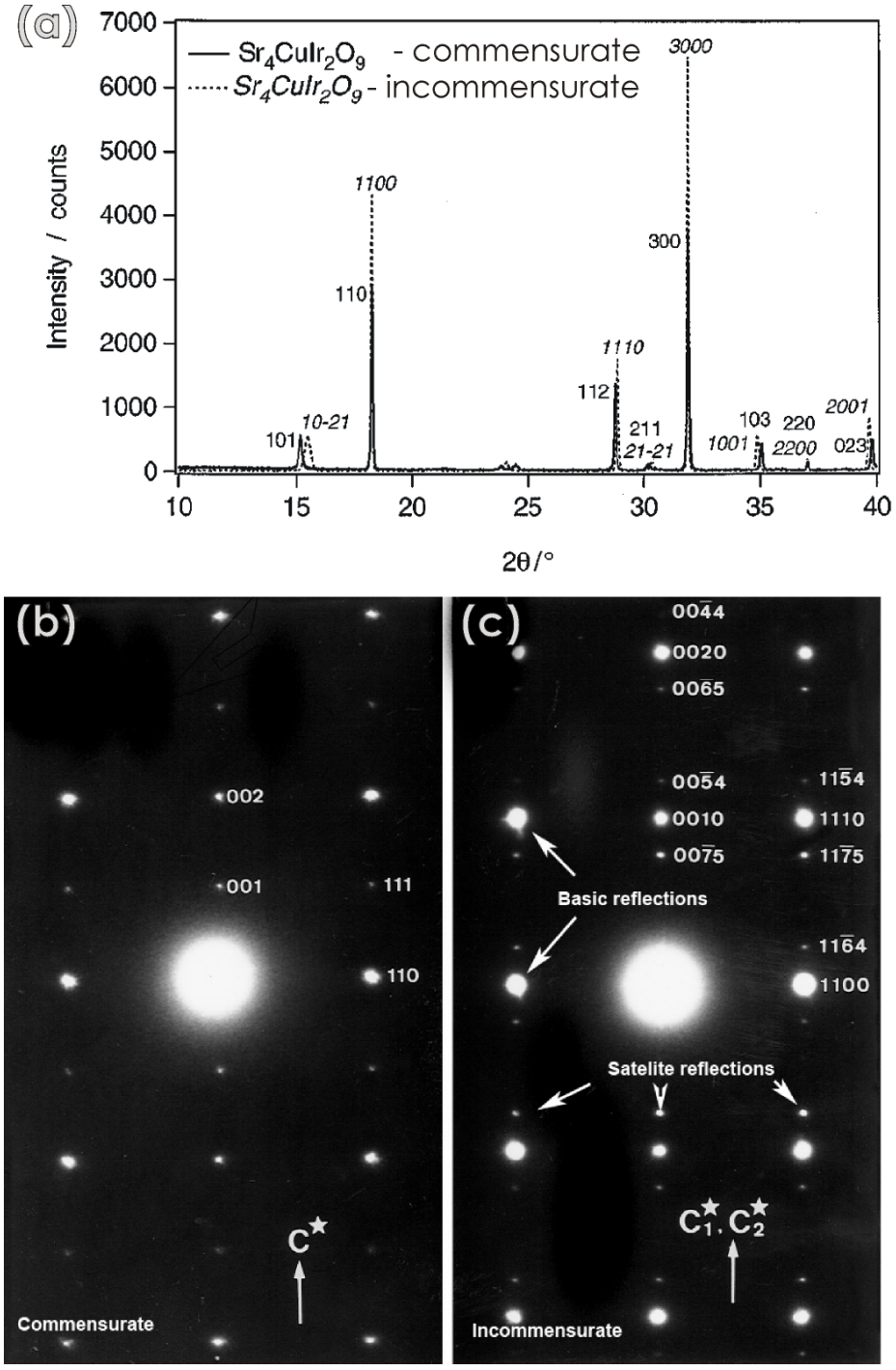

Figure 18: (a) The superposition of two X-ray diffraction patterns corresponding to commensurate (solid line) and incommensurate (dashed line) $Sr_4CuIr_2O_9$. The {*hk0*} reflections in both patterns perfectly overlie each other and allow the calculation of the unit-cell parameter *a* or *b*, since the symmetry of $Sr_4CuIr_2O_9$ is trigonal. The {*hklm*} reflections with $I \neq 0$ for incommensurate pattern are shifted to both higher and lower d-value then corresponding {*hkl*} peak with $I \neq 0$ in commensurate pattern and thus preventing the determination of a unique value of c. **(b)** The $[1\text{-}10]_H$ zone axis electron diffraction patterns of a commensurate $Sr_4CuIr_2O_9$ phase. **(c)** The $[1\text{-}10]_H$ zone axis electron diffraction patterns of an incommensurate $Sr_4CuIr_2O_9$ with pair of satellite reflections (by Battle *et al.*, 1998).

1.7.5.5. The layered structures with general formula $A_3A'BX_6$ based on $A_3A'X_6$ layers

A host of the oxides with the general formula $A_3A'BO_6$, where A indicates alkaline earth ions and A' as well B denotes large assortment of metals including alkali and alkaline earth, transition, main and REE metals, represent the end-member in $A_{3n+3m}A'_nB_{3m+n}O_{9m+6n}$ series (m = 1, n = 0). Their crystal structure is characterized by infinite one-dimensional chains of alternating face-sharing trigonal prism and octahedra along $[001]_H$ (Fig. 19a). Each column is surrounded by six parallel neighboring columns that are separated by A-site cations being in disordered square atiprismatic coordination [Darriet *et al.*, 1996]. As this crystal structure is made up of only $A_3A'X_6$ layers, it contains the maximum number the trigonal prisms in the columns, 50%.

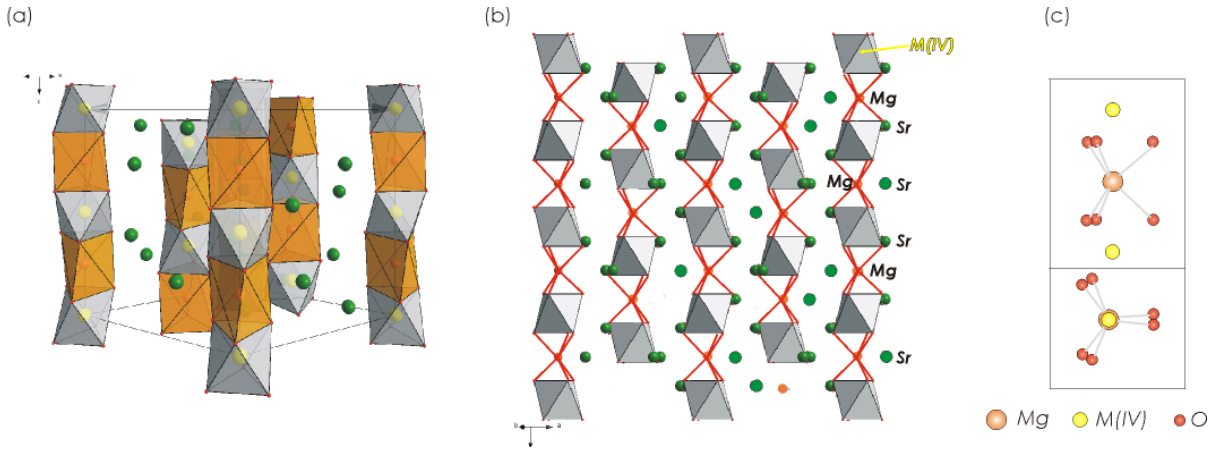

Figure 19: (a) The clinographic projection of rhombohedral aristotype with general formula $A_3A'BO_6$ (m=0, n=1). **(b)** The one-dimensional chain structure of Sr_3MgMO_6 (M = Pt, Ir, Rh) viewed along the $[100]_H$ direction. The IrO_6 octahedra are shown as gray polyhedra while trigonal prisms in the chain are pointed out by M-O bonds. **(c)** The coordination environment around the trigonal prismatic metal sites and corresponding model of twisted polyhedra (by Núñez *et al.*, 1997).

The ability to incorporate numerous of elements in various oxidation states into the layered crystal structure yield many compositional analogues. Both binary and ternary counterparts have been reported. The main feature of binary compounds is the occupancy of two crystallographically different cationic sites with identical ion. This might include identical cation on A and A' sites in the crystal structure as it is the case in K_3KMnCl_6 [Villars *et al.*, 2007] and Ca_4CaPtO_6 [Claridge *et al.*, 1997], or identical cations on A'- and B-site positions, i.e., Ca_3CoCoO_6 [Fjellvåg *et al.*, 1996 and Whangbo *et al.*, 2003]. On contrary, ternary compounds do not have identical A- and B-site cations [Stitzer *et al.*, 2002] but could have

identical A- and A'-cations as it was observed in the only known example with rare earths on the A site, *i.e.*, $(A_{3-x}Na_x)NaBO_6$, where A = La, Pr, Nd and B = Rh, Pt [Macquart *et al.*, 2006].

The combinations of cations in the crystal structure of both, binary and ternary compositions follow a hard and fast rule of oxidation state for cations in octahedral and prismatic sites. The sum of their oxidation state has to be identical to 6+. Thus the oxidation state for A'- and B-site cations are in the ratio 1+/5+ as in the case of Ca_3NaRuO_6 [Claridge *et al.*, 2004] or $NaBa_3IrO_6$ [Frenzen *et al.*, 1996], 2+/4+ as in Sr_3ZnPtO_6 [Smith *et al.*, 2001], 3+/3+ in $Sr_3(REE)RhO_6$ [Layland *et al.*, 1998] or MSr_3NiO_6 [James *et al.*, 2006] and 4+/2+ as known from Sr_3NiPtO_6 [Nguyen *et al*., 1994]. The examples of this homologue are quite diversified since A-site positions might include Ca, Sr, Ba, K, Cs, Rb, etc. Octahedral and trigonal prismatic sites accommodate a wide variety of metals in diverse oxidation (A' = Ca, Sr, Ba, Cu, Zn, Li, Na, Rb, Cs, REE; B = Nb, Ir, Pt, Ru, Rh, Sb, Pb). This indicates that trigonal prismatic site prefers the larger of the two elements, which can be either in the middle of the prism or located in one of the three square faces. The displacement from the threefold rotation axis in favour of the square faces is known in $A_3A'BO_6$ with Jahn-Teller ions, *e.g.*, Cr^{2+} or Cu^{2+} located in prismatic sites. Thus the strong preference of copper ion in Sr_3CuRhO_6 [Stitzer et al., 2002] to move from the center to near a face of trigonal prism results the crystal structure distortion and lowering the symmetry from rhombohedral aristotype with space group symmetry *R-3c* to monoclinic *C2/c*. Moreover, Sr_3CuRhO_6 may appear together with Sr_3NiRhO_6 analogue in an incommensurable form. There are two known processes involved in the transformation between a commensurate and an incommensurable phase. One is the incorporation of extra oxygen into trigonal prismatic sites, resulting in the conversion of one trigonal prismatic site into two octahedral. Another potential process involves the migration of $[A]_\infty$ chain cations into the transition metal $[(A',B)O_3]_\infty$ chain.

The cation displacement form the central positions in trigonal prisms (Fig. 19b) commonly accompanies their distortion away from ideal eclipsed geometry. The distortion, which is characterized by a twist of the opposite triangular faces about the threefold axis is known in $A_3A'BO_6$ phases with rare earth cations in trigonal prismatic positions [Layland *et al.*, 1998] and in platinum homologue, *i.e.*, Sr_3MgPtO_6 [Nguyen *et al.*, 1994 and Núñez *et al.*, 1997].

2. Aims and Hypothesis

The current worldwide proliferation of wireless communication technologies operating at microwave frequencies has been increasing the production of dielectric applications and development of dielectric materials, in particular, the perovskite based materials. Their compositional flexibility usually influences the crystal structure of the material and consequently electrical properties. This challenge has led to great efforts to develop a suitable ceramics for particular application. The progress in the production technology resulted in a wide variety of synthetic perovskite and perovskite-related materials, which exhibit a wide array of electrical properties, ranging from dielectrics [Barwick *et al*., 2006], ferroelectric [Zhang *et al*., 2006], piezoelectric [Xu *et al.*, 2005], trough semiconductors [Sahner, 2006] to high-temperature superconductors [Hegde *et al.*, 1992]. Many of these materials, which have already been used for commercial applications, are based on cubic close-packed perovskite crystal structure. Their microwave dielectric properties are relatively well understood; in particular the influence of B-site cation ordering and an octahedral tilting [Levin *et al.*, 2001, 2002], which are strongly related to the variation of the temperature coefficient of resonant frequency (τ_f) and quality factor (Q x f) of the ceramic.

Recently, there has been growing interest in the dielectric properties of hexagonal perovskite-like materials. The systems have enhanced compositional flexibility with respect to cubic perovskites, due to their ability to accommodate B-site cation vacancies, which influence ordering on B-sublattice and consequently dielectric properties of the material [Thirumal *et al*, 2005]. Interesting microwave dielectric properties of tantalate and niobate cubic perovskite-type ceramics (Kawashima *et al.*, 1977, Desu *et al.*, 1985, Yoon et al., 1994 and Liu *et al.*, 2006) encouraged us to study possible hexagonal phases within the BaO-rich region of the $BaO\text{-}Nb_2O_5$ binary and $BaO\text{-}Nb_2O_5\text{-}WO_3$ ternary system.

Even though the $BaO\text{-}Nb_2O_5$ binary system was extensively studied by several authors, the literature on many compounds in the BaO-rich part of this binary system, in particular of the $Ba_4Nb_2O_9$ polymorphs, is scarce and contradictive. However, four $Ba_4Nb_2O_9$ polymorphs have been identified by comparing the X-ray diffraction and thermo-gravimetric data. These include α, β', β and γ modifications. The crystal structure of these polymorphs has not yet been solved. Only the type of the unit-cell has been suggested and unit-cell dimensions assessed. Therefore, the primary objective of my research was to solve the crystal structure of individual $Ba_4Nb_2O_9$ modification in terms of transmission electron microscopy and X-ray diffraction analyses. Beside this, the inconsistencies regarding the polymorphic phase transitions suggested a detailed phase transition, synthesis condition and decomposition studies in $Ba_4Nb_2O_9$ system. However, understanding the behavior of $Ba_4Nb_2O_9$ as a function of temperature together with the crystal structure of individual polymorphs is of a crucial

importance for understanding a dielectric behavior of perovskite ceramic, mainly from the aspect of potential applications in communication systems.

Similar phases were observed within the BaO-rich part of the $BaO–WO_3–Nb_2O_5$ ternary system [Kemmler-Sack *et al.*, 1979-1981 and Rother *et al.*, 1980]. These include the $Ba_6W_{3-x}Nb_xO_{15-x/2}$ solid-solution ($1 \leq x \leq 2$) the $Ba_9Nb_6WO_{27}$, $Ba_4Nb_2WO_{12}$ and $Ba_3Nb_{2-x}W_xO_{9-x/2}$ for ($x \geq 2/3$).

The literature examination revealed that their formation is delicate and deserves more attention. We decided to investigate the synthesis conditions for both end-members (for x = 1, 2) laying on the virtual tie-line $Ba_4Nb_2O_9–Ba_2WO_5$ and for the three other ternary phases on the virtual tie-line between $Ba_5Nb_4O_{15}$ and $Ba_3W_2O_9$. Although a lot of research has been done on the crystal structure of the compounds with nominal compositions of $Ba_9Nb_6WO_{27}$, $Ba_4Nb_2WO_{12}$ and $Ba_3Nb_{2-x}W_xO_{9-x/2}$ for ($x \geq 2/3$), the crystal structure of $Ba_6W_{3-x}Nb_xO_{15-x/2}$ solid-solution in the compositional region $1 \leq x \leq 2$ has not been solved jet. The existing structural data for this solid-solution series indicate that the compounds across the whole composition range might crystallize as a 5-layered hexagonal perovskite with an *hhccc* stacking sequence in the *P-3m1* space group, where some Ba-atoms should occupy the octahedral sites of the structure [Kemmler-Sack *et al*. 1980]. Nevertheless, it seems very unlikely that relatively large Ba-atoms would occupy the octahedral sites, while the nominal composition implies that the compounds in this compositional range may form 6-layered hexagonal perovskite-like structures.

Moreover, there are no results reported on microwave dielectric properties of these hexagonal perovskite ceramics, although the materials are potentially interesting for applications in microwave communication systems. Hence, the sub-tusk of my research was to characterized dielectric properties of BaO-rich hexagonal phases within the $BaO–Nb_2O_5–WO_3$ binary system.

3. Methods

3.1. Methods for the phase observation

3.1.1. X-ray diffraction

The X-ray diffraction is an experimental technique used for the investigation of the crystal structure and phase analyses of the material. Additionally, the method can be applied to the study of phase equilibrium, stress and particle size measurements and to the determination of the orientation of one crystal or the ensemble of orientations in a polycrystalline aggregate.

The method is based on X-rays, *i.e.*, electromagnetic radiation with the wavelength in the range 0.1-100Å. The simplest and most commonly used source of X-ray radiation is the X-ray tube. This conventional device is composed of two metal electrodes (cathode and anode) placed inside meta/glass tube under vacuum. In the X-ray tube the cathode, *i.e.*, tungsten filament is electrically heated. Therefore it emits electrons, which are then accelerated towards the anode. The X-rays are generated after the impact of high-energy electrons on the water-cooled anode. These X-rays exit the tube through the beryllium windows. Typical anode materials that are used in X-ray tube produce characteristic wavelengths between 0.5 and 2.3 Å. This is characteristic wavelength for Ag and Cr anode. As an anode material could also be used Mo ($K\alpha_1$ = 0.71 Å) Cu ($K\alpha_1$ = 1.54 Å), Co ($K\alpha_1$ = 1.79 Å) and Fe ($K\alpha_1$ = 1.93 Å).The generated X-ray spectra consist of several intense peaks, *i.e.*, characteristic spectral lines, i.e., $K\alpha_1$, $K\alpha_2$ and $K\beta$ superimposed over continuous background, which is generated by electrons decelerating rapidly. The characteristic lines results from the transition of upper level electrons in the atom core to vacant lower energy levels, from which the electron was ejected by the impact of an electron originating from the cathode. These three characteristic lines produce a three Bragg peaks in the X-ray pattern for each plane of the studied material. In order to increase the quality of the X-ray diffraction spectra, *i.e.*, reduce the wavelength dispersion (polychromatic nature) and angular divergence, which yields the Bragg peak broadening, and its asymmetry, the monochromator and collimator are usually employed in diffraction system. The simplest collimation, *i.e.*, reduction of angular dispersion can be achieved either by divergence or soller slits. On another hand, the wavelength dispersion, including both the white radiation and undesirable characteristic wavelengths, can be reduced or even eliminated by applying monochromator; these can be either β-filters or monocrystal of Si, Ge and LiCl, etc.

Ideally, the perfectly monochromated X-rays are directed to the powder sample where they diffract at different angles. These diffracted beams are then directed to the detector, *e.g.,* scintillation, proportional or solid-state detector, which measures the beam intensity. Namely, the detector collects X-ray photon and then converts them into a measurable signal or eventually to the X-ray diffraction pattern.

The crystal structure of the material can be studied by X-ray method considering the Braggs' law, *i.e.*, $2d_{hkl} \sin\theta_{hkl} = n\lambda$ and therefore the relationship among the diffraction angle (θ), wavelength and interplanar spacing (d_{hkl}). This law explains that the diffraction from a crystalline sample appears on a series of parallel crystallographic planes having identical Miller indices. Therefore, these parallel and equally spaced (d_{hkl}) planes are considered as a separate scattering object, which contributes to the intensity of particular X-ray diffraction peak in the XRD spectrum. Moreover, the Bragg law additionally explains that the position of X-ray diffraction peak in the XRD pattern corresponds to the angle of incident beam at which the diffraction from the group of identical (*hkl*) planes occurs.

3.1.2. Thermal analyses

The term thermal analysis refers to a group of experimental techniques in which mass changes of the sample is monitored against time and temperature while the temperature of the sample, in a specified atmosphere, is programmed [Haines, 1995]. These methods follow and explain the physical properties of the material and the nature of its chemical changes. Thus one can study phase changes, mechanical changes, decomposition, an oxidation and a dehydration process of the compound. The methods also enable detection of the heat capacity, chemical and surface reactions, etc. The desirable experimental conditions for certain type of thermal analyses applied in particular studies of the powdered sample are reported by Haines [1995] but in general, the standard experiment for any of this method involves about 10–20 mg of the sample, which may be run against the inert, dry and pure reference material such as Al_2O_3 or SiC or nowadays just against the empty crucible. Depending on the applying temperature, the examined and the reference sample is weighed into the aluminum pan or into the platinum or the ceramic crucible (Al_2O_3).

However, the most commonly used thermal methods are: differential thermal analysis, differential scanning calorimetry, thermo-gravimetry, which could be coupled to the mass spectrometer (MS). A DTA method refers to monitoring of the difference in temperature (ΔT) between the specimen and the reference material against time. A DSC method refers to monitoring of the difference in heat flow to a sample and to a reference against time or temperature. Both methods are sensitive for detecting phase transitions and reactions during heating the sample, which is revealed from the endothermic and exothermic nature of event in the curve. On another site the thermo-gravimetry is the most frequently carried out in solids and is used for monitoring the mass changes of the sample against the temperature or time. The sample should be small, powdered and spread evenly in the crucible in order to provide a meaningful analyses and reproducible results. The problems might arise if the sample is not

homogeneous; whether one region of the sample is more porous, more easily oxidized or have a higher moister content. The method is very useful for analyzing the oxidation, dehydration or the decomposition, *e.g.*, decarbonatisation of the sample. The TG, DTA and DSC are regularly combined to TG/DTA or TG/DSC techniques, where the changes of mass and heat are simultaneously measured. Additionally, TG, DTA and DSC are often coupled to the mass spectrometry (MS), which enables the determination of evolved gasses during the thermal process. Therefore during the decarbonatisation of the material the decomposition products, *i.e.*, $CO_{2\ (g)}$ may be monitored against temperature. The gas phase is then introduced into the mass spectrometer under high vacuum (1.33×10^{-5} mbar), where the molecules of CO_2 are ionized into CO_2^+, CO^+, CO_2^{2+}, C^+ and O^+ by high energy electron impact. These positive ions are accelerated through the alternating electric field of the quadropole, which separate them according to the mass/charge ratio. Afterwards, the ions are detected by a detector, *i.e.*, an electron multiplier.

3.2. Methods for the crystal structure determination

A complete crystal structure determination can be divided into two distinct steps including solving the structure and refining it. Solving the crystal structure means finding an appropriate structural model for at least the most important atoms, usually the heaviest ones. For solving the crystal structure any methods including empiric accession may be used. The atomic position should be found within about 0.25 Å from their ideal position. To solve a crystal structure we need to know both the amplitudes and the phases of the largest structural factor. Various diffraction patterns, *i.e.*, X-ray, neutron and electron-diffraction patterns contain only the amplitude of the structural factors whiles the phases part is lost. It is possible to get both the amplitude and the phase of the structural factor directly from electron microscopy images. Commonly, these data are not sufficient to get the structural information about the material. One always has to confirm the structure reconstructed from the high-resolution transmission electron microscope images with simulation images calculated from suggested structural model. The accuracy of atomic coordinates obtained from a two-dimensional projection by HRTEM to 2 Å resolution is about 0.2 Å. The ED extends to much higher resolution, typically 0.8 to 0.5 Å. These data have the further advantage, compared with the image data, that they are not distorted by the contrast transfer function. The disadvantage is that they contain a higher proportion of multiply scattered electrons than that of HRTEM images, mainly because SAED patterns are taken from thicker regions than a thin parts of HRTEM images that are cut out and take for image processing. The fact that SAED patterns do not contain phase information is no disadvantage for the refinement, because only the amplitude is used at this stage of a structure determination. The following

chapter describes the equipments and experimental techniques used in the crystal structure determination procedure of $Ba_4Nb_2O_9$ and $Ba_6Nb_2WO_{14}$ phase.

3.2.1 The crystal structure refinement based on XRD data

The X-ray powder diffraction technique is a powerful tool in the field of crystallography. It is widely used not only for quantitative and qualitative phase composition of the material, but also for evaluation of crystallite size, strain parameters, preferential orientation and most importantly, for the crystal structure characterization. The XPRD data of a crystalline material are recorded in the form of powder diffraction profile, which is considered as a collection of individual reflection profiles each with its own peak height, a peak position and an integral area. The latter is related to the Bragg intensity (I_{hkl}), which is proportional to the square of the absolute value of the structural factor $|F_K|^2$. The crystal structure characterization from XRPD pattern is performed in combination with the Rietveld method. The principle of the Rietveld method is to minimize the difference between the entire observed powder diffraction pattern (y_{obs}) and the entire calculated powder profile (y_{calc}) [see the equation 1]. The quantity minimized in this least-squares refinement is the residual (S_y). The calculated intensities (y_{calci}) are determined from the structural factor calculated from the structural model by summing of the calculated contributions from neighbouring Bragg reflections and the background [2].

$$S_y = \sum_i w_i (y_{obsi} - y_{calci})^2 \qquad (1)$$

$w_i = 1/y_{obsi}$

y_{obsi} *is observed intensity at the* i^{th} *step*

y_{calci} *is calculated intensity at the* i^{th} *step*

$$y_{calci} = s\sum_K L_K |F_K|^2 \phi(2\theta_i - 2\theta_K) P_K A + y_{baci} \qquad (2)$$

s is scale factor

K represents Miller indices hkl for a Bragg reflection

L_K *includes the Lorentz, polarization and multiplicity factors*

ϕ *is the reflection profile function*

P_K *is the preferred orientation function*

A is an absorption factor

F_K *is the structure factor for the* K^{th} *Bragg reflection*

Y_{bi} *is the background intensity at the* i^{th} *step*

3.2.2. A Transmissions Electron Microscopy

A conventional transmission electron microscope is a close analogue of the optical transmission microscope. However, a light microscope is based on light rays therefore the image contrast is produced by changes in optical absorption from one region to another of the specimen. On another hand, the electron microscope uses a source of electrons, which can never be absorbed by a specimen, excluding the sample thickness effect. They can rather be lost from the image either by large angle scattering outside the objective aperture or, as a result of their energy loss being brought to a focus on a plane far distant from the plane showing the image of elastically scattered electrons. The electrons are convenient as a probe in the study of structures in solids since they are strongly scattered by solids, allowing scattering and imaging experiments to be performed with a high information level. Apart from structural information, electrons and their energy dissipation products are bearing valuable chemical information of the local structure owing to a wide variety of electronic transitions.

However, the transmission electron microscope uses a series of magnetic lenses to manipulate the electron beam (0.2 nm in diameter) generated at a high potential electron gun, *i.e.*, an electrically heated filament or FEG. The electrons emitted by the filament are accelerated towards the earth. On their trajectory they are focused, by a condenser lens system with field limiting aperture, onto the specimen. A diffraction pattern or an image from the specimen is obtained on the fluorescent screen via an objective, diffraction, intermediate and projector lens system. The region for obtaining the electron-diffraction may be chosen using a selected area aperture, while the image contrast information carried by transmitted electrons may be enhanced or restrained using an objective aperture.

Depending on the resolution of the microscope, different properties of electrons determine the contrast in electron microscope images. Thus, we distinguish a low and medium resolution imaging and high-resolution imaging. In the case of a low and medium resolution imaging the contrast in the image is mainly formed due to the variations in scattering intensity. This contrast is caused by variations in scattering potential of the sample and by intercepting the electrons scattered through angles larger than the objective aperture. Therefore it is known as *amplitude (scattering) contrast*. The amplitude contrast is increased at lower voltages and through the use of smaller objective apertures and thicker specimens. Additionally, less intense sections in image originate from the regions of larger scattering potential. At higher resolution the contrast formation mechanism becomes different. In this case the *phase contrast* becomes the dominant contrast formation mechanism. Phase contrast arises from the interference between scattered wave (included within the objective aperture) and the incident wave at the image point. High-resolution

images commonly require larger objective apertures and the thinnest possible part of the specimen. The phase contrast, unlike amplitude contrast, would increase with accelerating voltage and at the same time allow an examination of somewhat thicker specimens. The typical examples of phase contrast are *atomic lattice* fringes and *Frensel edge*. The observation of the specimen by transmission-electron microscope may induce the time-dependent changes in the material. These include sample *degradation* and a specimen *contamination*.

Sample degradation is the results of a sample heating, ionization damage and atomic displacement. These effects can be reduced by decreasing the sample exposure to the electron-beam or increasing the irradiation area. The heating effect depends on the sample thickness, thermal conductivity and its thermal contact with the specimen holder. Additionally, the ionization damage and atomic displacement can be controlled by controlling the microscope operating voltage. The cross-section for ionization damage is lower at higher operating voltage, while the atomic displacement can be reduced by not exceeding a certain but well-defined threshold. Therefore the operating voltage depends on the composition of material that has been studied. The sample irradiation may also results in the surface contamination with carbon, which forms during the decomposition of hydrocarbons. These might be present in the microscope vacuum system or can be introduced by the sample itself. The effect can be minimized with maintaining the high-quality vacuum or by using the heating stage, which removes hydrocarbons absorbed on the surface of the specimen.

3.2.2.1. Experimental conditions for a high-resolution and a conventional transmission electron microscopy

To obtain details on scale less than 0.5 nm consistently, it is essential that the instrument for high-resolution work is kept in excellent condition. This includes satisfactory microscope position with respect to vibrations, magnetic fields, humidity, temperature and dust. Objective lens and pole-piece current changes, electronic instabilities, and any kind of column contamination must be kept to a minimum. Another important issue is the alignment procedure. This is very much the same as for conventional TEM work. In generally, one should take a special care of the following:

- Center the condensor aperture – avoid condensor aperture shift
- Correct the HT-center
- Correct the gun alignment and condensor aperture shifts
- Keep (always) the objective lens current constant

- Check the crystal zone-axis orientation in order to avoid the possible specimen tilt and consequently prevent marked focus variations
- Auto alignment correction of the objective astigmatism and HT-center

Working at HRTEM mode requires the magnification in order of 500 000x and a perfect condensor aperture alignment. Before every high-resolution session one shall check for high-voltage (HT) stability. This means that the electron beam has to be parallel with the optical axis of the microscope. The HT-center should be corrected if the electron-beam flickers more than 20 seconds. Irregular flickering of the current during this time indicates that the instrument is unsuitable for a high-resolution work. One can stabilize it by increasing the magnification to one million, centering the position of the electron beam, finding the sharp part of the sample, then correct the Z value, turn on the HT-wobbler and with X- and Y-deflectors calm down flickering. Working with TEM requires the precisely aligned microscope. This means that the gun tilt, condenser aperture centering and condenser astigmatism shall be frequently checked (every 15 minutes in first two hours of operation) during high-resolution work. The control of these is important, since the maximum possible brightness is required using a small condenser aperture to produce a source of highly coherent parallel electrons. Usually there is not need to correct the gun alignment. Whether this has to be done one has to use the magnification in the order of one million and with the button Brightness assembles the electron-beam, which is seen in the form of the triangle. The gun tilt has to be corrected if the brightest spot in this triangle is not in the center of the triangle. The spot can be dragged into the center by deflectors after the button Gun is turn on. Afterwards the condenser astigmatism, which is visible from the triangle asymmetry, has to correct. Using X- and Y-deflectors after turn on the button condensor stigmatism and make the triangle equilateral. Of course for every set of high-resolution images the crystal has to be perfectly orientated, *i.e.*, in the zone-axis orientation. The procedure is as follows:

- Again center the condensor aperture
- Expand the electron beam
- Apply the projector aperture and center it
- Turn on the button DIFF (SAED) and set the camera length (L) to 100 cm.
- Use the projectors' buttons and put the SAED image into the center of screen
- Set the value of DV to zero with focus correction
- Use the button brightness and focus the diffraction spots
- Apply the object aperture and the mirror; the aperture should not be centered - it should cross a half of the mirror
- With the button DIFF FOCUS make the edge of the mirror sharp

After obtaining the required tilt condition it is important to check if the high-voltage centre coincides with the optical axis of the microscope. At the same time the specimen plane has to be brought close to the Gaussian focus plane, which can be done by the specimen height control. This shall not be done by changing the objective current; at least

not at this stage. The final adjustments will be the auto-alignment of the focus and objective astigmatism, which is critical at the high-resolution imaging. For more accurate correction one should use an amorphous layer, which is after ion milling frequently present on the crystal surface, i.e., on the edge of the sample. For this purpose an electron-optical magnification of at least 500 000 is needed. Expand the electron-beam on the size of the screen in the microscope. Then press the button Shutter auto and use the mirror in order to measure the exposition time, which has to be 1 sec. Whether it is greater than 1 sec the image on the monitor will not show. Run the program auto alignment and with the button object focus adjust the focus for minimum contrast (Gaussian focus) and then go to under-focus by a few tens of nanometers (Scherzer focus) in order to observe coarse-grained image of amorphous layer. An on-line Fourier transform of the image will show ellipsoidal or even hyperbolic bands if the image is astigmatic. When astigmatism is properly corrected with deflectors a Fourier transform shows concentric rings for any focus setting. In the image this would correspond to a homogeneous appearance of amorphous film with no preferential direction observed in the pattern. The most important thing about the astigmatism is that it is time independent and that it is correctable. It is also important to note, that astigmatism ought to be corrected for any movement of objective aperture. To record the high-resolution image, advance the film plate and wait for few seconds to prevent undesirable influence of mechanical vibrations during exposure. Vibrations from camera mechanism may alter the specimen height by few nanometers. Therefore check for focus setting after the film advance. Depress the shutter without otherwise touching the microscope. Do not make sounds or move during the exposure. Any of these may seriously influence the quality of a high-resolution image. Care should be taken that lattice images always include, if possible, some of amorphous wedge for later astigmatism check and actual focus setting determination.

3.2.2.2. Transmission electron-diffraction techniques

Electron diffraction is a rich source of crystallographic information complementary to X-ray or neutron diffraction. The strong electron-matter interaction, implying to consider the dynamic theory, has limited the development in materials science laboratories of the structural resolution based exclusively on the electron-diffraction data. Nonetheless, dynamical effects are advantageously used in techniques such as convergent beam electron-diffraction. These methods allow one to obtain accurate crystallographic information, which can be barely accessible by other diffraction techniques. More generally, electron diffraction methods are of great interest for the determination of the symmetry in crystalline materials. At lowest level of data collection it should be possible to deduce the crystal system, its Bravais lattice and the unit-cell dimensions. Additionally, the high-quality data obtained from CBED patterns,

microdiffraction patterns and SAED patterns obtained during the tilting experiment can give the accurate information about the space-group of the crystal structure and non-stoichiometry of the specimen as it is the case in columnar misfit crystal structures.

The quality of the data depends on the quality of the specimen under study, which can be significantly affected by specimen preparation technique and beam-induced degradation. The ideal specimens for the TEM observations in terms of electron-diffraction have to be thin (typically less than 100 nm). The fractures chips formed by crushing the sample in the agate mortar in acetone media is optimum specimens form in the case of the ceramic materials. Samples prepared by an ion milling have an inevitable surface layer of amorphous phase that can be of variable thickness. This layer frequently degrades the quality of information due to the diffuse scattering. Additionally, the effects of the amorphous layers may generate stresses leading into the bending of thin regions and strain in the thicker region that can distort the pattern symmetry and complicate lattice parameter determination.

3.2.2.2.1. The electron-diffraction methods for the space-group identification

The tilting method is a tool for a crystal structure identification and determination. This is a comparable experimental technique to the microdiffraction method, which is based on observation of the shifts and the periodicity difference between the reflections located in the zero-order Laue zone with respect to the ones located in the first-order Laue zone. Moreover, the ZOLZ represents the zero layer of the reciprocal space, while the FOLZ refers to the first layer of the reciprocal lattice (Fig. 1 and Fig. 2). There is an advantage if the electron-diffraction patterns obtained in tilting experiment exhibits the higher-order Laue zones.

Since the microdiffraction patterns contain at least two layers of the reciprocal lattice it directly gives the information about three-dimensional symmetry. On contrary, conventional SAED patterns usually display only ZOLZ and thus give two-dimensional symmetry. In order to obtain 3D symmetry, *i.e*., the Bravais lattice form SAED pattern the tilting method has to be applied. In addition, the tilting method enables orientation relationship between different zone-axis patterns of individual crystal. The electron-diffraction patterns are obtained on a specific area of the specimen, *i.e.* on individual grains or single-crystals. Therefore ZAP are considered as a spot diffraction patterns, which correspond to magnified image of planar section through the reciprocal lattice taken normal to the incident beam direction.

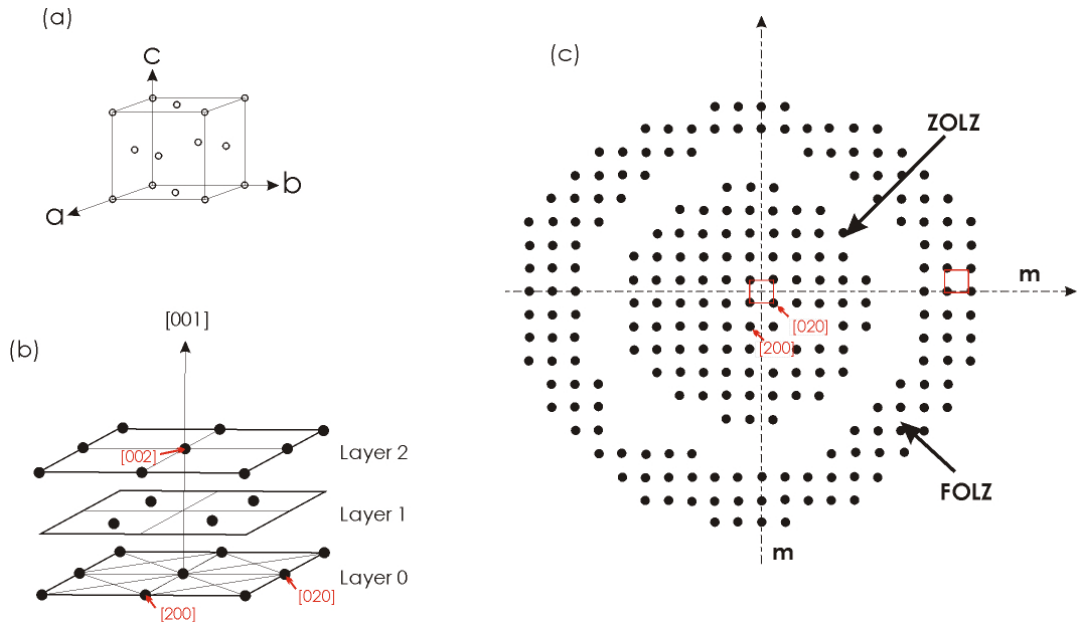

Figure 1: The effect of the centering type of the cell on the microdiffraction pattern, which shows a typical shift between the ZOLZ and the FOLZ reflections; **(a)** a direct space, **(b)** a reciprocal space and **(c)** micro-diffraction pattern in [001] zone-axis orientation (by Morniroli *et al.*, 1992).

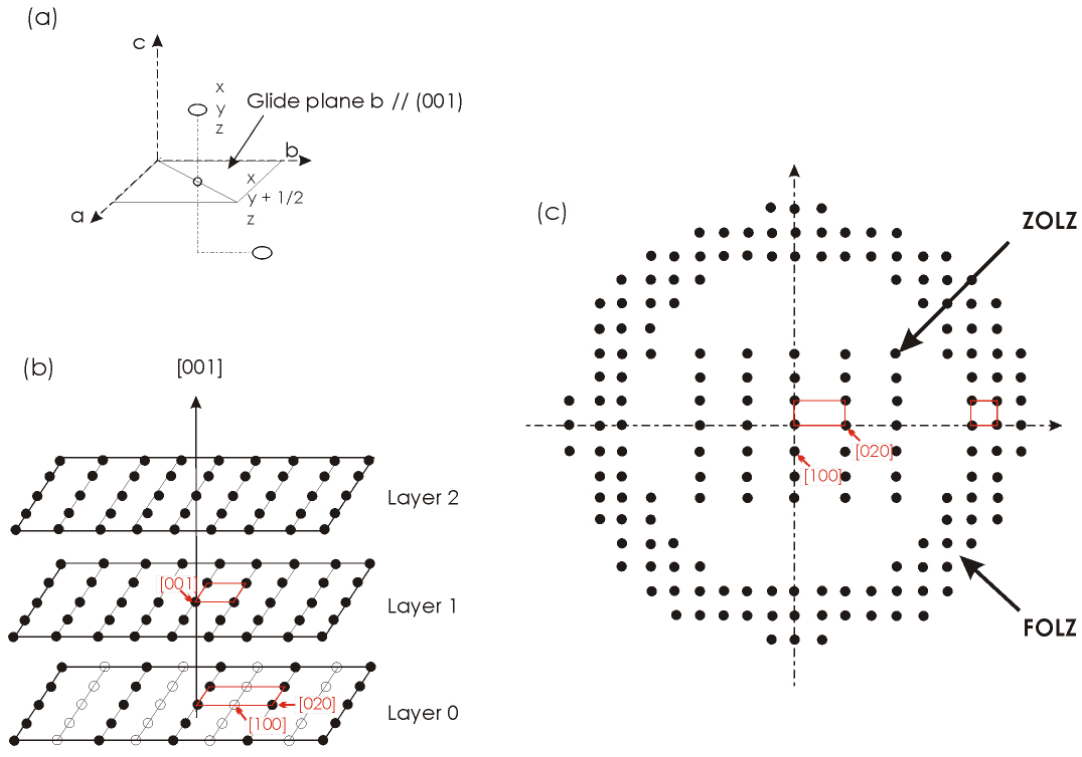

Figure 2: The effect of a glide plane on a microdiffraction pattern, which shows a typical periodicity difference between the ZOLZ and the FOLZ reflections; **(a)** a direct space, **(b)** a reciprocal space and **(c)** micro-diffraction pattern in [001] zone-axis orientation (by Morniroli *et al.*, 1992).

Stage 1: Determination of the crystal system

The first stage in identification of the possible space-group symmetry from the SAED patterns obtained in tilting experiment is the determination of the crystal system. This is made by searching for the zone-axis electron-diffraction pattern, which displays the highest "net" symmetry. Additionally the "net" symmetry takes into account only the positions of the reflections and not the intensity. In order to ascertain the symmetry, any zone axis of the crystal under examination should be set parallel to the electron beam. The crystal system is then easily deduced by means of table 1 [Morniroli *et al*., 1990].

Table 1: Deduction of the crystal lattice from the highest pattern "net" symmetry. The point groups in the parentheses refer to the SAED patterns containing only ZOLZ (by Morniroli *et al.*, 1992).

The highest "net" symmetry	***1***	***m*** or ***2***	***2mm***	***(4mm)***	***(4mm)***	***3m***	***6mm***
				absence (6mm) ↓	with (6mm) ↓	absence (4mm) ↓	
						Rhomb. latt.	Hex. latt.
Crystal system	**TRIC**	**MONO**	**ORTHO**	**TETRA** ↓	**CUBIC** ↓	**TRIG** ↓	**TRIG** ↓ **HEX** ↓
Zone axes				**[001]**	**<001>**	**[0001]**	**[0001] [0001]**
"Ideal" symmetry				↓ ↓ ***(4mm) (4)*** ↓ ↓	↓ ↓ ***(4mm) (2mm)*** ↓ ↓	↓ ↓ ***(6mm) (6m)*** ↓ ↓	↓ ↓ ↓ ↓ ***3m 3 6mm 6*** ↓ ↓ ↓ ↓
LAUE CLASS	**-1**	**2/m**	**mmm**	**4mmm 4/ m**	**m3m m3**	**-3m -3**	**-3m -3 6/mmm 6/m**

One notices that tetragonal, cubic and trigonal systems having rhombohedral Bravais lattice requires the subsequent identification. This is based on searching and identification for the extra ED patterns with characteristic high symmetry. Moreover, the table indicates that in the case of a ZOLZ net with (4mm) symmetry, a tetragonal or a cubic system is indicated and no further information is provided by the ZOLZ net (first layer in the reciprocal lattice) except for *Pa-3* cubic space group, which has (2mm) ZOLZ and 4mm FOLZ. In the case of rhombohedral or hexagonal primitive Bravais lattices the centering of the FOLZ reflections relative to the ZOLZ reflections is considered for the [0001] zone axis (Fig. 3). Whether the reflection coincides, the crystal system is either hexagonal or rhombohedral. If the reflections of one layer lay over half of the centers of the triangles formed from the net of the other layer, the

crystal system is trigonal. In this case the net symmetry is 3m, which corresponds to a primitive rhombohedral Bravais lattice. Once the crystal system is determined, the "net" symmetry allows one to identify the indexes of the zone axis

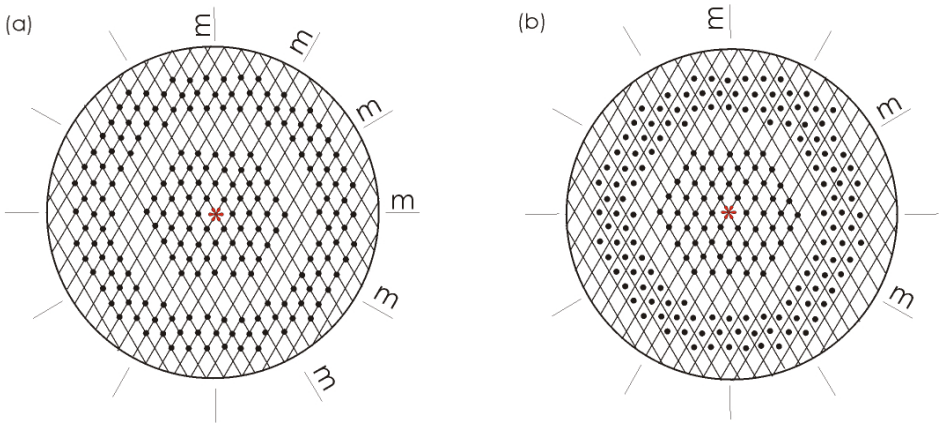

Figure 3: (a) The $[001]_H$ ZAP characteristic for a primitive hexagonal Bravais lattice. **(b)** The $[001]_H$ ZAP characteristic for a rhombohedral Bravais lattice (by Morniroli *et al.*, 1992).

Stage 2: Simultaneous identification of Bravais lattice and glide planes

The indexing of the zone-axes patterns strongly depends on the observation of the glide planes, the screw axes and the centering of the unit-cell. The glide planes give zonal extinctions (Fig. 2), as well as the screw axes (Fig. 4), while the centering produces systematic absence (Fig. 1). However, the any absence of reflections is quite frequently observed in the high-order Laue zones.

Stage 3: Deduction of the presence of screw axes

The screw axes produce serial extinctions. In the reciprocal lattice they give forbidden reflections located exclusively along the screw axis (Fig. 4b), which passes through the origin of the reciprocal lattice. These forbidden reflections can be observed for any zone-axis pattern, where the zone axis is perpendicular to the screw axis (Fig. 4c). The forbidden reflections in electron-diffraction patterns may also appear due to multiple scattering of the diffracted beam. In this case they can not be directly distinguished from the allowed reflections. One solution is to tilt the specimen around the reciprocal row containing the supposed forbidden reflections (Fig. 4d) in order to suppress the multiple diffraction paths of these reflections. This experiment should be preformed in consideration with table 2, which gives the list of screw axes and required zone-axes patterns for six crystal systems, where the forbidden reflection might be observed.

Stage 4: Deduction of the extinction symbols

The full extinction symbols are obtained by adding the partial extinction symbols deduced in stage 2 and stage 3.

Stage 5: Determination of the point group and final deduction of the possible space group

The "ideal" symmetry, which takes into the account the position and the intensity of the reflections, is directly related to the point group. The strategy to identify the point group was reported by Morniroli [1992].

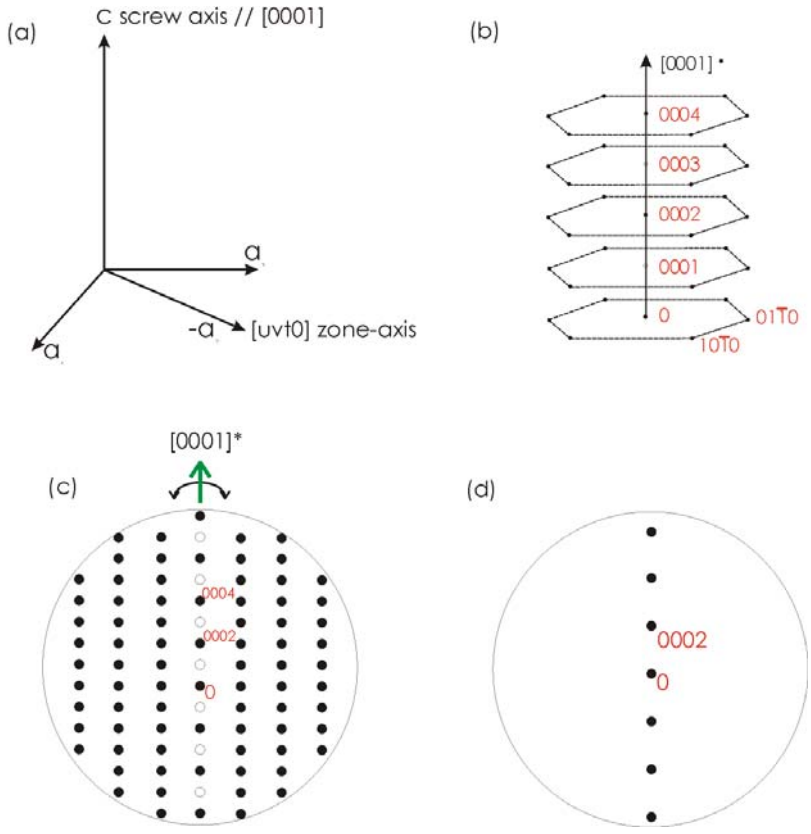

Figure 4: The effect of a 6_3 screw axis parallel to the [0001] in the hexagonal unit-cell on a microdiffraction pattern. **(a)** Direct lattice **(b)** Reciprocal lattice **(c)** [uvt0] zone-axis pattern **(d)** The effect of a rotation around the [0001]* reciprocal row (by Morniroli *et al.*, 1992).

Table 2: The list of zone-axes patterns which permits the characterization of forbidden reflections due to certain type of screw axis

Crystal system	Possible screw axes	Zone-axes required to observe the forbidden reflections due to the screw axes
Monoclinic	2_1 // [010]	[u0w]
Orthorhombic	2_1 // [001] 2_1 // [100] 2_1 // [010]	[uv0] [0vw] [u0w]
Tetragonal	4_1 // [001] 4_2 // [001] 4_3 // [001] 2_1 // <100>	[uv0] <0vw>
Cubic	2_1 // <001> 4_1 // <00>] 4_2 // <001> 4_3 // <001>	<uvo>
Hexagonal	6_1 // [0001] 6_2 // [0001] 6_3 // [0001] 6_4 // [0001] 6_5 // [0001]	[uvt0]
Trigonal	3_1 // [0001] 3_2 // [0001]	[uvt0]

3.2.2.2.2. The reconstruction of the unit cell based on specimen tilting experiment

(Example: La_2CuO_4)

Tilting method is used to recover the 3D information about the periodicities and symmetry elements present in a crystal from a set of 2D SAED patterns (Fig. 5). To this aim, the crystal has to be tilted around a direction of the reciprocal space (tilt-axis), which crosses the center of the ED pattern, until a new zone axis pattern is observed. The ED pattern perpendicular to the tilt axis, i.e., at 90° is reconstructed in this method. Hence this method is not applicable in triclinic cases, lacking the 90° symmetry.

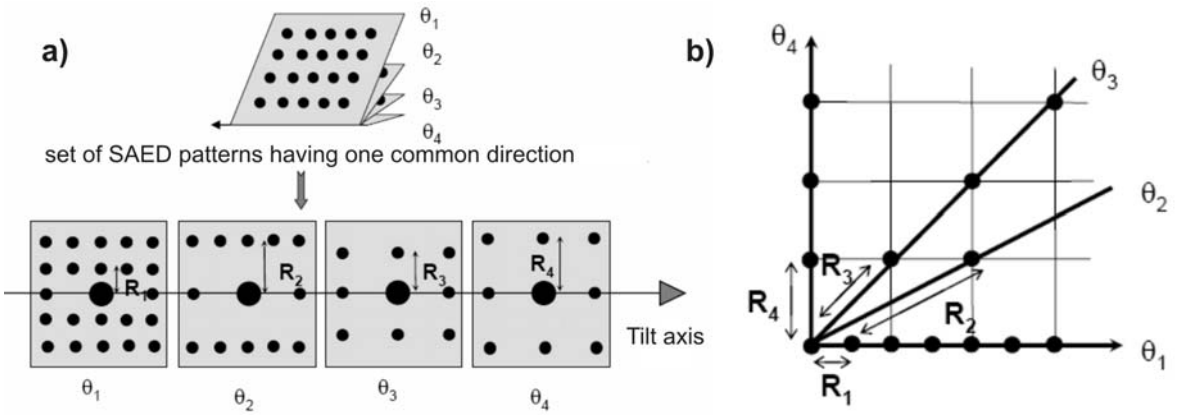

Figure 5: Schematic drawing that illustrates how to obtain a 3D view of the reciprocal space of a crystal by the tilting method. **(a)** A set of SAED patterns, which posse a common reciprocal rows (tilt axis) and that are related together by angles. **(b)** The information about the third dimension is obtained by the reconstruction of the section of the reciprocal space perpendicular to the tilt axis.

Usually the tilt-axis is chosen among the reciprocal rows having the smallest possible values of d*. As the crystal is tilted around chosen axis one should keep the same tilting direction until new zone-axis pattern is observed. When tilting from one zone-axis orientation to another the tilt position of the specimen; *i.e.* x and y tilt angles should be noted (see Table 3 as an illustration) and subsequently used for calculation of the angle between two successive zone axes patterns according to the equation: $\cos\theta = \cos(x_i - x_n)\cdot\cos(y_i - y_n)$.

Table 3: A list of x and y tilt angles of the crystal during the tilting and corresponding angle of tilt calculated according to the equation: $\cos\theta = \cos(x_i - x_n)\cdot\cos(y_i - y_n)$. To simplify the drawing of the scheme one can correspondingly add up or take from the tilt angle. Thus the values in the parenthesis in the column "Tilting angle" correspond to the tilt angle minus 45°.

Negative No.	Tilt x (°)	Tilt y (°)	Tilting angle θ (°)
JB 6449	$x_i = 54.6$	$y_i = 6.3$	0 (-45)
JB 6450	$x_1 = 29.1$	$y_1 = 0.2$	26.17 (~19)
JB 6451	$x_2 = 16.6$	$y_2 = -2.8$	39.02 (~ -6)
JB 6452	$x_3 = 4.2$	$y_3 = -0.8$	50.80 (~ 6)
JB 6453	$x_4 = -11.8$	$y_4 = -6.8$	67.53 (~23)
JB 6454	$x_5 = -25.6$	$y_5 = -10$	80.6 (~36)
JB 6455	$x_6 = -34.3$	$y_6 = -12.2$	89.74 (~45)

Preferably, the crystal should be rotated as much as possible in order to explore a large portion of the reciprocal space. Therefore the tilting method requires a microscope with a pole piece that allows high-angle specimen tilting (± 30° or higher) and a double-tilt or a tilt-rotation holder. In the case of a double tilt specimen holder, when tilting from one zone axis orientation to another the tilt position of the specimen, *i.e.,* x and y tilt angles.

Once having a set of zone-axis patterns with their angular relationships one can start with the reconstruction of the reciprocal plane perpendicular to the tilt axis (Fig. 5b) using the following procedure:

1. The first step to determine the orientation relationship between different zone-axis patterns is to find the crystal in low-indexed zone-axis orientation, *e.g.* [100], [010] or [001], which exhibit the highest possible net symmetry in order to deduce the crystal system as described above.

2. Draw the scheme of lines with common origin, which corresponds to the transmitted beam and to the arrowed direction in the zone-axis pattern, *i.e.*, tilting axis. The individual line in the scheme corresponds to the particular ZAP. The angles between these lines correspond to the angle between successive ZAPs (Fig. 6). Additionally, the lines in the scheme are perpendicular to the tilting axis too.

3. The particular lines are divided into segments. The length of these segments corresponds to the spacing between electron-diffraction spots in ZAPs lying on the line perpendicular to the tilting axis (arrowed direction) and passing through the origin. Considering the distance between diffraction spots one should take into the account the extinctions and the centering of the unit-cell. The forbidden reflections, *i.e.,* the reflections not present on the line perpendicular to the tilting axis in ZAP due to the extinctions are marked with empty circles, while the reflections clearly visible on this line should be marked with full circles. As an illustration in figure 6b, the distance (R_b) between the central (transmitted beam) and the first diffraction spot should be divided by two for the periodicity along this direction. On the corresponding line in the scheme, the first spot (absent due to extinction) will be indicated as an empty circle and the second (present) with a full circle. Once having the circles for all zone-axes patterns on the corresponding lines in the scheme, one should look for possible crystal axes by examining the reconstructed sections of the reciprocal space occurring for the existence of several layers (full/empty circles). One has to recognize the basic motif repeated in the reciprocal space in the scheme and identify a possible unit-cell. In the example of La_2CuO_4, the orthorhombic unit-cell is marked by equidistant dashed lines (Fig. 6). In this case the crystal was tilted around b*, *i.e.*, [010]* (see Fig. 6) and the two orthogonal lines in the scheme correspond to the reciprocal directions [100]* and [001]*. The zone-axes patterns in figure 6a and 6g corresponds to [100] and [001] ZAPs, and the reconstructed section to the [010 ZAP]. Since we are dealing with the reciprocal space the distances between the two diffraction spots in the ZAP do not correspond to the interplanar

spacing in direct space (d). The interplanar spacing (d) can be obtained from the spacing measured between spots (R_i) on each ZAP considering the camera constant (λL) characteristic for individual TEM. The following procedure has to be followed:

a) Use the [100] and [001] zone-axes patterns in order to obtain the interplanar distance $d_{100} = a$ and $d_{001} = c$. The $d_{010} = b$ is visible in all ZAPs (Fig. 5), since the crystal was rotated around [010]* = b*.

b) Considering the distance (Ra) between the central (transmitted beam) and first diffraction spot on the line perpendicular to the [010]* in figure 6a, *i.e.*, [100]*, the centering of the unit cell evident from the empty circles in the scheme (indicated by gray arrows), suggests that the distance between the two diffracted spots (R_a) have to be divided by two in order to obtain the interplanar distance $d_{100}=\lambda L\times(R_a/2)^{-1} = a$. The unit cell parameters *b* and *c* for La_2CuO_4 can be determined similarly.

c) Measure the distance (R_b) between the central (transmitted beam) and first diffraction spot along [010]* in any ZAP and divide it by two, due to extinction. Since this new parameter R_b' is characteristic for the interplanar spacing (*d*) and the magnification due to the lens settings; *i.e.*, camera constant. Therefore, convert R_b' distance into interplanar ($d_{010} = b$) values via the camera constant.

d) Using a table of interplanar spacings or appropriate software package for the particular substance (La_2CuO_4) and correlate the measured d_{hkl} values with d_{hkl} values in the data base and thus obtain the *hkl* index for the diffraction spot. According to these two electron-diffraction patterns the rest of zone-axes patterns obtained in the tilting experiment can be arbitrary indexed. After indexing the electron-diffraction patterns check the reflection conditions for experimental (*hkl*) indexes (Table 4) and interpret them in terms of table 5. Then look for all possible space-groups of the extended Hermann-Mauguin symbols characteristic for La_2CuO_4 (Table 4) by means of table 6. Afterward check the existing reflection conditions for each possible space-group (Table 7) and identify the one for La_2CuO_4. However, the crystal symmetry of La_2CuO_4 corresponds to the space-group *Bmab* within the Laue class *2/m2/m2/m*, which can be described in terms of figure 7.

e) The *hkl* indexes for the particular diffraction spot can be obtained from only three ZAPs including the information about d_{100}, d_{010} and d_{001}. Knowing the unit cell parameters we are able to index each ZAP and examine the reflection conditions:

- from [001] ZAP in figure 6a, hk0 : h=2n and k=2n
- from [100] ZAP in figure 6g, 0kl : l=2n (0k0 : k=2n)
- from [010] ZAP reconstructed, h0l : h=2n and l=2n

f) In the international tables for crystallography, one shall look at the table giving the reflection conditions, diffraction symbols and possible space groups (Table 7). For an orthorhombic cell having the observed reflection conditions the extinction symbol is B-(ac)b which is compatible with only two space groups *Bmab* (SGn°64) and *B2cb* (SGn°41). In the case of La_2CuO_4, the solution corresponds to the centrosymmetric space group *Bmab* (SGn°64). Generally speaking for an unknown compound, the choice between the centrosymmetric and non centrosymmetric solution shall be made on the basis of extra information that can be obtained by convergent beam electron diffraction or macroscopic physical properties measurements for instance.

The reconstruction of the reciprocal space presented for La_2CuO_4 is somewhat an ideal case where we explored a large portion of the reciprocal space with an access to the three basic ZAP [100], [010] and [001] which allows to obtain easily the reflections conditions. Presuming, for La_2CuO_4, we had only four ZAP (say 6c to 6f), we would have obtain the cell dimension but only partial information about the reflection conditions since one would have only a reconstruction of the [010] ZAP. In such a case one would need to go back to the microscope and look for the two missing basic ZAP either having them directly or by reconstruction using the tilting method.

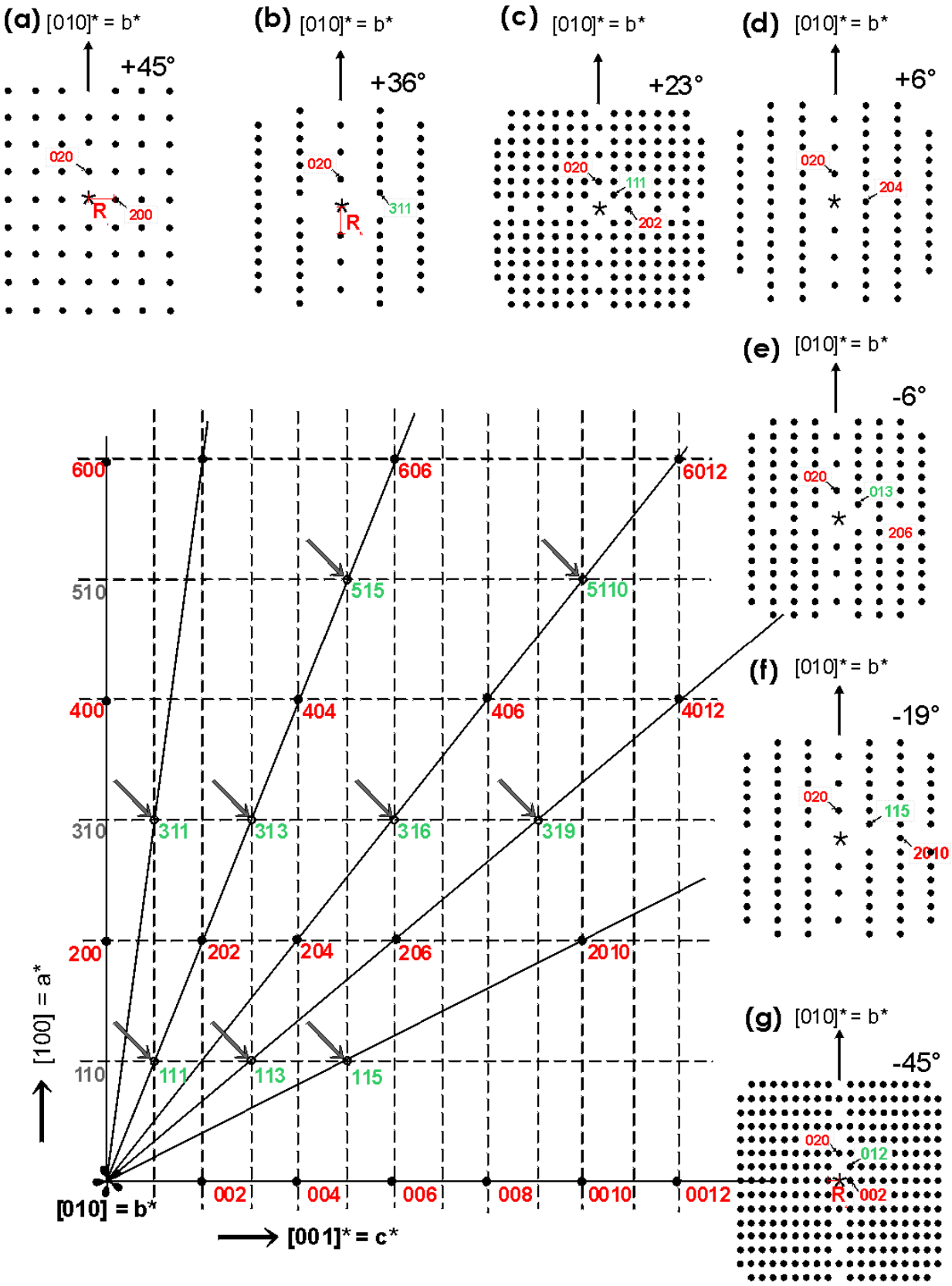

Figure 6: Reconstruction of the La_2CuO_4 unit cell from the zone-axis electron-diffraction pattern of La_2CuO_4; [010] represents the tiling axis of the crystal.

Table 4: Reflection conditions of La_2CuO_4 and their interpretation

	hkl	**0kl**	**h0l**	**hk0**	**h00**	**0k0**	**00l**
Reflection conditions and their interpretation	111 113 115 311 313 319 125 145 2110 ↓ h+l = 2n	012 022 042 052 ↓ l = 2n ↓ Plane: C // $\vec{a}$	202 204 206 2010 404 406 ↓ h+l = 2n h = 2n l = 2n ↓ Plane: n, c, a // $\vec{b}$	220 240 260 ↓ h = 2n k = 2n h+k = 2n ↓ Plane: a, b, n // $\vec{c}$	200 400 ↓ h = 2n ↓ 2_1 or 4_2	020 040 060 ↓ k = 2n ↓ 2_1 or 4_2	002 004 006 ↓ l = 2n ↓ 2_1 or 4_2 or 6_3
Hermann - Mauguin symbols	**B-centering**	$B\underline{\vec{a}}\underline{\vec{b}}\underline{\vec{c}}$ **B c n a** **c n** **a b**					

Table 5 Extinctions conditions

INDEXES	REFLECTION CONDITIONS	INTERPRETATION
HKL	H+K+L = 2n	I – centered
	H+K = 2n	C – centered
	H+L = 2n	B – centered
	K+L = 2n	A – centered
	H+K, K+L, H+L = 2n	F – centered
	-H+K+L = 3n	R – centered
0KL	K = 2n	Plane b // (100); (t = b/2)
	L = 2n	Plane c // (100); (t = c/2)
	K+L = 2n	Plane n // (100); (t = (b+c)/2)
	K+L= 4n	Plane d // (100); (t = (b+c/)4)
H0L	H = 2n	Plane a // (010); (t = a/2)
	L = 2n	Plane c // (010); (t = c/2)
	H+L = 2n	Plane n // (010); (t = (a+c)/2)
	H+L = 4n	Plane d // (010); (t = (a +c)/4)
HK0	H = 2n	Plane a // (001); (t = a/2)
	K = 2n	Plane b // (001); (t = b/2)
	H+K = 2n	Plane n // (001); (t = (a+b)/2)
	H+K = 4n	Plane d // (001); (t = (a +b)/4)
H00	H = 2n	axis [100], t = a/2; 2_1 or 4_2
	H = 4n	axis [100], t = a/4; 4_1 or 4_3
0K0	K = 2n	axis [010], t = b/2; 2_1 or 4_2
	K = 4n	axis [010], t = b/4; 4_1 or 4_3
00L	L = 2n	axis [001], t = c/2; 2_1, 4_2 or 6_3
	L = 3n	axis [001], t = c/3; 3_1, 3_2, 6_2 or 6_4
	L = 4n	axis [001], t = c/4; 4_1 or 4_3
	L = 6n	axis [001], t = c/6; 6_1 or 6_5

Table 6: Synoptic tables of space-group symbols; orthorhombic system (International tables for crystallography, Ch. 4, p. 58, 1996)

No. of space group	Schoenflies symbol	Standard full Hermann–Mauguin symbol **abc**	Extended Hermann–Mauguin symbols for various settings of the same unit cell					
			abc (standard)	**bac̄**	**cab**	**c̄ba**	**bca**	**ac̄b**
52	D_{2h}^{6}	$P\frac{2}{n}\frac{2_1}{n}\frac{2}{a}$	*Pnna*	*Pnnb*	*Pbnn*	*Pcnn*	*Pncn*	*Pnan*
53	D_{2h}^{7}	$P\frac{2}{m}\frac{2}{n}\frac{2_1}{a}$	*Pmna*	*Pnmb*	*Pbmn*	*Pcnm*	*Pncm*	*Pman*
54	D_{2h}^{8}	$P\frac{2_1}{c}\frac{2}{c}\frac{2}{a}$	*Pcca*	*Pccb*	*Pbaa*	*Pcaa*	*Pbcb*	*Pbab*
55	D_{2h}^{9}	$P\frac{2_1}{b}\frac{2_1}{a}\frac{2}{m}$	*Pbam*	*Pbam*	*Pmcb*	*Pmcb*	*Pcma*	*Pcma*
56	D_{2h}^{10}	$P\frac{2_1}{c}\frac{2_1}{c}\frac{2}{n}$	*Pccn*	*Pccn*	*Pnaa*	*Pnaa*	*Pbnb*	*Pbnb*
57	D_{2h}^{11}	$P\frac{2}{b}\frac{2_1}{c}\frac{2_1}{m}$	*Pbcm*	*Pcam*	*Pmca*	*Pmab*	*Pbma*	*Pcmb*
58	D_{2h}^{12}	$P\frac{2_1}{n}\frac{2_1}{n}\frac{2}{m}$	*Pnnm*	*Pnnm*	*Pmnn*	*Pmnn*	*Pnmn*	*Pnmn*
59	D_{2h}^{13}	$P\frac{2_1}{m}\frac{2_1}{m}\frac{2}{n}$	*Pmmn*	*Pmmn*	*Pnmm*	*Pnmm*	*Pmnm*	*Pmnm*
60	D_{2h}^{14}	$P\frac{2_1}{b}\frac{2}{c}\frac{2_1}{n}$	*Pbcn*	*Pcan*	*Pnca*	*Pnab*	*Pbna*	*Pcnb*
61	D_{2h}^{15}	$P\frac{2_1}{b}\frac{2_1}{c}\frac{2_1}{a}$	*Pbca*	*Pcab*	*Pbca*	*Pcab*	*Pbca*	*Pcab*
62	D_{2h}^{16}	$P\frac{2_1}{n}\frac{2_1}{m}\frac{2_1}{a}$	*Pnma*	*Pmnb*	*Pbnm*	*Pcmn*	*Pmcn*	*Pnam*
63	D_{2h}^{17}	$C\frac{2}{m}\frac{2}{c}\frac{2_1}{m}$	*Cmcm* *bnn*	*Ccmm* *nan*	*Amma* *ncn*	*Amam* *nnb*	*Bbmm* *nna*	*Bmmb* *cnn*
64	D_{2h}^{18}	$C\frac{2}{m}\frac{2}{c}\frac{2_1}{a}$	*Cmca* *bnb*	*Ccmb* *naa*	*Abma* *ccn*	*Acam* *bnb*	*Bbcm* *naa*	*Bmab* *ccn*
65	D_{2h}^{19}	$C\frac{2}{m}\frac{2}{m}\frac{2}{m}$	*Cmmm* *ban*	*Cmmm* *ban*	*Ammm* *ncb*	*Ammm* *ncb*	*Bmmm* *cna*	*Bmmm* *cna*
66	D_{2h}^{20}	$C\frac{2}{c}\frac{2}{c}\frac{2}{m}$	*Cccm* *nnn*	*Cccm* *nnn*	*Amaa* *nnn*	*Amaa* *nnn*	*Bbmb* *nnn*	*Bbmb* *nnn*
67	D_{2h}^{21}	$C\frac{2}{m}\frac{2}{m}\frac{2}{a}$	*Cmma* *bab*	*Cmmb* *baa*	*Abmm* *ccb*	*Acmm* *bcb*	*Bmcm* *caa*	*Bmam* *cca*
68	D_{2h}^{22}	$C\frac{2}{c}\frac{2}{c}\frac{2}{a}$	*Ccca* *nnb*	*Cccb* *nna*	*Abaa* *cnn*	*Acaa* *bnn*	*Bbcb* *nan*	*Bbab* *ncn*
69	D_{2h}^{23}	$F\frac{2}{m}\frac{2}{m}\frac{2}{m}$	*Fmmm* *ban* *ncb* *cna*	*Fmmm* *ban* *cna* *ncb*	*Fmmm* *ncb* *cna* *ban*	*Fmmm* *ncb* *ban* *cna*	*Fmmm* *cna* *ban* *ncb*	*Fmmm* *cna* *ncb* *ban*
70	D_{2h}^{24}	$F\frac{2}{d}\frac{2}{d}\frac{2}{d}$	*Fddd*	*Fddd*	*Fddd*	*Fddd*	*Fddd*	*Fddd*
71	D_{2h}^{25}	$I\frac{2}{m}\frac{2}{m}\frac{2}{m}$	*I mmm* *nnn*	*I mmm* *nnn*	*I mmm* *nnn*	*I mmm* *nnn*	*I mmm* *nnn*	*I mmm* *nnn*
72	D_{2h}^{26}	$I\frac{2}{b}\frac{2}{a}\frac{2}{m}$	*I bam* *ccn*	*I bam* *ccn*	*I mcb* *naa*	*I mcb* *naa*	*I cma* *bnb*	*I cma* *bnb*
73	D_{2h}^{27}	$I\frac{2_1}{b}\frac{2_1}{c}\frac{2_1}{a}$	*I bca* *cab*	*I cab* *bca*	*I bca* *cab*	*I cab* *bca*	*I bca* *cab*	*I cab* *bca*
74	D_{2h}^{28}	$I\frac{2_1}{m}\frac{2_1}{m}\frac{2_1}{a}$	*I mma* *nnb*	*I mmb* *nna*	*I bmm* *cnn*	*I cmm* *bnn*	*I mcm* *nan*	*I mam* *ncn*

Table 7: Space-group determination and diffraction symbols, Orthorhombic; Laue class *mmm* (2/*m* 2/*m* 2/*m*) (International tables for crystallography, Ch. 3, p. 44, 1996)

Reflection conditions							Laue class *mmm* (2/*m* 2/*m* 2/*m*)			
								Point group		
hkl	0*kl*	*h*0*l*	*hk*0	*h*00	0*k*0	00*l*	Extinction symbol	222	*mm*2 *m*2*m* 2*mm*	*mmm*
	l	*h* + *l*		*h*		*l*	*Pcn*–		*Pcn*2 (30)	*Pcnm* (53)
	l	*h* + *l*	*h*	*h*		*l*	*Pcna*			*Pcna* (50)
	l	*h* + *l*	*k*	*h*	*k*	*l*	*Pcnb*			*Pcnb* (60)
	l	*h* + *l*	*h* + *k*	*h*	*k*	*l*	*Pcnn*			*Pcnn* (52)
	k + *l*				*k*	*l*	*Pn*– –		*Pnm*2$_1$ (31)	*Pnmm* (59)
									*Pn*2$_1$*m* (31)	
	k + *l*		*h*	*h*	*k*	*l*	*Pn*–*a*		*Pn*2$_1$*a* (33)	***Pnma*** (62)
	k + *l*		*k*		*k*	*l*	*Pn*–*b*		*Pn*2*b* (30)	*Pnmb* (53)
	k + *l*		*h* + *k*	*h*	*k*	*l*	*Pn*–*n*		*Pn*2*n* (34)	*Pnmn* (58)
	k + *l*	*h*		*h*	*k*	*l*	*Pna*–		***Pna*2$_1$** (33)	*Pnam* (62)
	k + *l*	*h*	*h*	*h*	*k*	*l*	*Pnaa*			*Pnaa* (56)
	k + *l*	*h*	*k*	*h*	*k*	*l*	*Pnab*			*Pnab* (60)
	k + *l*	*h*	*h* + *k*	*h*	*k*	*l*	*Pnan*			*Pnan* (52)
	k + *l*	*l*			*k*	*l*	*Pnc*–		***Pnc*2** (30)	*Pncm* (53)
	k + *l*	*l*	*h*	*h*	*k*	*l*	*Pnca*			*Pnca* (60)
	k + *l*	*l*	*k*		*k*	*l*	*Pncb*			*Pncb* (50)
	k + *l*	*l*	*h* + *k*	*h*	*k*	*l*	*Pncn*			*Pncn* (52)
	k + *l*	*h* + *l*		*h*	*k*	*l*	*Pnn*–		***Pnn*2** (34)	***Pnnm*** (58)
	k + *l*	*h* + *l*	*h*	*h*	*k*	*l*	*Pnna*			***Pnna*** (52)
	k + *l*	*h* + *l*	*k*	*h*	*k*	*l*	*Pnnb*			*Pnnb* (52)
	k + *l*	*h* + *l*	*h* + *k*	*h*	*k*	*l*	*Pnnn*			***Pnnn*** (48)
h + *k*	*k*	*h*	*h* + *k*	*h*	*k*		*C*– – –	***C*222** (21)	***Cmm*2** (35)	***Cmmm*** (65)
									*Cm*2*m* (38)	
									*C*2*mm* (38)	
h + *k*	*k*	*h*	*h* + *k*	*h*	*k*	*l*	*C*– –2$_1$	***C*222**$_1$ (20)		
h + *k*	*k*	*h*	*h*,*k*	*h*	*k*		*C*– –(*ab*)		*Cm*2*a* (39)	***Cmma*** (67)
									*C*2*mb* (39)	*Cmmb* (67)
h + *k*	*k*	*h*,*l*	*h* + *k*	*h*	*k*	*l*	*C*–*c*–		***Cmc*2**$_1$ (36)	***Cmcm*** (63)
									*C*2*cm* (40)	
h + *k*	*k*	*h*,*l*	*h*,*k*	*h*	*k*	*l*	*C*–*c*(*ab*)		*C*2*cb* (41)	***Cmca*** (64)
h + *k*	*k*,*l*	*h*	*h* + *k*	*h*	*k*	*l*	*Cc*– –		*Ccm*2$_1$ (36)	*Ccmm* (63)
									*Cc*2*m* (40)	
h + *k*	*k*,*l*	*h*	*h*,*k*	*h*	*k*	*l*	*Cc*–(*ab*)		*Cc*2*a* (41)	*Ccmb* (64)
h + *k*	*k*,*l*	*h*,*l*	*h* + *k*	*h*	*k*	*l*	*Ccc*–		***Ccc*2** (37)	***Cccm*** (66)
h + *k*	*k*,*l*	*h*,*l*	*h*,*k*	*h*	*k*	*l*	*Ccc*(*ab*)			***Ccca*** (68)
										Cccb (68)
h + *l*	*l*	*h* + *l*	*h*	*h*		*l*	*B*– –	*B*222 (21)	*Bmm*2 (38)	*Bmmm* (65)
									*Bm*2*m* (35)	
									*B*2*mm* (38)	
h + *l*	*l*	*h* + *l*	*h*	*h*	*k*	*l*	*B*–2$_1$–	*B*22$_1$2 (20)		
h + *l*	*l*	*h* + *l*	*h*,*k*	*h*	*k*	*l*	*B*– –*b*		*Bm*2$_1$*b* (36)	*Bmmb* (63)
									*B*2*mb* (40)	
h + *l*	*l*	*h*,*l*	*h*	*h*		*l*	*B*–(*ac*)–		*Bma*2 (39)	*Bmam* (67)
									*B*2*cm* (39)	*Bmcm* (67)
h + *l*	*l*	*h*,*l*	*h*,*k*	*h*	*k*	*l*	*B*–(*ac*)*b*		*B*2*cb* (41)	*Bmab* (64)
h + *l*	*k*,*l*	*h* + *l*	*h*	*h*	*k*	*l*	*Bb*– –		*Bbm*2 (40)	*Bbmm* (63)
									*Bb*2$_1$*m* (36)	
h + *l*	*k*,*l*	*h* + *l*	*h*,*k*	*h*	*k*	*l*	*Bb*–*b*		*Bb*2*b* (37)	*Bbmb* (66)
h + *l*	*k*,*l*	*h*,*l*	*h*	*h*	*k*	*l*	*Bb*(*ac*)–		*Bba*2 (41)	*Bbcm* (64)
h + *l*	*k*,*l*	*h*,*l*	*h*,*k*	*h*	*k*	*l*	*Bb*(*ac*)*b*			*Bbab* (68)
										Bbcb (68)
k + *l*	*k* + *l*	*l*	*k*		*k*	*l*	*A*– – –	*A*222 (21)	***Amm*2** (38)	*Ammm* (65)
									*Am*2*m* (38)	
									*A*2*mm* (35)	
k + *l*	*k* + *l*	*l*	*k*	*h*	*k*	*l*	*A*2$_1$– –	*A*2$_1$22 (20)		
k + *l*	*k* + *l*	*l*	*h*,*k*	*h*	*k*	*l*	*A*– –*a*		*Am*2*a* (40)	*Amma* (63)
									*A*2$_1$*ma* (36)	
k + *l*	*k* + *l*	*h*,*l*	*k*	*h*	*k*	*l*	*A*–*a*–		***Ama*2** (40)	*Amam* (63)
									*A*2$_1$*am* (36)	
k + *l*	*k* + *l*	*h*,*l*	*h*,*k*	*h*	*k*	*l*	*A*–*aa*		*A*2*aa* (37)	*Amaa* (66)
k + *l*	*k*,*l*	*l*	*k*		*k*	*l*	*A*(*bc*)– –		***Abm*2** (39)	*Abmm* (67)
									*Ac*2*m* (39)	*Acmm* (67)
k + *l*	*k*,*l*	*l*	*h*,*k*	*h*	*k*	*l*	*A*(*bc*)–*a*		*Ac*2*a* (41)	*Abma* (64)
k + *l*	*k*,*l*	*h*,*l*	*k*	*h*	*k*	*l*	*A*(*bc*)*a*–		***Aba*2** (41)	*Acam* (64)
k + *l*	*k*,*l*	*h*,*l*	*h*,*k*	*h*	*k*	*l*	*A*(*bc*)*aa*			*Abaa* (68)
										Acaa (68)

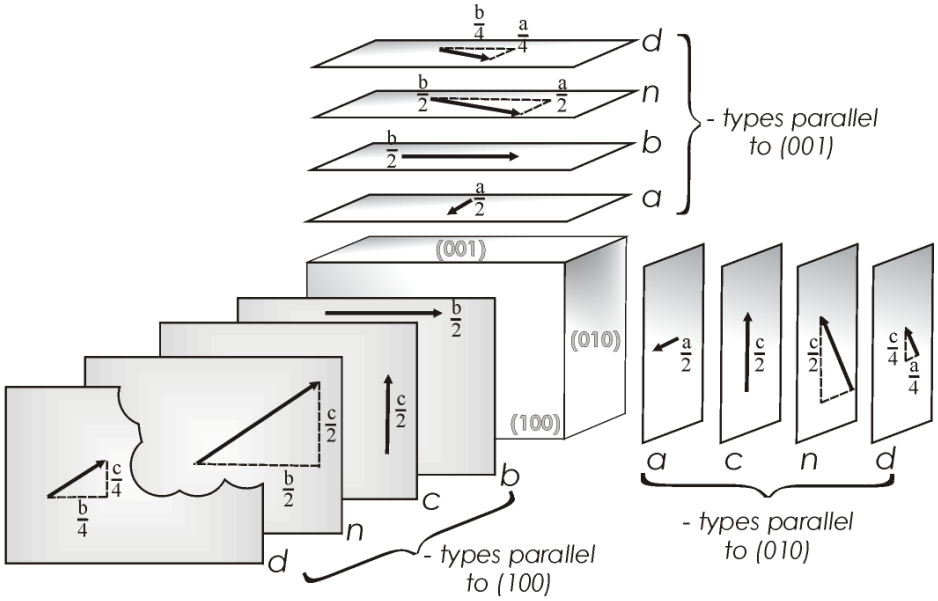

Figure 7: The possible types of glide planes parallel to the (100), (010) and (001) faces for an orthorhombic crystal (by Bloss *et al.*, 1971); for each possible glide plane, *i.e.* a, b, c, n and d, the direction and the length of the glide component is shown by an arrow. The dashed line represents the vector parallel to the crystallographic axes into which the glide plane can be resolved.

4. THE BaO-RICH HEXAGONAL PHASES WITHIN THE $BaO–Nb_2O_5$ BINARY SYSTEM

To understand the phase transitions in $Ba_4Nb_2O_9$, we have to study the crystal structure of individual polymorph. In the first step, we reinvestigated the formation conditions of $Ba_4Nb_2O_9$ and phase stability of particular modification. This step is then followed by decomposition studies of $Ba_4Nb_2O_9$ induced by various thermal and atmosphere treatments. At the end of this chapter the crystal structure of low- and high-temperature $Ba_4Nb_2O_9$ modifications is discussed.

Index

4.1. Introduction

4.1.1. The formation of BaO-rich phases in the BaO–Nb_2O_5 binary system, their stability and phase transitions

Recently, cation-deficient hexagonal perovskite-based ceramics started to attract attention due to their low dielectric losses (Q*f < 58 000 GHz), relatively high permittivity (ε_r < 53) and small temperature coefficient of resonant frequency (-50 < τ_f < +50) at MW frequencies [Ratheesh *et al.*, 1997, Kamba *et al.*, 2001, Keith *et al.*, 2004, Wada *et al.*, 2005, Zhao *et al.*, 2006, Kan *et al.*, 2006 and Kuang *et al.*, 2006]. Moreover, Bieringer *et al.* [2003] demonstrated that an 8-layer hexagonal perovskite, $Ba_8ZnTa_6O_{24}$, forms as a consequence of ZnO volatilization from the cubic perovskite $Ba_3ZnTa_2O_9$, which is widely utilized for the production of high-Q base-station resonators in wireless telecommunications networks [Deau *et al.*, Vanderah, 2002]. $Ba_8ZnTa_6O_{24}$ material exhibits excellent dielectric properties with a high unloaded quality factor Q_u = 20 800 at 3.28 GHz, high relative permittivity ε_r = 29 and a temperature coefficient of resonant frequency τ_f = 29.4 ppm/°C [Moussa *et al.*, 2003]. Promising dielectric properties were afterwards reported for $Ba_8Nb_4Ti_3O_{24}$ by Rawal *et al.* [2006]. A little later, Mallinson *et al.* [2006] identified the new, 10-layer hexagonal perovskites $Ba_{10}Mg_{0.25}Ta_{7.9}O_{30}$ and $Ba_{10}Co_{0.25}Ta_{7.9}O_{30}$, and determined dielectric properties of both materials. Among these hexagonal perovskite, the extended numbers of $A_nB_{n-1}O_{3n}$ polytypes with ordered distribution of cation vacancies have been reported [Trolliard *et al.*, 2004 and Kuang *et al.*, 2006]. These vacancies reduce the repulsions between large B-site cations in face-sharing octahedra and hence stabilize the crystal structure. Consequently, this leads to a fully ordered distribution of B-site cations and vacancies influencing τ_f [Zhao *et al.*, 2007] and Q [Mallinson *et al.*, 2006] of the ceramic, *e.g.*, $Ba_5Nb_4O_{15}$-based ceramic, which was considered as potential candidate for microwave dielectric resonators. Moreover, MW dielectric properties of $Ba_5Nb_4O_{15}$ [Ratheesh *et al.*, 2000 and Kim *et al.*, 2002] can be considerably improved by mixing it with $BaNb_2O_6$ [Kim *et al.*, 2002].

Similar compounds containing transition metals in oxidation states with d^0 electronic configuration were additionally reported within the BaO-rich part of the BaO-Nb_2O_5 binary system. These include $Ba_3Nb_2O_8$ and $Ba_4Nb_2O_9$, both containing more than 75 mol % of BaO. The composition makes them sensitive to the decomposition in ambient air [Vanderah *et al.*, 2002]. While $Ba_3Nb_2O_8$ (ICSD # 95193) [Vanderah *et al.*, 2002], which forms through the solid state reaction between $Ba_5Nb_4O_{15}$ and $Ba_4Nb_2O_9$, is well known to crystallize as a palmierite [González *et al.*, 2000], the crystal structures of $Ba_4Nb_2O_9$ polymorphs have not yet been solved. Several modifications of $Ba_4Nb_2O_9$ with unknown crystal structures have been isolated in an atmosphere of air between the room temperature and 1500 °C based on X-ray

diffraction data. Leschenko *et al.* [1979 and 1985] reported on four different polymorphs of $Ba_4Nb_2O_9$: α, β, β' and γ. The α-modification was obtained by quenching the sample from 750 °C in an atmosphere of air, the β-modification was formed by slow cooling from 1400 °C, and the γ-modification was obtained by quenching the sample from 1500 °C [Leshchenko *et al*, 1979]. The α-$Ba_4Nb_2O_9$ also forms during slow cooling from about 1130 °C, while quenching the sample from above 1130 °C results in the formation of the γ-modification. Upon annealing at between 260 and 320 °C the γ-modification converts into the β-modification, which subsequently converts to the β'-modification when heated in a temperature range between 530 and 700 °C, and undergoes an irreversible phase transition into the α-modification at 700-1130 °C [Leshchenko *et al*, 1985].

4.1.2. The crystal structure of compounds with general formula $A_4A'B_2O_9$

Recently, a special interest has been focused on anion-deficient hexagonal perovskites associated with the presence of $A_3A'O_6$-layers perpendicular to the $[001]_H$ [Dussarrat, 1998 and Mitchell, 2002]. Different polytypes can be formed by the variation in hexagonal stacking of AO_3 and $A_3A'O_6$ close-packing layers. Their alternations create columns of face-sharing octahedra and trigonal prism along the hexagonal *c*-crystallographic axes. These sequences were observed in $Sr_4Ru_2O_9$ [Dussarrat *et al.*, 1995], $Sr_4Ni_3O_9$,[Abraham *et al.*, 1994 and Huve *et al.*, 1998], $A_4A'Ir_2O_9$ (A = Sr, Ba; A' = Cu, Zn) [Battle *et al., 1998*] and $Ba_4Mn_2NaO_9$ [Quarez *et al.*, 2004]. The crystal structure of $Sr_4Ru_2O_9$ is built up from the periodic stacking of one close-packing SrO_3 layer and three Sr_3O_6 layers [Dussarrat *et al.*, 1995]. As reported by Dussarrat *et al.* [1995] the $Sr_4Ru_2O_9$ crystal structure could be successfully refined in *P-62c* space group. The crystal structural model comprises two types of columns. The first type consists of only RuO_6 face-sharing octahedra, while the second type corresponds to alternation of RuO_6 face-sharing octahedra with empty trigonal prisms. The suggested structural model (ICSD #79310) with fully occupied Ru(1) and O(4) positions give rise to unusual thermal parameters and an unrealistic Ru(1)-Ru(1) interatomic distances [Dussarrat *et al.*, 1995]. Therefore the author suggested an alternative structural model that has a half occupied Ru(1) and O(4) positions and can be described in P321 space group. The partial occupancy then leads the formation of columns lined along the hexagonal *c*-axis, which consists of alternating sequence of Ru_2O_9 dimmers and one empty trigonal prism. Contrary, Abraham *et al.,* [1994] has succeeded in making the vacancy-free phase $Sr_4Ni_3O_9$, which has fully occupied both B-site positions by Ni^{4+} ions. Recently, TEM studies revealed that $Sr_4Ni_3O_9$ [Huve *et al.*, 1998] may occur in several closely related microphases including incommensurable 4H polytype, which transforms to 9R or 18R-type structure during heating. Furthermore, the $Sr_4Ni_3O_9$ crystal structure is very similar to that of $Sr_4Cu'Ir_2O_9$ [Battle *et al.,* 1998] which consists of alternation Ir_2O_9 dimmers and CuO_3

prism. Battle *et al.* [1998] observed that prolonged heating of $Sr_4Cu'Ir_2O_9$ at 1120 °C as well as the replacement of Sr^{2+} by Ba-ions leads to the adoption of an incommensurate crystal structure. Moreover, Battle *et al.* [1998] reported that the remaining compounds $Sr_4A'Ir_2O_9$ (A' = Zn, Ni) as well as $Ba_4Zn'Ir_2O_9$ are all incommensurate along $[001]_H$ [Battle *et al.,* 1998] and their composite structure cannot be simply described in terms of mixed layer sequences but has to be considered to consist of two substructures, characterized by the unit-cell parameters c_1 and c_2. The additional isomorphs with a composition $Ba_4Mn_2NaO_9$ was described by Quarez *et al.*[2004] The main characteristic of its crystal structure is the presence of mixed Mn^{4+}/ Mn^{5+} valence in octahedral positions and off-centering for some B-site cations. All these compound can be described with general formula $A_{3n+3m}A'_nB_{3m+n}O_{9m+6n}$ for (n = 3, m = 1) [Perez-Mato *et al*, 1999] where *n* and *m* stands for the number of $A_3A'O_6$ and AO_3 layers. Based on this formalism it is most likely that the isoformulated α-$Ba_4Nb_2O_9$ is one of the isomorphs if not at least the member of this hexagonal perovskites-like series. Recent investigation of polymorphic phase transitions in $Ba_4Nb_2O_9$ revealed that the compound appears in two stable polymorphs [Bezjak *et al.*, 2008, 2009]. These include the low-temperature α- and the high-temperature γ-modification. The α-$Ba_4Nb_2O_9$ is observed below 1176°C, while γ-$Ba_4Nb_2O_9$ is thermodynamically stable above this temperature. The crystal structures of both $Ba_4Nb_2O_9$ polymorphs have not yet been solved. Only the type of the unit-cell has been suggested and unit-cell dimensions assessed. According to Leshchenko *et al.* [1979] the crystal symmetry of high-temperature γ-modification appears to be orthorhombic with unit-cell constants *a* = 12.03Å, *b* = 20.99Å and *c* = 24.81Å while the α-modification might crystallize in hexagonal-cell (*a* = 5.923Å and *c* = 4.23Å). Since super-structural peaks were not considered in the calculation of the unit-cell dimensions, Trunov *et al.*[1979] suggested, based on an analogy with the $Ba_4Ta_2O_9$, [Paramova *et. al.*, 1976] that α-$Ba_4Nb_2O_9$ crystallizes in a hexagonal super-structural cell (*a* = 20.52Å and *c* = 8.452Å). Comparable results were very recently reported by Bezjak *et al.* [2008] Their SAED analyses revealed that the unit-cell suggested by Trunov *et al.* [1979] is rotated by 30° with respect to the sub-cell of Leshchenko *et al.* [1979] and multiplied along the *a*-axis [Bezjak *et al.*, 2008] Moreover, Kemmler-Sack *et al.* [1981] multiplied the c parameter of the unit-cell suggested by Leshchenko *et al.* [1979] and proposed that α-$Ba_4Nb_2O_9$ crystallizes as 36-layerd hexagonal-perovskite having part of Ba-cations in octahedral coordination. Reportedly Ba-cations in B-site position increase the distance between BaO_3 close-packed layers along $[001]_H$ on to ~2.58Å [Kemmler-Sack *et al.*, 1981] since the characteristic distance for perovskite crystal structure is ~2.35Å.

4.2. Experiment

4.2.1. Sample preparation

The starting materials employed were high-purity powders of $BaCO_3$ (99.8%, Alfa Aesar) and Nb_2O_5 (99.8%, Alfa Aesar). The mixture of powders with a nominal composition corresponding to $Ba_4Nb_2O_9$ was first ball-milled for 2h (200rpm) with yttria-stabilized zirconia balls using ethanol as a mixing medium. After drying the powder was calcined at 800 °C in air for 20 h, then ground, and recalcined at 900 and 1000 °C with 20 h duration at each temperature in order to ensure a complete reaction between the $BaCO_3$ and the Nb_2O_5. The calcined powders were then uniaxially pressed into 10-mm pellets, under a force of 2 kN. The green bodies were fired on a sacrificial pellet of the same composition in an alumina crucible at various temperatures between 300-1400°C in ambient air. The selected temperatures ensured sub-solidus conditions according to the phase-diagram reported by Leshchenko *et al*. [1979]. Therefore it did not exceed the decomposition temperatures of compounds.

For TEM observations the samples were cut into 3-mm discs, which were mechanically thinned and polished to a thickness of ~100 μm and dimpled (Dimple Grinder, Gatan Inc., Warrendale, PA) to ~20 μm in the disk centre. The TEM specimens were produced by ion-milling (RES 010, Bal-Tec AG, Balzers, Liechtenstein) with 4 keV Ar^+ ions at an incidence angle of 10° until perforation of the central disk area. The polymorphic phase transitions in $Ba_4Nb_2O_9$ were studied by thermal analyses, high-temperature X-ray powder diffraction and high-temperature TEM analyses.

The samples for high-temperature transmission electron microscopy were prepared from γ-$Ba_4Nb_2O_9$ powders crushed in an agate mortar to obtain small crystalline fragments that were put in a suspension in alcohol. A drop of the suspension was then deposited and dried on a copper grid previously coated with a thin film of amorphous carbon.

4.2.2. Experimental methods and experimental conditions

The homogeneity and the microstructures of the sintered pellets were examined with a scanning electron microscope (SEM; Jeol JSM-5800, Jeol Ltd., Tokyo, Japan) operated at 20 kV and equipped with a back-scattered electron detector and an energy-dispersive X-ray spectrometer (EDS; Link ISIS 300, Oxford Instruments, Oxford, UK).

The progress of solid-state reactions after each calcination step and the phase stability was monitored by X-ray powder diffraction using a high-resolution X-ray

diffractometer (PAnalytical X'Pert PRO MPD, Almelo, The Netherlands) with Cu_{Ka1} radiation (1.5406 Å) operated at 45 kV and 40 mA. The XRD data were collected in the 2θ range of 10-70 ° with a step of 0.008, a counting time of 50 s and a variable V10 slit.

The high-temperature X-ray powder diffraction analyses were carried out in the temperature range of 25-1200°C in air and in vacuum (10^{-3} mbar) using the same XRD spectrometer as above equipped with an environmental high-temperature oven-chamber (HTK 1200N, Anton Paar Ltd., Hertford, UK).

Differential scanning calorimetry (DSC 204 F1, NETZSCH-Geraetebau GmbH, Selb, Germany) was performed from room temperature up to 700 °C, with heating and cooling rates of 20 °/min using a Pt pan with a lid. Differential thermal and thermo-gravimetric analyses were studied on a simultaneous thermal analysis instrument (STA; Jupiter 449) coupled with a quadrupole mass spectrometer (QMS 403C Aëoloss, Netzsch, Selb, Germany). The STA was operated in air from 25-1300°C with the heating and cooling rates of 20 °C/min using an Al_2O_3 pan with a lid.

The presence of possible secondary phases at the grain boundaries of different $Ba_4Nb_2O_9$ modifications was studied using a transmission electron microscope (TEM, JEM-2100, Jeol Ltd., Tokyo, Japan and EM, JEM-2010, Jeol Ltd., Tokyo, Japan).

High-temperature transmission electron microscopy (HT-TEM) experiments were performed at CRISMAT Lab (Caen, France) on both JEOL 2010 and 2010F using a GATAN double tilt heating holder that allows experiments in the temperature range of 20-1000 °C.

4.3. Results: Phase formation and phase transitions of $Ba_4Nb_2O_9$

4.3.1. Solid-state synthesis of $Ba_4Nb_2O_9$ modifications

4.3.1.1. $Ba_4Nb_2O_9$ polymorphs and their phase stability

4.3.1.1.1. α-$Ba_4Nb_2O_9$ modification

The X-ray diffraction analysis of the powder mixture with a molar ratio $BaO:Nb_2O_5$ = 4:1 after firing at different temperatures between 800 and 1000 °C (Fig.1) for 20 hours indicates that the first binary phase, which forms below 800 °C, is a five-layered (5L) hexagonal perovskite $Ba_5Nb_4O_{15}$ (ICSD # 95192) [Vanderah *et al.*, 2002]. Additional peaks in the XRD spectra, accompanied by a decrease of the $BaCO_3$ and $Ba_5Nb_4O_{15}$ peaks appear after firing at 900 °C. These peaks could be assigned to the α-$Ba_4Nb_2O_9$ modification described by Leschenko *et al.*, [1979] (PDF file #35-1154). By increasing the firing temperature to 1000 °C the diffraction peaks of the $BaCO_3$ disappear, whereas the peaks of $Ba_5Nb_4O_{15}$ disappear after firing at 1100°C.

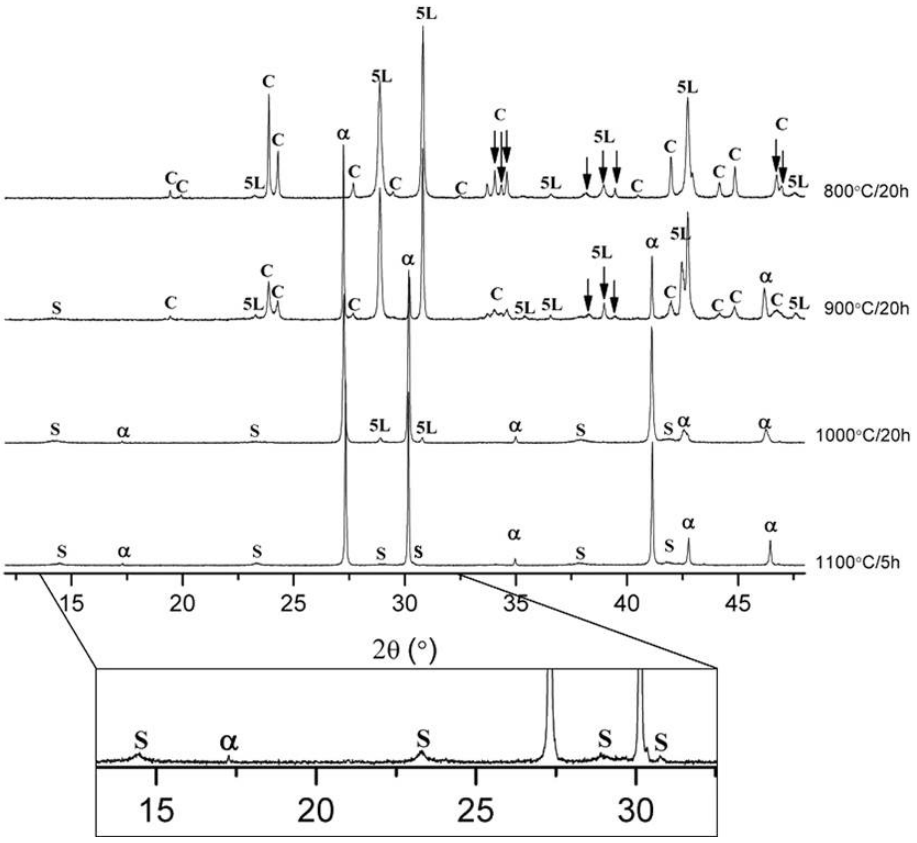

Figure 1: X-ray powder diffraction data for $Ba_4Nb_2O_9$ over the temperature range 800 < T < 1100 °C (a indicate α-$Ba_4Nb_2O_9$ phase, 5L indicates $Ba_5Nb_4O_{15}$ phase, C indicates $BaCO_3$ and S indicates unidentified weak and broad peaks).

The microstructure of the sample heated at 1100 °C for 5 hours is very porous and contains only up to 10 μm large agglomerates of dense material (Fig. 2. a-b). This indicated that the mechanism of the grain growth in $Ba_4Nb_2O_9$ ceramic did not achieve the initial stage of densification. The results are in agreement with sintering curve, which indicates that the early stage of sintering begins just above 1200 °C (Fig. 3). Density of the ceramic with composition corresponding to α-$Ba_4Nb_2O_9$ can be considerably increased by firing the sample at 1400 °C for 10 hours and slowly cooling down to room temperature (Fig. 2c-d). The microstructure of the surface of the pellet is very different from its central part. However, the surface of this sample has essentially higher porosity, which forms up to 40 μm thick layer. The X-ray diffraction analyses performed on the pellets' surface revealed that it composition corresponds to $BaCO_3$ and $Ba_5Nb_4O_{15}$, which indicate decomposition of α-$Ba_4Nb_2O_9$ at the contact with ambient air (Fig. 4.).

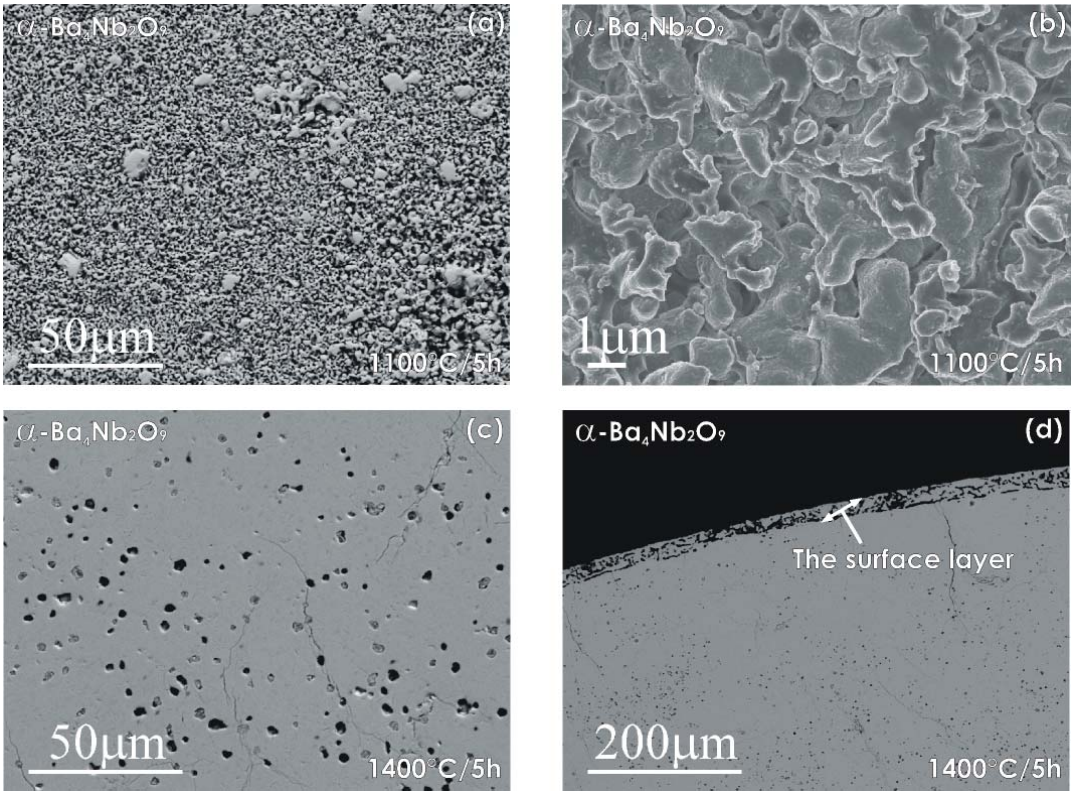

Figure 2: (a-b) Back-scattered electron-images of microstructures of sample with starting composition $BaO:Nb_2O_5$ = 2:1 sintered at 1100 °C for 5h **(c-d)** Back-scattered electron image of the sample sintered at 1400 °C for 10 hours and slowly cooled down to room temperature.

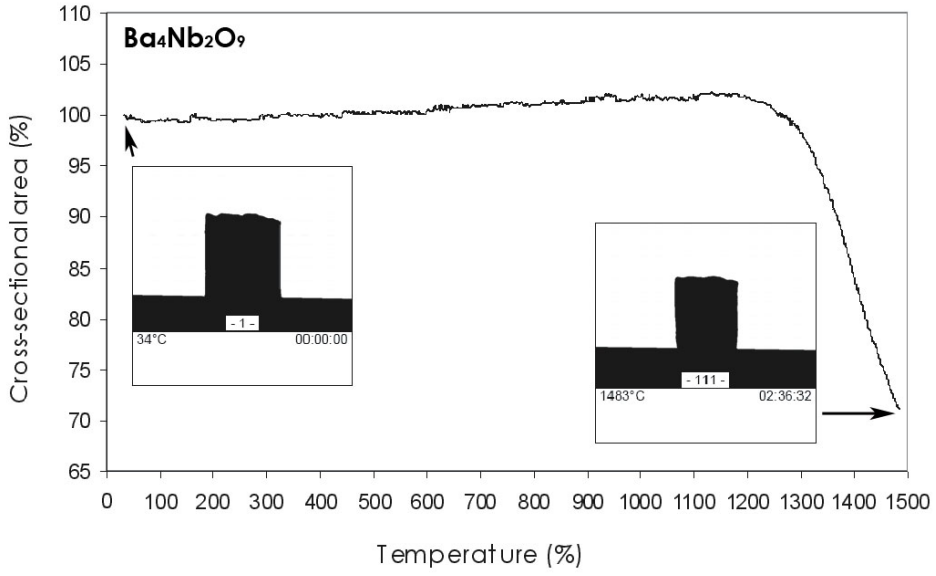

Figure 3: Sintering profiles of $Ba_4Nb_2O_9$ powder indicates that the ceramic start sinter above 1200 °C and melts above 1480°C.

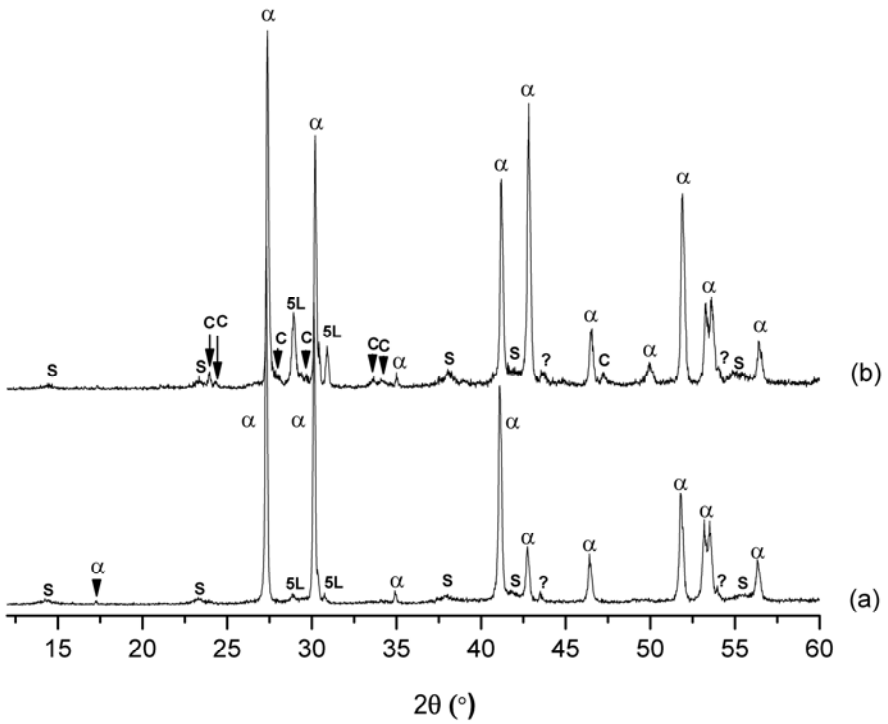

Figure 4: The room temperature X-ray diffraction patterns of $Ba_4Nb_2O_9$ fired at 1400 °C for 10h and slowly cooled down to room temperature recorded on **(a)** the powder and **(b)** on the surface of the pellet.

Furthermore, the X-ray diffraction patterns shown in Fig. 1(inset) reveal the presence of broad peaks with low intensity, which appear after firing above 900 °C. These diffraction peaks could either be a consequence of the presence of a secondary phase or a type of super-structural ordering in the $Ba_4Nb_2O_9$ phase or even the incommensurability of the crystal structure. The analysis of the ceramics prepared from α-$Ba_4Nb_2O_9$ powder sintered at 1100 °C in air showed no evidence for the presence of any secondary phases. As the unidentified reflections in the XRD pattern are weak and broad, this could indicate that secondary phases, if at all present, are nano-crystalline. In order to identify possible secondary phases at the grain boundaries in this sample we used a TEM (Fig. 5a). Even with moderate magnifications we were able to observe an abundant amorphous inter-granular phase between individual $Ba_4Nb_2O_9$ grains. At higher magnifications we found that this inter-granular phase is not homogeneous, but contains scattered 2-5 nm large nano-crystals (Fig. 5b). The selected area electron diffraction patterns of these nano-crystals (inset in Fig. 5b) correspond to the $Ba_5Nb_4O_{15}$ phase. This is further confirmed by the EDS analysis of the nano-crystals, which shows a decrease in the Ba/Nb ratio with respect to the well-crystallized $Ba_4Nb_2O_9$ grains. On the other hand, the composition of the amorphous phase indicates a higher Ba/Nb ratio than that found for the $Ba_4Nb_2O_9$ grains. The presence of a BaO-rich amorphous phase and the nano-crystals of $Ba_5Nb_4O_{15}$ suggest the decomposition of α-$Ba_4Nb_2O_9$.

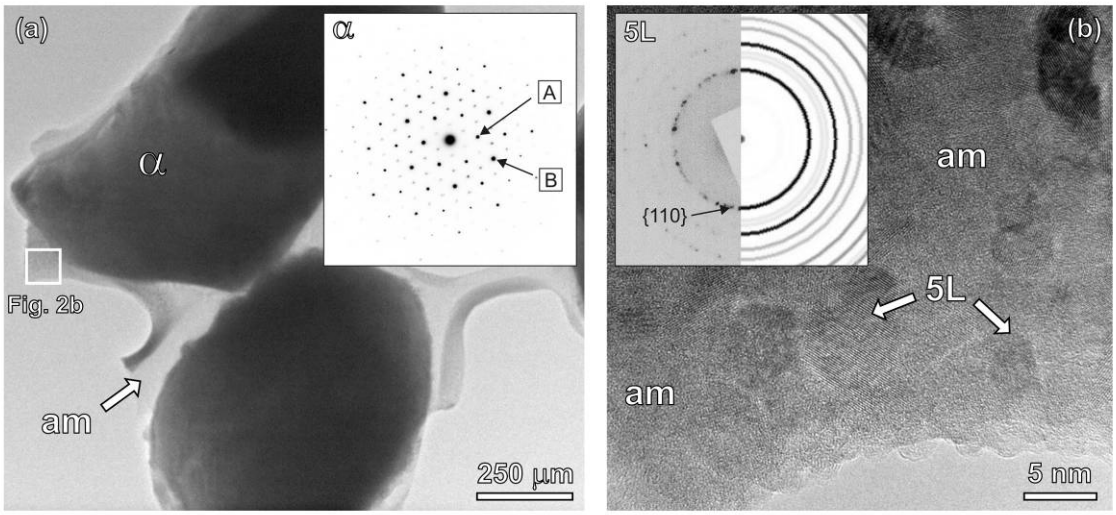

Figure 5: **(a)** A Bright-field TEM micrograph of α-$Ba_4Nb_2O_9$ shows matrix-phase grains (α) and inter-granular amorphous phase (am). The inset in upper-right corner shows a SAED pattern collected from α-$Ba_4Nb_2O_9$ grains. The diffraction spot A corresponds to $(100)_L=(220)_T$, and the spot B corresponds to $(110)_L=(600)_T$ (the subscripts L and T refer to indexing according to Leshchenko *et al*. [1979] and Trunov *et al.*, [1979] respectively). The square on the left side of the micrograph shows the area enlarged in Fig. b. **(b**) A HRTEM micrograph shows the presence of nano-sized $Ba_5Nb_4O_{15}$ crystals (5L) within the amorphous phase. The inset shows a SAED pattern collected from nano-crystals and the simulated pattern corresponding to $Ba_5Nb_4O_{15}$ crystals.

These observations, however, do not explain the weak, broad reflections in the XRD spectra. The SAED patterns of the matrix-phase grains (inset in Fig. 5a) indicate their hexagonal symmetry and the main diffraction spots can be indexed either to the reduced hexagonal-cell of the a-$Ba_4Nb_2O_9$ modification, as proposed by Leshchenko *et al*. [1979] or to the hexagonal super-structure (PDF file #46-0939), as reported by Trunov *et al.* [1979]. Based on analogy with the $Ba_4Ta_2O_9$ structure, [Paramova *et al.*, 1976] Leshchenko *et al.* [1979] described some reflections as super-structural. For this reason the unit-cell constants (a = 5.923 Å and c = 4.230 Å) were interpreted as sub-structural, while the super-structural peaks evident from the XRD pattern were not considered in the calculation of the unit-cell dimensions. In the analysis of the XRD data by Trunov *et al*. [1979] most of the weak reflections were included and indexed as a hexagonal super-structural cell (a = 20.52 Å and c = 8.452 Å), which also corresponds to recorded electron diffraction data. If SAED pattern recorded in this experiment is indexed according to the unit-cell proposed by Leshchenko *et al*. [1979] the diffraction spot A (see the inset of Fig. 5a) would be indexed as (100), whereas according to Trunov *et al*. [1979] this spot is indexed as (220), indicating that their unit-cell is rotated by 30°, with respect to the sub-cell of Leshchenko *et al*. [1979] and multiplied along the *a*-axis. Similarly, the reflection spot B from our SAED pattern, can be indexed using the unit-cell of Leshchenko *et al*. [1979] as (110), and according to Trunov *et al*. [1979] as (600). The super-structural reflections in the SAED pattern (see the inner ring of weak reflections in the inset of Fig. 5a) and most of the remaining weak reflections in our XRD pattern suggest that the structure of α-$Ba_4Nb_2O_9$ indeed has a hexagonal symmetry with unit-cell parameters that correspond to those proposed by Trunov *et al*. [1979].

4.3.1.1.2. γ-$Ba_4Nb_2O_9$ modification

When a-$Ba_4Nb_2O_9$ is heated above 1200 °C and quenched to room temperature the recorded XRD pattern corresponds to the γ-modification of $Ba_4Nb_2O_9$ (PDF file #35-1156) [Leshchenko *et al.*, 1979]. The XRD spectra of the samples sintered at 1200, 1300 and 1400 °C for 5 h and quenched to room temperature are shown in figure 6. In addition to this modification the XRD and SEM (Fig. 7) analyses of the samples quenched from T > 1200 °C did not reveal the presence of any other phase, which implies that the γ-modification is the high-temperature polymorph of $Ba_4Nb_2O_9$.

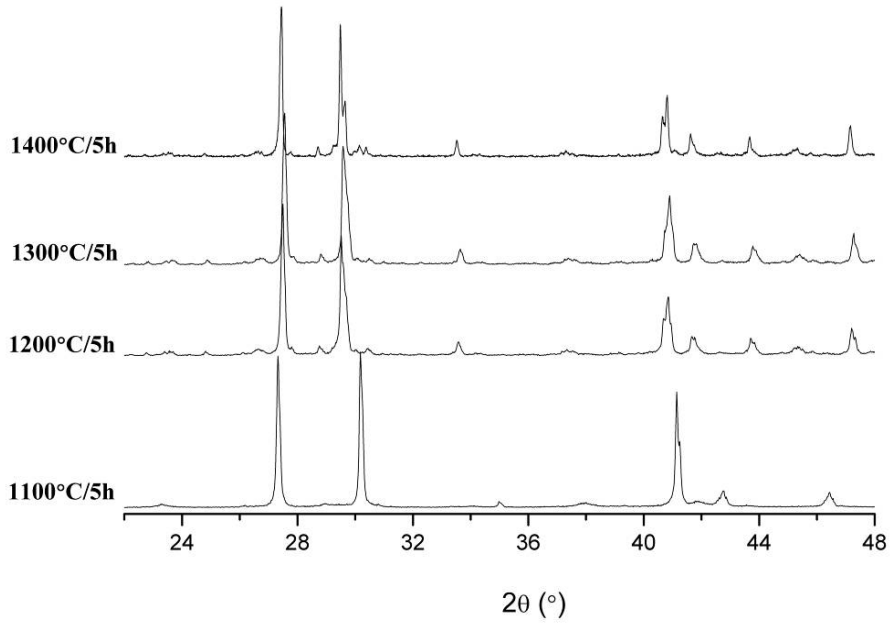

Figure 6: X-ray diffraction patterns of $Ba_4Nb_2O_9$ samples quenched to room temperature from 1100, 1200, 1300 and 1400 °C.

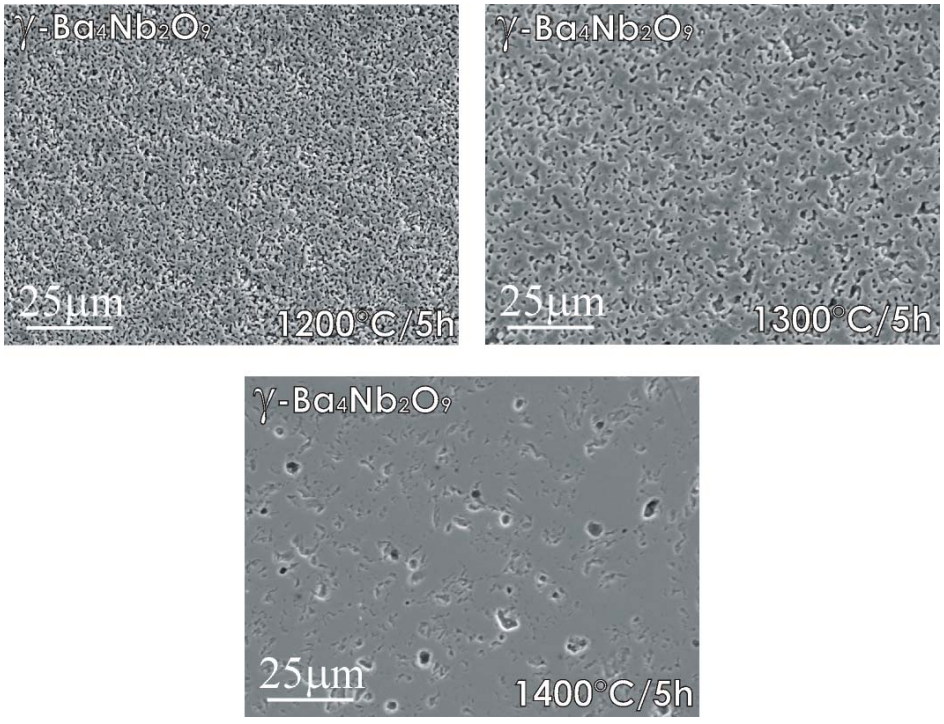

Figure 7: Secondary-electron image of microstructure of $Ba_4Nb_2O_9$ samples quenched to room temperature from 1200, 1300 and 1400 °C.

4.3.1.1.3. β-$Ba_4Nb_2O_9$ modification

Leshchenko *et al*. [1985] reported that the γ-modification transforms to yet another polymorph, the β-modification, as it is heated in the temperature range 257-317 °C. In order to prove the existence of this modification at low temperatures we annealed a pre-sintered γ-$Ba_4Nb_2O_9$ phase at 300 °C in air for 5 hours. All the major peaks in the XRD spectrum of this specimen correspond to the β-$Ba_4Nb_2O_9$ phase, as described by Leschenko *et al*. [1979] (Fig. 8). Additionally, some minor reflections, which can be ascribed to $BaCO_3$, are also present in the spectrum. They could either be a consequence of the slightly more Nb_2O_5-rich chemical composition of the β-$Ba_4Nb_2O_9$ modification or it could be due to a partial decomposition of the β-$Ba_4Nb_2O_9$. Furthermore, we found that after repeated heating at 1300 °C and slow cooling (via an intermediate α-modification) to room temperature the $Ba_4Nb_2O_9$ progressively converts into the β-polymorph (Fig. 9). Following each firing/cooling cycle (5h annealing time each) the samples were homogenized and re-pressed into pellets. After the third cycle some peaks of the β-$Ba_4Nb_2O_9$ modification appeared in the XRD pattern. In addition to the β- and α-peaks some low-intensity peaks that correspond to $Ba_5Nb_4O_{15}$ and $BaCO_3$ could be detected after the third cycle. The intensity of the β-peaks gradually increased with the increasing number of sintering cycles, whereas the diffraction peaks of the α-modification gradually decreased and finally disappeared in the 6th cycle (after a total of 30 hours of annealing). However, the β-phase does not form when the α-phase is heated at 300 °C and quenched, even after annealing for times as long as 60 hours.

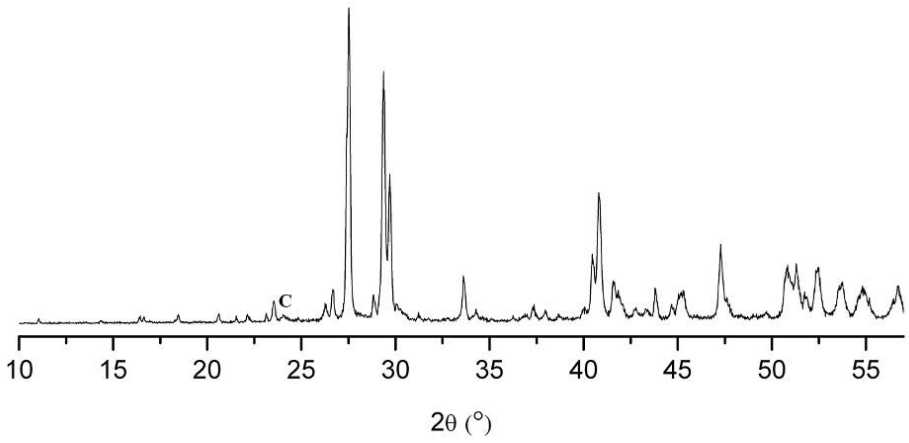

Figure 8: X-ray powder diffraction pattern of $Ba_4Nb_2O_9$ heated at 300 °C for 5 hours and quenched. Most of the diffraction peaks correspond to β-$Ba_4Nb_2O_9$ modification (β), and C indicates minor $BaCO_3$ peaks.

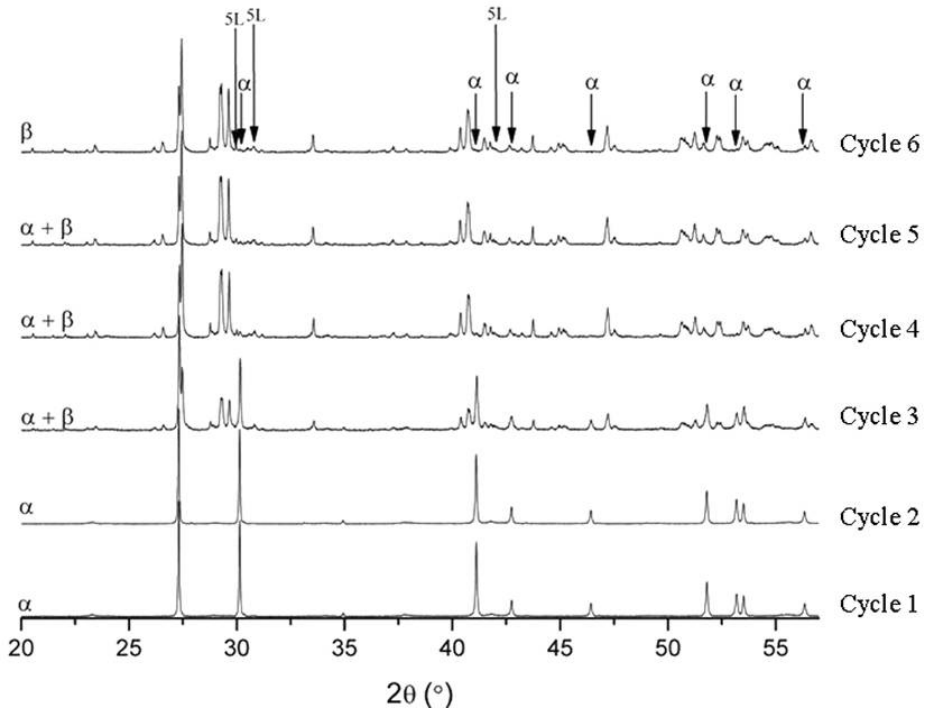

Figure 9: X-ray diffraction patterns of $Ba_4Nb_2O_9$ show α → β phase transition. The peaks indicated by a belong to α-$Ba_4Nb_2O_9$, by β to β-$Ba_4Nb_2O_9$ and by 5L to the $Ba_5Nb_4O_{15}$.

In addition to the β-$Ba_4Nb_2O_9$, Leshchenko *et al.* [1985] reported the existence of the β'-$Ba_4Nb_2O_9$. According to their findings, the β-phase should be converted into the hexagonal β'-modification between 530 °C and 700 °C. To confirm the existence of β'-$Ba_4Nb_2O_9$ the sample was quenched from 560 °C after heating for 100 hours. The composition of the sample corresponded to the $Ba_5Nb_4O_{15}$, $BaCO_3$ and α-modification, which, according to Leschenko *et al.* [1985] should appear above 700 °C. We did not observe the β'-modification in any of the samples fired in the temperature range 560-1000 °C for 5h; however, we regularly observed the presence of $Ba_5Nb_4O_{15}$ and $BaCO_3$ in addition to both the α- and γ-reflections. The appearance of the γ-modification at these temperatures, the conversion of the γ-phase after quenching into the β-phase or its slow formation from α-phase after repeated reheating and grinding implies that β-modification could in fact be a disordered γ-modification, where the structural changes could also be induced by mechanical deformation. The additional peaks in the X-ray spectrum that correspond to the secondary $Ba_5Nb_4O_{15}$ and $BaCO_3$ phases coincide with the peaks reported for the β'-phase, suggesting that this intermediate phase, as reported by Leschenko *et al*. [1985] does not exist.

4.3.1.2. The stability and decomposition of the $Ba_4Nb_2O_9$ phases

Based on these results we identified the β-polymorph as the low-temperature modification observed below 500 °C, the a-polymorph as the medium-temperature modification observed in the temperature range between 560 °C and 1160 °C, and the γ-polymorph as the high-temperature modification found above 1160 °C. We further investigated the stability of the individual polymorphs by annealing the pelletized samples of the γ-$Ba_4Nb_2O_9$ polymorph at 300, 560, 1000 and 1300 °C for 100 hours in air. The corresponding XRD spectra recorded from the pellets' surfaces are shown in Fig. 10.

After annealing the sample at 300 °C for 100 hours and quenching it to room temperature, the recorded XRD pattern corresponds to that of the β-modification, which confirms its formation at low temperatures. The XRD pattern of the sample fired at 560 °C for 100 hours, where according to Leschenko et al. [1985] the β'-modification should be stable, corresponds to $Ba_5Nb_4O_{15}$ and $BaCO_3$ instead of any $Ba_4Nb_2O_9$ polymorph. The reason for the observed instability could be the reactivity with the atmosphere, as was described by Vanderah *et al.* [2002] to be the case with the $Ba_3Nb_2O_8$ compound. After annealing at 1000 °C for 100 hours and quenching to room temperature the prevailing reflections in the XRD spectrum are those of α-$Ba_4Nb_2O_9$ and $Ba_5Nb_4O_{15}$, whereas $BaCO_3$ reflections were not observed. This condition reflects the situation observed with the TEM on the α-$Ba_4Nb_2O_9$ samples, where the secondary phases were the amorphous BaO-rich phase and the nano-crystalline $Ba_5Nb_4O_{15}$, which is, after an extended annealing time, well crystallized.

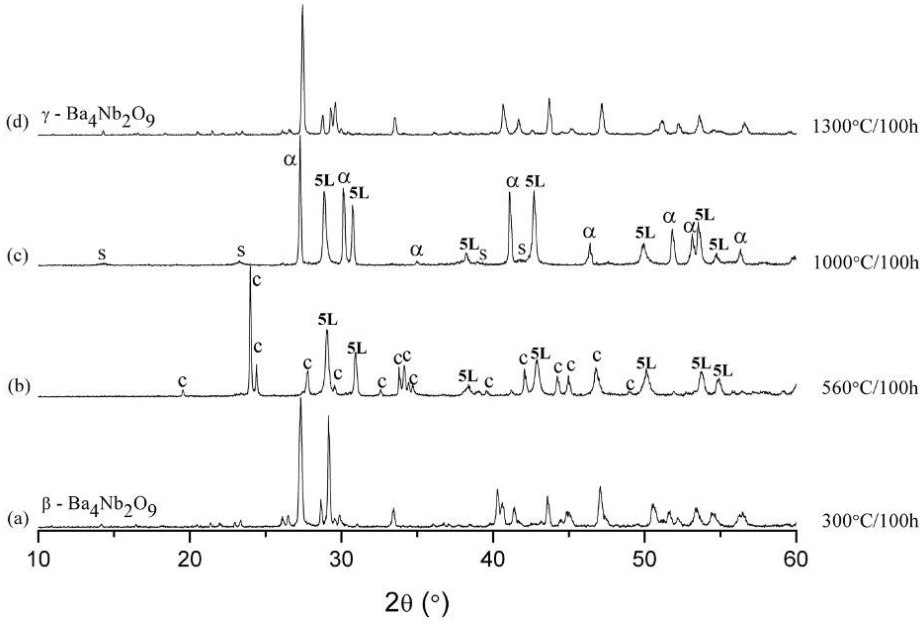

Figure 10: X-ray diffraction pattern of the surface of pellets quenched to room temperature after annealing for 100 hours at: **(a)** 300 °C, **(b)** 560 °C, **(c)** 1000 °C and **(d)** 1300 °C. The peaks indicated by a belong to α-$Ba_4Nb_2O_9$, whereas the peaks indicated by 5L and C correspond to the $Ba_5Nb_4O_{15}$ and $BaCO_3$.

The final sample fired at 1300 °C showed a relatively pure γ-modification with no decomposition products. These observations imply that the a-$Ba_4Nb_2O_9$ modification is very prone to decomposition into $Ba_5Nb_4O_{15}$ and the BaO-rich phase, whereas the β- and γ-modifications of $Ba_4Nb_2O_9$ are more stable and do not tend to decompose either at the firing temperature or at room temperature when exposed to air. We assume that the crystal structure of the hexagonal α-polymorph, which differs from the orthorhombic β and γ, may explain its instability in the presence of water and CO_2 in ambient air.

4.3.1.3. Polymorphic phase transitions in $Ba_4Nb_2O_9$

4.3.1.3.1. Room temperature studies of phase transitions in $Ba_4Nb_2O_9$

The polymorphic phase transitions in $Ba_4Nb_2O_9$ were followed by quenching the pre-sintered γ-$Ba_4Nb_2O_9$ modification (from 1300 °C) in the temperature range from 300 to 1300 °C for 20 hours at each temperature. After each experiment the same sample was ground, repressed into a pellet and then annealed at the next temperature. The XRD measurements were performed at room temperature (Fig. 11).

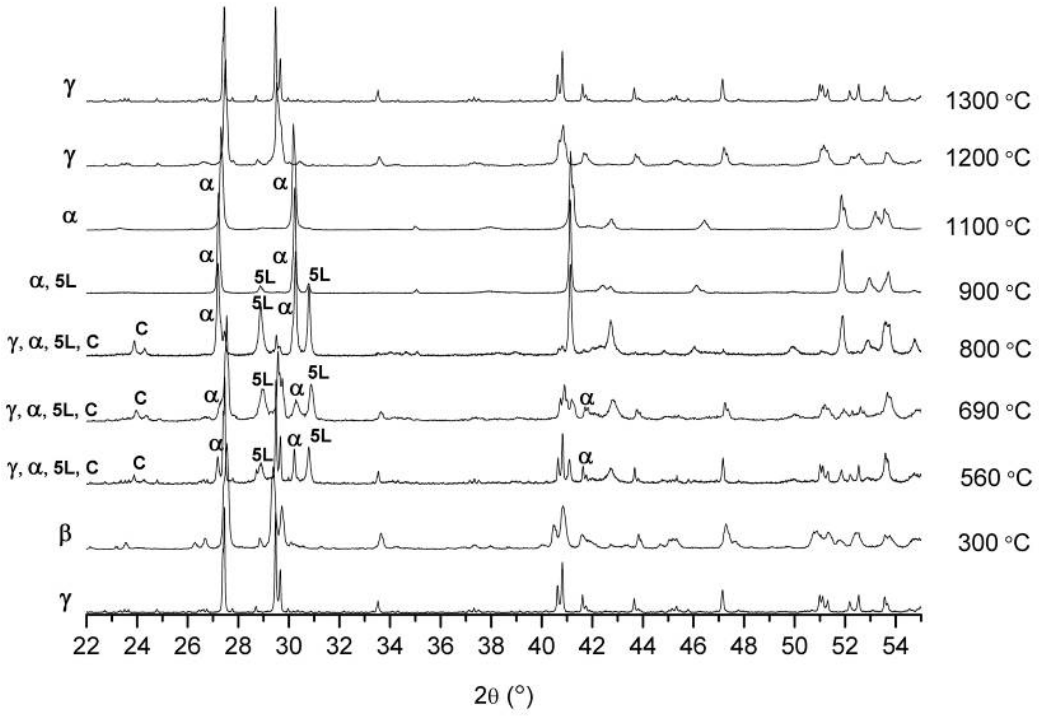

Figure 11: Room temperature X-ray powder diffraction patterns of samples repeatedly heated for 20 hours in the temperature range 300-1300 °C and quenched to room temperatures. (α = α-$Ba_4Nb_2O_9$ phase, β = β-$Ba_4Nb_2O_9$ phase, γ = γ-$Ba_4Nb_2O_9$ phase, 5L = $Ba_5Nb_4O_{15}$ phase and C = $BaCO_3$).

The first change in XRD spectra observed after reheating the γ-modification at 300 °C (Fig. 11) is related with the apparent broadening and slight peak displacements. This could reflect an initial stage of γ → α phase reconstruction through the formation of structural defects in the γ-phase. The gradual γ → α conversion accompanied by decomposition byproducts such as $Ba_5Nb_4O_{15}$ and $BaCO_3$ completes around 900 °C. These results show that both secondary phases appear either due to the sensitivity of $Ba_4Nb_2O_9$ to ambient air or as a decomposition products of γ-$Ba_4Nb_2O_9$, which are subsequently consumed for a-phase formation. The room temperature XRD pattern of the sample quenched from 1100 °C finally corresponds to pure α-$Ba_4Nb_2O_9$ (PDF # 35-1154) (Leshchenko *et al.*, 1980). This implies that after the complete γ → α conversion above 900 °C the further formation of α-$Ba_4Nb_2O_9$ is assisted by the reaction between $Ba_5Nb_4O_{15}$ and BaO-rich amorphous phase (Fig. 5) (not visible in the XRD spectrum) that remains after the decomposition of $BaCO_3$ close to 850 °C. The decomposition of $BaCO_3$ to BaO and CO_2 is evident from the mass fragment 44 that belongs to CO_2 and from the TG curve, which indicates about 0.25% mass loss in the temperature range 750-950 °C (Fig. 12).

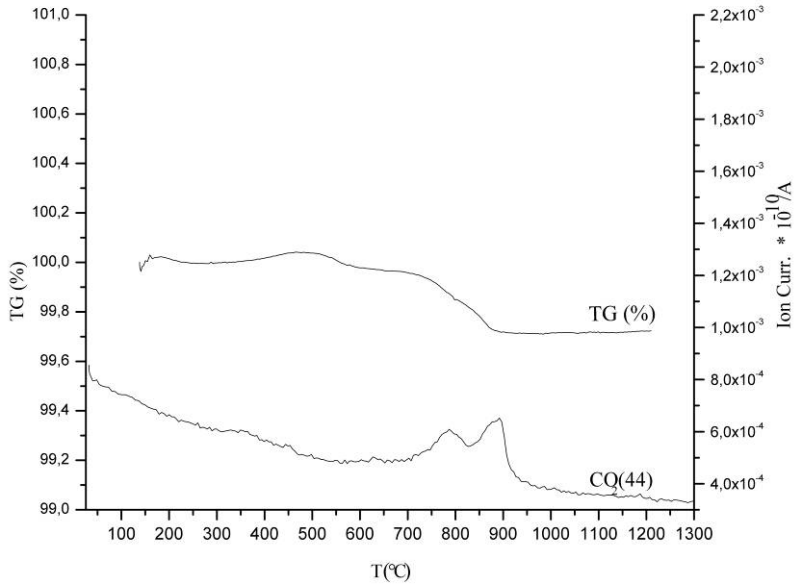

Figure 12: A thermo-gravimetric curve of a starting powder with γ-phase composition conducted from room temperature up to 1300 °C at the heating rate of 20 °C/min.

Regarding the XRD analyses the composition of the sample heated above 1200 °C corresponds to high-temperature γ-$Ba_4Nb_2O_9$. The γ-peaks at 1200 °C are less sharp than those at 1300 °C implying that the crystallinity of the sample is improved at higher firing temperatures. The XRD spectra of the samples from above 1200 °C did not reveal the presence of any other phase. The phase composition of the $Ba_4Nb_2O_9$ samples fired in air at 1100 °C (α-phase) and 1300°C (γ-phase) was further studied by the TEM/EDS analyses. In both cases the TEM analyses revealed the presence of very fine partly crystallized secondary phase surrounding the agglomerates of primary $Ba_4Nb_2O_9$ grains. The 1100 °C sample

consisted of large α-$Ba_4Nb_2O_9$ grains with minor intergranular amorphous BaO-rich phase, which is embedding nanosized $Ba_5Nb_4O_{15}$ crystallites (Fig. 5). On the other hand the 1300 °C sample consists of large grains with numerous γ-$Ba_4Nb_2O_9$ domains. In figure 13a γ-$Ba_4Nb_2O_9$ grain is viewed along the $[001]_\gamma$ zone axis. In this orientation the domains are rotated by 120° with respect to each other. The SAED pattern of a single γ-$Ba_4Nb_2O_9$ domain in $[001]_\gamma$ orientation shows that the basic reflections closely resemble the hexagonal SAED pattern of α-$Ba_4Nb_2O_9$ modification along the $[001]_\alpha$ zone axis (Fig. 5). The only difference between the two polymorphs is the presence of additional reflections in γ-phase (inset in Fig 13a) along the $[010]_\alpha$ direction.

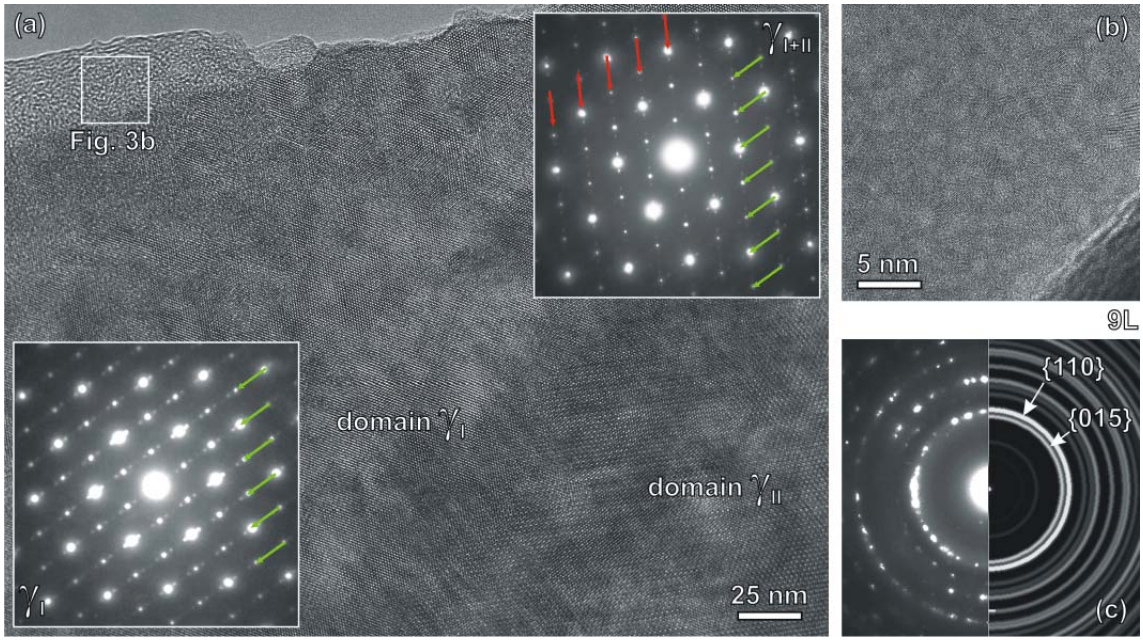

Figure 13: (a) A HRTEM micrograph of multi-domain γ-$Ba_4Nb_2O_9$ grain with SAED patterns from a single domain (γ_I) and two overlapping domains (γ_{I+II}) (shown as insets) at the angle of 120° (see the green and red arrows). The area of the overlapping domains shows an interference Moireé pattern. **(b)** An area with nanocrystalline BaO-deficient $Ba_3Nb_2O_8$ phase. **(c)** The SAED pattern (experimental – left; simulated - right) confirms the presence of nanocrystalline $Ba_3Nb_2O_8$ (9L).

The extra reflections in $[001]_\gamma$ pattern result from an orthorhombic expansion of the *a*-parameter of the γ-$Ba_4Nb_2O_9$ unit-cell. If SAED is recorded over a grain with multiple γ-$Ba_4Nb_2O_9$ domains we obtain a complex pattern with rows of superstructure γ-reflections crossing at 60° (see the inset in Fig 13a). Multiple domains form due to both microstructural steric limitations and a unit-cell volume change that takes place during α → γ phase transition. The domain structure was observed only in larger γ-$Ba_4Nb_2O_9$ grains, while the smaller grains often show only a single γ-$Ba_4Nb_2O_9$ domain. The extra reflections and the formation of the domain structure implies that γ-phase has a lower symmetry, as suggested by

Leshchenko *et al.* [1985], who reported that γ-modification is noncentrosymmetric and exhibits a pyroelectric behaviour along the $[010]_\gamma$ direction. The γ-grains are in contrast to those of α-$Ba_4Nb_2O_9$ surrounded by pockets of nanocrystalline $Ba_3Nb_2O_8$ (Fig. 13b), which reportedly forms above 1200 °C [Vanderah *et al.*, 2002]. The appearance of $Ba_3Nb_2O_8$ in γ-sample (fired at 1300 °C for 20 h) is a result of the reaction between the remaining BaO-rich amorphous phase and nanocrystalline $Ba_5Nb_4O_{15}$ find in low-temperature α-sample, since the α-$Ba_4Nb_2O_9$ is a precursor material for γ-phase formation. The presence of $Ba_3Nb_2O_8$ was confirmed by SAED patterns (see the inset in Fig. 13b) and semi-quantitative EDS analysis, which indicates lower Ba/Nb ration with respect to than that found for $Ba_4Nb_2O_9$ and consequently suggests a partial loss of BaO from the system.

4.3.1.3.2. In-situ high-temperature studies of phase transitions in $Ba_4Nb_2O_9$

4.3.1.3.2.1. Decomposition of $Ba_4Nb_2O_9$ studied by high-temperature XRD in air

The decomposition of $Ba_4Nb_2O_9$ close to 560 °C (Fig. 11) was studied by high-temperature X-ray diffractometry (HT-XRD) in air (Fig. 14). For this purpose we used a γ-$Ba_4Nb_2O_9$ powder and allowed sample holding times at each temperature for its efficient surface reaction with air. The HT-XRD pattern recorded at room temperature could be indexed to the orthorhombic γ-$Ba_4Nb_2O_9$ (PDF # 35-1156).

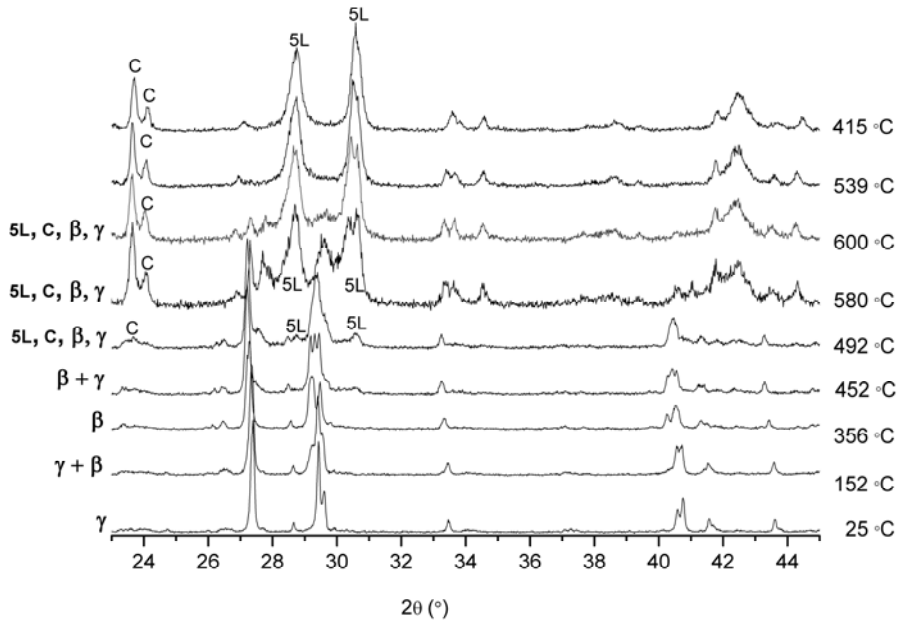

Figure 14: A segment from the observed high-temperature XRD patterns recorded on γ-$Ba_4Nb_2O_9$ showing the evolution of phase transitions at low temperature for $Ba_4Nb_2O_9$ and its decomposition around 500 °C in air. The heating/cooling rate employed was 12 °C/min and the holding time was 1 h at each temperature. (β = β-$Ba_4Nb_2O_9$, γ = γ-$Ba_4Nb_2O_9$, 5L = $Ba_5Nb_4O_{15}$ and C = $BaCO_3$).

The XRD spectra recorded at 152 °C shows that the peak at 2θ ~29 ° starts to split indicating the formation of defects in the crystal structure of γ-modification. There was no sign of the significant peak splitting in the pattern recorded at ~356 °C. The γ-peak triplets are reduced to two peaks, {230} and {400}, characteristic for β (γ')-$Ba_4Nb_2O_9$ [Bezjak *et al.*, 2008]. The γ-peak triplets reappear at ~452 °C. The XRD pattern at ~492 °C already shows the presence of $Ba_5Nb_4O_{15}$ and $BaCO_3$ as the surface decomposition products of $Ba_4Nb_2O_9$ in air. The XRD spectra recorded in the temperature range 580-600 °C revealed that most of $Ba_4Nb_2O_9$ is decomposed. The broadening of the diffraction peaks indicates the presence of nanocrystalline form of the decomposition products. $Ba_5Nb_4O_{15}$ and $BaCO_3$ remain stable after cooling the sample down to room temperature. These results suggest a considerable surface instability and decomposition of $Ba_4Nb_2O_9$ under ambient conditions above ~492 °C.

4.3.1.3.2.2. Phase transitions in $Ba_4Nb_2O_9$ studied by high-temperature XRD in air

To determine the nature of phase transformations in $Ba_4Nb_2O_9$ in-situ experimental studies including HT-XRD and thermal analyses (DTA, DSC) were performed. The experiments were preformed in ambient air starting from the γ-$Ba_4Nb_2O_9$ sample. An excessive decomposition of the sample in this HT-XRD experiment was avoided by relatively short holding times at each temperature. The HT-XRD data at 330 °C (Fig. 15) suggest that γ-$Ba_4Nb_2O_9$ completely converts into β (γ')-$Ba_4Nb_2O_9$. This transition is also shown by an exothermic peak at ~330 °C in the DSC curve (Fig. 16) implying a γ → γ' structural transformation that is accompanied by a release of an accumulated internal energy.

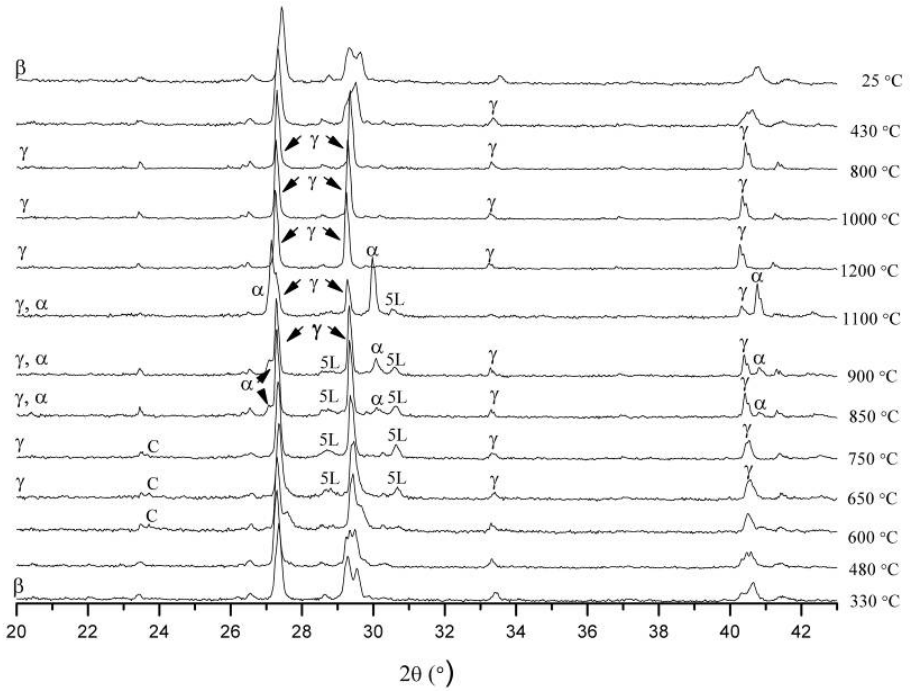

Figure 15: The HT-XRD data obtained during reheating γ-$Ba_4Nb_2O_9$ over the temperature range 25→1200→25 °C in an ambient air. The heating/cooling rate employed was 3 °C/min with 9 min holding time at each temperature.

The first XRD spectrum recorded on the starting γ-powder at 330°C shows a pattern that corresponds to β (γ')-modification. The {230} and {400} reflections of this metastable phase start to split into triplets at 480 °C, leading to the reappearance of γ-peaks at elevated temperatures. The supplemental evidence for reappearance of the γ-phase is an endothermic peak in the DSC curve with the maxima at 512 °C (Fig. 16). Together with γ-reflections the peaks corresponding to $Ba_5Nb_4O_{15}$ become evident above 600 °C. The formation of the $Ba_5Nb_4O_{15}$ phase coincides with the small exothermic peak at 644 °C in the DSC curve (Fig. 16). Due to a relatively short holding times (9 min) at each temperature the formation of $BaCO_3$ is less pronounced but still visible in the XRD spectra. At 850 °C the peaks of α-$Ba_4Nb_2O_9$ emerge in the XRD pattern.

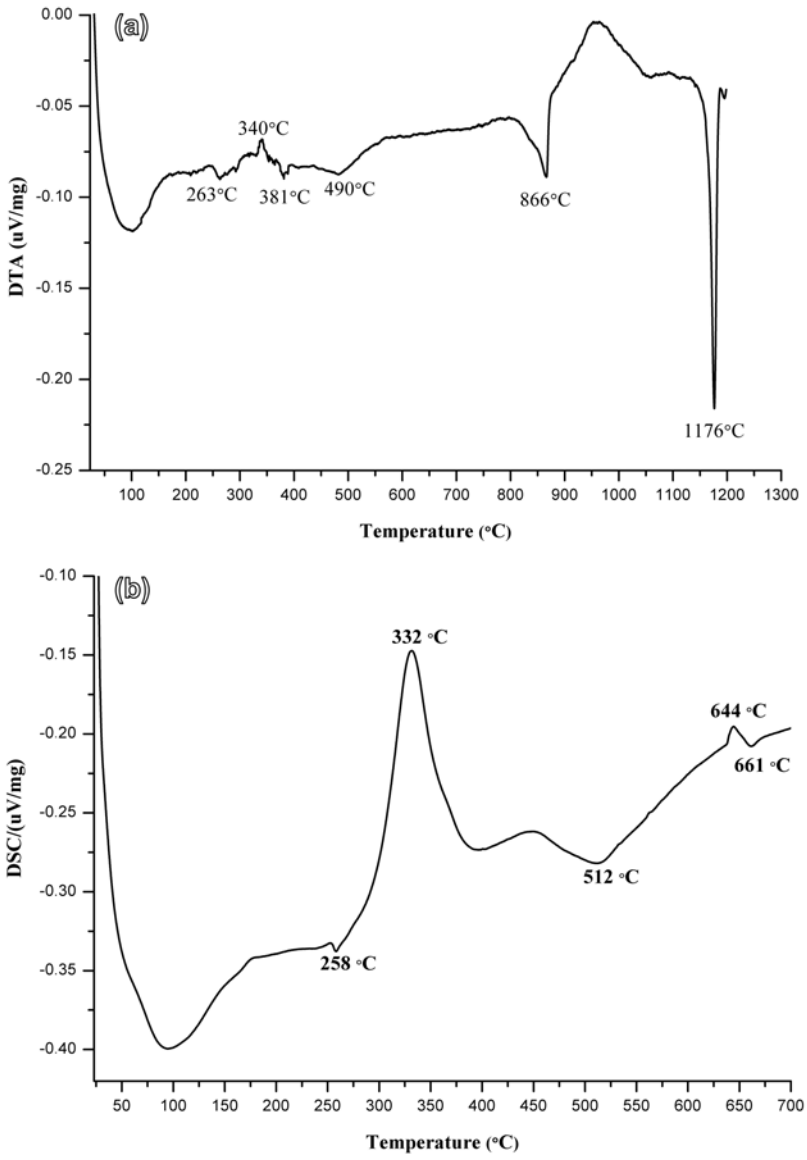

Figure 16: (a) A differential thermal analysis curve recorded on the starting γ-phase powder conducted from the room temperature up to 1300 °C at the rate of 20 °C/min. **(b)** A differential scanning calorimetric curve recorded up to 700 °C at the rate of 20 °C/min to reveal the γ → γ' phase transition at 332 °C.

The appearance of the α-phase coincides with the endothermic peak at 866 °C in the DTA curve (Fig. 16). The intensity of the α-peaks increases with an increasing temperature while the peaks of the γ-phase gradually decrease but never disappear due to a relatively high heating rate and short holding time during the HT-XRD experiment, which is also the main reason that we never observed a complete γ → α conversion up to 1100 °C. At 1200°C the XRD spectrum shows only the peaks of pure γ-phase. The α → γ phase transition in this temperature range coincides with the sharp endothermic peak at 1176 °C in the TGA curve (Fig. 16), which is in agreement with the α → γ transition temperature reported by Leshchenko *et al.* [1985]. While the conversion into γ-modification was completed with a relatively fast heating rate during the HT-XRD experiment, the reverse phase transition into a-modification did not occur at the same rate of cooling. This suggests that the α → γ transformation is relatively faster than the reverse transformation from γ → α, implying that the kinetics of the formation of γ-$Ba_4Nb_2O_9$ domains is faster than their recrystallization into single crystal a-grains. Further cooling of the sample down to room temperature did not yield any a-phase. Surprisingly, after cooling we obtain the reflections that correspond to β (γ')-$Ba_4Nb_2O_9$ modification below 430 °C. This could be explained that the rate of cooling applied to the γ-$Ba_4Nb_2O_9$ sample strongly affects the nature of phase transitions. Namely, if the sample of γ-phase is rapidly cooled down (quenched) to room temperature the γ-modification is retained, if the cooling rate is slower (~3 °C/min, as in the present HT-XRD experiment) the resulting modification corresponds to β (γ'), however if the cooling is even slower (1-2 °C/min) we obtain a pure a-modification. It is interesting to note that the presence of β (γ')-modification was observed also on the surface of quenched γ-$Ba_4Nb_2O_9$ sample, which suggests that even after the rapid cooling some surface reconstruction takes place in the γ-phase. The β (γ')-modification could therefore be understood as a distorted γ-modification after its unsuccessful transformation into a-phase during rapid cooling.

4.3.1.3.2.3. Phase transitions in $Ba_4Nb_2O_9$ studied by high-temperature SAED analyses in vacuum

The phase transition sequence in $Ba_4Nb_2O_9$ was also studied by high-temperature TEM. The experiment started at room temperature with γ-$Ba_4Nb_2O_9$ crystal in the $[001]_\gamma$ zone axis orientation (SAED in Fig. 17a) that can actually be indexed using the orthorhombic cell parameters given by Leshchenko *et al*. [1979] (*a* = 1.203 nm, *b* = 2.099 nm and *c* = 2.481 nm) with the condition hk0: h = 2n. The first change in the SAED pattern was observed at 360°C and corresponds to the γ → β (γ') phase transition observed by DTA/DSC and XRD. Additional rows of reflections (see arrows in Fig. 17b) appear along the [010]* direction between the rows of superstructure reflections of the γ-phase. These extra reflections show that the basic SAED pattern of β (γ')-modification is closely related to that of the γ-phase and could be, at first, interpreted as a doubling of the *a*-parameter keeping the condition hk0: h = 2n or as the suppression of the condition hk0: h = 2n keeping the *a*-parameter unchanged.

From the lattice image recorded at 440 °C, such an interpretation is less obvious since the γ → β (γ') transition seems to be associated with some kind of twinning process (see the image in the central part of the Fig. 17). According to Leshchenko *et al.* [1978] γ-$Ba_4Nb_2O_9$ has a noncentrosymmetric (polar) structure, while β-$Ba_4Nb_2O_9$ displays a centrosymmetric character. The higher symmetry could also be explained by an inversion twinning of γ-phase on the structural level to produce the symmetry elements as observed in the β (γ')-modification. Further studies involving the observation of several zone axis patterns would be required to obtain more details on the true nature of this so-called β-modification. By a further increase of the temperature to 585 °C the extra rows of reflections clearly disappear and the SAED pattern resembles the starting SAED pattern of the γ-phase. In this way we have confirmed that γ → β (γ') → γ transformations indeed take place below 600°C and that β (γ')-modification can be considered as a distorted γ-$Ba_4Nb_2O_9$. The observed transition of β (γ') into γ-modification is also in good agreement with the endothermic effect in the DSC curve appearing in this temperature range (Fig. 16). By increasing the temperature we observe a progressive suppression of the orthorhombic superstructure reflections up to 840°C where the SAED patterns correspond to the α-phase viewed along the $[001]_\alpha$ zone axis considering either hexagonal or primitive trigonal unit cell. This is in fairly good agreement with the onset of the endothermic peak reflecting the γ → α phase transition in the TGA curve (Fig. 16). The last α → γ phase transition occurring at 1176 °C was out of the range of the heating holder and the experiment was stopped at 850 °C. On cooling to room temperature the a-modification is retained without any transition over the β (γ')-modification in the temperature range of 585-360 °C. This proves that a-phase is the only stable low-temperature polymorph of $Ba_4Nb_2O_9$.

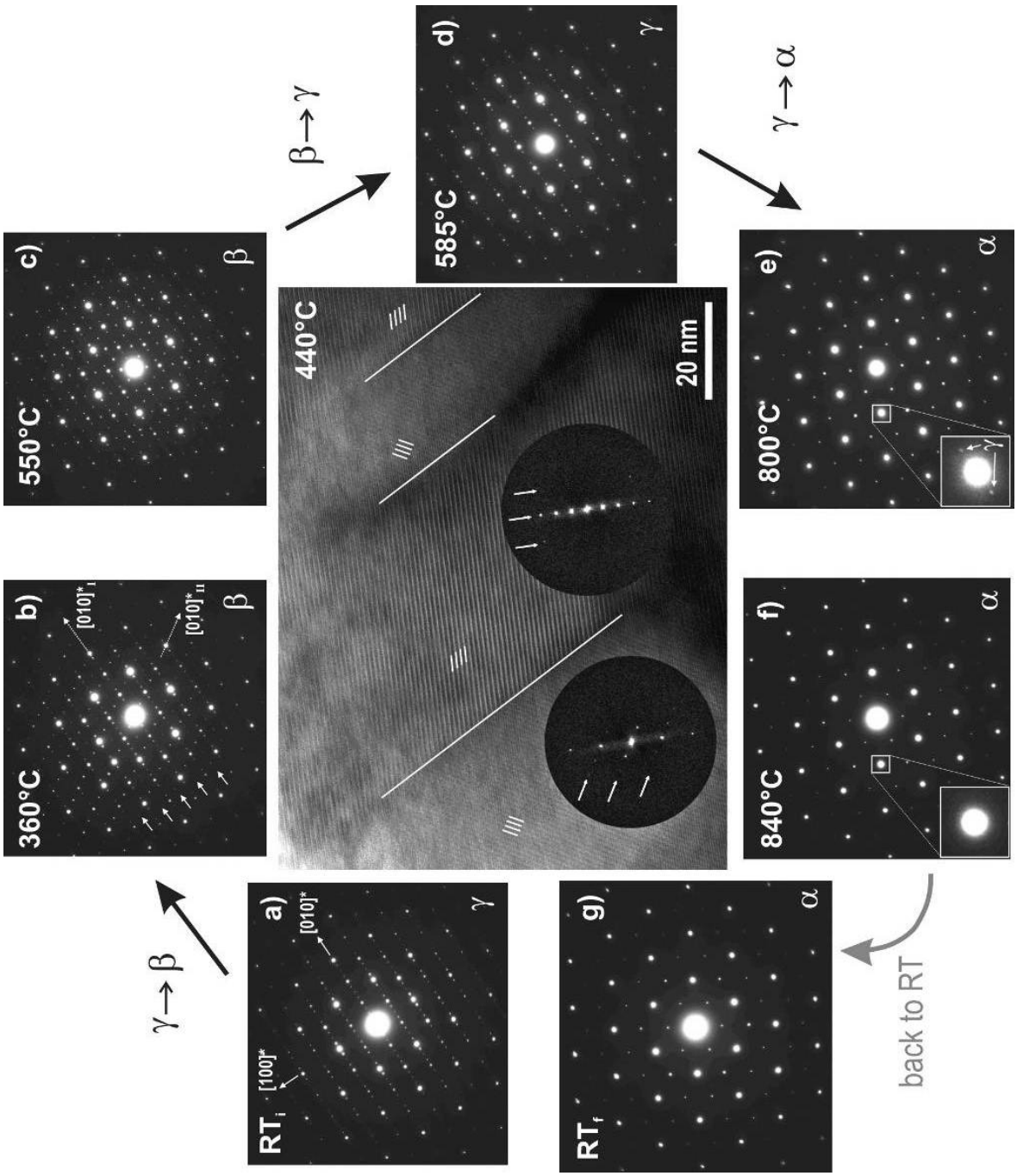

Figure 17: SAED patterns recorded on the initial γ-$Ba_4Nb_2O_9$ grain in [001]-orientation in the temperature range of 20-850 °C and backwards. **(a)** The SAED pattern at room temperature corresponds to the initial γ-modification with rows of superstructure reflections characteristic for the orthorhombic γ-phase. These reflections appear along the $[010]_\alpha$ directions with respect to the basic hexagonal pattern of the α-phase [Bezjak *et al.*, 2008]. **(b)** At 360 °C extra rows of reflections (indicated by arrows) appear in the SAED pattern that correspond to the distorted γ-modification (*i.e.,* β (γ')-modification). The β (γ') –phase transition come with the appearance of 120 ° oriented domains as illustrated in the central image recorded at 440 °C. **(c)** β (γ')-modification is retained up to 550 °C. **(d)** At 585 °C the SAED pattern transforms back into the pattern characteristic for the γ-phase. **(e)** At 800 °C the SAED pattern shows almost complete transformation of γ into α-modification with some remaining traces of γ-phase (see the inset) that completely disappears at **(f)** 840 °C, implying that $\gamma \rightarrow \alpha$ transition is gradual. **(g)** Upon cooling to room temperature the α-modification is retained.

4.3.1.3.2.4. Phase transitions in $Ba_4Nb_2O_9$ studied by high-temperature XRD analyses in vacuum

The phase transitions observed in the transmission electron microscope took place in a relatively high operating vacuum (~10^{-6} mbar). To verify the influence of atmosphere conditions on both phase transitions and phase decomposition we have performed additional HT-XRD analyses in vacuum (~10^{-3} mbar). Heating the γ-$Ba_4Nb_2O_9$ sample to 350°C results in broadening of the XRD peaks (Fig. 18) as already observed in the XRD spectra recorded in ambient air. This broadening can be attributed to the twinning process observed during the HT-TEM experiment in relation with the apparition of the β (γ')-modification, which obviously forms either under both vacuum and ambient conditions.

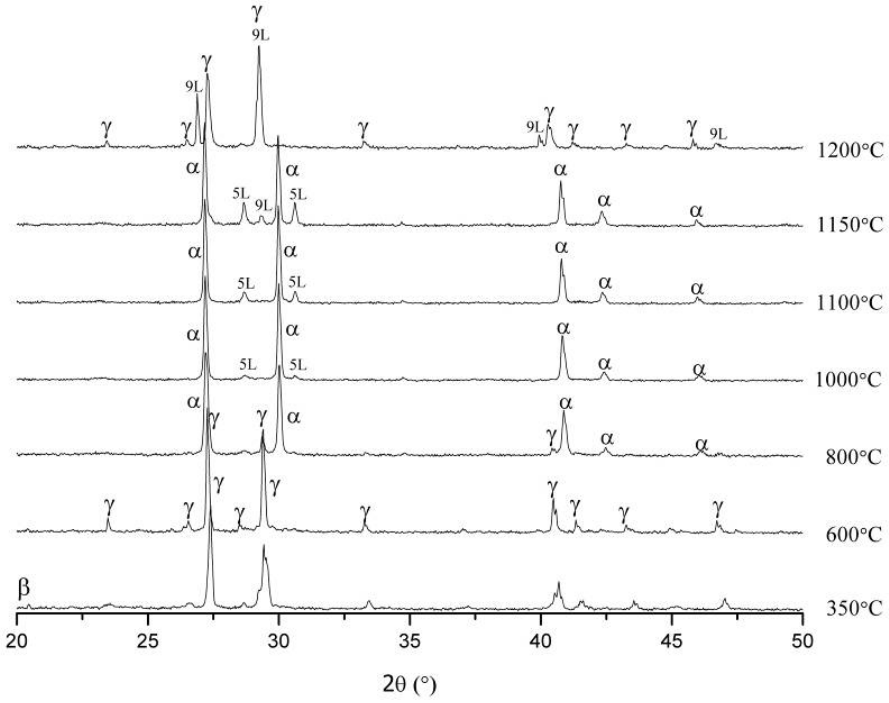

Figure 18: The HT-XRD patterns recorded during reheating γ-$Ba_4Nb_2O_9$ over the temperature range 25 → 1200 °C in vacuum. The heating/cooling rate employed was 3 °C/min with 9 min holding time at each temperature. (β = β-$Ba_4Nb_2O_9$ phase, γ = γ-$Ba_4Nb_2O_9$ phase, 5L = $Ba_5Nb_4O_{15}$ phase and 9L = $Ba_3Nb_2O_8$).

At 800 °C the majority of γ-$Ba_4Nb_2O_9$ is transformed into a-modification. While γ → α phase transition was never completed in the HT-XRD experiment conducted at the same heating rate in air (Fig. 15), we observe a rapid and complete conversion to a-phase in vacuum (Fig. 18) above 800°C. This effect could be explained by re-examination of the HT-XRD spectra recorded in air and their comparison of the phase formation sequences under vacuum. In atmospheric air conditions partial decomposition of γ-$Ba_4Nb_2O_9$ is assisted by its reaction with

an ambient CO_2 to form $BaCO_3$ and $Ba_5Nb_4O_{15}$ at temperatures as low as 650 °C. This is far below the $\gamma \rightarrow \alpha$ phase transition temperature, as observed by both our HT-TEM experiment (Fig. 17e-f) as well as the HT-XRD analysis conducted in vacuum. In the preparatory stage of $\gamma \rightarrow \alpha$ phase transformation the surfaces of $Ba_4Nb_2O_9$ grains react with atmospheric CO_2 to form $BaCO_3$ and the reaction by-product $Ba_5Nb_4O_{15}$ when exposed to ambient air (Fig. 15). A thin layer of reaction products prevents a further decomposition of γ-$Ba_4Nb_2O_9$ grains. In this way γ-phase remains in the sample to higher temperatures and the formation of the a-phase is delayed up to ~866 °C in air (Fig. 16). In vacuum the $BaCO_3$ peaks, which were consistently present in the XRD spectra recorded in air, are absent; as there is no available CO_2 to react with decomposing γ-$Ba_4Nb_2O_9$, which then undergoes a transformation into α-phase already at 800 °C. At 1000 °C the peaks corresponding to $Ba_5Nb_4O_{15}$ appear in the XRD spectrum (Fig. 18). The surplus of BaO remains amorphous after the partial decomposition of α-$Ba_4Nb_2O_9$ and is therefore not visible in the XRD spectra. The formation temperature of $Ba_5Nb_4O_{15}$ in vacuum (Fig. 18) is shifted to higher temperatures for about 200 °C when compared to the experiment conducted in air (Fig. 15). The early formation of $Ba_5Nb_4O_{15}$ in air is triggered by surface sublimation of BaO from the γ-phase and its reaction with CO_2 into $BaCO_3$, which suppress further decomposition of γ-$Ba_4Nb_2O_9$. On the contrary, in vacuum this compound forms by surface decomposition of a-phase at higher temperatures and the formation of amorphous BaO at the grain boundaries. The process of $Ba_5Nb_4O_{15}$ formation in vacuum could be therefore motivated by the loss of BaO from the system. This effect is indirectly shown in a gradual increase of the amount of $Ba_5Nb_4O_{15}$ phase with the increasing temperature. Heating the sample above 1150 °C results in disappearance of a and $Ba_5Nb_4O_{15}$ reflections and appearance of the reflections corresponding to $Ba_3Nb_2O_8$ and γ-phase (Fig. 18). The formation of $Ba_3Nb_2O_8$ phase suggests a considerable loss of BaO from the system during the HT-XRD experiment in vacuum. The loss of BaO is commonly observed in the compounds having above ~70 mol % of BaO, as this is the case in $Ba_4Nb_2O_9$. The presence of this BaO-deficient phase has been also confirmed by our TEM investigation of the γ-phase shown in Fig. 3. SEM/EDS analysis performed on a pellet of γ-$Ba_4Nb_2O_9$ heated at 1300 °C in a vacuum furnace revealed that the composition of the surface of the pellet is BaO-deficient with respect to the matrix $Ba_4Nb_2O_9$ composition (Fig. 19). The loss of BaO and the formation of the $Ba_3Nb_2O_8$ phase are more pronounced during firing under vacuum conditions than in ambient air. The formation of $Ba_3Nb_2O_8$ phase at 1150 °C is in agreement with the results reported by Spitsyn *et al.* [1982].

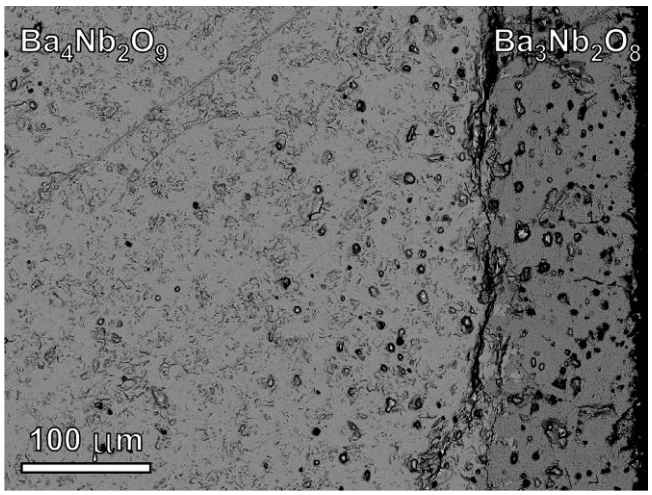

Figure 19: A back-scattered SEM micrograph of γ-$Ba_4Nb_2O_9$ sintered in ultra-high diffusion vacuum at 1300 °C for 15h. Darker secondary phase with the BaO/Nb_2O_5 = 3/1 corresponds to $Ba_3Nb_2O_8$, which forms on the surface of the γ-$Ba_4Nb_2O_9$ pellet due to evaporation of BaO.

4.4. Results: The crystal structure of α-$Ba_4Nb_2O_9$

The crystal structure characterization of α-$Ba_4Nb_2O_9$ was studied on two samples prepared by solid-state method. The first sample, *i.e.*, α-BNO-1, was annealed at 1100 °C for 5 hours and than slowly cooled down to room temperature, while the second sample, *i.e.*, α-BNO-2, was quenched from 1100 °C after annealing for two days (48 hours). The crystal structure studies on two different samples were performed because the preliminary research revealed dissimilarities in SAED and XRD patterns for the samples fired at 1100 °C for different period of time.

4.4.1. α-BNO-1: in terms of the selected area electron diffraction

The selected area electron-diffraction studies revealed the similarities in electron-diffraction patterns of α-$Ba_4Nb_2O_9$ with those of cation-deficient hexagonal perovskite $Ba_8Ti_{2.75}Nb_{4.125}Lu_{0.125}O_{24}$ reported by Trolliard *et al.* [2004]. This implied that α-$Ba_4Nb_2O_9$ might crystallize as a hexagonal perovskite. Based on these similarities it was possible to index some zone-axes patterns of α-$Ba_4Nb_2O_9$. The highest "net" symmetry of ED patterns corresponds to 6mm (Fig. 20a), which is in agreement with a hexagonal or trigonal crystal system. Identical ED pattern with 6mm symmetry could be eventually found if α-$Ba_4Nb_2O_9$ would crystallize

within the cubic crystal system. Since subsequent searching for extra ED patterns with characteristic high symmetry exclude the possibility of α-$Ba_4Nb_2O_9$ having cubic Bravais lattice, the observed electron-diffraction pattern can be indexed as $[001]_H$. Additionally, $[001]_H$ revealed two sets of diffraction spots, which form two hexagons rotated by 30° with respect to each other. The spots of the first hexagon have significantly lower intensity than those of the second hexagon and are located at the center of triangles created by strong reflections (Fig 1a). Their presence increases the *a*-parameter of the basic unit-cell reported by Leshchenko *et al.* [1979] by the value of √3. With respect to these super-structural diffraction spots, the *a*-parameter of α-$Ba_4Nb_2O_9$ calculated from $[001]_H$ ZAP corresponds to 1.025 nm, which is approximately half of the dimensions suggested by Trunov *et al.* [1979].

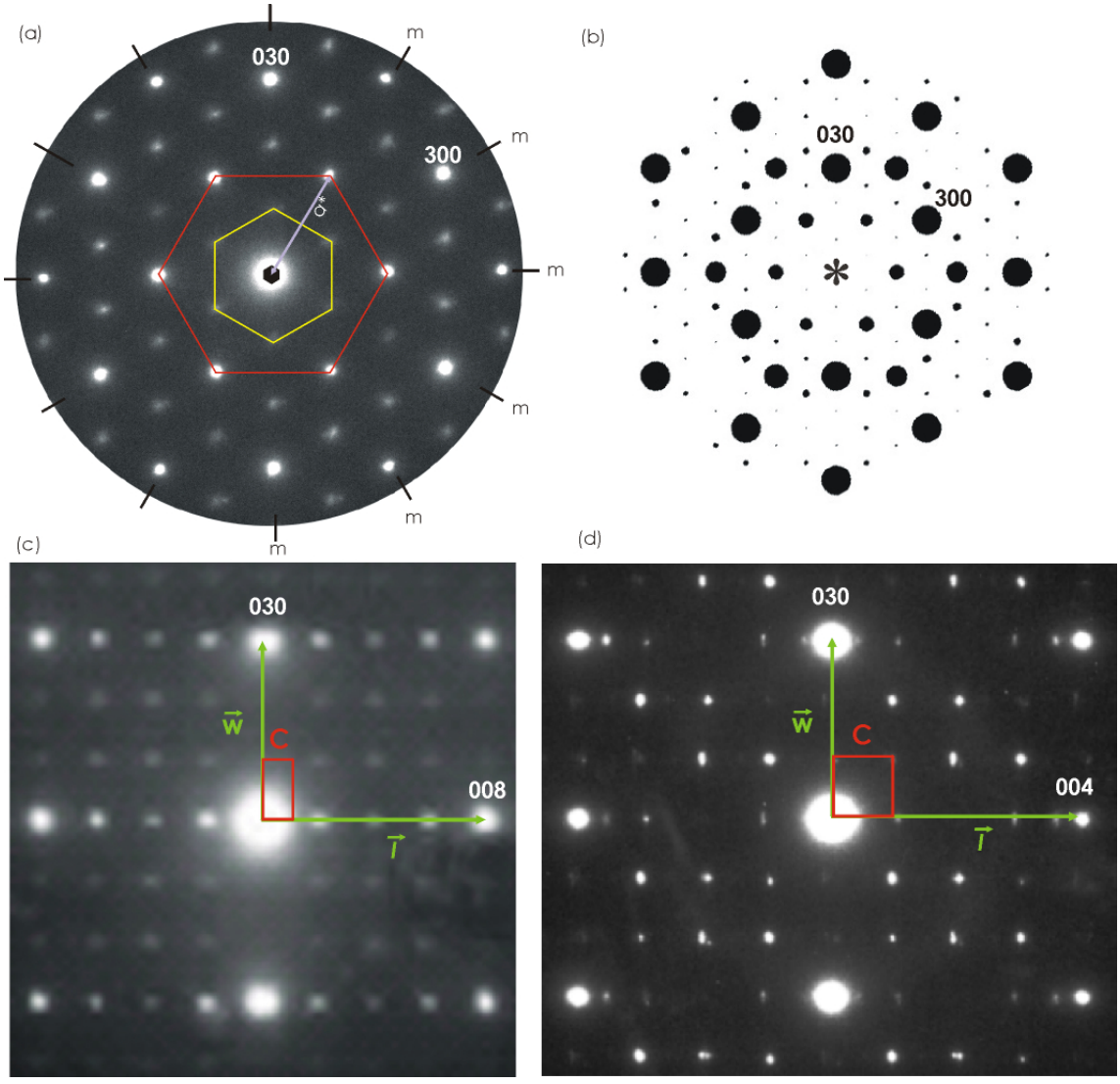

Figure 20: (a) The $[001]_H$ zone-axis electron-diffraction pattern of α-$Ba_4Nb_2O_9$ for α-BNO-1. Yellow and read hexagon refers to super- and sub-structural diffraction spots, *a** indicate the parameter *a* of the reciprocal lattice, m denotes mirror planes and black hexagon in the position of transmitted beam refers to the six-fold rotation axis. **(b)** The calculated $[001]_H$ ZAP for α-$Ba_4Nb_2O_9$.with the data of $Sr_4Ru_2O_9$ **(c)** The $[010]_H$ ZAP of the $Ba_8Ti_{2.75}Nb_{4.125}Lu_{0.125}O_{24}$ single crystal (Trolliard *et al.*, 2004). **(d)** The $[010]_H$ ZAP of α-$Ba_4Nb_2O_9$ single crystal for α-BNO-1. $\vec{w}$ and $\vec{l}$ denote the reciprocal vectors of basic reflections, c indicate the parameter c of the unit-cell in the real space.

Even more striking is the similarity of $[010]_H$ ZAP of $Ba_8Ti_{2.75}Nb_{4.125}Lu_{0.125}O_{24}$ with ED pattern of α-$Ba_4Nb_2O_9$ (Fig. 20c-d). Generally, this zone-axis orientation reveals the stacking sequence of Ba-O layers and the parameter *c* of the hexagonal perovskite-type unit-cell. The most intense diffraction spots in $[010]_H$ zone-axis electron-diffraction pattern form a rectangle denoted by reciprocal vector *w* and *l* (Fig. 20c-d). The reciprocal vector parallel to length of the rectangle ($\vec{l}$) corresponds to the distance between Ba-O layers stacked along c-crystallographic axis. This vector is in fact divided in eight equal parts in the case of eight-layered hexagonal-perovskite $Ba_8Ti_{2.75}Nb_{4.125}Lu_{0.125}O_{24}$ although the figure shows only four intervals. This is due to the extinction of intermediate reflections. However, the same vector is divided in four intervals in α-$Ba_4Nb_2O_9$. The results suggest that α-$Ba_4Nb_2O_9$ is composed of four Ba-O layers stacked along the *c*-crystallographic axis. With these regard one reciprocal period, *i.e.*, one interval of reciprocal vector $\vec{l}$ corresponds to the parameter *c* of the real unit-cell, which is consistent with 0.848 nm.

The type of the unit-cell, *i.e.*, the crystal system was subsequently confirmed by refining the crystal structure in terms of *hkl* indexes (*i.e.,* Le Bail fit) of α-$Ba_4Nb_2O_9$ reported by Leshchenko *et al.*, [1979] in PDF file #35-1154. The results show that the Bravais lattice of α-$Ba_4Nb_2O_9$ is certainly hexagonal (Fig. 21), but appears to be bigger then one suggested by Leshchenko *et al.*, [1979] (a = 0.5923 nm, c = 0.423 nm). Since the interpretation of inter-granular secondary phases by means of transmission-electron microscopy (Fig. 5) do not explain all of the weak and broad reflections in the XRD spectra, it was conclude that part of unidentified reflections in XRD pattern can be ascribed either to the superstructure of α-$Ba_4Nb_2O_9$ or more likely to the incommensurability of α-$Ba_4Nb_2O_9$. The later presumption is taken for granted due to the presence of slightly inclined satellite reflections evident from $[010]_H$ zone-axis pattern in figure 20d. The incommensurability of the crystal structure will be explained a little latter in chapter 4.4.5.

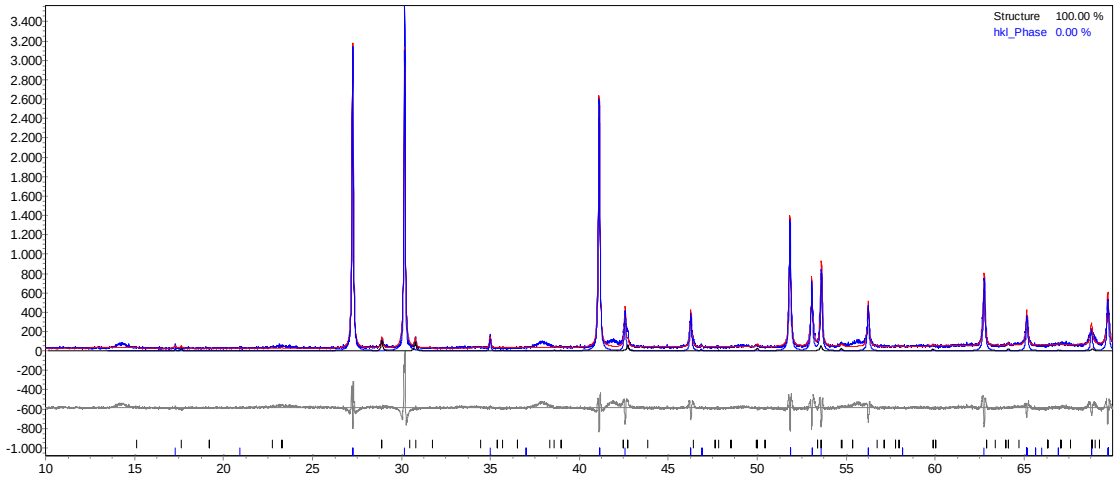

Figure 21: The X-ray powder diffraction pattern fitting of α-$Ba_4Nb_2O_9$ by means of *hkl* indexes suggested by Leshchenko *et al.*, [1979] after using the unit-cell parameters consistent with *a* = 0.5923 nm, *c* = 0.423 nm (PDF #35-1154). The broad and weak reflections are not included into the refinement. Black vertical bars indicate the peak positions of a secondary phase $Ba_5Nb_4O_{15}$.

Furthermore, the $[010]_H$ zone-axis pattern revealed large discrepancy in the distance between Ba-O layers (d_{00l}) consistent with 0.21 nm, which is far from the interlayer distance characteristic for hexagonal perovskites having B-site cations in octahedral coordination (~ 0.24 nm). This suggests on alternative coordination for B-site cations with the assumption that an alternative coordination affects the inter-layered spacing along *c*-crystallographic axis. Moreover, the length ratio of basic reciprocal vectors, *i.e.*, ~1.23 indicate close relationship of α-$Ba_4Nb_2O_9$ crystal structure to those of 4H-type compounds with general formula $A_4A'B_2O_9$, *e.g.*, $Sr_4Ni_3O_9$ [Huve *et al.*, 1998] and $Sr_4Ru_2O_9$ [Dussarrat *et al.*, 1995]. Therefore the crystal structure model for α-$Ba_4Nb_2O_9$ was constructed from the suggested crystal structure of $Sr_4Ni_3O_9$ and $Sr_4Ru_2O_9$ (see chapter 4.4.2.).

4.4.2. Hypothetical crystal structure for α-$Ba_4Nb_2O_9$

The distance between Ba-O layers and the stoichiometry of the compound indicate that α-$Ba_4Nb_2O_9$ may be isostructural with $Sr_4Ru_2O_9$ or $Sr_4Ni_3O_9$. Therefore, the crystal structure of α-$Ba_4Nb_2O_9$ arises from an alternation of BaO_3 and $Ba_3A'O_6$ layers. Their hexagonal stacking in $[001]_H$ direction creates chains of face-sharing octahedra and face-sharing trigonal prisms parallel with the *c*-crystallographic axis. The occupancy of these sites depends on the nominal composition of the compounds. For example, by comparing the stoichiometry of α-$Ba_4Nb_2O_9$ and $Sr_4Ni_3O_9$ one can see the difference in the number of B-site cations. Assuming

that the crystal structure of α-$Ba_4Nb_2O_9$ is analogue to that of $Sr_4Ni_3O_9$ the difference in stoichiometry must be compensate with the partial occupancy of BO_6 polyhedra in α-$Ba_4Nb_2O_9$. This means that there is a succession of two fully-occupied face-sharing octahedra followed by an empty trigonal prism along each 1dimensional chain (Fig. 22a). On contrary, the stoichiometry of α-$Ba_4Nb_2O_9$ is identical to that of $Sr_4Ru_2O_9$. In this regards the crystal structure α-$Ba_4Nb_2O_9$ can be described very similarly as $Sr_4Ru_2O_9$, in the space group *P*-62c. This implies that niobium ions in the columns created exclusively by face-sharing octahedra are halfly occupied and that part of oxygen ions in the same chain should be removed (see the read arrows in Fig. 22b). Generally, this shows that the crystal structure model of $Sr_4Ru_2O_9$ is similar to that of $Sr_4Ni_3O_9$ [Huve *at al.*, 1998], which crystallizes in space-group *P321*. However, the space-group of *P321* is a subgroup of *P*-62c. The main difference is that nickel cations in $Sr_4Ni_3O_9$ occupy also trigonal prismatic sites, while equivalent sites in $Sr_4Ru_2O_9$ remain vacant. In both structural models the columns are shifted along their length axes over either one or two structural units relative to adjacent ones. Therefore trigonal prism within the same layer can not occur in adjacent position.

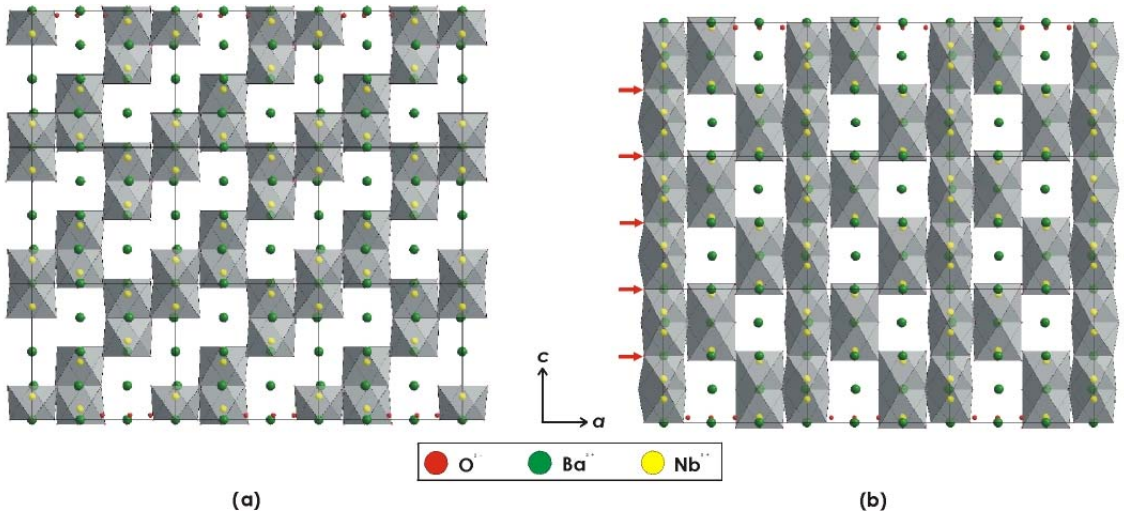

Figure 22: *The two structural models for α-$Ba_4Nb_2O_9$ in $[010]_H$ zone-axis orientation*. **(a)** The crystal structure model based on $Sr_4Ni_3O_9$ with the symmetry corresponding to the space-group *P321* and vacancies on A'-sublattice. The model is composed of chains of two face-sharing octahedra and one trigonal prism alternating along $[001]_H$ **(b)** The crystal structure model based on $Sr_4Ru_2O_9$, which consist of two sets of chains per unit-mesh; the two chains consist of alternating trigonal prism and two face-sharing octahedra, while the second type of chains is build up of exclusively face-sharing octahedra. This model can be described with space-group *P*-62c.

4.4.3. α-BNO-2: The reconstruction of the unit-cell from electron-diffraction patterns (The tilting experiments)

In order to obtain more information for the space-group determination of α-$Ba_4Nb_2O_9$ and compare its reciprocal lattice with the ones of $Sr_4Ni_3O_9$ and $Ba_4Ru_2O_9$, several crystals were studied by means of SAED using the tilting experiment. The preliminary TEM analysis revealed that ED patterns of α-$Ba_4Nb_2O_9$ prepared by quenching from 1100°C after firing for 48 h exhibit the "net" symmetry with periodic reflection positions. Therefore this sample (α-BNO-2) was subsequently used in a tilting experiment for a crystal structure determination. However, all SAED patterns of α-$Ba_4Nb_2O_9$ recorded in preliminary TEM investigations contain only ZOLZ reflections, which indicates that all of the interactions present in ZAP are two-dimensional. Because the ED patterns lacking HOLZ reflections, they did not provide information about a Bravais lattice, a glide plane and screw axes usually evident from the typical shift and the periodicity difference between ZOLZ and HOLZ reflection nets. Since that sort of data are highly important for the space-group determination of α-$Ba_4Nb_2O_9$, this is an additional reason to study the crystal structure of α-$Ba_4Nb_2O_9$ by the tilting experiment. This method is based on searching the angular relationship between different zone-axis patterns and allows a three dimensional reconstruction of the reciprocal unit-cell from the ZOLZ reflections observed on various zone-axes patterns (see details in the chapter 3.2.2).

The first tilting experiment was performed around the reciprocal $[001]_H^*$ axis with respect to the hexagonal unit-cell and is represented in the figure 23. The reciprocal-layer normal to the tilt-axis [001]* was reconstructed from the basic reflections observed in electron-diffraction patterns. Considering the distance between particular spots and their arrangement the reconstructed pattern appears to be in the $[001]_H$ zone-axis orientation (Fig. 20b). This experiment revealed the reappearance of ZAP during tilting α-$Ba_4Nb_2O_9$ crystal around the reciprocal $[001]_H$ axis. The initial electron-diffraction pattern (Fig. 23a) recurs after tilting the crystal for 60° (Fig. 23e). Tilting the crystal for 20° from initial position results the ZAP (Fig. 23b), that shows again after subsequent tilting for 20° (Fig. 23d). Moreover, tilting the crystal for 30° from initial zone-axis orientation generates the additional ZAP (Fig. 23c). However, the results obtained in this tilting experiment, including reconstructed pattern indicate the presence of six mirror planes normal to the $[001]_H$ ZAP with the common intersection at six-fold rotation axis (Fig. 20a-b). Their mutual interactions result in the repetition of SAED patterns during tilting the crystal around $[001]_H^*$ (Fig. 23). Therefore the two ZAPs observed at initial position (Fig. 23a) and after tilting the crystal for 60° (Fig. 23d) corresponds to $[100]_H$ and $[0\text{-}10]_H$ zone-axes orientation. These two zone-axes orientations are in addition to $[1\text{-}10]_H$ the most important zone-axis orientations for the space-group identification of hexagonal or trigonal crystals [Morniroli, 1992].

Considering the space groups *P321* (SG n° 150 with hkl: no condition) and *P-62c* (SG n°190 with hh-2hl: l=2n), the examination of the $[1\text{-}10]_H$ ZAP (Fig. 23c) alone allows to distinguish between these two possibilities as illustrated by the simulations of the $[100]_H$ and $[1\text{-}10]_H$ ZAP in figure 24 (see the draft). On the $[100]_H$ ZAP, the difference lies only on the single *00l* row with *l=2n* for *P-62c*. Looking at the experimental pattern $[100]_H$ (Fig. 23a) and equivalent $[0\text{-}10]_H$ (Fig. 23e) this condition does not seem to be fulfilled. This particular 00l: l=2n+1 reflections can be also find in $[2\text{-}10]_H$ (Fig. 23b) and $[1\text{-}20]_H$ (Fig. 23d) zone-axis patterns. Nonetheless such a condition that implies extinctions along one reciprocal row only can be removed due to multiple scattering of the diffracted beams and can lead to the misinterpretation. This is not the case for the $[1\text{-}10]_H$ ZAP where the condition hhl: l=2n implies extinctions of every l=2n+1 reciprocal rows for the *P-62c* space group without possible paths for multiple scattering. In the experimental ZAP (Fig. 23c) the hhl l=2n reciprocal rows exhibit intense spots, while the hhl: l=2n+1 reciprocal rows (indicated by red arrows in figure 23c) rather appear as diffuse streaks with some intensity reinforcement (diffuse nodes) that do not correspond to the positions of the spots expected for the *P321* space group. At this point one would thus consider that the reciprocal lattice defined by the set of intense spots is better to index by considering the space group *P-62c* rather than *P321*. Nevertheless, the diffuse streaks present in the $[1\text{-}10]_H$ ZAP are not compatible with the *P-62c* space group.

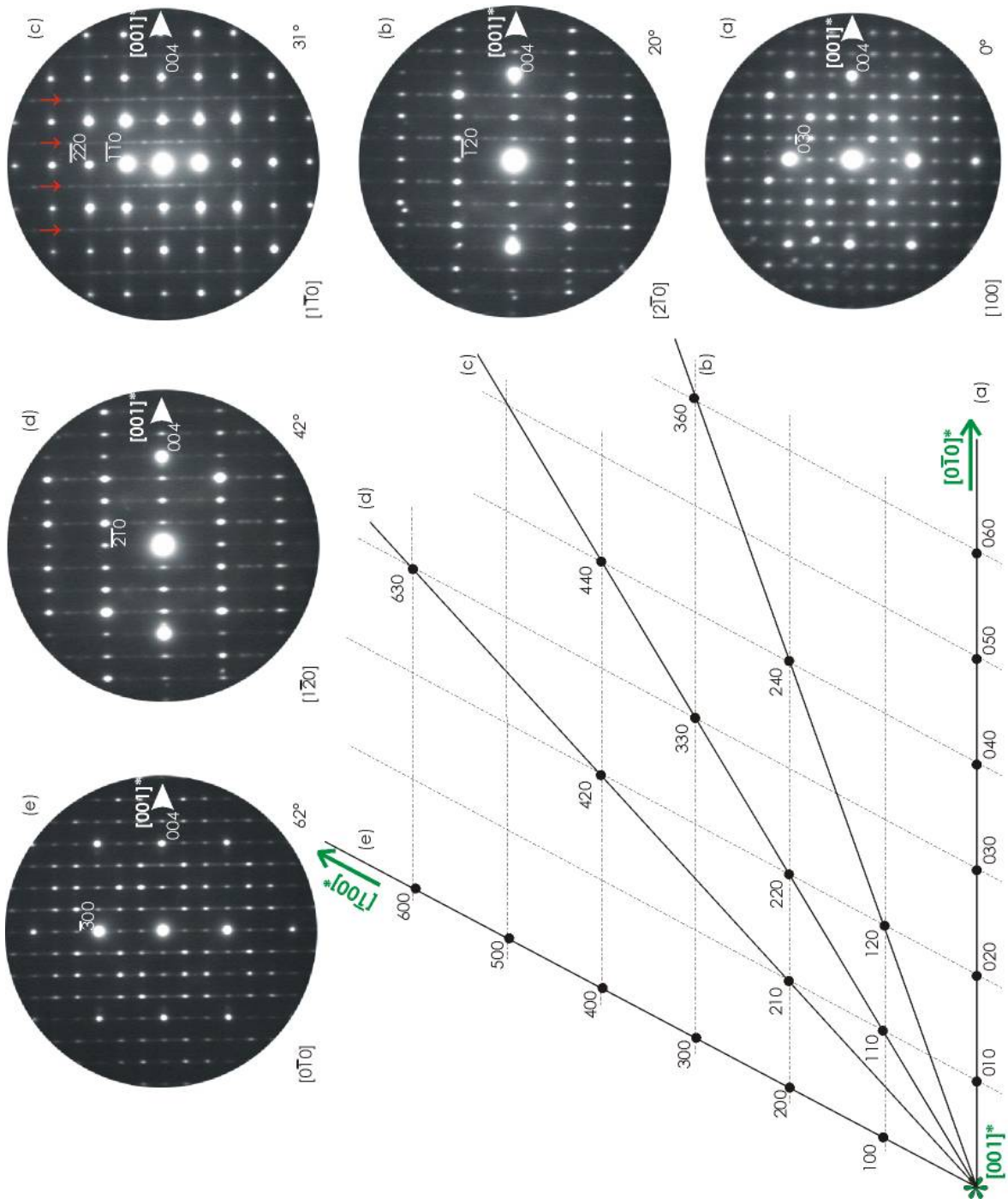

Figure 23: A set of selected-area electron-diffraction patterns from a single α-$Ba_4Nb_2O_9$ crystal (Crystal I) obtained in tilting experiment. The fundamental reflections are indexed according to the hexagonal *P*-62*c* structure with $a \approx 1.025$ nm and $c \approx 0.848$ nm.

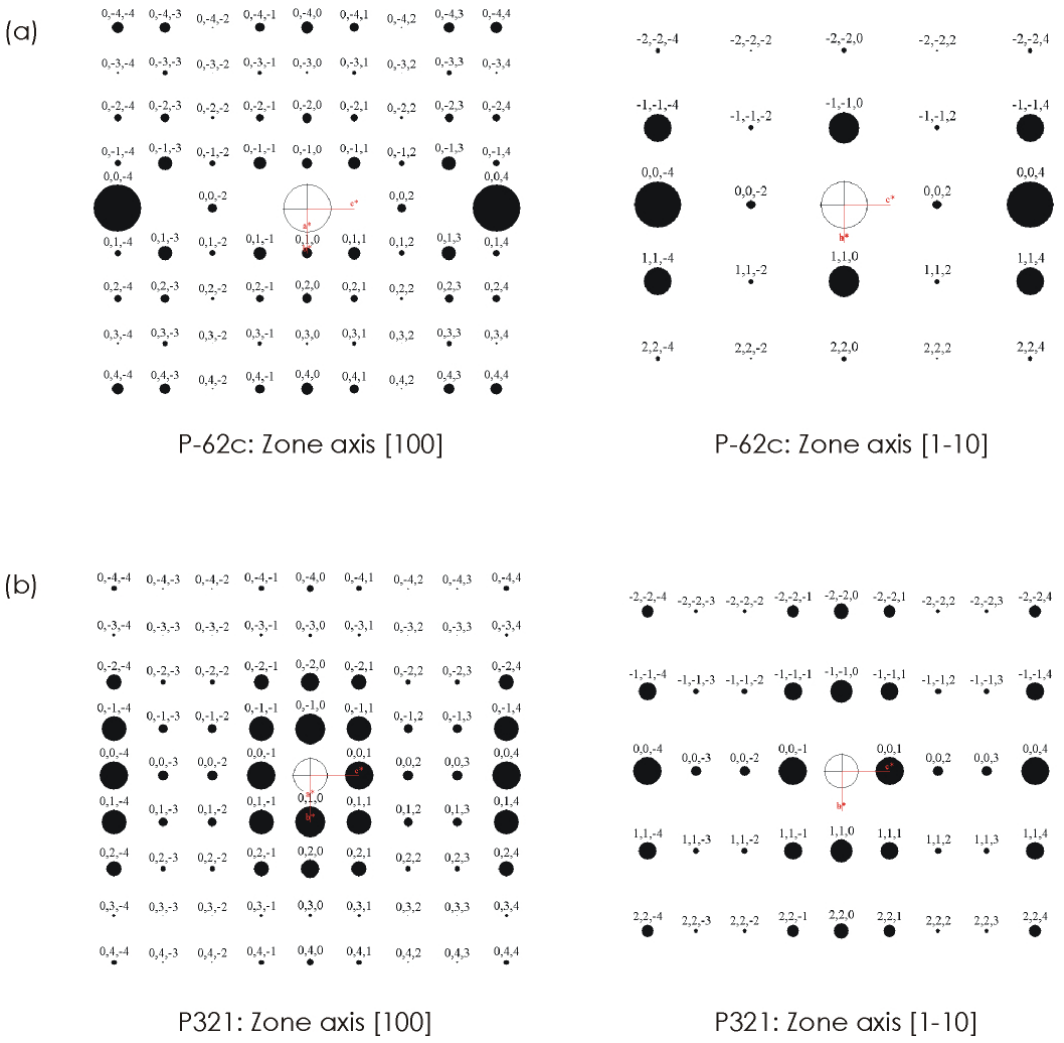

Figure 24: Simulations of the spot patterns expected for **a)** the *P-62c* space group **b)** the *P321* space group.

Additionally, the EDP observed after the crystal was tilted into the $[2\text{-}10]_H$ or $[1\text{-}20]_H$ zone-axes orientation shows the presence of fine structure, *i.e.*, diffuse streaks with nodes (of the same type as in $[1\text{-}10]_H$ ZAP) normal to the $[001]_H^*$ with a tendency to be more intense for the reciprocal rows corresponding to l=2n+1. This diffuse intensity can arise because of modifications to the shape of reciprocal lattice points that can be related to the shape of crystal defect, *e.g.*, stacking faults, or the lattice strain associated with them. Similar phenomenon was observed in $[0\text{-}10]_H$ ZAP parallel to the $[100]_H^*$.

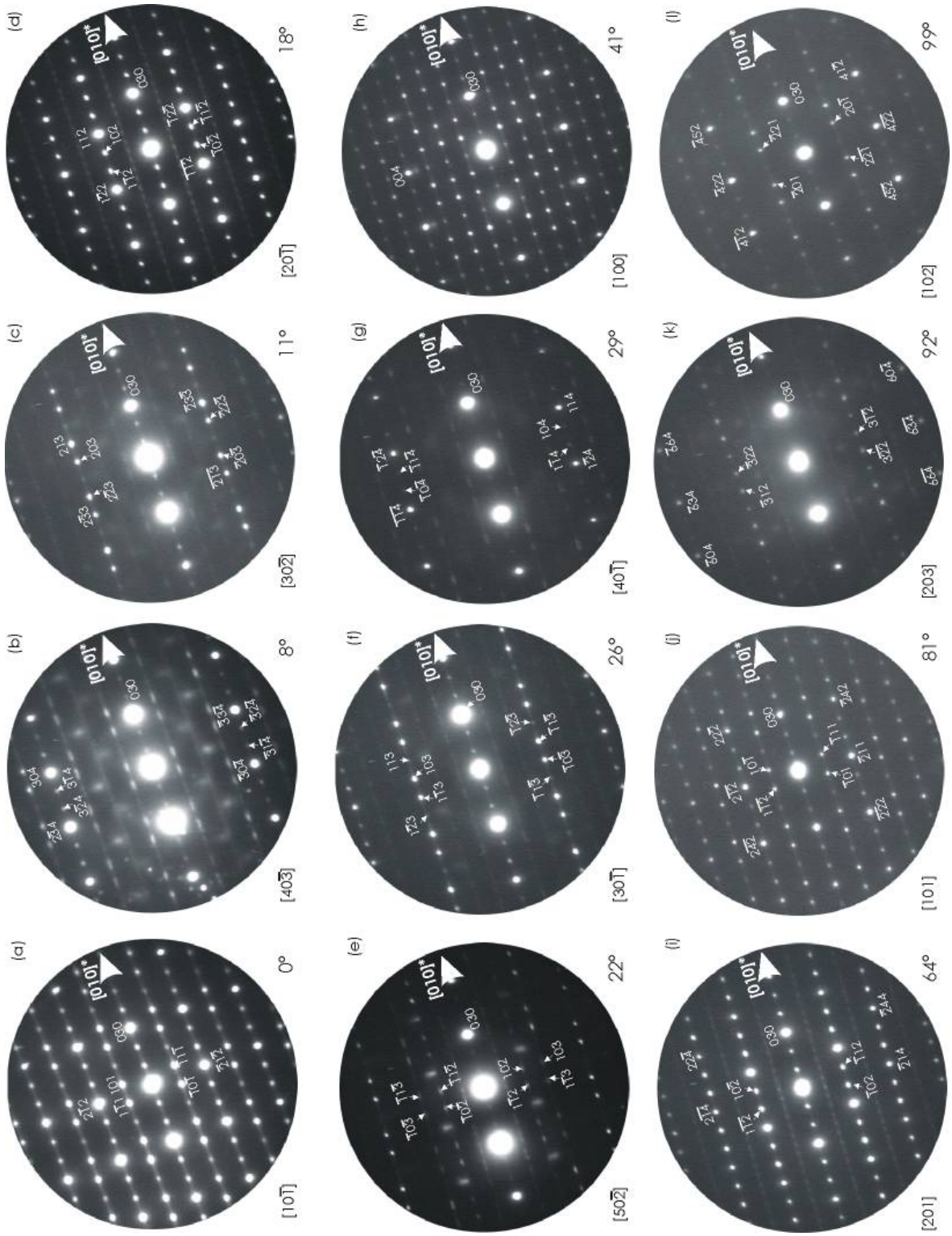

Figure 25: The zone-axes electron-diffraction patterns of α-$Ba_4Nb_2O_9$ obtained during tilting the crystal (Crystal II) around [010]* from the initial position, *i. e.*, ⟨100⟩ zone-axis orientation; the fundamental reflections are indexed according to the hexagonal P-62c structure with $a_H \approx 1.025$ nm and $c_H \approx 0.848$ nm.

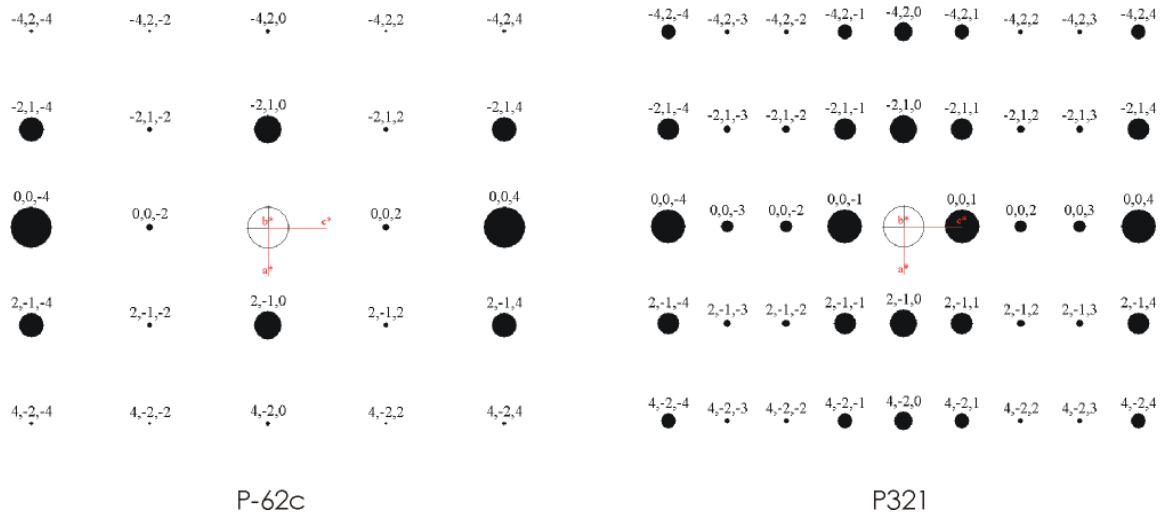

Figure 26: Calculated $[120]_H$ zone axis patterns expected for the space groups P-62c and P321 (intensities are spurious).

In order to understand and collect more information on the appearance of the diffuse scattering and to confirm the reliability of indexing the ED pattern in terms of a space group *P-62c*, crystals of α-$Ba_4Nb_2O_9$ were tilted around $[010]_H$* (Fig. 25). Tilting the crystal around $[010]_H$*, enables the reconstruction of $[120]_H$ ZAP, which is also one of the most important zone-axis pattern to draw a distinction between *P-62c* and *P321* as illustrated in the calculated patterns figure 26. In the experimental $[120]_H$ reconstructed patterns presented figure 27, only the spots lying on a line perpendicular to the tilting $[010]_H$* direction are indicated with green spots. These spots are found in several zone-axes patterns represented by lines a, c-d, f, and h-l figure 27. With the exception of the spots found in the $[100]_H$ ZAP (Fig. 27h), which can likely be attributed to multiple scattering in this dense reciprocal plane, they are all compatible with the *P-62c* space group. A particular attention can be paid on the ZAP in figure 27c, 27e and 27l where the spots expected in the case of a *P321* space group are not observed.

Regarding the diffuse intensity, the rows of additional reflections located parallel to [010]* were observed in both, the $[20\text{-}1]_H$ and $[201]_H$ zone-axes patterns (Fig. 25d and 25i). These reflections have weak, diffuse intensity and are slightly elongated along the $[010]_H$* direction. Similar reflections accompanying the strong Bragg spots of an underlying average crystal structure were observed in other high-index electron-diffraction patterns (Fig. 25). These diffuse nodes cannot be indexed considering the cell parameters used for the spot patterns and suggest to use a larger cell as well as another space group not yet identified. Moreover, considering the varying intensity and the shape of accompanying scatterings, they can be grouped at least in two different sets. This is evident from additional reflections of

a weak intensity in $[40\text{-}3]_H$ zone-axis pattern (Fig. 25b), where more diffuse reflections occur at positions other than the long-range order positions should appear. Worse still, it is evident that the position of these diffuse maxima is variable. Their distribution creates walls of diffuse intensities. These features in electron-diffraction patterns imply the compositional and/or displace flexibility of the crystal structure commonly observed in adaptive phases; *e.g.*, columnar misfit structures, which are strongly related to the 2H hexagonal perovskites.

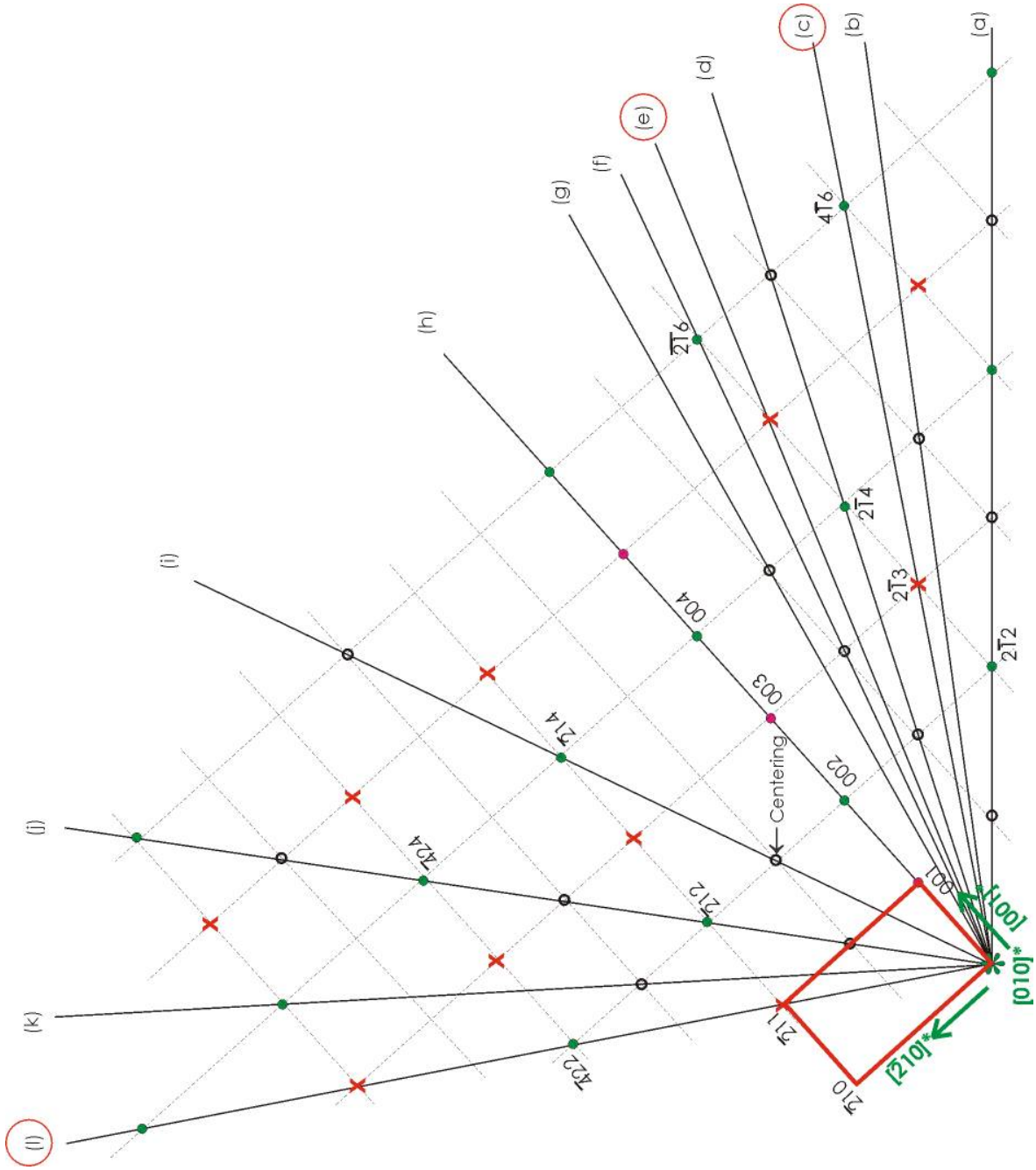

Figure 27: The reconstructed $[120]_H$ ZAP for single α-$Ba_4Nb_2O_9$ crystal normal to the [010]* tilt-axis (Crystal II). Green points indicate the observed spots on the experimental patterns used for the reconstruction. The pink spots are likely due to multiple scattering. The red crosses indicate the position where spots would have been observed in the case of a *P321* space group.

The third tilting experiment (Fig. 28) was carried out along the two reciprocal directions, i.e., along $[100]_H$* and $[010]_H$* on a single α-$Ba_4Nb_2O_9$ crystal (Crystal III) starting from the $[001]_H$ zone-axis orientation (Fig. 28h). Once again, it appears that the description of the reciprocal space using a hexagonal unit-cell and the space-group *P-62c* is only an approximation. The results of this tilting experiment show that it does not come to the same thing if the crystal is rotated along [100]* or along $[001]_H$*. Thus the $[013]_H$ ZAP (Fig. 28g) obtained after the crystal was rotated for ~20° around $[100]_H$* from the initial position contains stronger diffuse scattering with respect to the $[103]_H$ zone-axis electron-diffraction pattern (Fig. 28e). More intriguing is the phenomena clearly evident from the $[102]_H$ and $[012]_H$ ZAPs where a part of the reflections (one out of three) along the *hkl* rows with l = odd are split with a kind of "wobbling" effect (see Figs. 28d and 28h and corresponding enlargements). Notice that in both reconstructions (Fig. 29), these split spots (marked as red "**s**") are found on positions compatible with the space group *P321*. Nonetheless, such a feature can not be explained considering a conventional 3D crystallographic approach and strongly suggests that the true nature of α-$Ba_4Nb_2O_9$ is an incommensurably modulated.

Furthermore, the centering evident from the reconstruction of the unit-cell in figure 27 defines the crystallographic parameter *a*. Nevertheless, the empty circle in the reconstructed pattern indicates that interlayer distance d_{h00} has to be doubled. Accordingly, the parameter *a* was estimated from $[001]_H$ ZAP and corresponds to 1.025 nm, while the lattice parameter c = 0.848 was deduced from ⟨010⟩ ZAP (Fig. 9m).

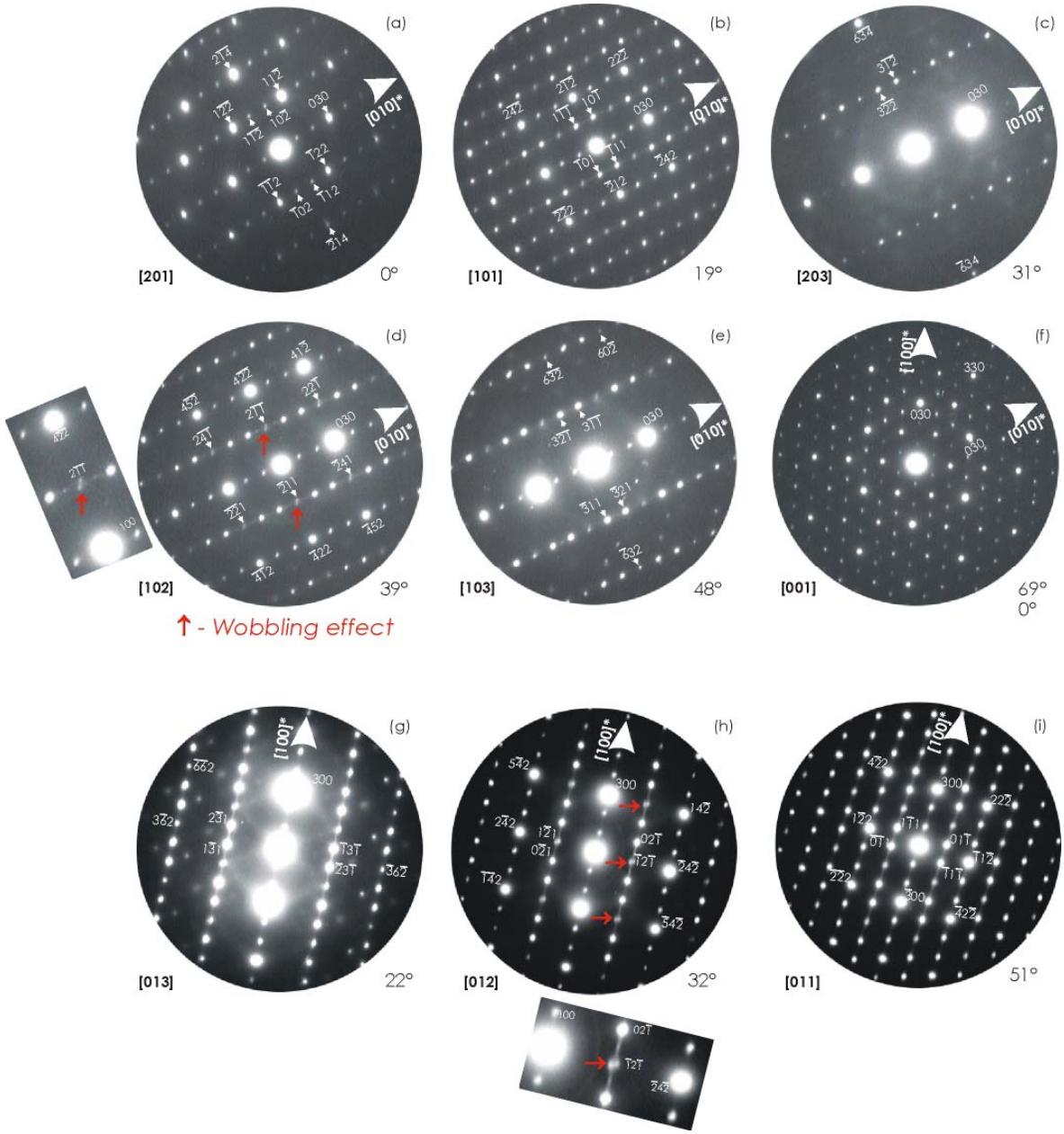

Figure 28: The zone-axes electron-diffraction patterns of α-$Ba_4Nb_2O_9$ single crystal obtained during third tilting the crystal around $[010]_H$ and $[100]_H$ tilt-axis.

(a)

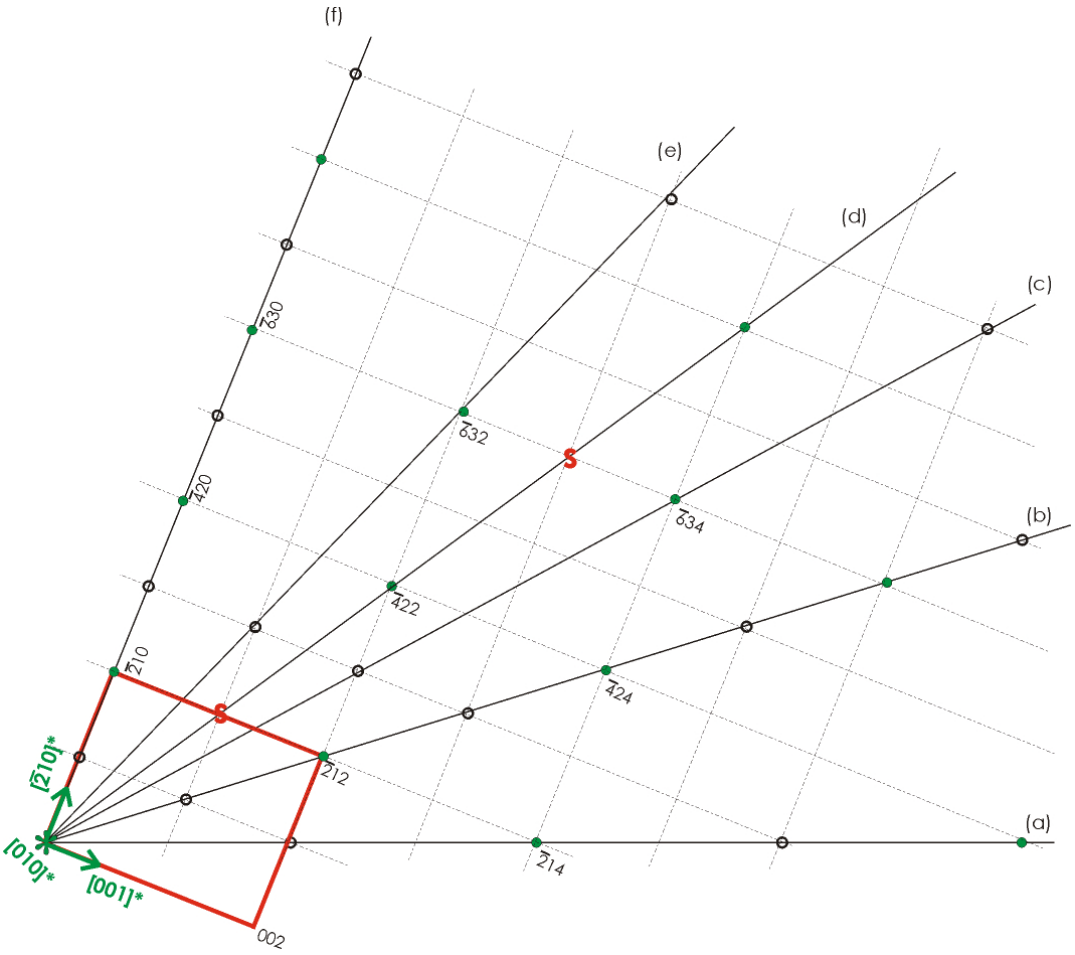

(b)

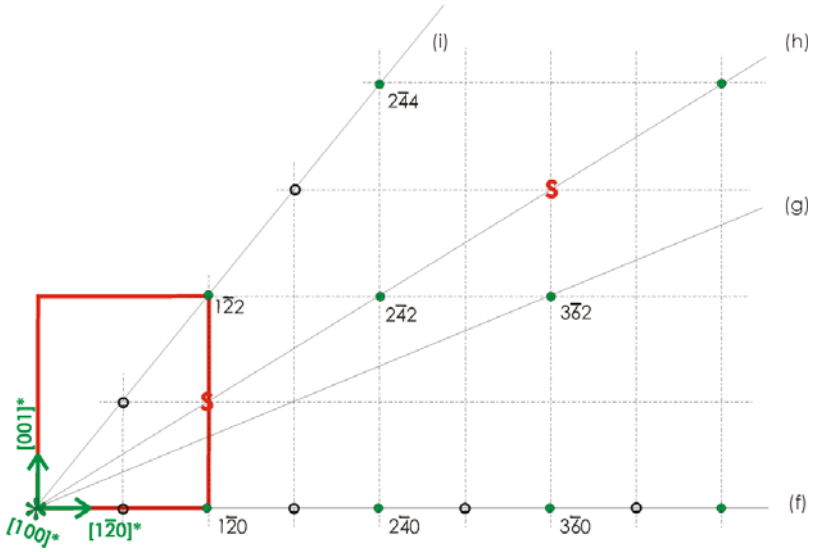

Figure 29: The reconstructed reciprocal plane for α-$Ba_4Nb_2O_9$ normal to the $[010]_H$ **(a)** and $[100]_H$ **(b)** tilt-axis.

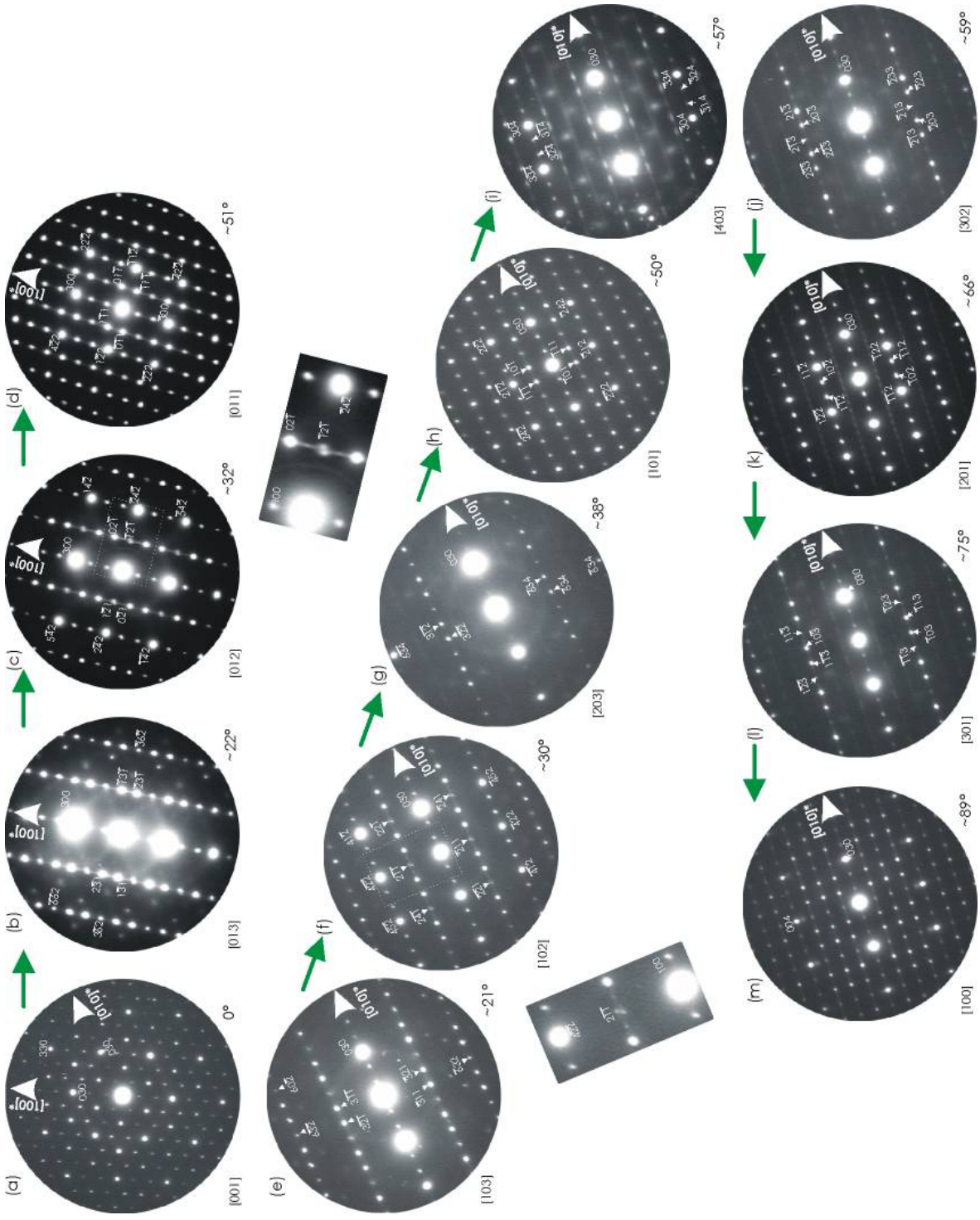

Figure 30: Summary of the exploration of the reciprocal space of α-$Ba_4Nb_2O_9$ by selected area electron diffraction. ZAP are indexed considering the cell parameters *a* = 1.025 nm, *c* = 0.848 nm and the space group *P*-62*c*.

4.4.4. The crystal structure refinement of α-$Ba_4Nb_2O_9$ using a three-dimensional approach (SG P-62c) from X-ray powder diffraction data

The crystal structure of α-$Ba_4Nb_2O_9$ was refined from X-ray powder diffraction data using the space-group *P*-62*c*. The unit-cell parameters (*a* = 1.025 nm, *c* = 0.848 nm) were obtained from previous electron microscopy tilting experiments. The results confirm that the average crystal structure of α-$Ba_4Nb_2O_9$ is related to the $Sr_4Ru_2O_9$ crystal structure.

Rietveld refinements were carried out with the JANA2006 program [Petricek *et al*., 2006]. Preliminary whole profile refinements based on a space group *P*-62*c* and unit-cell parameters calculated from $[010]_H$ and $[001]_H$ zone-axes electron-diffraction patterns showed that some broad reflections with low intensity (see peaks at 2θ = 14.46 and 23.29 ° in Fig. 31) are not indexed. These observations are consistent with electronic microscopy studies, which show the presence of diffuse steaks present in $[1\text{-}10]_H$ or $[20\text{-}1]_H$ ZAP. However, these findings can be explained in terms of incommensurably modulated crystal structure. The same is true for the splitting reflections in the form of "wobbling effect" in $[102]_H$ and $[012]_H$ ZAP (Fig. 28d and Fig. 28h), respectively. Assuming the relative poor crystallization quality of the sample we have only refined the average structure of α-$Ba_4Nb_2O_9$.

The first structural refinements with the atomic positions of $Sr_4Ru_2O_9$ crystal structure, *i.e.*, *Model I* yield a large R-factor, *i.e.*, R_F(obs) = 21%. After assuming the preferential orientation of the crystallites the refinement of the correspondent parameter decreased the R(obs) value to 16 %. Additionally, the refinement of anisotropic atomic displacement parameters for the Ba and Nb atoms (see value of U in Table 1) decreased the R_F(obs) value to 5.96 % (Table 2) but resulted in unrealistic values for some atoms. Since α-$Ba_4Nb_2O_9$ is considered as inorganic ionic compound the displacement parameters at room temperature are expected to be positive and in a relatively narrow range, *i.e.*, up to ~ 0.5 $Å^2$ or eventually ~1 $Å^2$. Thus the low negative thermal parameters for barium atoms in 6h, niobium in 4e, and especially for oxygen in 6h and 6g positions refer to the disorder and defaults in the crystal structure. Unusually high isotropic thermal parameter of Nb atoms in 4f position (U_{33} = 1.83 $Å^2$) refers to delocalization of these atoms; they appears to be off-centered along the c-crystallographic axis. A displacement parameter of Nb in 4f position refers to the fact that these atoms are placed in octahedral positions, which should be partly occupied. For this particular case, all interatomic distances in α-$Ba_4Nb_2O_9$ (Table 3) were normal except those between niobium atoms in 4e positions, *i.e.*, the octahedral sites in chains of face-sharing octahedra. This Nb1–Nb1 distance is considerably low (1.1296 Å). In general, this means that only half of 4e positions are occupied by niobium atoms. Consequently, oxygen atoms were allowed to occupy only half of 6*g* positions. This implies that niobium atoms in 4e positions would constitute equivalent type of columns along c-crystallographic axis as niobium atoms in 4f sites. However, the average Nb–O distances in these "4e-columns" is then 1.98 Å and is in

a good agreement with those reported for Nb^{5+} (1.98 Å) in $Ba_5Nb_2O_{11}$ [Grasset *et al.*, 1999], while the Nb–O average distance within the NbO_6 octahedra in "4f-columns" is consistent with 2.16 Å. This show that the shape and the size of octahedra in "4e- and "4f-columns" significantly differ. Additionally, the strong repulsion between highly charged Nb^{5+} ions resulted in displacement of niobium cations from 4f sites at the centers of the octahedra towards the triangular faces created by oxygen ions in 12i Wyckoff positions. Similar displacement of niobium ions is expected in 4e octahedral centers.

Table 1: Atomic parameters and atomic displacement parameters (U) for α-$Ba_4Nb_2O_9$

Atomic parameters							
Atom	**Wyckoff position**	**Site**	**Occupancy**	**x/a**	**y/b**	**z/c**	**U (Å)**
Ba(1)	6g	.2.		0.6675(6)	0	0	*
Ba(2)	6h	m..		0.3389(5)	0.0101(3)	1/4	*
Nb(1)	4e	3..	0.5	0	0	0.1734(4)	*
Nb(2)	4f	3..		2/3	1/3	0.462(2)	*
O(1)	12i	1		0.669(4)	0.499(3)	0.5379(16)	0.015(5)
O(2)	6h	m..		0.501(3)	0.345(4)	1/4	-0.009(5)
O(3)	6h	m..		0.020(6)	0.844(7)	1/4	0.081(15)
O(4)	6g	.2.	0.5	0.137(3)	0	0	-0.027(6)

*$U = \exp{-2\pi^2} (h^2U_{11}a^{*2} + k^2U_{22}b^{*2} + l^2U_{33}c^{*2} + 2hkU_{12}a^*b^* + 2hlU_{13}a^*c^* + 2klU_{23}b^*c^*)$

Table 1a: Atomic displacement parameters (U) for α-$Ba_4Nb_2O_9$

Anisotropic displacement parameters; U (Å²)						
Atom	**U_{11}**	**U_{22}**	**U_{33}**	**U_{12}**	**U_{13}**	**U_{23}**
Ba(1)	0.029(2)	0.031(4)	0.073(3)	0.015(2)	0.0138(11)	0.028(2)
Ba(2)	0.018(2)	0.016(2)	-0.0048(7)	0.013(2)	0.00000	0.00000
Nb(1)	0.021(4)	0.021(4)	-0.030(2)	0.011(2)	0.00000	0.00000
Nb(2)	0.009(2)	0.009(2)	1.83(8)	0.0043(12)	0.00000	0.00000

Table 2: The refined lattice parameters, unit-cell volume, reliability factors and goodness of fit indicator for α-$Ba_4Nb_2O_9$ compound

Phase information	
Formula sum	$Ba_4Nb_2O_9$
Formula weight	879.2 g/mol
Crystal system	hexagonal
Space-group	P -6 2 c (190)
Cell parameters	a = 1.02694 (1) nm c = 0.84573 (1) nm
Cell volume	V = 772.42(1) Å^3
Z	3
Calc. density	5.66996 g/cm^3
R factors (%)	R_F(obs) = 5.96 R_B(obs) = 6.98 R_Fw(obs) = 6.57
Profile R factors (%)	Rp = 8.05 Rwp = 11.49

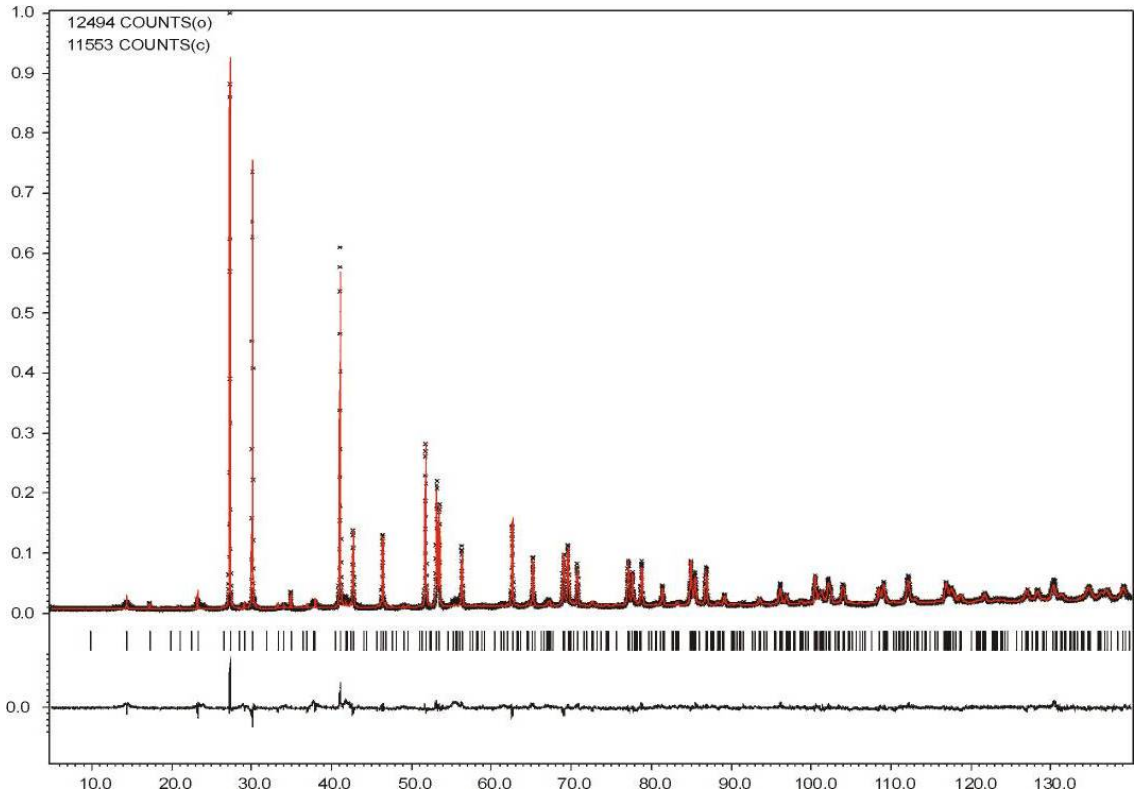

Figure 31: The observed (points), calculated (red solid line) and difference (bottom) X-ray powder diffraction profiles for α-$Ba_4Nb_2O_9$. The black vertical ticks stand for the diffraction positions.

Table 3: Main interatomic distances in α-$Ba_4Nb_2O_9$

Interatomic distances (Å)					
Atom 1-Atom 2	**d (Atom 1-Atom 2) [Å]**	**Atom 1-Atom 2**	**d (Atom 1-Atom 2) [Å]**	**Atom 1-Atom 2**	**d (Atom 1-Atom 2) [Å]**
Ba1—O1^{i}	2.96(3)	Ba2—O3^{xi}	2.83(5)	Nb2—O2	2.51(3)
Ba1—O1^{ii}	2.96(3)	Ba2—O4	2.92(2)	Nb2—O2^{iii}	2.51(4)
Ba1—O2^{iii}	2.70(4)	Ba2—O4^{xii}	2.92(2)	Nb2—O2^{xvi}	2.51(3)
Ba1—O2^{iv}	2.697(18)	Nb1—Nb1^{xii}	1.296(5)	O1—O1^{iii}	2.92(5)
Ba1—O3^{v}	2.73(6)	Nb1—Nb1^{vi}	2.933(5)	O1—O1^{xvi}	2.92(7)
Ba1—O3^{vi}	2.73(5)	Nb1—O3^{xi}	1.83(7)	O1—O2	2.94(2)
Ba1—O4^{iii}	2.972(6)	Nb1—O3^{xiii}	1.83(6)	O3—O3^{xvii}	2.97(11)
Ba1—O4^{vii}	2.97(4)	Nb1—O3^{xiv}	1.83(9)	O3—O3^{xviii}	2.97(13)
Ba2—O1^{iii}	2.95(2)	Nb1—O4	2.04(2)	O3—O4^{xix}	2.56(3)
Ba2—O1^{viii}	2.95(2)	Nb1—O4^{xv}	2.04(2)	O3—O4^{xx}	2.73(5)
Ba2—O1^{ix}	2.55(4)	Nb1—O4^{v}	2.035(16)	O3—O4^{xxi}	2.56(3)
Ba2—O1^{x}	2.55(4)	Nb2—O1	1.80(4)	O3—O4^{xxii}	2.73(5)
Ba2—O2	2.98(4)	Nb2—O1^{iii}	1.80(3)	O4—O4^{xv}	2.44(4)
Ba2—O2^{iii}	2.82(4)	Nb2—O1^{xvi}	1.80(5)	O4—O4^{v}	2.44(4)

Coordinates for symmetrically equivalent points :
(i) 1-x+y, 1-x, 0.5-z; **(ii)** y, -1+x, -0.5+z; **(iii)** 1-y, x-y, z; **(iv)** 1-x, -x+y, -z;
(v) -x+y, -x, z; **(vi)** y, x, -z; **(vii)** 1-x+y, -x, z; **(viii)** 1-y, x-y, 0.5-z;
(ix) 1-x, -x+y, 1-z; **(x)** 1-x, -x+y, -0.5+z; **(xi)** x, -1+y, z; **(xii)** x, y, 0.5-z;
(xiii) 1-y, 1+x-y, z; **(xiv)** -1-x+y, -x, z; **(xv)** -y, x-y, z; **(xvi)** 1-x+y, 1-x, z;
(xvii) 1-y, 2+x-y, z; **(xviii)** -1-x+y, 1-x, z; **(xix)** x, 1+y, z; **(xx)** -x+y, 1-x, z;

(xxi) x, 1+y, 0.5-z; **(xxii)** -x+y, 1-x, 0.5-z

Since the refinement of the isotropic displacement parameter of the Nb2 atoms (*i.e.*, 4f Wyckoff position) gave large value (U_{33} = 1.83 Å^2) the partial occupancy of this atomic sites were assumed in the second refinement (*model II*) (Fig. 32). Therefore the positions of Nb2b and O5 atoms were found from the Fourier difference. With respect to the crystal structure *Model I* the Nb2b atoms take its trigonal prismatic sites. The same is true for O5 atoms, which are localized at approximately half of the height of trigonal prisms. Accordingly, this creates two octahedral sites instead of one trigonal prismatic in "4f-columns". In order to satisfy the chemical formula $Ba_4Nb_2O_9$ half occupation parameters were attributed to the O2 and O5 atoms (Table 4). Occupation parameter of Nb2 and Nb2b atoms were also refined. Their sum was constrained to be equal to 1 from the same reasons as for O2 and O5 atoms. Niobium atoms in 4f Wyckoff positions are only partly occupied, which is in agreement with short metal-metal distances, *i.e.*,~1.2 Å (Table 5). Comparable short interatomic distances were observed for Nb2b atoms (~1.17 Å). On analogy with niobium atoms in 4f positions Nb2b atoms are also partly occupied. The distance between two Nb2 atoms within the Nb_2O_9 dimmers in "4e columns" is much bigger (~2.985 Å) than the distance between two Nb^{5+} (1.98 Å) in $Ba_5Nb_2O_{11}$ [Grasset *et al.*, 1999]. In general, this value indicates strong repulsion between niobium atoms within the Nb_2O_9 dimmers in "4e columns" and no metal-metal bonding.

The crystal structure refinement of α-$Ba_4Nb_2O_9$ in terms of *Model II* yields positive and realistic values of atomic displacement parameters for niobium atoms, on the contrary to the *Model I*. However, this indicates that the crystal structure of low-temperature α-$Ba_4Nb_2O_9$ is much closer to the crystal structure of the *Model II*. The structural similarities between *Model I* and *Model II* are demonstrated in figure 33. The final R-factor and all the details considering the second way of the refinement are evident from the table 6.

Alike for $Sr_4Ni_3O_9$ [Huve *et al.*, 1998] one can expect disordering on an anion sublattice in α-$Ba_4Nb_2O_9$ due to the sideways displacement of a trigonal prismatic interstice in one column into adjacent one by the local diffusion of three oxygen atoms out of Ba_3O_9-layer (making it locally Ba_3O_6) to the neighboring trigonal prism, transforming the latter into two face-sharing octahedra. Simultaneously the vacancies created by the removal of the three oxygen atoms give rise to a "hole" in Ba_3O_9 layer and thus to a trigonal prism. Most likely, this oxygen-vacancy diffusion mechanism also controls dislocation of barium atoms from their original position. However, the observed and expected displacements surely introduce disorder into the α-$Ba_4Nb_2O_9$ crystal structure, which is clearly evident from diffuse reflections in most of electron-diffraction patterns and from broad peaks of low intensity in X-ray powder-diffraction spectra.

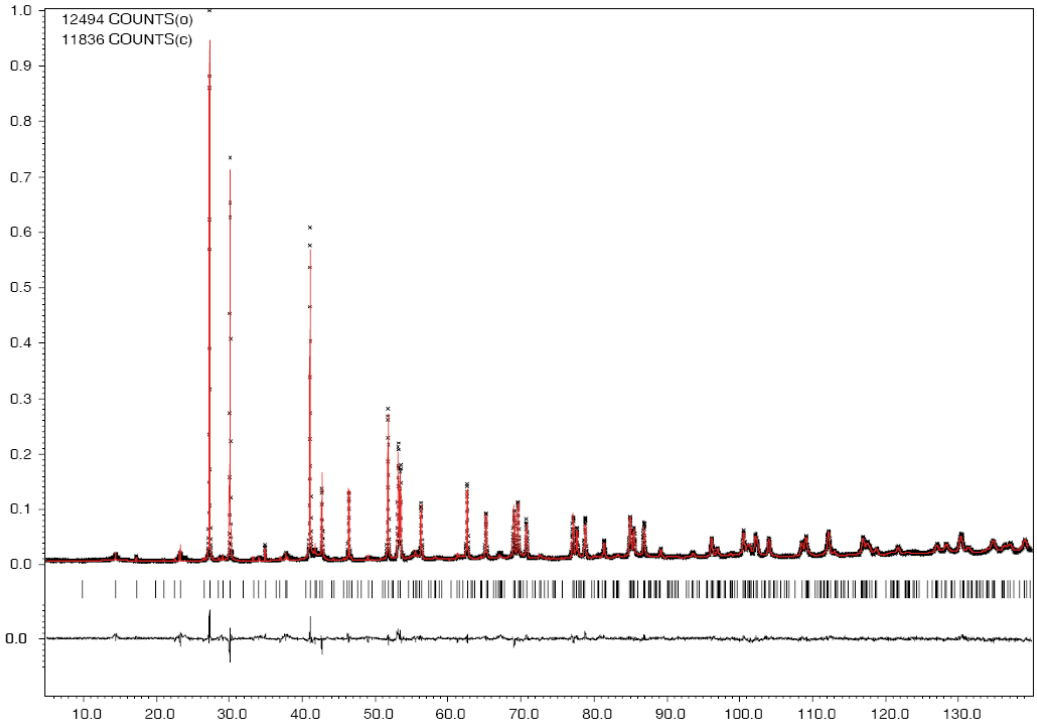

Figure 32: The observed (points), calculated (red solid line) and difference (bottom) X-ray powder diffraction profiles for α-$Ba_4Nb_2O_9$. The black vertical ticks stand for the diffraction positions.

Table 4: Atomic parameters and atomic displacement parameters (U) for α-$Ba_4Nb_2O_9$

Atomic parameters							
Atom	**Wyckoff position**	**Site**	**Occupancy**	**x/a**	**y/b**	**z/c**	**U [Å²]**
Ba1	6g	.2.		0.6700(7)	0	0	0.018(2)*
Ba2	6h	m..		0.3348(8)	0.0016(4)	1/4	0.024(3)*
Nb1	4e	3..	0.5	0	0	0.1791(12)	0.002(2)
Nb2	4f	3..	0.461	2/3	1/3	0.4265(12)	0.016(3)
Nb2b	4f	3..	0.5391	0.333(4)	0.667(4)	0.3192(14)	0.0113(18)
O1	12i	1		0.668(8)	0.489(10)	0.52301	0.0096(18)
O2	6h	m..	0.5	0.515(3)	0.330(4)	1/4	0.0096(18)
O3	6h	m..		-0.020(8)	0.83983	1/4	0.0096(18)
O4	6g	.2.	0.5	0.16366	0	0.0000(6)	0.010(3)
O5	6h	m..	0.5	0.269(5)	0.467(6)	1/4	0.0096(18)

** Ueq = exp-2π² ($h^2U_{11}a^{*2} + k^2U_{22}b^{*2} + l^2U_{33}c^{*2} + 2hkU_{12}a^*b^* + 2hlU_{13}a^*c^* + 2klU_{23}b^*c^*$)*

Table 4a: Anisotropic atomic displacement parameters (U) for α-$Ba_4Nb_2O_9$

Anisotropic displacement parameters U [Å²]						
Atom	U11	U22	U33	U12	U13	U23
Ba1	0.02014	0.01865	0.01325	0.00932	-0.00702	-0.01403
Ba2	0.02986	0.02361	0.01547	0.01146	0.00000	0.00000

Table 5: Main interatomic distances in α-$Ba_4Nb_2O_9$

Interatomic distances (Å)					
Atom 1-Atom 2	**d (Atom 1-Atom 2) [Å]**	**Atom 1-Atom 2**	**d (Atom 1-Atom 2) [Å]**	**Atom 1-Atom 2**	**d (Atom 1-Atom 2) [Å]**
Ba1—O1^{i}	2.97(8)	Nb1—O3^{xiii}	1.66(3)	Nb2b—O5	1.90(7)
Ba1—O1^{ii}	2.97(7)	Nb1—O3^{xi}	1.66(3)	Nb2b—O5^{xi}	1.90(5)
Ba1—O2^{iii}	2.84(4)	Nb1—O3^{xiv}	1.66(9)	Nb2b—O5^{xxiii}	1.90(9)
Ba1—O2^{iv}	2.84(2)	Nb1—O4	2.262(8)	O1—O1^{iii}	2.76(15)
Ba1—O3^{v}	2.81(6)	Nb1—O4^{xv}	2.262(8)	O1—O1^{xvii}	2.76(18)
Ba1—O3^{vi}	2.81(3)	Nb1—O4^{v}	2.262(8)	O1—O2	2.81(4)
Ba1—O4^{iii}	2.935(6)	Nb2—Nb2^{xii}	2.985(14)	O1—O2^{xvii}	2.78(6)
Ba1—O4^{vii}	2.935(6)	Nb2—Nb2b^{xvi}	2.150(15)	O1—O5^{xvi}	2.89(6)
Ba1—O5^{iii}	2.78(4)	Nb2—O1	1.79(10)	O1—O5^{xxiv}	2.27(6)
Ba1—O5^{iv}	2.78(5)	Nb2—O1^{iii}	1.79(8)	O2—O2^{iii}	2.68(8)
Ba2—O1^{iii}	2.94(5)	Nb2—O1^{xvii}	1.79(13)	O2—O2^{xvii}	2.68(5)
Ba2—O1^{viii}	2.94(5)	Nb2—O2	2.15(3)	O3—O3^{xxv}	2.69(7)
Ba2—O1^{ix}	2.66(10)	Nb2—O2^{iii}	2.15(4)	O3—O3^{xxvi}	2.69(13)
Ba2—O1^{x}	2.66(10)	Nb2—O2^{xvii}	2.15(2)	O3—O4^{xxvii}	2.76(3)
Ba2—O2	2.93(4)	Nb2b—Nb2b^{xii}	1.171(17)	O3—O4^{xxiii}	2.57(5)
Ba2—O2^{iii}	2.98(4)	Nb2b—O1^{xvi}	2.08(9)	O3—O4^{xxviii}	2.76(3)
Ba2—O3^{xi}	2.79(7)	Nb2b—O1^{xviii}	2.08(7)	O3—O4^{xxix}	2.57(5)
Ba2—O4	2.744(7)	Nb2b—O1^{xix}	2.08(11)	O3—O5^{xxiii}	2.96(12)
Ba2—O4^{xii}	2.744(7)	Nb2b—O1^{xx}	2.97(7)	O4—O4^{xv}	2.911
Ba2—O5^{v}	2.41(5)	Nb2b—O1^{xxi}	2.97(5)	O4—O4^{v}	2.911
Nb1—Nb1^{xii}	1.200(15)	Nb2b—O1^{xxii}	2.97(8)		

Coordinates for symmetrically equivalent points :

(i) 1-x+y, 1-x, 0.5-z; **(ii)** y, -1+x, -0.5+z; **(iii)** 1-y, x-y, z; **(iv)** 1-x, -x+y, -z;

(v) -x+y, -x, z; **(vi)** y, x, -z; **(vii)** 1-x+y, -x, z; **(viii)** 1-y, x-y, 0.5-z;

(ix) 1-x, -x+y, 1-z; **(x)** 1-x, -x+y, -0.5+z; **(xi)** x, -1+y, z; **(xii)** x, y, 0.5-z;

(xiii) 1-y, 1+x-y, z; **(xiv)** -1-x+y, -x, z; **(xv)** -y, x-y, z; **(xvi)** 1-x+y, 1-x, z;

(xvii) 1-y, 2+x-y, z; **(xviii)** -1-x+y, 1-x, z; **(xix)** x, 1+y, z; **(xx)** -x+y, 1-x, z;

(xxi) x, 1+y, 0.5-z; **(xxii)** -x+y, 1-x, 0.5-z

Table 6: The refined lattice parameters, unit-cell volume, reliability factors and goodness of fit indicator for α-$Ba_4Nb_2O_9$ compound

Phase information	
Formula sum	$Ba_4Nb_2O_9$
Formula weight	879.2 g/mol
Crystal system	hexagonal
Space-group	P -6 2 c (190)
Cell parameters	a = 1.02693 (1) nm c = 0.845704 (8) nm
Cell volume	V = 772.38(1) Å^3
Z	3
Calc. density	5.66996 g/cm^3
R factors (%)	R_F(obs) = 5.74 R_B(obs) = 6.67 R_Fw(obs)= 6.16
Profil R factors(%)	Rp = 7.63 Rwp = 10.67

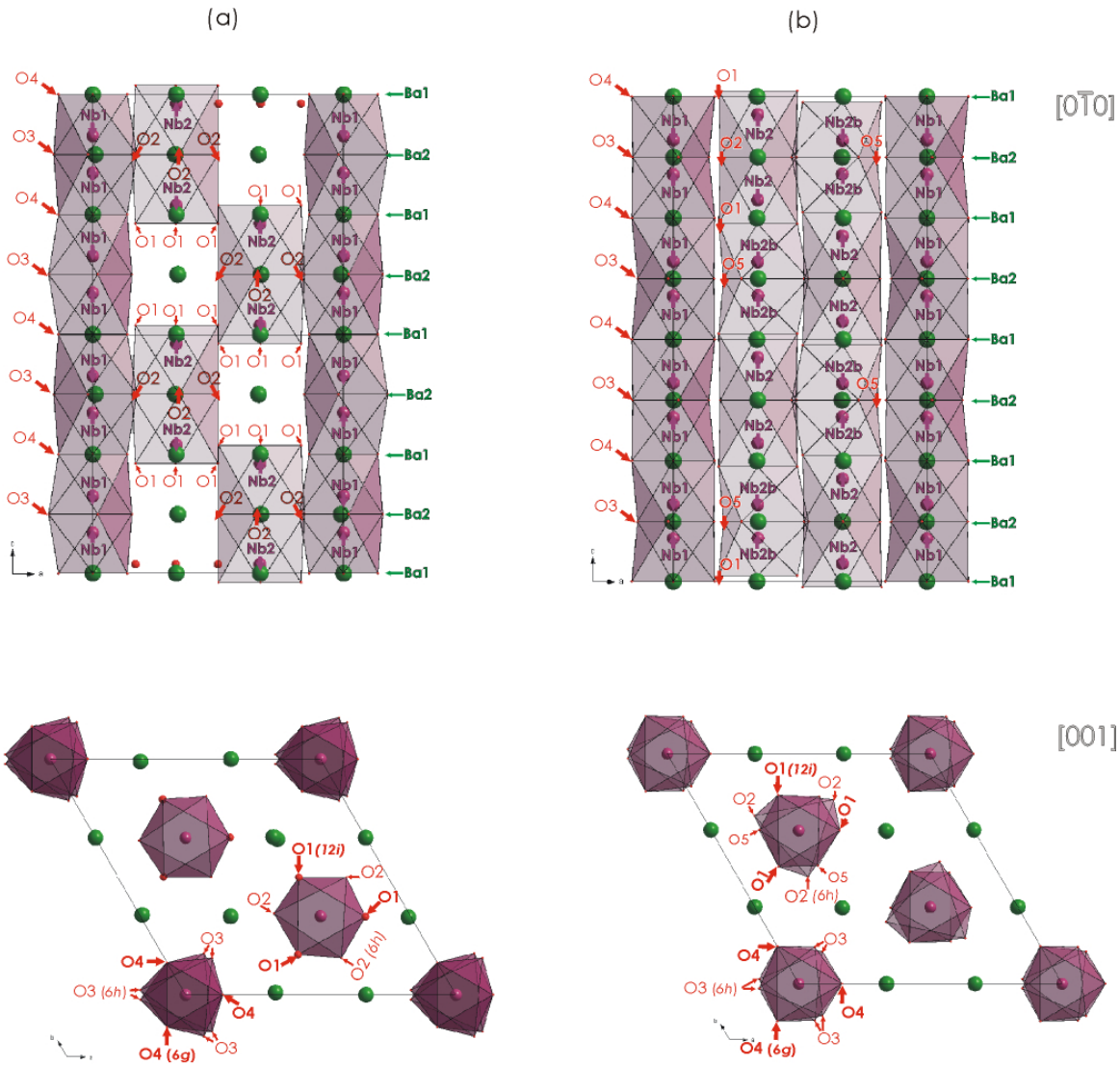

Figure 33: The clinographic projection of Model I (a) and Model II (b) along $[0\text{-}10]_H$ and $[001]_H$ crystallographic projection.

4.4.5. The (in)commensurability of α-$Ba_4Nb_2O_9$ crystal structure and SAED analyses

The TEM specimen tilting experiments and the XRD crystal structure refinement in space group *P-62c*, appears to have only limited success, since we were not able to identify the wide peaks with low intensity in XRD spectra and diffuse diffraction spots in ED patterns. Additionally, the appearance of peak splitting with a kind of the "wobbling" effect at the positions compatible with the space group *P-62c* (see the corresponding enlargements in Figs. 28d and 28h) can not be explained in terms of a conventional 3D crystallographic approach. These features in α-$Ba_4Nb_2O_9$ patterns are therefore in agreement with the modulated or intergrowth modulated crystal structure; either commensurable or incommensurable, which can be explained using a superspace formalism in (3 + 1)-

dimensional space [Perez-Mato *et al.*, 1999, Zakhour-Nakhla *et al*. 2000]. However, to the first approximation, α-$Ba_4Nb_2O_9$ can be described as intergrowth modulated crystal structure with a general formula $A_{1+x}A'_xB_{1-x}O_3$ composed of two subsystems. These include the subsystem [(Nb,A')O_3] and the subsystem [Ba].

The [(Nb,A')O_3] groups form a hexagonal lattice of columns with a certain sequence of octahedra and trigonal prismatic units along the c-direction. On another hand, the subsystem [Ba] is based on barium cations, which constitute chains between $[(Nb,A')O_3]_\infty$ columns. Still more, the two subsystems have a common *crystallographic* parameter *a* but differ in the crystallographic parameter *c*. Thus the c parameter of [(Nb,A')O_3] substructure corresponds to $c_1 = c_P/2$, while the *c* parameter of the second substructure composed of barium cations is consistent with $c_2 = c_{perov}$. Each of these two substructures is periodic according to its own lattice, but the crystal structure of the intergrowth compound is given by these two subsystems being modulated. The modulated period of [(Nb,A')O_3] substructure is given by the average c-parameter of the [Ba] subsystem and vice versa; *e.g.*, the modulation wave vector of subsystem 1 is given by c_2^*. The ration of prism and octahedra in the [(Nb,A')O_3] subsystem can be expressed as N_{prism}/N_{octa}. = x (1– x)$^{-½}$. Considering the stochiometry of α-$Ba_4Nb_2O_9$ the value of x corresponds to 1/3. This value reveals that the ration N_{prism}/N_{octa} is consistent with ½, which indicates that $[(Nb,A')O_3]_\infty$ columns consist of the repeated sequence of two consecutive NbO_6 octahedra sharing faces followed by one trigonal-prism. These observations are in a good agreement with the "hypothetical" average crystal structure in figure 22. Furthermore, the value of parameter x is very important in the interpretation of crystal structure modulation [Perez-Mato *et al*., 1999]. However, the structure of a compound $A_{1+x}A'_xB_{1-x}O_3$ would be formally incommensurate only if x has an irrational value (this would correspond to an aperiodic sequence of layers). Indeed, a rational value of x is a necessarily and sufficient condition for the structure being commensurate [Perez-Mato *et al*., 1999]. Considering the stochiometry of α-$Ba_4Nb_2O_9$ one can see that both values x and γ, where γ = (1+x)/2, are rational numbers consistent with 1/3 and 2/3, respectively. Therefore the α-$Ba_4Nb_2O_9$ is formally commensurate modulated with a modulation vector defined as $q = \gamma c_1^* = \gamma c^*_2$ and a superstructure unit-cell parameter $c_s = c_1k = c_2p$, where k and p are related to the γ as follows γ = p/k. Considering the two equations, *i.e.*, $c_s = c_1k = c_2p$ and γ = $p/k = c_1/c_2 = c_2^*/c_1^*$, and the [010] ZAP in figure 20, which revealed that c_s corresponds to 0.848 nm the *c* parameters of both substructures can be calculated and subsequently used in the LeBail fit (see chapter 4.8.). Thus the c_1 = 0.2827 nm and the c_2 = 0.424 nm.

The intergrowth modulated crystal structure of α-$Ba_4Nb_2O_9$ was confirmed by the electron microscopy on single α-$Ba_4Nb_2O_9$ crystals in [010] zone-axis orientation (Fig. 34). Surprisingly, the TEM results show the existence of two slightly different electron-diffraction patterns for α-$Ba_4Nb_2O_9$ annealed at 1100 °C for 5h and than slowly cooled down to room temperature, *i.e.*, α-BNO-1 sample (Fig. 34a), and by quenching the sample from 1100 °C after firing for 48h, *i.e.*, α-BNO-2 sample (Fig. 34b). The ED pattern recorded on α-BNO-2 (Fig.

34a) has periodic distribution of diffraction spots but contains diffuse streaks normal to the c* direction. Considering the "ideal" symmetry of this [010] ZAP one can see relatively higher intensity of the spots situated close to one diagonal of the rectangle of the principal reflections (Fig. 34). Nevertheless, the [010] ZAP recorded on α-BNO-1 (Fig. 34b) is more complex. It shows an aperiodic distribution of at least two types of fundamental reflections in addition to low intensity satellites. The latter are slightly inclined over a small angle with respect to the basic vector normal to the c* reciprocal lattice direction. These particular features indicate that α-$Ba_4Nb_2O_9$ also appears in a slightly incommensurate modulated crystal structure form, in addition to commensurate analogue, which crystal structure is reflected in [010] ZAP in figure 34a. The explanation for the appearance of these satellite reflections is the mutual interactions of the two subsystems, which giving rise to the modulations of atoms (see the explanation in chapter 4.7.). However, the satellites in figure 34b imply that the value of γ is not exactly of 2/3 but seems to slightly deviate from the estimated value – most likely also due to the compositional variation of this BaO-rich binary system. Generally, knowing the value of γ component enables one to derive the complete crystal structure. Usually neither the crystal structure refinement is needed. Nevertheless, in the case of α-$Ba_4Nb_2O_9$ there is a complication with niobium atoms and vacancies distribution, which makes difficulties in the complete crystal structure determination directly from knowing the value of γ. Still more, the exact γ determination is problematic not only due to the distortion on B-sublattice but also due to the compositional variation in α-$Ba_4Nb_2O_9$ on behalf of BaO sublimation and the water absorption. However, water absorption is characteristic for BaO-rich systems [Vanderah *et al.*, 2002] since the BaO has the tendency to uptake water from the atmosphere. This water may be incorporated into the crystal structure of α-$Ba_4Nb_2O_9$ in the form of hydroxyl anions on the anion sublattice. In this case one can expect drastic changes in the lattice parameters with respect to the lattice parameters of an ordinary α-$Ba_4Nb_2O_9$. This statement is confirmed by the splitting of the subcell reflections [Leshchenko *et al.*, 1979] in XRD pattern of α-BNO-2 sample (Fig. 35). The Le Bail fit clearly shows that the peak splitting correspond to two hexagonal phases with close sublattice parameters. The *phase I* has *a* = 0.59249 nm, *c* = 0.42320 nm and *phase II* has *a* = 0.59143 nm, *c* = 0.42474 nm (Fig. 35). These "phase separation" is definitely not related to the hexagonal lattice distortion, which could eventually results the coexistence of monoclinic and hexagonal phases. The splitting of (00l) group of reflections is a valid evidence for not dealing with a lattice distortion (see inset in figure 35).

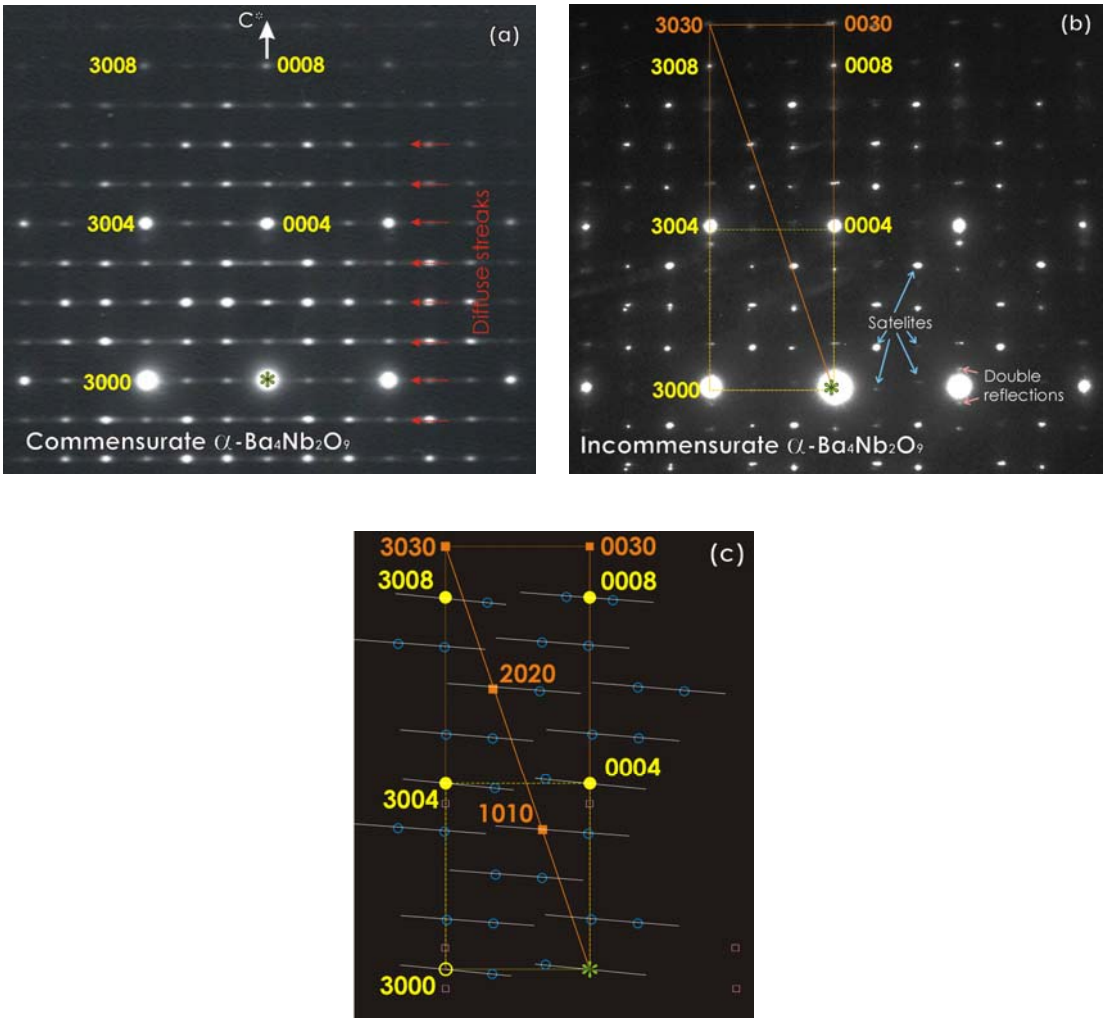

Figure 34: (a) The SAED patterns of α-$Ba_4Nb_2O_9$ crystal in $[010]_H$ zone-axis orientation recorded on the sample heated at 1100 °C for 48h and than quenched to room temperature corresponds to commensurate but highly disordered 4H crystal structure **(b)** The SAED patterns of α-$Ba_4Nb_2O_9$ crystal in $[010]_H$ zone-axis orientation recorded on the sample heated at 1100 °C for 5h and than slowly cooled down to room temperature can be ascribed to strongly incommensurate 4H polytype **(c)** The indexation scheme of the electron diffraction pattern for an incommensurate modification. The orange rectangle outlines the unit cell of the $[Nb,A')O_3]_\infty$ subsystem while the yellow rectangle outlines the unit-cell of $[Ba]_\infty$ subsystem. Full orange squares mark the reflections of the $[NbO_3]_\infty$ subsystem; full yellow circles mark the reflections of the $[Ba]_\infty$ subsystem; open yellow circle belongs to the reflections common to both subsystems; open blue circles corresponds to the satellites, while pink squares represents the reflections caused by a double diffraction.

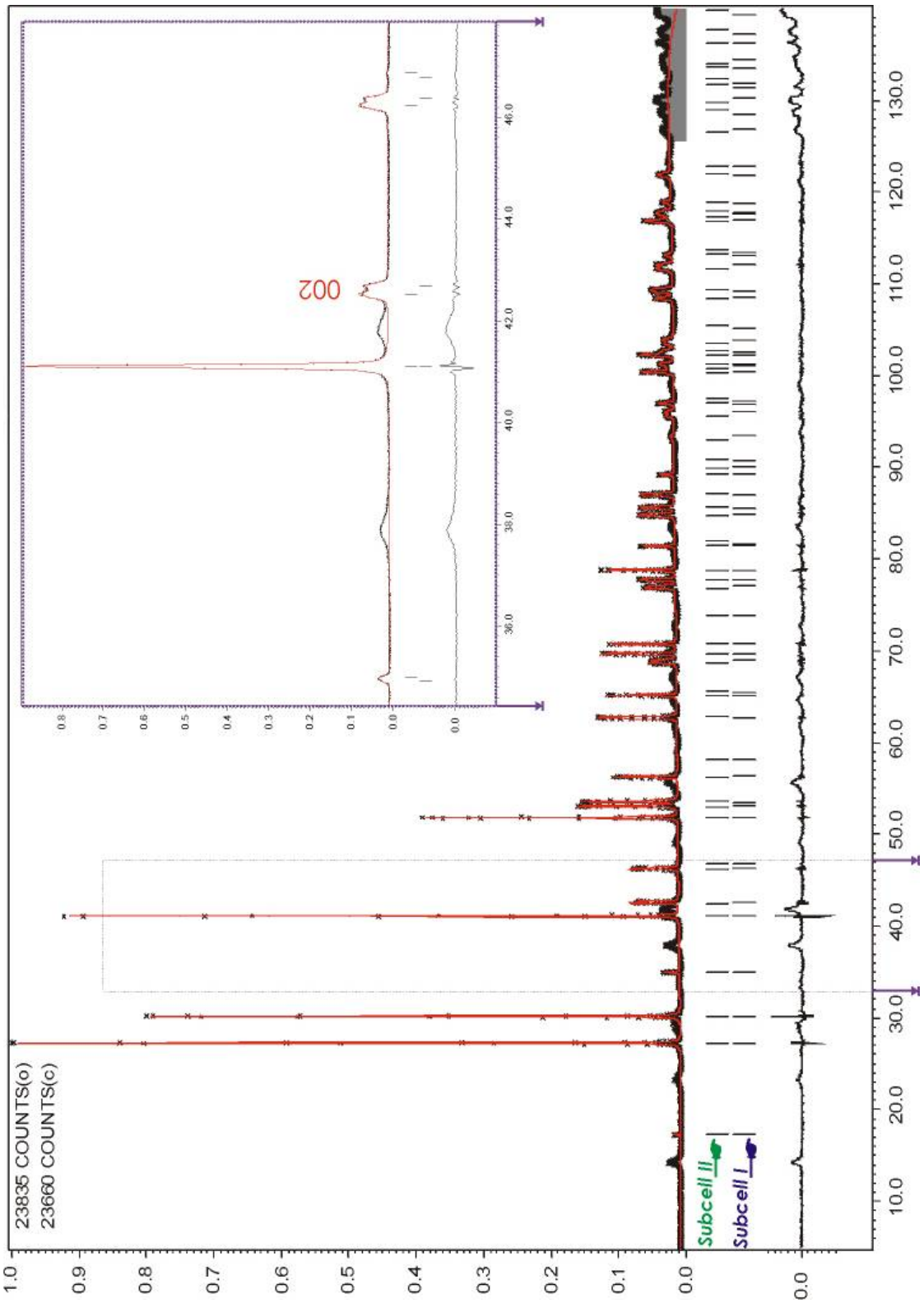

Figure 35: The experimental (black points), calculated and difference X-ray diffraction profile of α-$Ba_4Nb_2O_9$ recorded on α-BNO-2 sample. The two sets of ticks mark the positions of the main hkl0 reflections. Each set refers to one of the two hexagonal phases. The inset on the right side of the figure represents the enlarged area of the XRD profile in the range of 45°<2θ <48°. The (002) reflection shows obvious splitting related with the separation of the two hexagonal phases.

Furthermore, for the successful extraction of information on the crystal unit-cell of the modulated structure, the length and orientation of the modulated vector in reciprocal space has to be determined from electron-diffraction data. Indeed, this makes demands upon full indexing of recorded electron-diffraction pattern. The indexation of EDP of a modulated α-phase was possible after the reflections were divided into two groups (Fig. 34b); one describing the $[(Nb,A')O_3]_\infty$ subsystem, while the second one corresponds to the $[Ba]_\infty$ subsystem. Four indexes (*hklm*) are necessarily to index each reflection in reciprocal space and to elucidate the crystal structure of α-$Ba_4Nb_2O_9$. Therefore, the crystal structure of α-$Ba_4Nb_2O_9$ can be unequivocally considered as (3+1)-dimensional modulated. The main reflections of the $[(Nb,A')O_3]_\infty$ subsystem have hkl0 indexes, while hk0m reflections are the main reflections for the $[Ba]_\infty$ subsystem and hk00 reflections are common to both substructures. The unit-cells for each subsystem are outlined with solid and dashed lines in figure 34b-c. However, the so called "authentic satellite" reflections are indexed by (*hklm*), where both $l \neq 0$ and $m \neq 0$. The positions of satellites in the indexation scheme of the [010] ZAP (Fig. 34) shows that α-$Ba_4Nb_2O_9$ is modulated along [001]*. Figure 34 implies that the crystal structure of α-$Ba_4Nb_2O_9$ can be either commensurably or incommensurably modulated. The modulation vector *q* was estimated only for a commensurate phase (Fig. 34a). Since $c_1 = 0.2827$ nm and $\gamma = 2/3$ the modulation vector is consistent with $q_1 = c_2^* \sim 2.358$ nm^{-1}.

Considering the special feature of unindexed reflections in XRD spectra they could eventually belong to the satellites of the (in)commensurable modulated and not to intergrowth modulated crystal structure. These broad *hklm* reflections with low intensities can namely form a dense sets being projected on the 2θ axis. For non-modulated structures the same sets would become discrete. In general, modulated crystal structures are also described in superspace group as evident from the four index notation but their interpretation is independent of the choice of the initial phase (ϕ) of the atomic modulation function. On contrary when dealing with interpenetrating incommensurately modulated crystal structures the choice of the phase ϕ in one subsystem will fix the phases in all others. Nevertheless, based on ED patterns the α-$Ba_4Nb_2O_9$ is an intergrowth modulated crystal structure, which in general can be described in one subsystem like a modulated structure. But in this case the modulation of the second subsystem would be too large.

4.4.6. α-BNO-1: The Le Bail XRD profile fitting using a (3 + 1)-dimensional approach (SSG R-3m(00γ)0s)

The superstructure observed in electron-diffraction patterns is compatible with the crystal structure of modulated composites with a general formula $A_{3m+3n}A'_nB_{3m+n}O_{9m+6n}$ where m = 1 and n = 3 (see chapter 1.7.5.). In order to confirm the statement that α-$Ba_4Nb_2O_9$ crystal structure corresponds to composite one-dimensional hexagonal perovskite (2H) the Le Bail fit was performed using the information on reflection positions and the super-space group proposed for the whole family of $A_{3m+3n}A'_nB_{3m+n}O_{9m+6n}$ (m = 1, n = 3) compounds [Perez-Mato *et al.,* 1999]. The unit-cell parameters used in this profile fitting were obtained from [010] and [001] zone-axes pattern (Figs. 20a, 20d) and correspond to a = 1.025 nm, c_s = 0.848 nm.

In view of the fact that α-$Ba_4Nb_2O_9$ crystal structure consists of two subsystems, i.e., $[(Nb,A')O_3]_\infty$ and $[Ba]_\infty$, the Le Bail fit was carried out by considering the two sets of unit-cell parameters; one is consistent with the *subsystem I* (a = 1.025 nm, c_1 = 0.2827 nm), while the second corresponds to the *subsystem II* (a = 1.025 nm, c_2 = 0.424 nm). The well-known mutual interaction of both subsystems causes their modulation along c*. Thus the *subsystem I* is modulated with a period given by the average c parameter of the *subsystem II* and vice versa. Accordingly, the modulation vector of *subsystem I* corresponds to $1/c_2$ = 2.358 nm^{-1}, while the *subsystem II* is modulated by the vector of $1/c_1 = c_1^*$ = 3.538 nm^{-1}. The modulation of both subsystems, however, generates the "authentic satellite" reflections. For composite crystal structures it is convenient to choose an arbitrary subsystem as a reference. Thus for α-$Ba_4Nb_2O_9$ phase the $[(Nb,A')O_3]$ subsystem was chosen as the reference system. In this case, the subsystem I and subsystem II are related to the (3+1)D super-space group by application of inter-lattice matrix W^1 and W^2 [Smaalen, 1991]. In other words this inter-lattice matrix represents the relationship between the unit-cell parameters, modulation vectors and symmetry operations of both subsystems. Therefore the Le Bail fit of both subsystems has to be performed simultaneously. Since the whole family of compounds with general formula $A_{3m+3n}A'_nB_{3m+n}O_{9m+6n}$ (m = 1, n = 3) can be described with the super-space *R-3m (00γ)0s* (No. 166.2) symmetry irrespectively on the composition and actual atoms A, A' and B involved in the compounds, the centrosymmetric super-space group *R-3m (00γ)0s* was therefore compatible with the reference subsystem $[(Nb,A')O_3]$. This super-space (3 + 1)D group is parental to the 3D *R-3m* (No. 166) derivative (Elcoro *et al.*, 2003), which describes the average structure of modulated $[(Nb, A')O_3]$ subsystem as well as the average structure of intergrowth modulated α-$Ba_4Nb_2O_9$. This implies that the average unit-cell of $[(Nb,A')O_3]$ subsystem and α-$Ba_4Nb_2O_9$ structure is rhombohedral (R) (Fig. 34b). On the other hand the average unit-cell of the second subsystem, which is formed by barium ions, is a primitive (P) since the symmetry of [Ba] subsystem can be described by the symmetry of centrosymmetric

superspace group *P-3c1(001/γ)*. The primitive average unit-cell contains two types of barium cations. The first cation, Ba1 is located in a A_3O_9 layer at the position (⅓, 0,¼), while the second one Ba2 is in $A_3A'O_6$ layer at the position of (⅔, 0, ¾) according to the primitive average unit-cell. However, using such a model and a Le Bail methods in the profile fitting (Fig. 36) one can see that the *hk00* reflections common to both subsystems and those of subsystem $[Ba]_\infty$ indexed as *hk0m* ($m \neq 0$) stay sharp and intense. On another hand hkl0 ($l \neq 0$) reflections corresponding to the $[(Nb,A')O_3]$ subsystem and satellite reflections *hklm* ($m \neq 0$, $l \neq 0$) are either very broad or very weak. This represents well established order in the [Ba] sublattice and one-dimensional disorder in the $[(Nb,A')O_3]$ sublattice. Comparing the nominal $A_4A'B_2O_9$ composition and actual $Ba_4Nb_2O_9$ composition one can speculate that there are cation vacancies in the $[(Nb,A')O_3]$ subsystem. However, the lack of ordering of niobium atoms and vacancies can be the reason for the appearance of broad reflections with low intensities. Still more the particular one-dimensional disorder additionally produces sheets of diffuse intensities normal to the reciprocal c-direction clearly evident from recorded ED patterns. At this stage of profile fitting the profile residual R_p and the weighted profile residual R_{wp} are consistent with 11.20 % and 15.44 %, respectively (see appendix III).

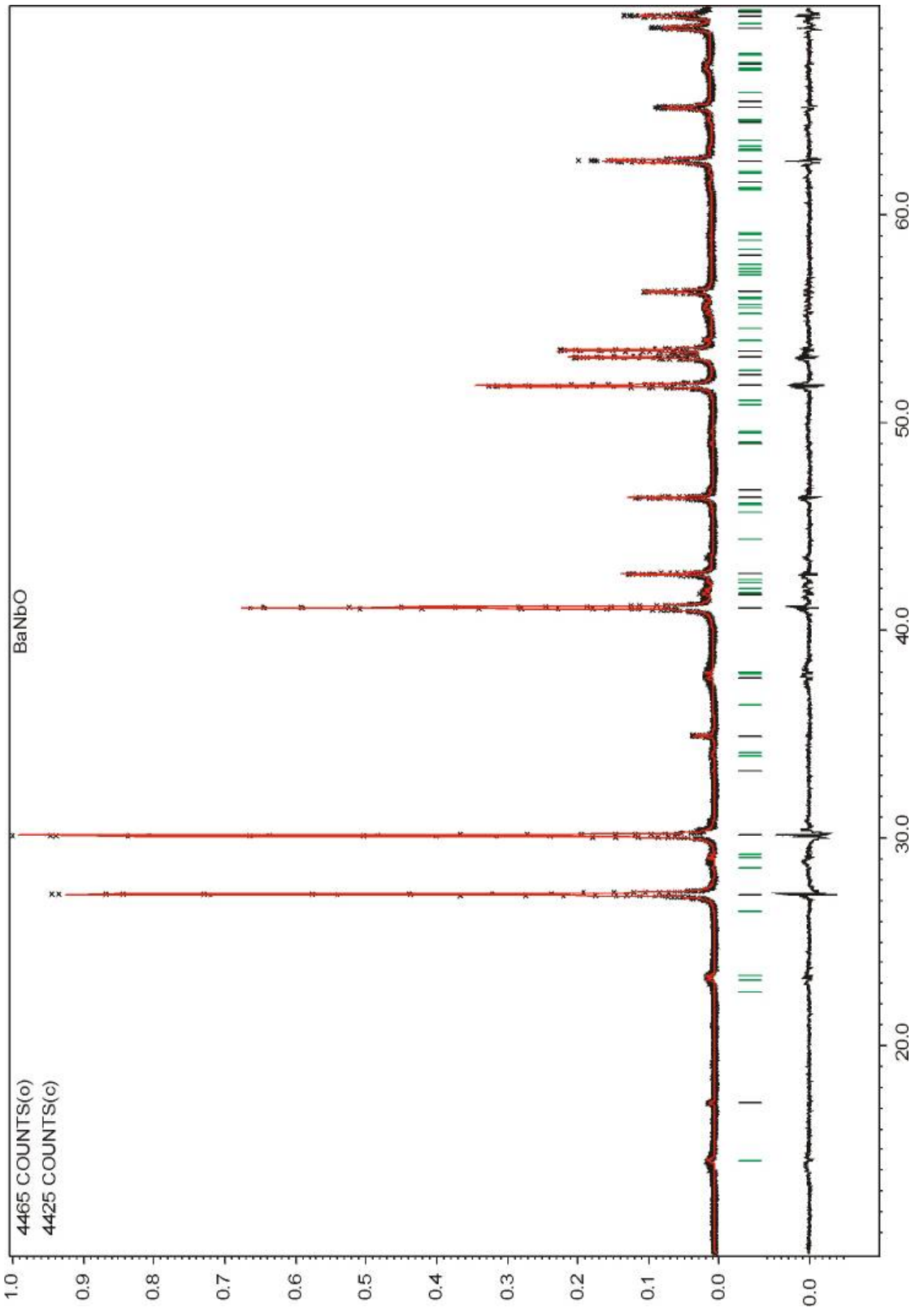

Figure 36: The observed (points), calculated (red solid line) and difference (bottom) X-ray powder profile for an intergrowth incommensurate modulated $Ba_4Nb_2O_9$. The green vertical lines indicate the positions of satellite reflections while the black vertical line denote the positions of main reflections corresponding to [(Nb,A')O_3] and [A] subsystem.

4.4.7. α-$Ba_4Nb_2O_9$ – a commensurate interface modulated crystal structure

The "fractional shift" method was additionally used for the interpretation of an incommensurable modulation along [001]* and so as to confirm the hypothetical crystal structural model suggested in section 4.4.2. With this respect the incommensurable analogue of α-$Ba_4Nb_2O_9$ is considered as a commensurate interface modulated as in the case of $Sr_4Ni_3O_9$ [Huve *et al.*, 1998]. The new crystal structural model obtained in this approach was derived by the periodic introduction of translational interplanar faces into the related "basic" structure (which does not necessarily exist as such) of higher symmetry (Fig. 37a-b). The initial "basic" model is composed of chains of face-sharing octahedral dimmers and alternating trigonal prism (Fig. 37a). Chains are shifted along c-crystallographic directions with respect to each other. The range of chains displacement along c-axis corresponds to the distance between the Ba-O layers. Considering the sequence of polyhedra in a single chain and the initial "basic" model, the equivalent polyhedral level reappear every fourth chain. Thereby the unit mesh vectors of the initial model correspond to a' and c'. The repeated units, *i.e.*, blocks of three chains are then virtually separated by conservative translational interfaces. Shift of blocks along these boundaries at a latter stage results the crystal structural model of a commensurate structure with the unit mesh vectors *a* and *c*, as schematically represented in figure 37b. The reciprocal lattices of both, initial "basic" and "hypothetical" structures are given in figure 37c and outlined by the reciprocal vectors a'*, c'* and a*, c*. One can see that the basic diffraction spots of the "hypothetical" structure are associated with linearly arranged equidistant satellite reflections, which appear to be perpendicular to the c* direction, *i.e.*, perpendicular to the prismatic interfaces. Unambiguously, their position is geometrically associated with the positions of basic reflections of an initial "basic" structure (Fig. 37a). The set of chain displacements along translational interfaces by the value of ±¼ *c* namely, result the fractional shift (g*R) of basic reflections (green spots in Fig. 35c) into the new positions corresponding to the satellites. The values of fractional shift thus corresponds to the ¼, ½ and ¾ for the successive row of spots k = 1, k = 2 and k = 3. The "fractional shift" approach proved successful not only in the prediction of "net" symmetry but also in the reproduction of electron-diffraction pattern "ideal" symmetry. One can see that the most intense spots in a calculated ED pattern coincide with the smallest fractional shift, *i.e.*, g*R = ±¼ succeed to g*R = ±½. In this regard the higher intensity of diffraction spots situated close to one diagonal of the rectangle of the principal reflections in [010] ZAP for commensurate and incommensurate α-$Ba_4Nb_2O_9$ can be interpreted (Fig. 34a-b). The satellite reflections perpendicular to the c* direction, i.e., to the prismatic interfaces in commensurate α-$Ba_4Nb_2O_9$ became slightly inclined with respect to that direction in an incommensurate analogue (Fig. 37b-c). The inclination of satellites can be interpret in terms of systematic

"lateral shift" of prismatic planes as in the case of $Sr_4Ni_3O_9$ [Huvé *et al.*, 1998]. That sort of lateral shift should cause changes in the number of face-sharing octahedra at the level of ledging ("lateral shift"). Depending on the sense of the lateral shift, *i.e.*, a change in the orientation of the interfaces, triplet of face-sharing octahedra or single octahedra is created at the level of ledging ("lateral shift"). Consequently, the angle of inclination of the satellite rows depends on the average separation of layers at which the lateral shift of interfaces occurs.

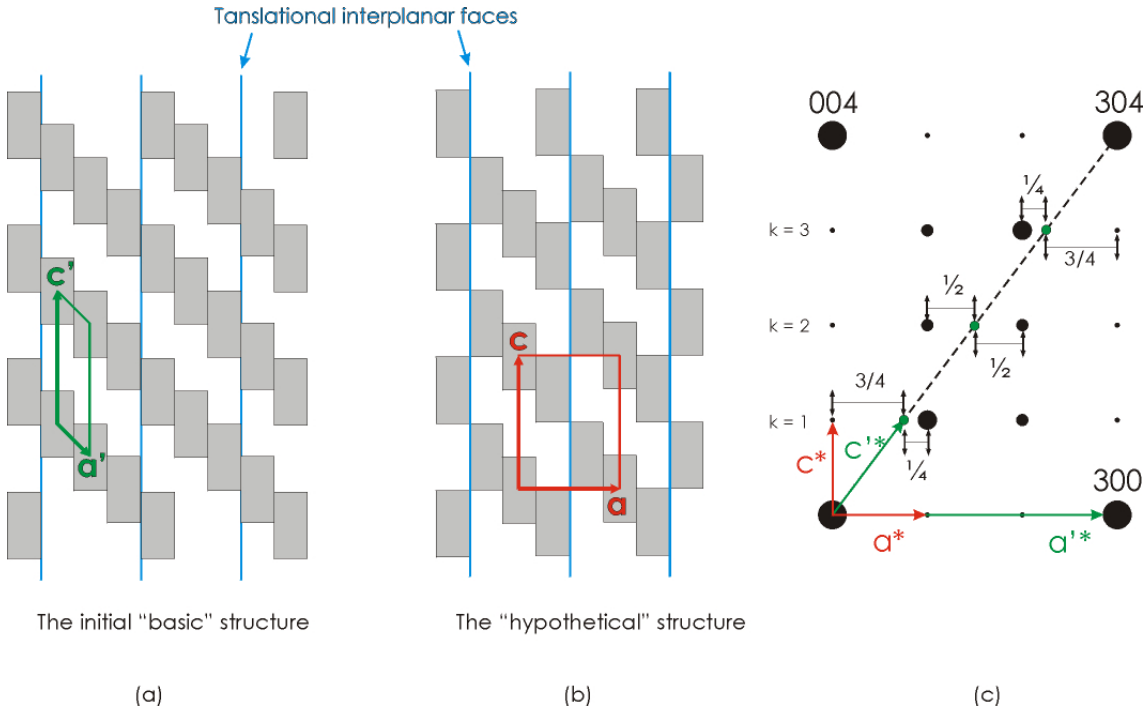

Figure 37: (a) The crystal structural model of the "basic" structure with the unit-cell parameters a' and c'. **(b)** The "Hypothetical" structure of a commensurate α-$Ba_4Nb_2O_9$ with unit-cell parameters a and c. **(c)** The calculated electron-diffraction pattern of a "basic" and "hypothetical" crystal structure of a commensurate α-$Ba_4Nb_2O_9$ with the reciprocal lattice parameters a'*, c'* and a*, c*. [by Huve et al., 1998].

4.4.8. A rigid structural mode of α-$Ba_4Nb_2O_9$ – HRTEM reconstruction

The results of "fractional shift" method were additionally used to understand the positions of bright spots in high-resolution transmission-electron micrographs (HRTEM) and their symmetry. The HRTEM images were recorded along two the most prominent zone-axis orientation; [010] and [001] direction. The HRTEM image recorded along the crystallographic c-axis unambiguously shows a simple hexagonal pattern of the atomic columns (Fig. 38a). The bright dots corresponds to the projection of barium columns whereas the niobium columns are imaged as dark circles surrounding the bright spots at this particular thickness and defocus value. Image simulations were performed using the atomic model of $Sr_4Ru_2O_9$, assuming vacant prismatic sites [Abraham *et al.*, 1994]. Simulations show a good match with the experimental image (Fig. 38a, 38c). Much more structural details are revealed from the HRTEM image recorded along the prismatic [010] zone-axis orientation (Fig. 38d). One can see that the bright dots are arranged in a quasi-square lattice, which resembles the atomic arrangement of α-modification in real space. Its shape is comparable with the unit mesh represented in the "hypothetical" crystal structure model (Fig. 37b) and with the reciprocal lattice denoted by the red arrows in [010] zone-axis pattern in figure 37c. The experimental image is quite well reproduced in simulation using the $Sr_4Ru_3O_9$-based atomic model. Moreover, the image shows the triplets of bright dots following the diagonal of the unit mesh and their shift along the c-direction approximately for one Ba-O layer (see the yellow line in figure 38 e-f. The appearance of these triplets is in a good agreement with the "hypothetical" structural model reconstructed by the introduction of translational interplanar faces into the "basic" structural model. The occurrence of bright dots in the HRTEM image (Fig. 36e-f) thus coincides with the prismatic sites in the suggested structural model (Fig. 22 and Fig. 35b). Thereby, it appears that niobium ions may occupy also the trigonal-prismatic sites. This can be eventually possible since refining the atoms positions in α-$Ba_4Nb_2O_9$ revealed high anisotropic thermal parameter for niobium atoms consistent with U_{33} = 1.83 Å^2. If this would be true, then the bright dots in HRTEM image could be explained as in terms of interpretation given by Abakumov *et al.* [2003] for the case of $Sr_{4/3}Mn_{2/3}Cu_{1/3}O_3$ and Boulahya et al., [1999] for $A_{3m+3n}A'_nB_{3m+n}O_{9m+6n}$ structures in the A–Co–O (A = Ca, Sr, Ba) systems. In this regards the brightest spots in the HRTEM image would correspond to niobium atoms in trigonal prisms and barium atoms at the level of centers of trigonal prisms along this projection. On contrary, barium atoms situated along the c-axis at the level of oxygen triangles would produce less bright dots. The [010] HRTEM image on this stage of investigation is not possible to quantify the partial occupancy of B-sites; however the basic spot pattern is correctly reproduced in the simulated images.

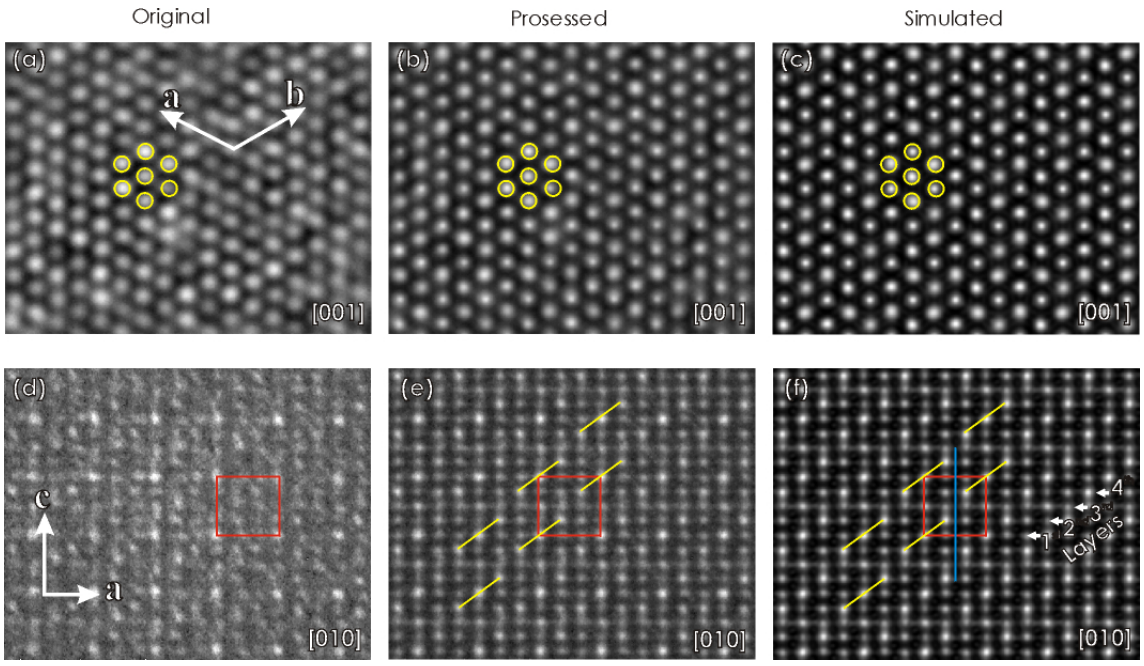

Figure 38: HRTEM images of incommensurate α-$Ba_4Nb_2O_9$: **(a-c)** along the $[001]_H$ zone show the perfect hexagonal arrangements of atomic columns (df = - 47 nm; th = 5 nm) **(d-f)** along the $[010]_H$ zone showing the rectangular array of bright dots; this configuration of bright spots corresponds to the four layered unit-mesh along $[010]_H$ outlined with the red rectangle (df = - 97 nm; th = 4 nm). The vertical blue line mark the approximate position of the translational interplanar face, while yellow lines link together the triplets of bright dots shifted along translational interfaces. The magnitude of average shift is comparable with the width of one BaO-Layer.

4.5. Results: The crystal structure of γ-$Ba_4Nb_2O_9$

The preliminary thermal analyses, high-temperature transmission electron microscopy (TEM) and X-ray powder diffractometry (XRD) (see chapter 4.3.1.) revealed the existence of two stable modifications in $Ba_4Nb_2O_9$ compound. This includes low-temperature α-modification and high-temperature γ-modification, with the endothermic phase transition at 1176 °C. In order to understand the α → γ phase transition the crystal structure of γ-$Ba_4Nb_2O_9$ was additionally studied in terms of transmission electron microscopy.

The preliminary TEM analyses revealed several problems considering the γ-$Ba_4Nb_2O_9$ sample observation. The investigation was hindered because of the sample sensitivity to the electron beam in spite of the fact that the specimen was coated by carbon layer. This particular specimen was prepared by the following procedure. The cut edge of the pellet corresponding to γ-$Ba_4Nb_2O_9$ was mounted eccentrically into a brass ring with diameter of 3 mm to prevent fracturing of the specimen and to bring the surface area of the γ-$Ba_4Nb_2O_9$ sample near the centre of the TEM beam. Then the specimen was mechanically thinned to 130 μm, dimpled to 20 μm and finally ion-milled using 4 kV Ar^+ ions at an incident angle of 10° to obtain large transmission area for TEM investigations. However, the rigorous charging

caused the sample fracturing. At the thicker part of the specimen the instability of the central electron-beam manifested with its obvious jumping from the optical axis of the microscope during slight shift of the specimen. Still more, the electron-beam being at the steady position for longer period (~1-2 min) created the hole in the material. With respect to all these, the applied TEM analyses have to be performed as fast as possible to reduce the sample damaging. In fact it has turned out that the observation can be drastically improved by using the small crystalline fragments of γ-$Ba_4Nb_2O_9$ deposited on a copper grid previously coated with a thin film of amorphous carbon. Therefore, the further tilting experiment was carried out on powdered γ-$Ba_4Nb_2O_9$.

4.5.1. γ-$Ba_4Nb_2O_9$ – The reconstruction of the unit-cell from SAED patterns (The tilting experiment)

In order to obtain more information for the space-group determination of γ-$Ba_4Nb_2O_9$ several crystals were studied by SAED using the tilting experiment in combination with a high-resolution transmission-electron microscope imaging. The previous HRTEM investigations (Fig. 13) revealed that the high-temperature γ-modification has a domain structure. The formation of domains is associated with the BaO-layers, which appears to be normal to the crystallographic c-axis. To be exact, the geometry of basic reflections and the "net" symmetry of ED pattern, which refers to the hexagonal array of atoms in real space is comparable to the [001] zone-axis pattern of α-$Ba_4Nb_2O_9$ (compare the insets in Fig. 13a and Fig. 5a). Moreover, the high-temperature TEM analyses subsequently revealed that the hexagonal "net" symmetry of zone-axes pattern does not change at the temperature of $\gamma \leftrightarrow \alpha$ phase transition. The same was observed for the arrangements of atoms in corresponding HRTEM micrographs. Indeed, this particular crystal orientation is consistent with [001] zone-axis orientation for gamma and alpha phase. However, the obtained results revealed the basic "net" symmetry of [001]γ-ZAP, which turns out to be valuable information for further structural analyses by means of a TEM tilting experiment.

With this in mind the tilting experiment started by searching γ-$Ba_4Nb_2O_9$ single crystals close to [001] zone-axis orientation. After finding the appropriate ZAP the crystal was tilted around [010]* axis (Fig. 39). The reciprocal-layer normal to the tilt-axis was reconstructed from the basic reflections in recorded electron-diffraction patterns (Fig. 40). Considering the distance between particular spots and their arrangement the reconstructed pattern appears to be in the [010] zone-axis orientation. This reconstruction was used together with the ZOLZ "net" symmetry of [001] ZAP (Fig. 37d) to deduce the Bravais lattice in the reciprocal space.

In view of the fact that the geometry of ZOLZ reflections can be represented by the rectangle (see the red rectangle in the enlargement of figure 37d) and in view of the rectangular shape of the unit-mesh in the reconstructed [010] pattern, the high-temperature γ-polymorph appears to crystallizes within the orthorhombic crystal system. Indeed, this statement is in agreement with the interpretation of unit-cell for γ-$Ba_4Nb_2O_9$ given by Leshchenko *et al*. [1978]. The electron-diffraction patterns recorded in this tilting experiment were further used for estimation of orthorhombic lattice parameters. However, the *a* and *b* parameters were directly measured from [001] ZAP and are consistent with *a* = 1.26 nm an b = 2.18 nm. On another hand, the crystallographic parameter c was deduced from the reconstructed layer and is nearly about *c* = 2.6 nm. In order to confirm its range and exclude its possible multiplication, the investigation proceed with searching for [010] or [100] zone-axes orientations, which would eventually perform the information about the *c* parameter. After finding the corresponding ZAP and measure the value of c* (*c* = 2.55 nm) the γ-crystal was tilted around [001]* direction. Once having [100] zone-axis pattern (Fig. 41a) and thus the information about the extinction conditions for all relevant zone-axes orientations of an orthorhombic crystal system, *i.e.*, [100], [010] and [001], one can start with the determination of the space group. Unambiguously, the (0kl) indexes in [100] ZAP fulfill the reflection condition *k+l = 2n*, which indicate the presence of glide plane n *II* 100. Moreover the reflection conditions *hk0*; h = 2n in [001] ZAP imply the existence of a glide *a II* 001. No reflection conditions for *h0l* reflections in the reconstructed [010] layer hint on the mirror plane perpendicular to the crystallographic *b*-axis. Likewise, there are no integral reflection conditions for *hkl* nodes. Accordingly, the Bravais lattice has no centering. The observed reflection conditions thus reveal that the crystal structure symmetry of γ-$Ba_4Nb_2O_9$ can be described by a space group *Pnma*. Astonishingly, the second tilting experiment (Fig. 39) revealed that the reciprocal directions are not perpendicular to each other paraphrasing that the γ-phase may crystallizes within a triclinic or monoclinic crystal family. The deviation from the right angle is demonstrated in figure 41 by the inclined red line binding together the equivalent reciprocal reflections with respect to two mutually perpendicular yellow lines. Even though, the crystal symmetry of γ-$Ba_4Nb_2O_9$ can be considered as a pseudo orthorhombic.

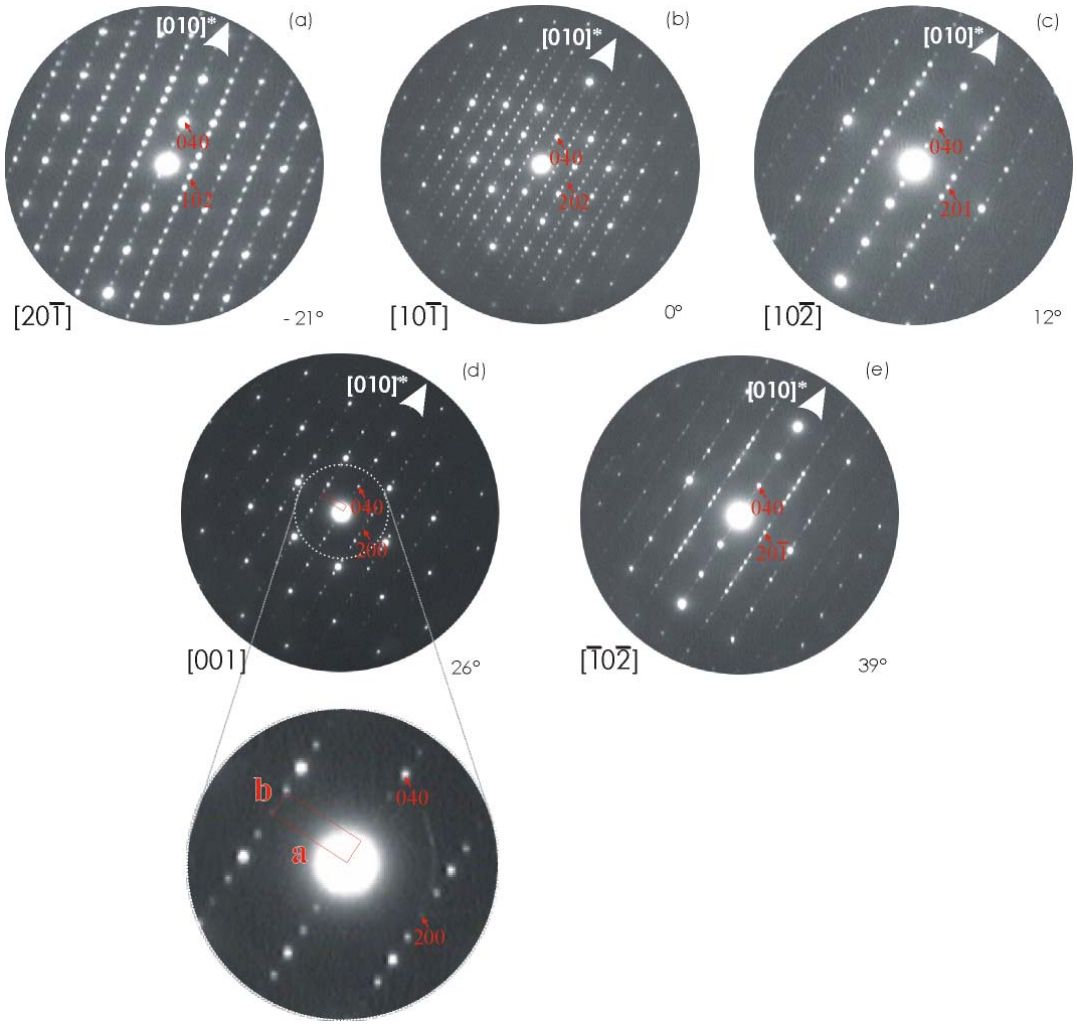

Figure 39: The zone-axes electron-diffraction patterns of γ-$Ba_4Nb_2O_9$ obtained during tilting the crystal around [010]*; the fundamental reflections are indexed according to the orthorhombic *Pnma* space group with $a \approx 1.26$ nm $b = 2.18$ nm and $c \approx 2.25$ nm. The red rectangle in (d) and in the corresponding enlargement represent the orthorhombic Bravais lattice.

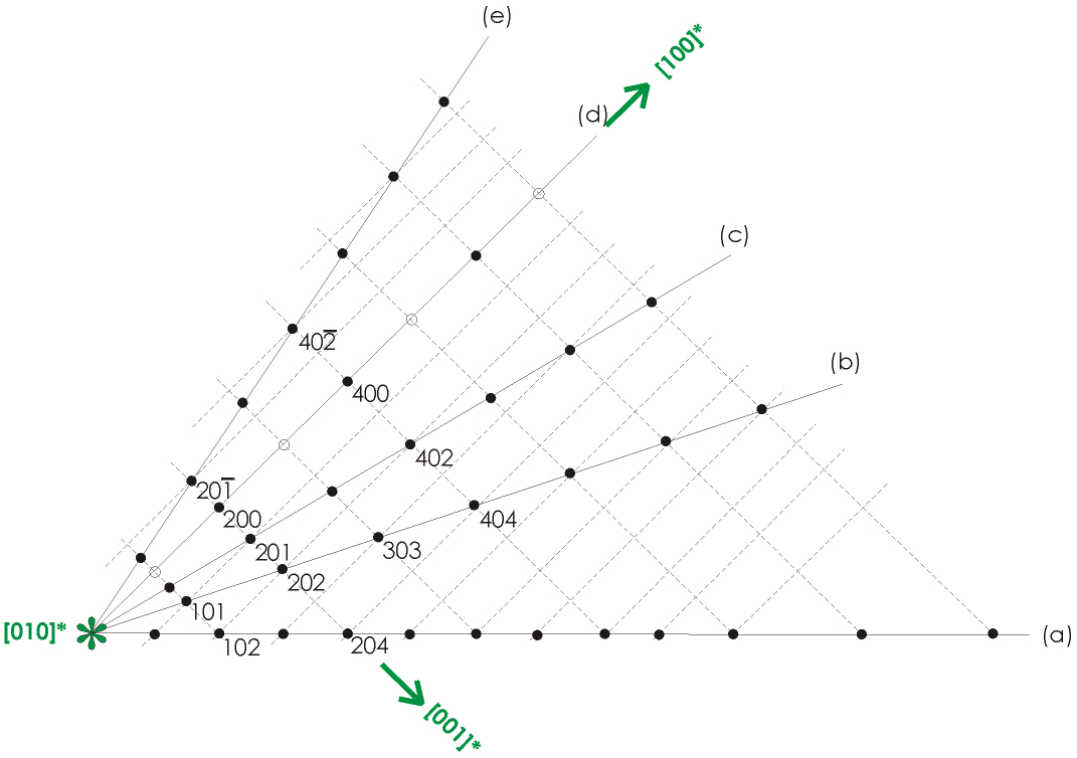

Figure 40: The reconstructed reciprocal plane for γ-$Ba_4Nb_2O_9$ normal to the [010] tilt-axis.

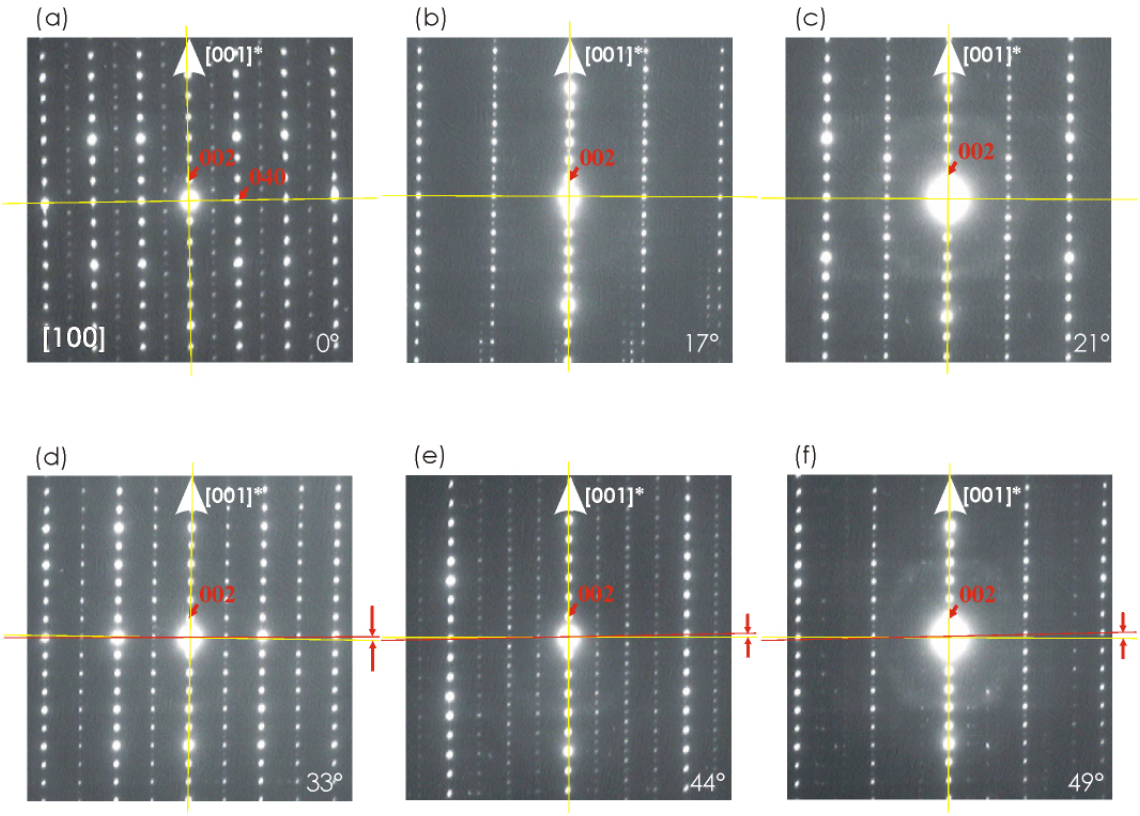

Figure 41: A set of selected-area electron-diffraction patterns from a single γ-$Ba_4Nb_2O_9$ crystal obtained in tilting experiment II. The yellow cross of two mutually perpendicular lines overlapping the ED patterns refers to two perpendicular directions in reciprocal space. The red lines link together the equivalent reciprocal reflections. The red arrows indicate the deviation from fundamentally perpendicular directions characteristic for an orthorhombic lattice.

5. THE BaO-RICH HEXAGONAL PEROVSKITE LIKE PHASES WITHIN THE $BaO–Nb_2O_5–WO_3$ TERNARY SYSTEM

The investigations, presented in this chapter are focused on the phase relation and phase stability of BaO-rich hexagonal phases within the $BaO–Nb_2O_5–WO_3$ ternary system. The first part of this chapter is dedicated to the phase formation and microstructural properties of the ceramic with corresponding compositions, while the second part is related to the crystal structure of high-temperature $Ba_6Nb_2WO_{14}$ polymorphs. At the end of this chapter microwave dielectric properties of the ceramics are discussed.

Index

5.1. Introduction

5.1.1. Hexagonal perovskite phases within the $BaO–WO_3–Nb_2O_5$ ternary system

The phase stability studies of $Ba_4Nb_2O_9$ revealed similarity in the X-ray powder diffraction spectra between high-temperature γ-phase and the ternary compound $Ba_6Nb_2WO_{14}$. However, $Ba_6Nb_2WO_{14}$ is an end-member of a solid-solution $Ba_6W_{3-x}Nb_xO_{15-x/2}$ ($1 \leq x \leq 2$), which lies on a virtual tie-line $Ba_4Nb_2O_9$–Ba_2WO_2. The comparable XRD pattern of $Ba_4Nb_2O_9$ and $Ba_6Nb_2WO_{14}$, and the fact that both compounds lie on a common virtual tie-line implies the similarities in their crystal structures, which have not yet been solved. Nevertheless, the existing structural data for the solid-solution series indicate that the compounds across the whole composition range might crystallize as a hexagonal perovskite [Kemmler-Sack, 1980]. Similar hexagonal-perovskite phases within the $BaO–WO_3–Nb_2O_5$ ternary system were observed on the tie-line $Ba_3W_2O_9$–$Ba_5Nb_4O_{15}$ [Kemmler-Sack *et al.* 1979, 1980 and 1981]. These include $Ba_9Nb_6WO_{27}$ [Kemmler-Sack, 1980 and Kemmler-Sack *et al.*, 1981], $Ba_4Nb_2WO_{12}$ [Kemmler-Sack, 1979 and Rother *et al.*, 1980], and $Ba_3Nb_{2-x}W_xO_{9-x/2}$ for ($1/3 \leq x \leq 2$) [Kemmler-Sack, 1980 and Kemmler-Sack *et al.*, 1980]. All these members have a unit-cell parameter *a* close to 5.8 Å and differ in the value of the *c* parameters, which is related to the number of close-packed BaO_3-layers stacked along the hexagonal *c*-axis. The *c*-parameter increases from the 9-layered $Ba_3Nb_{2-x}W_xO_{9-x/2}$ (20.99 Å) [Kemmler-Sack *et al.*, 1981], over 12-layered $Ba_4Nb_2WO_{12}$ (28.055 Å) [Rother *et al.*, 1980] to the 27-layered $Ba_9Nb_6WO_{27}$ (63.40 Å) [Kemmler-Sack, 1980]. Moreover, the structure of the $Ba_6W_{3-x}Nb_xO_{15-x/2}$ ($1 \leq x \leq 2$) solid-solution [Kemmler-Sack *et al.*, 1980] allegedly consist five BaO_3 layers layers stacked along the $[001]_H$-axis, resulting in a *c*-parameter close to 12.4 Å.

In addition, Kemmler-Sack *et al.* [1980] stated that the phase stability of $Ba_6W_{3-x}Nb_xO_{15-x/2}$ in the composition range of $1 \leq x \leq 2$ is problematic, but much less than for the niobium end-member, $Ba_6W_{3-x}Nb_xO_{15-x/2}$ ($x = 3$), which compositionally corresponds to $Ba_4Nb_2O_9$. Recently, Bezjak *et al.* [2008] reported that this compound is not stable under atmospheric conditions. Similar observations were reported by Vanderah *et al.* [2002] for binary compounds having more than 75 mol % of BaO. Furthermore, investigations of other compositions suggest that not only $Ba_6W_{3-x}Nb_xO_{15-x/2}$ ($1 \leq x \leq 2$), but also *27L*-$Ba_9Nb_6WO_{27}$, *12L*-$Ba_4Nb_2WO_{12}$ and *9L*-$Ba_3Nb_{2-x}W_xO_{9-x/2}$ ($x \geq 1$) phases are prone to the formation of secondary phases [Kemmler-Sack, 1979, 1980]. However, their appearance was reportedly hindered by adding approximately 1–5 wt % of $BaCO_3$ to the stoichiometric composition during the pre-sintering stage.

While several studies exist on the crystal structures of the compounds with nominal compositions of *27L*-$Ba_9Nb_6WO_{27}$, *12L*-$Ba_4Nb_2WO_{12}$ and *9L*-$Ba_3Nb_{2-x}W_xO_{9-x/2}$ for ($x \geq 2/3$), the crystal structure of the $Ba_6Nb_xW_{3-x}O_{15-x/2}$ ($1 \leq x \leq 2$) compounds has not yet been solved. However, the compounds across the whole composition range might crystallize as a 5-layered hexagonal perovskite with an *hhccc* stacking sequence in the *P-3m1* space group, where some Ba-atoms should occupy the octahedral sites of the structure [Kemmler-Sack, 1980]. On the other hand, it seems very unlikely that relatively large Ba-atoms would occupy the octahedral sites, while the nominal composition implies that the compounds in this compositional range may form 6-layered (6L) hexagonal structures. Therefore we decided to reinvestigate the crystal structure of *5L2*-$Ba_6Nb_xW_{3-x}O_{15-x/2}$ ($x = 2$) suggested by Kemmler-Sack [1980]. The study was in part motivated by the observation that the composition of the ceramic is based on complex oxides containing transition metals in oxidation states, which favors the formation of cationic non-stoichiometry in perovskite-like crystal structures, *i.e.* B-site cationic vacancies [Moussa *et al*., 2003, Mallinson *et al*., 2005 and Zhao *et al.*, 2007]. In particular compounds the B-site cations and vacancies on B-sublattice may be ordered distributed through the crystal structure, which essentially influence dielectric properties of the ceramic [Sreemoolanadhan *et al.*, 1995, Keith *et al.*, 2004, Vineis *et al.*, 1996, Wada *et al.*, 2005, Kim *et al.*, 2002, Jawahar *et al.*, 2003 and Liou *et al.*, 2006]. Therefore, the entitled materials are potentially interesting for applications in microwave communication systems.

5.2. Experiment

5.2.1. Sample preparation

Samples with nominal compositions of *5L2*-$Ba_6Nb_xW_{3-x}O_{15-x/2}$ ($x = 2$), *27L*-$Ba_9Nb_6WO_{27}$, *12L*-$Ba_4Nb_2WO_{12}$ and *9L*-$Ba_3Nb_{2/3}W_{4/3}O_{26/3}$ were synthesized by a conventional solid-state reaction. The starting materials used to prepare a sample of the required composition were high-purity powders of $BaCO_3$ (99.8%, Alfa Aesar), WO_3 and Nb_2O_5 (99.8%, Alfa Aesar). The corresponding mixtures were first ball-milled for 2 hours (200/min) with yttria-stabilized zirconia balls using ethanol as a mixing medium. After drying, the powders were initially calcined for 20 hours at 800 °C in air, then ground, and re-calcined at 900 and 1000 °C for 20 hours in order to ensure a complete reaction between the $BaCO_3$, WO_3 and Nb_2O_5. The powders were then uniaxially pressed into 10-mm-diameter pellets, under a force of 2 kN. The green bodies were sintered on a sacrificial pellet of the same composition in an alumina crucible at 1100, 1200, 1300, 1400 and 1500 °C in air. After annealing they were placed on Al-metal block to cool.

For the TEM observations the samples were cut into 3-mm discs, which were mechanically thinned and polished to a thickness of ~100 μm and dimpled (Dimple Grinder, Gatan Inc., Warrendale, PA) down to ~20 μm in the disk centre. The TEM specimens were produced by ion-milling (RES 010, Bal-Tec AG, Balzers, Liechtenstein) with 4-keV Ar^+ ions at an incidence angle of 10° until the central disk area became perforated. In addition, some $Ba_6Nb_2WO_{14}$ samples were analyzed by crushing the ceramics in *n*-butanol and depositing the suspension on a carbon-coated grid for the TEM. For the dielectric measurements in the microwave frequency range (6–10 GHz) the surfaces of the pellets were coated with InGa paste and measured using a 4284A Precision LCR meter (Agilent technologies Inc., Santa Clara, USA) at 20Hz to 1MHz.

5.2.2. Experimental methods and experimental conditions

The reactions were studied by powder X-ray diffraction (XRD) using a high-resolution X-ray diffractometer (PAnalytical X'Pert PRO MPD, Almelo, The Netherlands) and $Cu_{K\alpha1}$ radiation (1.5406 Å) operated at 45 kV and 40 mA.

The homogeneity and the microstructures of the sintered pellets were examined with a scanning electron microscope (SEM; Jeol JSM-5800, Jeol Ltd., Tokyo, Japan) operated at 20 kV and equipped with a back-scattered electron (BE) detector and an energy-dispersive X-ray spectrometer (EDS; Link ISIS 300, Oxford Instruments, Oxford, UK).

In order to verify the reported crystal structure of *5L2*-$Ba_6Nb_xW_{3-x}O_{15-x/2}$ (x = 2) and the presence of secondary phases at the grain boundaries a transmission electron microscope (TEM; JEM-2100, Jeol Ltd., Tokyo, Japan) operated at 200 kV was used.

The microwave dielectric properties were characterized with a network analyzer (HP 8719C) using the closed air-cavity-reflection method. The permittivity (ε) and quality-factor (Qxf_r) values were calculated at the resonance conditions ($TE_{01\delta}$ mode) from the S_{11}-parameter. To determine the temperature coefficient of resonant frequency (τ_f) the test cavities were inserted into a temperature-controlled chamber. The dielectric characteristics of the samples were analyzed in the temperature range 20–60 °C.

5.3. Results: Solid-state synthesis and phase formation of $Ba_4Nb_2O_9$

Five BaO-rich hexagonal phases within the BaO–WO_3–Nb_2O_5 ternary system (Fig. 1) were analyzed in terms of their phase stability. These included the two end-members of the solid-solution series $Ba_6Nb_xW_{3-x}O_{15-x/2}$ ($1 \leq x \leq 2$) and three ternary compounds with the nominal compositions *9L*-$Ba_9Nb_2W_4O_{26}$, *12L*-$Ba_4Nb_2WO_{12}$ and *27L*-$Ba_9Nb_6WO_{27}$. Both end-members of the solid-solution lie on the virtual tie-line $Ba_4Nb_2O_9$–Ba_2WO_5, while the three other phases lie on the virtual tie-line between $Ba_3W_2O_9$ and $Ba_5Nb_4O_{15}$ (Fig. 1).

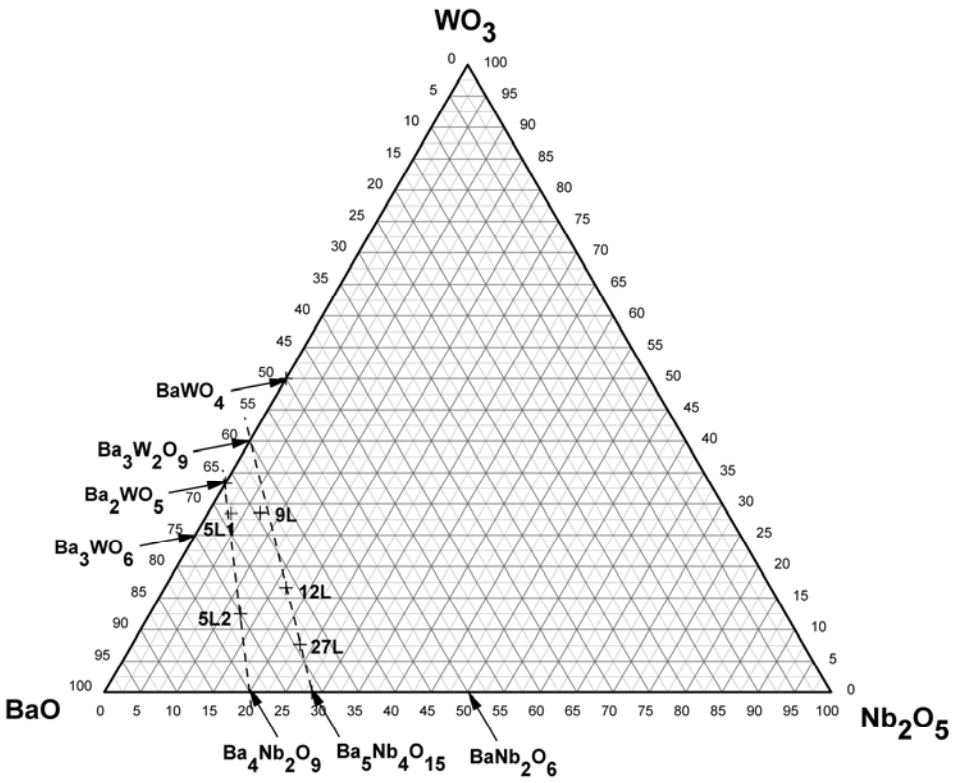

Figure 1: The compositions of the investigated BaO-rich hexagonal perovskite-type phases within the ternary system BaO–Nb_2O_5–WO_3; 9L = $Ba_9Nb_2W_4O_{26}$, 12L = $Ba_4Nb_2WO_{12}$, 27L = $Ba_9Nb_6WO_{27}$, 5L1 = $Ba_6Nb_xW_{3-x}O_{15-x/2}$ (x = 1) and 5L2 = $Ba_6Nb_xW_{3-x}O_{15-x/2}$ (x = 2).

5.3.1. The phase composition of the $Ba_6Nb_xW_{3-x}O_{15-x/2}$ (x = 1, x = 2) ceramics

The XRD patterns of the samples with the composition *5L2*-$Ba_6Nb_xW_{3-x}O_{15-x/2}$ (x = 2) recorded at room temperature after calcination at 800, 900 and 1000 °C for 10h are shown in Fig. 2.

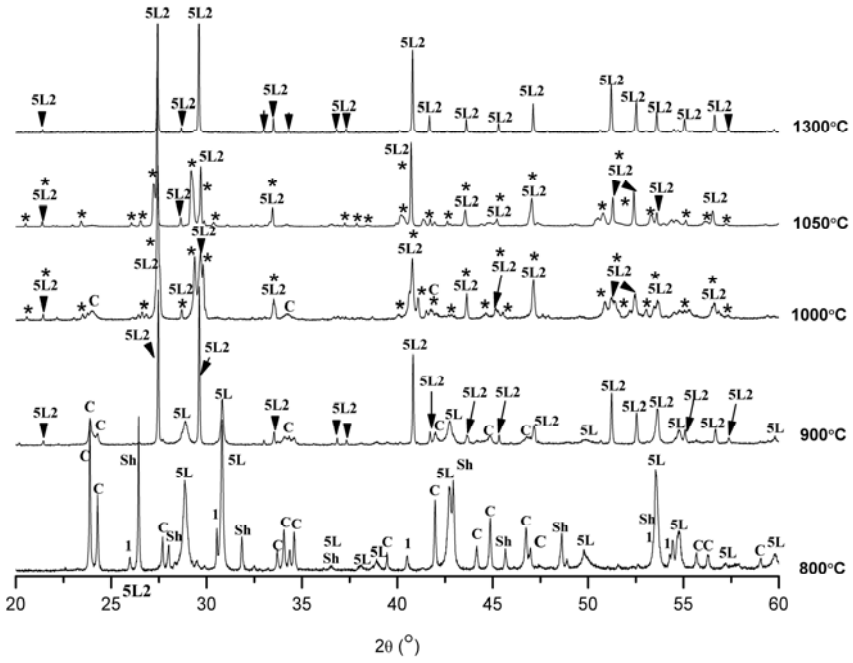

Figure 2: X-ray powder-diffraction patterns of *5L2*-$Ba_6Nb_xW_{3-x}O_{15-x/2}$ (x = 2) slowly cooled to room temperature after heating at 800, 900 and 1000 °C for 10 hours, and quenched from 1050 and 1300 °C; 5L2 = $Ba_6Nb_xW_{3-x}O_{15-x/2}$ (x = 2), 5L = $Ba_5Nb_4O_{15}$, C = $BaCO_3$, 1 = $Ba_3W_2O_9$, Sh = $BaWO_4$ and * = β-$Ba_4Nb_2O_9$.

The sample calcined at 800 °C was composed of $BaCO_3$, $BaWO_4$, $Ba_3W_2O_9$ and $Ba_5Nb_4O_{15}$. Additional peaks appeared in the XRD patterns when the calcination temperature was further increased to 900°C. The new peaks could be indexed to the hexagonal $Ba_6Ta_2WO_{14}$ (PDF # 35-0187) [Kemmler-Sack, 1980]. The formation of a new phase was accompanied by a gradual decrease in the amounts of $BaCO_3$ and $Ba_5Nb_4O_{15}$, whereas the two binary phases, $BaWO_4$ and $Ba_3W_2O_9$, completely disappeared.

Increasing the calcination temperature to 1000 °C resulted in the occurrence of diffraction peaks corresponding to the orthorhombic γ-$Ba_4Nb_2O_9$ (PDF # 35-1155) [Leshchenko *et al.*, 1979, 1985]. The $Ba_5Nb_4O_{15}$ completely vanished at 1000 °C, while the $BaCO_3$ finally disappeared after heating at 1050 °C for 100h (Fig. 2). The most intense diffraction peaks in the XRD spectra recorded at room temperature for the sample fired at 1050 °C could be

ascribed either to $Ba_6Ta_2WO_{14}$ [Kemmler-Sack, 1980] or γ-$Ba_4Nb_2O_9$ [Leshchenko *et al.*, 1979, 1985], which also accounts for all the low-intensity diffraction peaks.

By increasing the firing temperature the intensity of the diffraction peaks that closely resemble the γ-$Ba_4Nb_2O_9$ compound gradually decreased, whereas the intensity and the distribution of the peaks matching the $Ba_6Ta_2WO_{14}$ increased. Neither of these compounds, of course, was not present in our sample, which implies that we are dealing with two modifications of the *5L2*-$Ba_6Nb_2WO_{14}$ that closely resemble the structures of the γ-$Ba_4Nb_2O_9$ and $Ba_6Ta_2WO_{14}$ compounds. Above 1300 °C the composition of the samples fired and quenched to room temperature was single phase and corresponded to *5L2*-$Ba_6Nb_2WO_{14}$ (*i.e.* $Ba_6Nb_xW_{3-x}O_{15-x/2}$; x = 2). In order to prove the phase composition we investigated the samples using electron microscopy (Fig. 3). Our SEM/EDS results confirmed the single-phase composition of the *5L2*-$Ba_6Nb_2WO_{14}$ over the entire temperature range (Fig. 3). Due to the relatively low sintering temperature the microstructure of the sample sintered at 1050 °C was porous (Fig. 3a), while the sample sintered at 1300°C was relatively compact and exhibited equi-dimensional anhedral grains with a uniform size distribution of 1–3 μm (Fig. 3b). Moreover, the SEM/EDS analyses and the back-scattered electron investigation of the sample fired at 1300 °C for 10 hours indicated the single-phase composition of the ceramics, consistent with our XRD data.

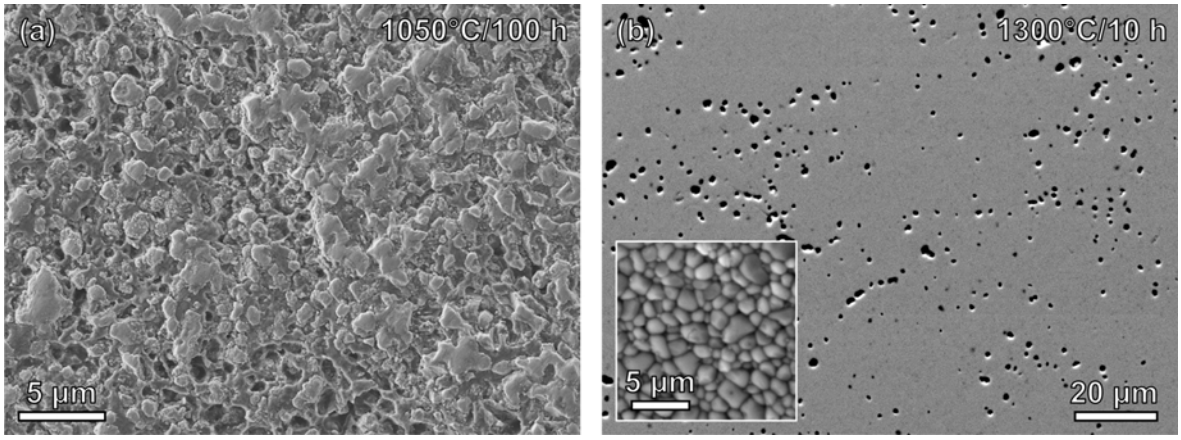

Figure 3: (a) SEM image of the polished, porous microstructure of the ceramic with a nominal composition *5L2*-$Ba_6Nb_xW_{3-x}O_{15-x/2}$ (x = 2) sintered at 1050 °C for 100 hours. **(b)** SEM/BE image of polished sample fired at 1300 °C for 10 hours. The inset shows uniform $Ba_6Nb_2WO_{14}$ grains within the pore. The EDS analyses of individual grains showed the single-phase composition of the sample.

Our results suggest the existence of at least two different modifications of *5L2*-$Ba_6Nb_xW_{3-x}O_{15-x/2}$ (x = 2), which are structurally related to the orthorhombic γ-$Ba_4Nb_2O_9$ [Leshchenko *et al.*, 1985] and hexagonal $Ba_6Ta_2WO_{14}$ [Kemmler-Sack *et al.*, 1980]. While the high-temperature modification of $Ba_6Nb_2WO_{14}$ appeared to be isostructural with $Ba_6Ta_2WO_{14}$, the intensity and the positions of the main diffraction peaks did not coincide entirely. In addition, a few

diffraction peaks of low intensity at 2θ > 40° could not be indexed to $Ba_6Ta_2WO_{14}$. The additional reflections implied that the crystal structures of the high-temperature *5L2*-$Ba_6Nb_2WO_{14}$ and $Ba_6Ta_2WO_{14}$ were closely related but not quite identical. Additionally, *5L2*-$Ba_6Nb_xW_{3-x}O_{15-x/2}$ (x = 2) was analyzed with heating and scanning-electron microscopy. The obtained sintering curve revealed that the ceramics start densify above 1100 °C (Fig. 4), which is also evident form Figure 3. The microstructural analyses of thermally etched samples annealed at 1200, 1300, 1400 and 1500 °C for 5h (Fig. 5 and Fig 6a) indicated significant increase of the grain size with increasing temperature. At very low sintering temperature, *i.e.*, 1200 °C, the grains are small and of different size not exceeding 3 μm in diameter. Moreover, the grain size drastically increased after the sample was annealed at 1500 °C for 5 hours. This ceramic consist of 100-μm grains (Fig. 6a).

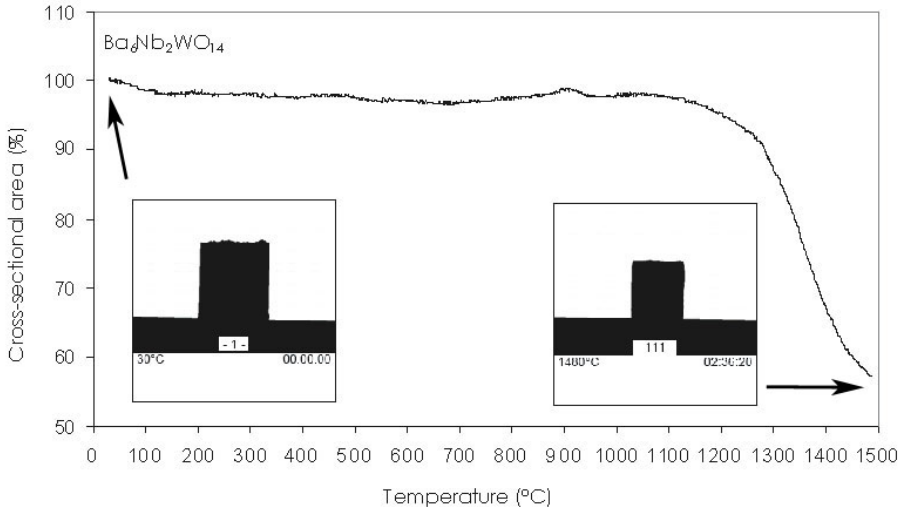

Figure 4: The sintering profile of *5L2*-$Ba_6Nb_2WO_{14}$ and the cross-sectional area of the pellet at room temperature and 1480 °C show no evidence of melting.

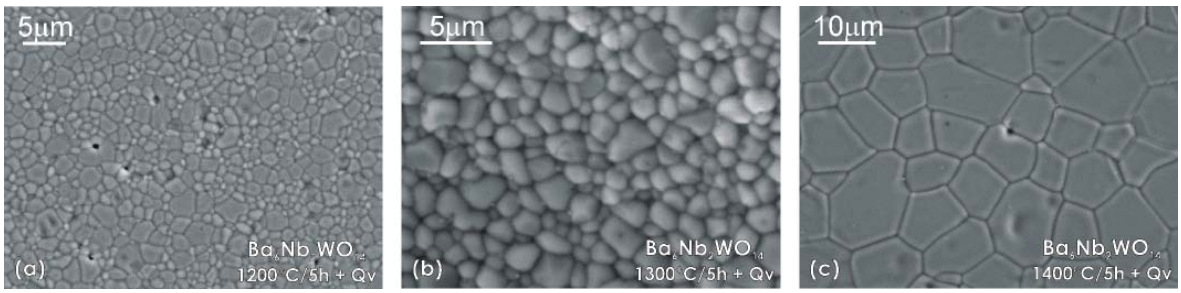

Figure 5: Secondary electron micrographs of *5L2*-$Ba_6Nb_2WO_{14}$ ceramic annealed at 1200, 1300 and 1400 °C for 5h and quenched to room temperature.

Additionally, the effect of annealing time was studied in terms of the grain size and the porosity of the ceramics. Therefore the sample with the sample was annealed at 1500 °C for 5 and 15 hours (Fig. 6a-b). The microstructure of the sample fired for 5 hours showed 100-µm large grains with intragranular porosity (Fig. 6a). After 15 hours of annealing the grains became significantly larger (Fig. 6b) and the surface of sintered pellets was covered with fine particles. Semi-quantitative EDS analyses and X-ray diffractometry of the sample surface (Fig. 6c) revealed that the composition of these particles corresponded to $BaCO_3$. The appearance of this $BaCO_3$ on the surface of *5L2*-$Ba_6Nb_xW_{3-x}O_{15-x/2}$ (x = 2) grains appears to be related to the WO_3 loss from the system at the firing temperature. This results in formation of W-deficient secondary phase, which decomposes to $Ba_4Nb_2O_9$, while the excess of BaO further reacts with CO_2 from the ambient air into $BaCO_3$. The TEM analyses excluded the possible existence of any intergranular BaO-rich phase that might be present due to an incomplete reaction of the BaO with Nb_2O_5 and WO_3 after the decomposition (calcination) of the $BaCO_3$. The *5L2*-$Ba_6Nb_2WO_{14}$ grain boundaries (Fig. 6d) and triple points were found to be free from any secondary phases.

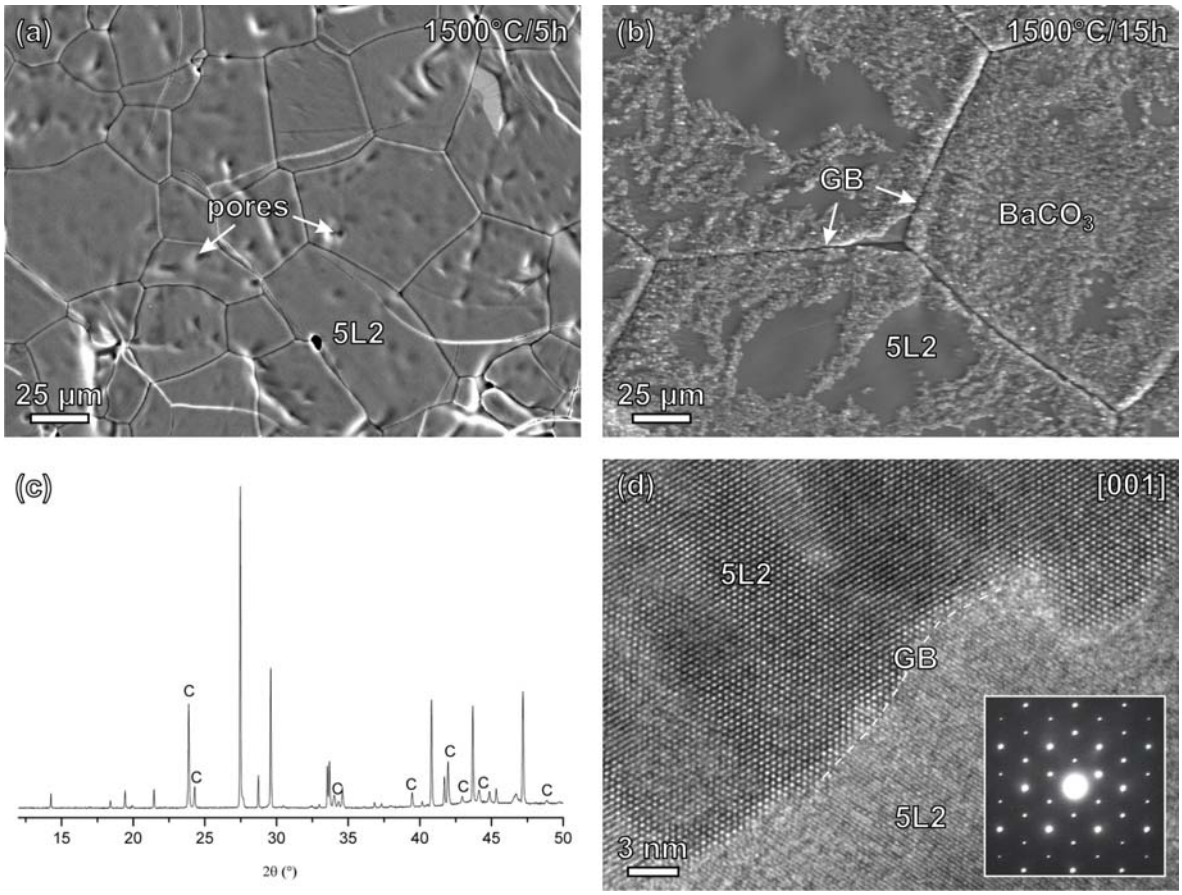

Figure 6: (a) Secondary-electron (SE) micrograph of the surface of the pellet with the composition *5L2*-$Ba_6W_{3-x}Nb_xO_{15-x/2}$ (x = 2) fired at 1500 °C for 5 hours **(b)** SEM image of the surface of the sample fired at 1500 °C for 15 hours. The surface of the sample is covered with $BaCO_3$ particles. **(c)** XRD patterns recorded on the surface of the pellet sintered at 1500 °C for 15 hours at room temperature indicates the presence of $BaCO_3$ (c = $BaCO_3$). The unmarked XRD peaks correspond to *5L2*-$Ba_6W_{3-x}Nb_xO_{15-x/2}$ (x = 2). **(d)** A high-resolution TEM image of an arbitrary grain boundary

between two *5L2*-$Ba_6W_{3-x}Nb_xO_{15-x/2}$ (x = 2) grains illustrates that the interfaces are free of any secondary phases or amorphous layers. Inset shows the diffraction patterns corresponding to the upper-left grain oriented along $[001]_H$.

Further attention was focused on the phase stability of a *5L1*-$Ba_6Nb_xW_{3-x}O_{15-x/2}$ (x = 1) lying on the virtual tie-line Ba_2WO_5–$Ba_4Nb_2O_9$ (Fig. 1). XRD analyses of the powder mixture with a nominal composition $Ba_6Nb_xW_{3-x}O_{15-x/2}$ (x = 1) fired at different temperatures between 900 and 1400 °C (Fig. 7) for 10 hours indicated that the formation of *5L1*-$Ba_6NbW_2O_{14.5}$ (*i.e.*, $Ba_6Nb_xW_{3-x}O_{15-x/2}$ for x = 1) is initiated by the appearance the α-$Ba_4Nb_2O_9$ and Ba_2WO_5 reflections. A further increase of the sintering temperature to 1000 °C was accompanied by a decrease in the amount of the Ba_2WO_5 and α-$Ba_4Nb_2O_9$. Above 1100 °C additional peaks appear in the XRD pattern of the *5L1*-$Ba_6Nb_xW_{3-x}O_{15-x/2}$ (x = 1) sample. These peaks could be assigned to $Ba_6Ta_2WO_{14}$, *i.e.*, *5L2*- $Ba_6Nb_xW_{3-x}O_{15-x/2}$ (x = 2). By increasing the firing temperature to 1200 °C the XRD peaks of the secondary phases gradually decrease and almost completely disappeared at 1300 °C. Because the main XRD peaks of the *5L1*-$Ba_6Nb_xW_{3-x}O_{15-x/2}$ (x = 1) samples could be ascribed to $Ba_6Ta_2WO_{14}$ (*i.e.*, *5L2*-$Ba_6Nb_2WO_{14}$) this indicated the existence of a solid-solution, which extends from x = 1 to x = 2 along the tie-line Ba_2WO_5–$Ba_4Nb_2O_9$ as previously reported by Kemmler *et.al.*, [1980]. These results indicate that *5L1*-$Ba_6Nb_xW_{3-x}O_{15-x/2}$ (x = 1) always forms over the binary α-$Ba_4Nb_2O_9$, in contrast to *5L2*-$Ba_6Nb_xW_{3-x}O_{15-x/2}$ (x = 2), which formed through a reaction between binary $Ba_5Nb_4O_{15}$ and other barium-tungsten oxides.

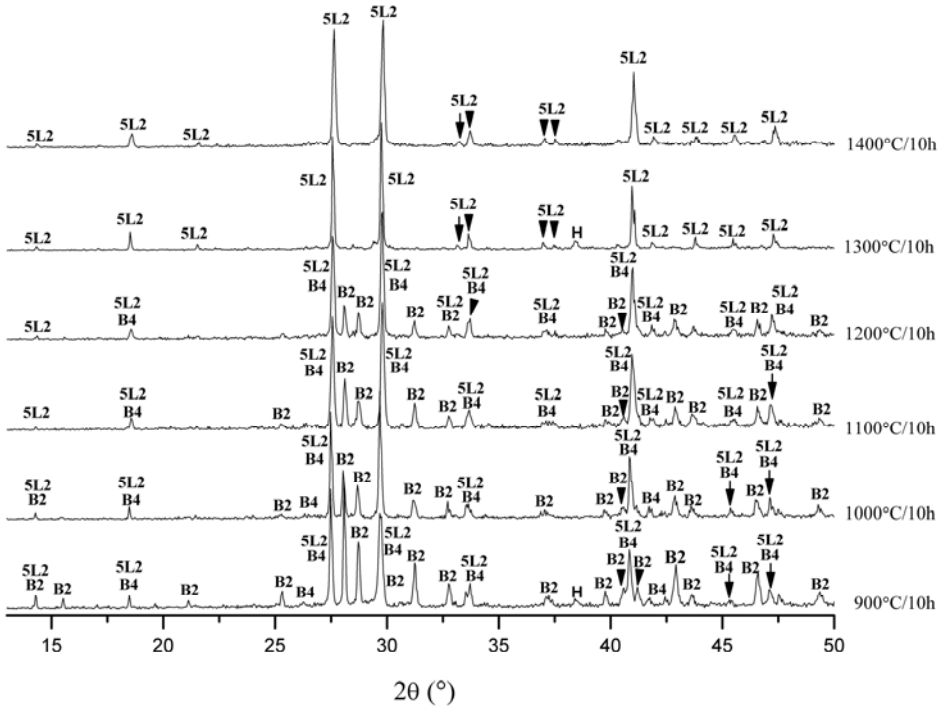

Figure 7: X-ray powder-diffraction patterns of *5L1*-$Ba_6Nb_xW_{3-x}O_{15-x/2}$ (x = 1) slowly cooled to room temperature after heating at 900 and 1000 °C for 10 hours, and quenched from 1100, 1200, 1300 and 1400 °C. (5L2 = $Ba_6Ta_2WO_{14}$, B2 = Ba_2WO_5 and B4 = a-$Ba_4Nb_2O_9$).

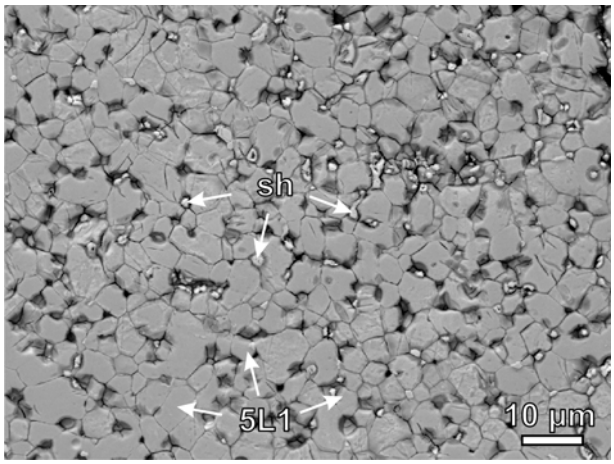

Figure 8: Back-scattered electron micrograph of *5L1*-$Ba_6W_{3-x}Nb_xO_{15-x/2}$ (x = 1) fired at 1400 °C for 10 hours. Arrows indicate the presence of $BaWO_4$ (Sh) at the grain boundaries.

While the XRD analyses showed no evidence for the presence of any secondary phases in the *5L1*-$Ba_6Nb_xW_{3-x}O_{15-x/2}$ (x = 1) ceramics sintered at 1400 °C in air, semi-quantitative EDS analyses revealed the existence of $BaWO_4$ at the grain boundaries (Fig. 8). The $BaWO_4$ particles were homogeneously distributed throughout the sample; they were exclusively intergranular and never observed as inclusions in the *5L1*-$Ba_6Nb_xW_{3-x}O_{15-x/2}$ (x = 1) grains.

5.3.2. The phase composition of the 9L-$Ba_9Nb_2W_4O_{26}$ *ceramics*

In general, the formation of $Ba_9Nb_2W_4O_{26}$ (Fig. 9) began with the appearance of $Ba_3W_2O_9$ at 800°C and continued with the formation of the $Ba_5Nb_4O_{15}$ and *12L*-$Ba_4Nb_2WO_{12}$ at 900 °C. A gradual increase in the intensity of the *12L*-$Ba_4Nb_2WO_{12}$ reflections occurred simultaneously with a decrease of $Ba_5Nb_4O_{15}$ and $Ba_3W_2O_9$ peaks. With a further increase of the calcination temperature to 1000 °C, the reaction continued with the formation of *9L*-$Ba_9Nb_2W_4O_{26}$. Moreover, the XRD pattern of the sample heated at 1100 °C revealed the presence of $BaCO_3$ and $BaWO_4$. The single-phase composition was not obtained even after the sample was annealed at 1200 °C for 5 hours and slowly cooled or quenched to room temperature. It always contained an admixture of $BaWO_4$ and $Ba_5Nb_4O_{15}$. According to the phase diagram (Fig. 1), an excess of the BaO-phase should be present in the sample. Since this was not observed in the XRD spectra it might have been present in the amorphous form. Normally, BaO would immediately react to form $BaCO_3$ when in contact with the ambient air and then decompose to BaO and CO_2 above 850 °C. Consequently, it could not be observed in the

sample quenched to room temperature from 1200 °C. However, the main diffraction peaks in the XRD pattern of the sample annealed at 1200 °C can be indexed by a hexagonal cell with a_H = 5.848 Å and c_H = 20.99 Å (ICSD #15506) [Kemmler-Sack, 1981].

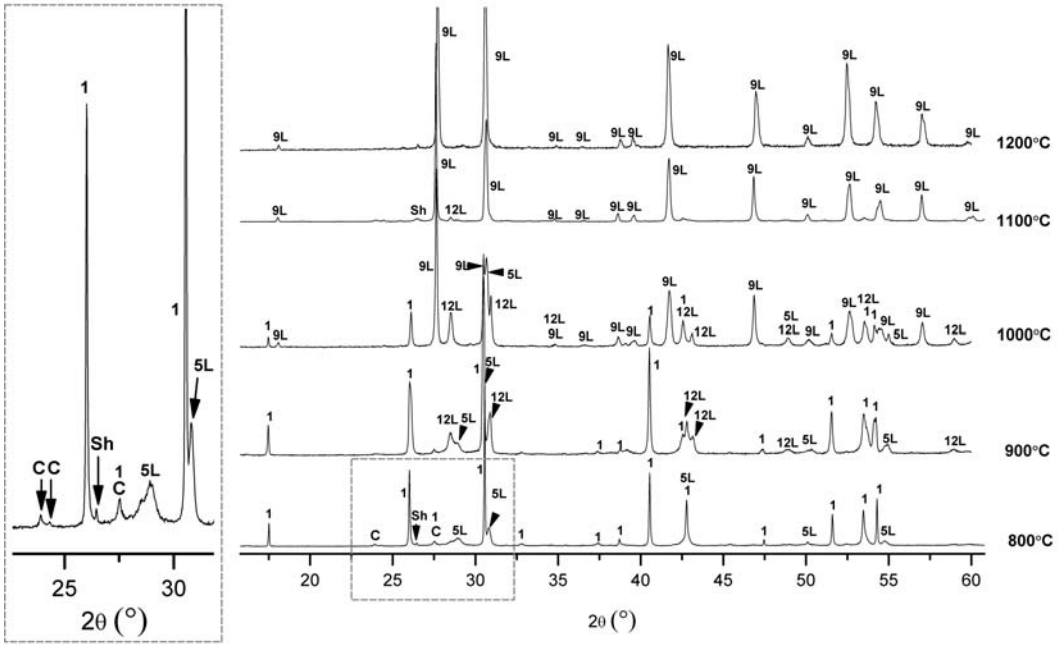

Figure 9: X-ray powder diffraction patterns of 9*L*-$Ba_9Nb_2W_4O_{26}$ slowly cooled to room temperature after heating at 800, 900, 1000, 1100 °C for 20 hours and from 1200 °C after heating for 5 hours. (5L = $Ba_5Nb_4O_{15}$, 9L = $Ba_9Nb_2W_4O_{26}$, 12L = $Ba_4Nb_2WO_{12}$, C = $BaCO_3$, 1 = $Ba_3W_2O_9$ and Sh = $BaWO_4$).

The microstructures of the samples with starting composition of 9*L*-$Ba_9Nb_2W_4O_{26}$, sintered at different temperatures, are shown in Figure 10. The microstructures are porous up to 1200 °C (Fig. 10a). The lowest porosity was observed for the sample fired at 1300 °C for 5 hours and quenched to room temperature (Fig. 10b). With a further increase of the temperature; the sample porosity increased, which can be attributed to the grain size and shape; the grains started an exaggerated and anisotropic growth. However, the ceramic sintered at 1450 °C consisted of 100-µm plate-like grains (Fig. 10c). The 9*L*-$Ba_9Nb_2W_4O_{26}$ grains exhibited some closed porosity and intragranular fractures. The plate-like grains were intergrown, which causes strong tensions on cooling. Therefore the 9*L*-$Ba_9Nb_2W_4O_{26}$ ceramics sintered at ~1400°C and quenched to room temperature contained many cracks (Fig. 10c).

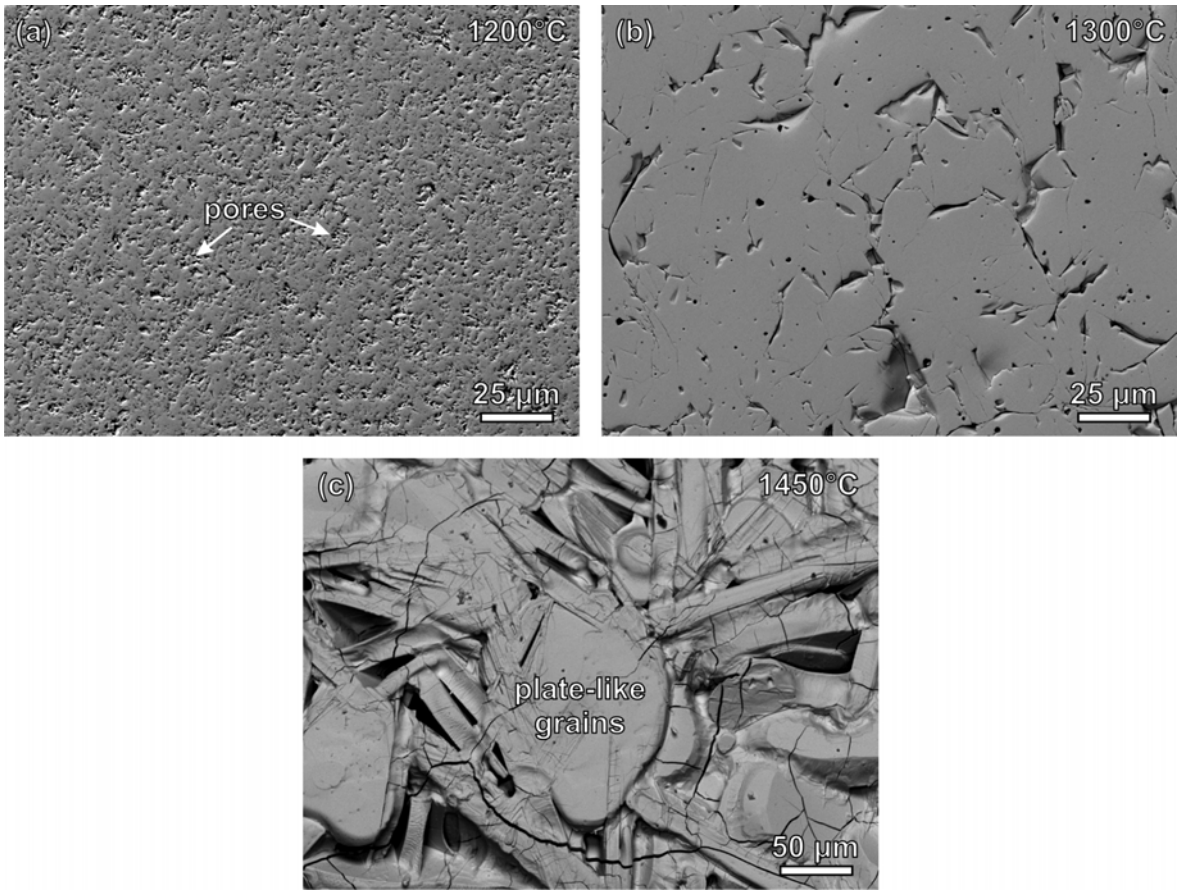

Figure 10: Secondary electron images of microstructures of non-etched samples with the composition $Ba_9Nb_2W_4O_{26}$ sintered at different temperatures. The grains grow exaggeratedly and anisotropically close to 1450 °C. In addition the $Ba_9Nb_2W_4O_{26}$ grains with obvious intragranular porosity are overgrown and contain several post-cooling fractures.

We further investigated the stability of 9*L*-$Ba_9Nb_2W_4O_{26}$ by annealing the samples at 1200 and 1300°C for 5 hours in air. The corresponding XRD spectra recorded from the pellets' surfaces (SP) are shown in Fig. 11. After annealing the sample at 1200 °C for 5 hours and quenching to room temperature low-intensity peaks appeared in the X-ray diffraction spectra. The new peaks could be ascribed to $BaWO_4$ and $Ba_5Nb_4O_{15}$ and indicate the decomposition of the sample at the contact with the ambient air. The amount of both secondary phases on the surface of the pellet increased with increasing the sintering temperature to 1300 °C. The secondary phase formation as results of sample reactivity with an ambient air was additionally observed with back-scatter electron microscopy (Fig. 12).

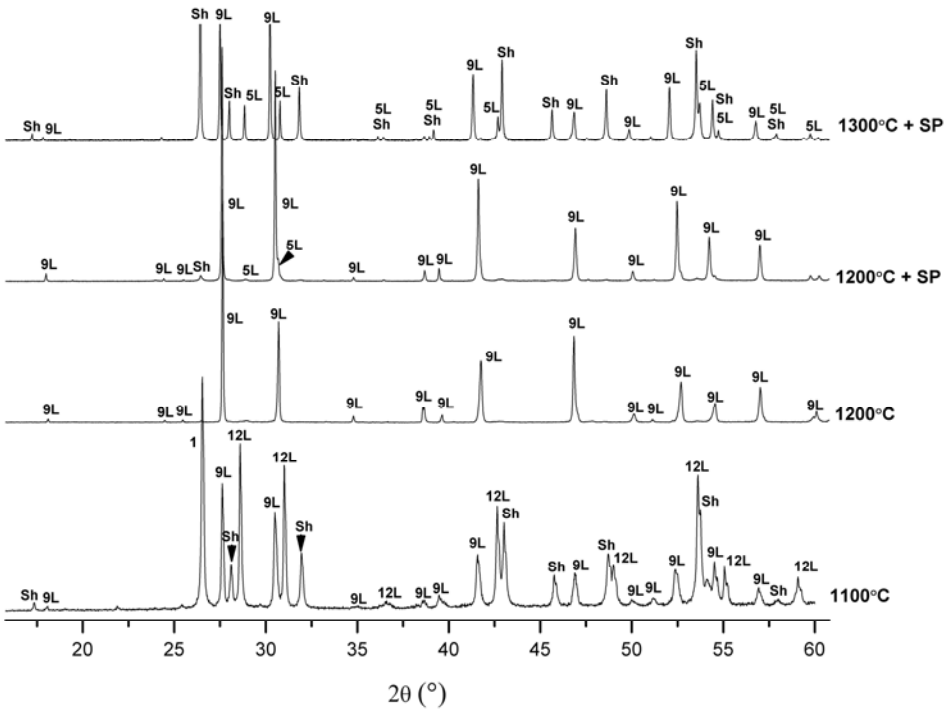

Figure 11: X-ray powder-diffraction pattern of the surface of the pellets quenched to room temperature after annealing for 5 hours at 1200 and 1300 °C and X-ray powder-diffraction patterns of the same samples; 5L = $Ba_5Nb_4O_{15}$ phase, 9L = $Ba_9Nb_2W_4O_{26}$, 12L = $Ba_4Nb_2WO_{12}$, C = $BaCO_3$, Sh = $BaWO_4$; SP refers to the surface of the pellet.

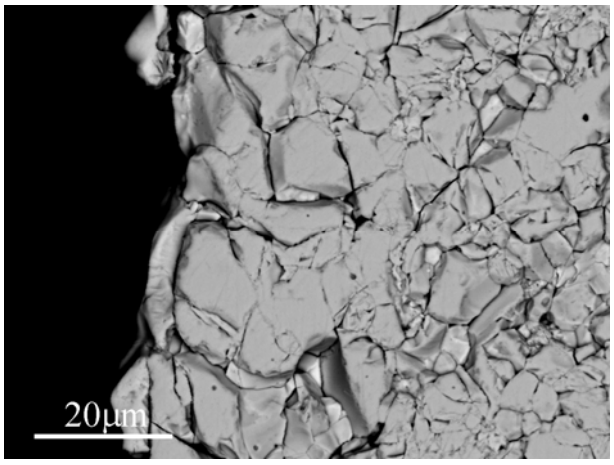

1300°C

Figure 12: The Back-scattered electron image of the 9L-$Ba_9Nb_2W_4O_{26}$ fired at 1300 °C shows non-uniformly distributed secondary phase throughout the sample. This is concentrated mainly on the surface of the pellet due to sample sensitivity to ambient conditions.

5.3.3. The phase composition of the 12L-$Ba_4Nb_2WO_{12}$ ceramics

According to our XRD data (Fig. 13) the *12L*-$Ba_4Nb_2WO_{12}$ compound started to form near 900°C. The solid-state reaction began over the binary compounds $Ba_3W_2O_9$, $BaWO_4$ and $Ba_5Nb_4O_{15}$ then proceeded with the formation of *9L*-$Ba_9Nb_2W_4O_{26}$, and completed with *12L*-$Ba_4Nb_2WO_{12}$ close to 1100 °C. The XRD study of the polycrystalline sample annealed at 1100 °C for 10 hours suggested a multiphase composition of the sample. The secondary phases in the sample corresponded to $BaWO_4$. Increasing the firing temperature to 1200 °C resulted in the decomposition of *12L*-$Ba_4Nb_2WO_{12}$ accompanied by the formation of hexagonal perovskite-type phases *9L*-$Ba_9Nb_2W_4O_{26}$ and *27L*-$Ba_9Nb_6WO_{27}$. The amount of the secondary phases further increased at higher temperatures.

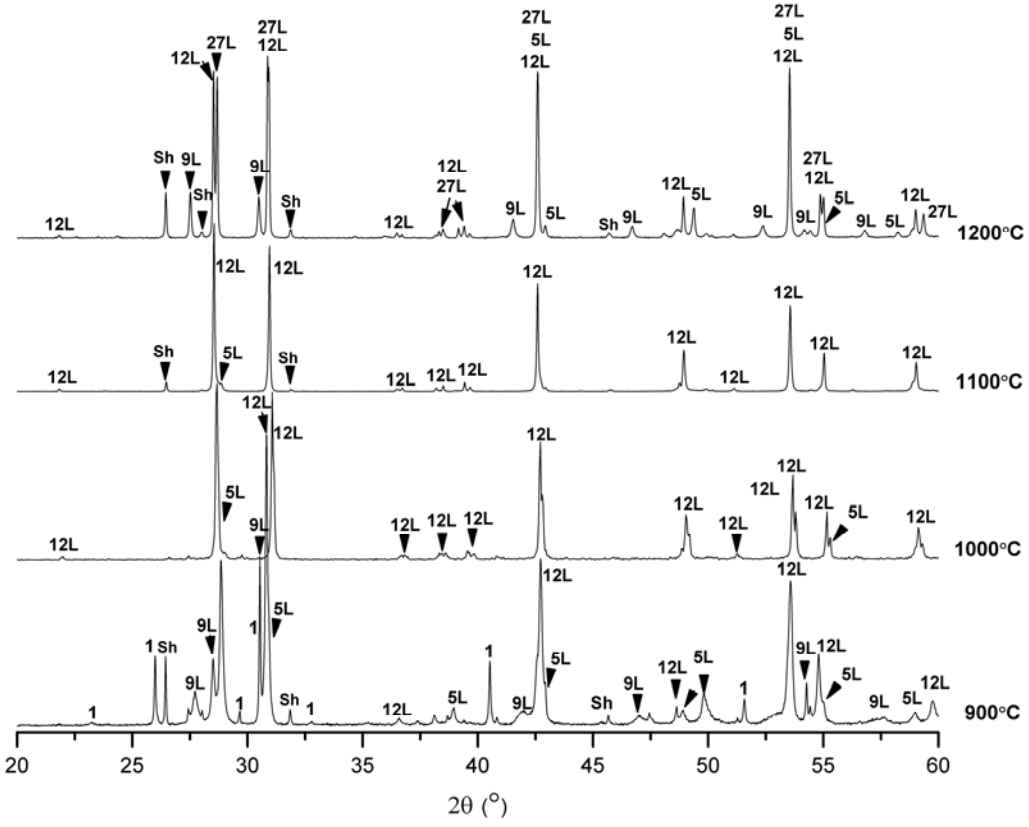

Figure 13: X-ray powder-diffraction data for *12L*-$Ba_4Nb_2WO_{12}$ over the temperature range 900 < T < 1200 °C; 5L = $Ba_5Nb_4O_{15}$, 9L = $Ba_9Nb_2W_4O_{26}$, 12L = $Ba_4Nb_2WO_{12}$, 27L = $Ba_9Nb_6WO_{27}$, C = $BaCO_3$, 1 = $Ba_3W_2O_9$ and Sh = $BaWO_4$.

5.3.4. The phase composition of the 27L-$Ba_9Nb_6WO_{27}$ ceramics

The formation of *27L*-$Ba_9Nb_6WO_{27}$ via solid-state reactions started by the formation of binary $BaWO_4$, Ba_2WO_5, $BaNb_2O_6$ and $Ba_5Nb_4O_{15}$ compounds below 800 °C. Furthermore, the XRD pattern of the sample fired at 800°C (Fig. 14) shows the existence of $Ba_5Nb_4O_{15}$ together with minor amounts of $BaWO_4$ and $Ba_3W_2O_9$. The first ternary oxides evident from the recorded XRD spectra occurred on calcination at 900 °C (Fig. 14). Their reflections could be assigned to *12L*-$Ba_4Nb_2WO_{12}$ and *27L*-$Ba_9Nb_6WO_{27}$. Since the XRD peaks of *12L*-$Ba_4Nb_2WO_{12}$ nearly overlap with those of *27L*-$Ba_9Nb_6WO_{27}$ it was difficult to distinguish the two individual components from the XRD spectra at an early stage of their formation. A further increase of the temperature led to a continuous increase in the intensity of the $Ba_9Nb_6WO_{27}$ peaks, whereas the intensities of the *12L*-$Ba_4Nb_2WO_{12}$ reflections gradually decreased and finally disappeared at 1100 °C (Fig. 15). Quenching the sample after firing at 1100 and 1200 °C for 10 hours did not result in a single-phase composition. There was always an admixture of $BaWO_4$ and $Ba_5Nb_4O_{15}$. Semi-quantitative EDS analyses of the different phases, observed in the BE images (Fig. 16), confirmed the results of the phase composition obtained by the X-ray powder diffraction. The microstructure of the sample fired at 1300 °C contained three different phases – plate-like grains of *27L*-$Ba_9Nb_6WO_{27}$, which were surrounded by the $Ba_5Nb_4O_{15}$ phase, and the $BaWO_4$ grains occurred in 1– 2 µm agglomerates.

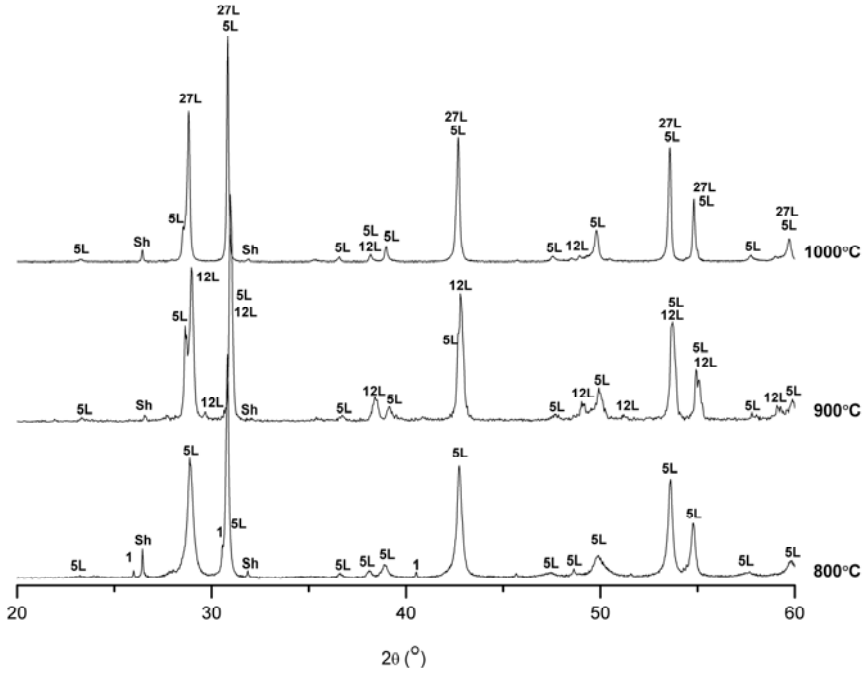

Figure 14: X-ray diffraction patterns of *27L*-$Ba_9Nb_6WO_{27}$ samples recorded at room temperature after calcination in the temperature range between 800 and 1000 °C for 20h; 5L = $Ba_5Nb_4O_{15}$, 12L = $Ba_4Nb_2WO_{12}$, 27L = $Ba_9Nb_6WO_{27}$, 1 = $Ba_3W_2O_9$ and Sh = $BaWO_4$.

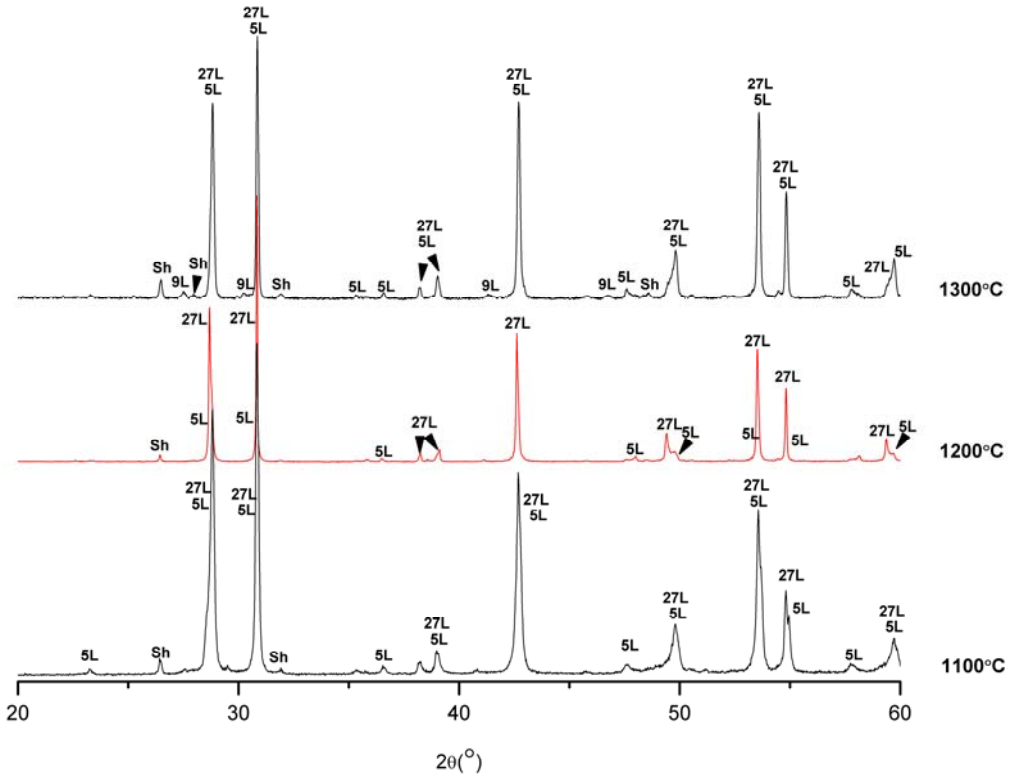

Figure 15: X-ray powde-diffraction patterns recorded at room temperature for *27L*-$Ba_9Nb_6WO_{27}$ samples after they were fired at 1100 °C for 20 hours and slowly cooled too room temperature; and after they were fired at 1200 and 1300 °C for 10 hours and quenched too room temperature; 5L = $Ba_5Nb_4O_{15}$, 12L = $Ba_4Nb_2WO_{12}$, 27L = $Ba_9Nb_6WO_{27}$, 1 = $Ba_3W_2O_9$ and Sh = $BaWO_4$.

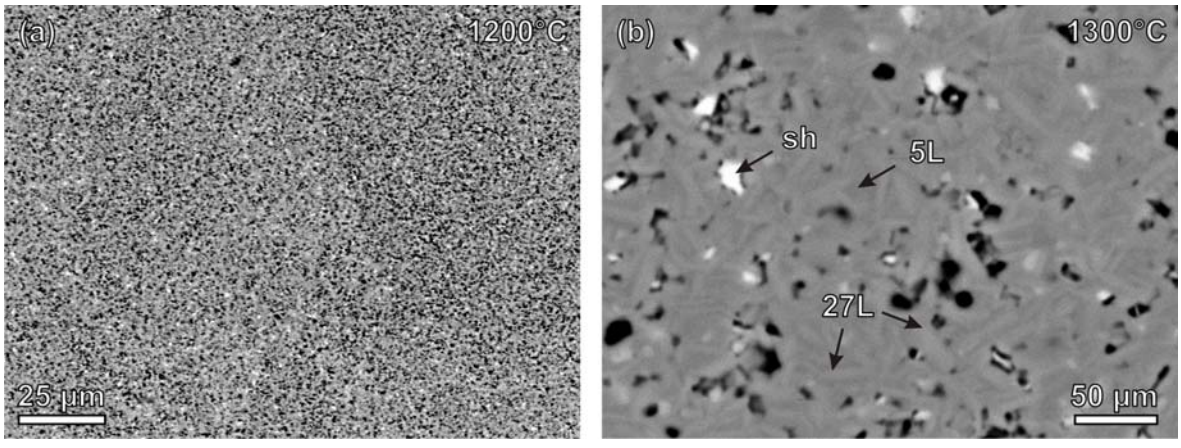

Figure 16: Back-scattered electron images of polished and non-etched microstructures of *27L*-$Ba_9Nb_6WO_{27}$ sample fired at 1200 and 1300 °C for 10h and then quenched to room temperature. Both images show that secondary phases are uniformly distributed throughout the sample, while their amount increases with higher temperature; 27L = $Ba_9Nb_6WO_{27}$, 5L = $Ba_5Nb_4O_{15}$ and Sh = $BaWO_4$.

5.4. Results: Dielectric properties of hexagonal perovskite based ceramic with the composition in BaO-rich part of $BaO–Nb_2O_5–WO_3$ ternary system

5.4.1. $Ba_6Nb_xW_{3-x}O_{15-x/2}$ (x = 1, x = 2)

The dielectric measurements on both end-members of a solid-solution $Ba_6Nb_xW_{3-x}O_{15-x/2}$ ($1 \geq x \geq 2$) indicated that the dielectric properties of the ceramics from this system can be considerably improved by decreasing the W content (Table 1). Thus, the ceramics with a composition corresponding to *5L1*-$Ba_6Nb_xW_{3-x}O_{15-x/2}$ (x = 1) exhibited a dielectric permittivity of 18, a negative temperature coefficient of resonant frequency τ_{fr} = -32 ppm/°C and a very low quality factor, Qxf_r ~ 2900 GHz (Table 1). The microwave dielectric properties for *5L2*-$Ba_6Nb_xW_{3-x}O_{15-x/2}$ (x = 2) were measured on ceramics quenched to room temperature after heating at 1050, 1300 and 1500 °C (Table 1). The ceramic being sintered at 1050 °C exhibited a higher dielectric constant, a higher temperature coefficient of resonant frequency and a lower quality factor with respect to the ceramic sintered above 1300 °C. A possible explanation for such a behavior is the change in the crystal structure related to the phase transition observed between 1050 and 1300 °C (Fig. 2) and in the bad sinterability of the ceramic sintered at 1050 °C (Fig. 3).

Microwave dielectric properties were also measured for the ceramics sintered at 1500 °C for 10 hours to study the effect of sintering temperature on the dielectric performance. The ceramic fired at 1300 °C exhibited a higher Qxf_r and a lower τ_{fr} with respect to the ceramic sintered at 1500 °C (Table 1). This might also be partly attributed to the microstructure of the ceramic, in particular to the grain size, which changed from 2 to 200 μm in the temperature range between 1300 and 1500 °C (Fig. 3b and Fig. 4b). These results indicated that the hexagonal, perovskite-based ceramics sintered at a lower temperature, *i.e.,* 1300 °C, exhibited better dielectric properties than the ceramic sintered at 1500 °C (Table 1).

5.4.2. 9L-$Ba_9Nb_2W_4O_{26}$

The dielectric measurements for *9L*-$Ba_9Nb_2W_4O_{26}$ were performed on ceramics fired in the temperature range 1250–1350 °C, since a single-phase composition and increasing densification characterized the samples sintered above 1200 °C. The results indicated that these ceramics combine a dielectric permittivity in the range of 21–24 with a negative τ_{fr}, varying between -24 and -29 ppm/°C, and with a Qxf_r up to 8 874 GHz (Table 1). Considering the microstructural analyses, the densification of *9L*-$Ba_9Nb_2W_4O_{26}$ ceramics fired above 1300 °C decreased, which might be attributed to inequi-dimensional grains of plate-like shape, the

exaggerated grain growth and cracks (Fig. 10c). However, the observed morphology of the sample further enhanced the dielectric losses of the *9L*-$Ba_9Nb_2W_4O_{26}$ ceramic.

5.4.3. 12L-$Ba_4Nb_2WO_{12}$

The smallest amount of the secondary phases was observed in the samples sintered at 1100 °C for 10 hours (Fig. 13). Therefore, these ceramics were chosen for the microwave dielectric analyses (Table 1). The most interesting feature of these results is the near-zero temperature coefficient of resonant frequency (τ_{fr} = - 5 ppm/°C). The dielectric losses (Qxf_r) were close to 22 000 GHz and the permittivity around 20.

5.4.4. 27L-$Ba_9Nb_6WO_{27}$

The lowest amount of secondary phases in the *27L*-$Ba_9Nb_6WO_{27}$ ceramic (Fig. 15) was observed in the samples sintered at 1200 °C. Consequently this ceramic was chosen for microwave dielectric measurements (Table 1). In spite of a relatively high porosity, the ceramic with the composition *27L*-$Ba_9Nb_6WO_{27}$ exhibited the most promising dielectric properties (ε' = 23.71, Qxf_r = 23 241 GHz, τ_{fr} = -7 ppm/°C) from among all the BaO-rich hexagonal phases in the BaO–Nb_2O_5–WO_3 ternary system (Table 1).

Table 1: The dielectric properties measured in the microwave frequency region for ceramics with the compositions 5L1- and *5L2*-$Ba_6Nb_xW_{3-x}O_{15-x/2}$ (x = 1, x = 2), *9L*-$Ba_9Nb_2W_4O_{26}$, *12L*-$Ba_4Nb_2WO_{12}$ and *27L*-$Ba_9Nb_6WO_{27}$; Qv = a quenched sample, Slc = a slowly cooled sample, LT = a low-temperature modification and HT = a high-temperature modification

Compound	f_r	Qxf_r (Ghz)	ε'	τ_{fr} (ppm/°C)	Sintering temperature (°C)
5L1-$Ba_6Nb_xW_{3-x}O_{15-x/2}$ (x = 1)	9,726	2 893	18.33	-32	1300/10h
5L2-$Ba_6Nb_xW_{3-x}O_{15-x/2}$ (x = 2)	7.788	16 608	23.26	-30	**LT:** 1050/100h+Qv
5L2-$Ba_6Nb_xW_{3-x}O_{15-x/2}$ (x = 2)	8.882	24 514	15.54	-18	**HT:** 1300/10h+Qv
5L2-$Ba_6Nb_xW_{3-x}O_{15-x/2}$ (x = 2	7.566	18 262	20.09	-25	**HT:** 1500/10h+Qv
9L-$Ba_9Nb_2W_4O_{26}$	8.022	8 874	24.22	-24	1250/10h+Slc
9L-$Ba_9Nb_2W_4O_{26}$	8.359	8 359	22.23	-24	1300/10h+Slc
9L-$Ba_9Nb_2W_4O_{26}$	8.307	6 010	21.49	-29	1350/10h+Slc
12L-$Ba_4Nb_2WO_{12}$	7.494	21 949	20.64	-5	1100/10h
27L-$Ba_9Nb_6WO_{27}$	7.450	23 241	23.71	-7	1200/10h

The results indicated that BaO-rich hexagonal phases within the $BaO–WO_3–Nb_2O_5$ ternary system possess encouraging microwave dielectric properties. In particular, the τ_f values were comparable with those of many shifted perovskites, such as $(Ba_{5-x}Sr_x)Nb_4O_{15}$ (-9 to +85 ppm/°C), [Liou *et al.*, 2006, Sreemoolanadhan *et al.*, 1995] $Ba_8CoNb_6O_{24}$ (16 ppm/°C) [Mallinson *et al.*, 2005] and $BaTi_{1/2}Mn_{1/2}O_3$ (-4 ppm/°C) [Keith et al., 2004]. In addition, the ceramics exhibit Qxf_r values as good as $(Ba_{5-x}Sr_x)Nb_4O_{15}$ (~14 600 - 23 300) [Liou *et al.*, 2006] and $BaTi_{1/2}Mn_{1/2}O_3$ (11 600) [Keith et al., 2004], but ε' values are lower than those of shifted perovskites (31–51) [Liou et al., 2006, Sreemoolanadhan et al., 1995, Keith et al., 2004, Vineis et al., 1996].

5.5. Results: The crystal structure of high-temperature 5L2-$Ba_6W_{3-x}Nb_xO_{15-x/2}$ for (x = 2)

The XRPD pattern of *5L2*-$Ba_6W_{3-x}Nb_xO_{15-x/2}$ (x=2) fired at 1500 °C for 15h and quenched to room temperature can be fitted (Fig. 17) using the whole-pattern matching procedure implemented in JANA2006 [Petricek et al., 2006] considering the *P-3m1* space group and the unit-cell parameters a_H = 0.6030(1) nm and c_H = 1.244(1) nm as suggested by Kemmler-Sack *et al*. [1980].

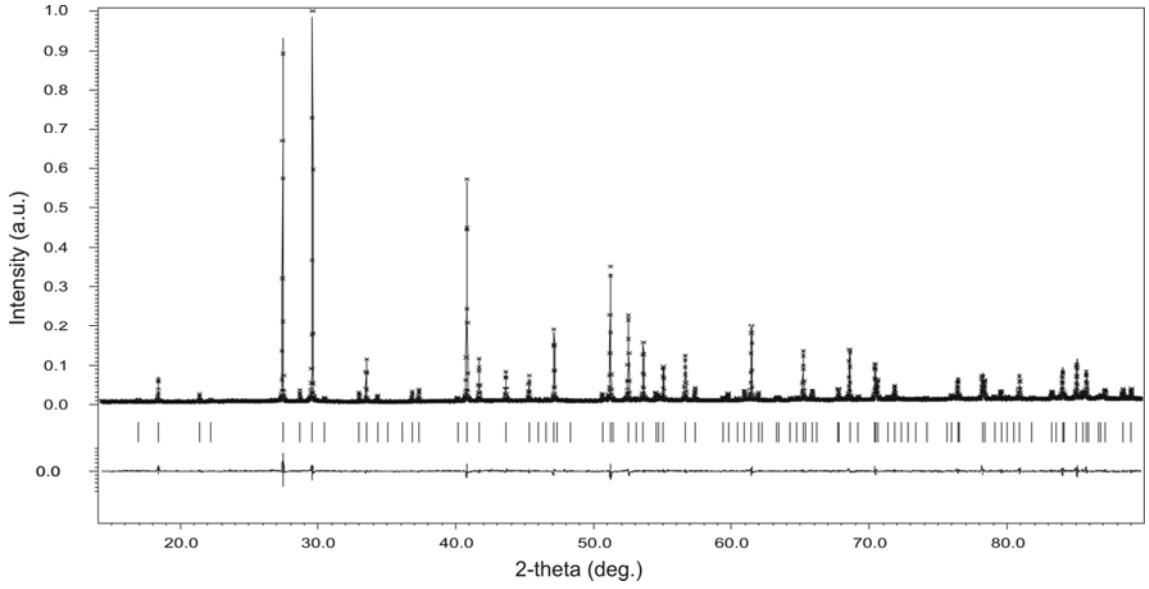

Figure 17: Whole-pattern fitting of the XRPD patterns obtained for *5L2*-$Ba_6W_{3-x}Nb_xO_{15-x/2}$ (x = 2) fired at 1500 °C for 15h and quenched to room temperature, when considering the *P-3m1* space group and the cell parameters a_H = 0.6030(1) nm and c_H = 1.244(1) nm (GoF: 1.29 and Rwp: 8.14 %).

5.5.1. The reconstruction of the unit-cell from SAED patterns based (The tilting experiment)

The existing structural data for *5L2*-$Ba_6W_{3-x}Nb_xO_{15-x/2}$ (x = 2) indicate that the compound crystallizes as 5-layered B-site cation-deficient hexagonal perovskite with *hhccc* stacking sequence [Kemmler-Sack, 1980]. In order to allow this stacking model author suggested that part of barium atoms occupy corner-sharing octahedra of the structure. Therefore, the crystal structure of *5L2*-$Ba_6W_{3-x}Nb_xO_{15-x/2}$ (x = 2) was described with the centro-symmetric primitive unit-cell and *P-3m1* space-group symmetry [Kemmler-Sack, 1980], similarly as $Ba_5Nb_4O_{15}$ [Vanderah *et al.*, 2002]. However, it seems very unlikely that Ba-atoms with relatively large ionic radii would occupy the octahedral positions. Considering the stoichiometry of *5L2*-$Ba_6W_{3-x}Nb_xO_{15-x/2}$ (x = 2) it is most probable that the compound has the hexagonal-perovskite-like crystal structure with six BaO-layers (6L) stacked along *c*-crystallographic axis.

To confirm the reliability of the suggested six-layered structural model several crystals were studied by means of SAED using the tilting methods. The experiment started by searching for potential zone-axes patterns, which would reveal the stacking sequence along the c-crystallographic direction. After finding the corresponding ED pattern, *i.e.* $[100]_H$ ZAP (Fig. 18), the crystal was tilted around [010]* axis (Fig. 19). This and especially the second tilting experiment (Figs. 20 and 21) revealed two sets of extra spots (see the orange and white arrows in figure 20), which accompany the strong Bragg reflections of an underlying average structure. One set of reflections has a diffuse intensities distribution, while the reflections of the second set are discrete although with much low intensities if comparing them with the main diffraction spots of the substructure. In generally, the additional spots have variable intensity and appear in two mutually perpendicular directions. They were observed in all sections of the reciprocal space except in $[001]_H$ zone-axis patterns (see Fig. 20a). Moreover, the SAED patterns recorded for different *5L2*-$Ba_6W_{3-x}Nb_xO_{15-x/2}$ (x = 2) crystals (Figs. 18 and 20) show at least two types of discrete additional reflections. They appear in a regular and elongated form. The latter imply the presence of discrete phases related to structural differences on the atomic scale (see the yellow arrows in Fig. 18). However, the strong Bragg peaks in the reciprocal lattice can all be indexed on the basis of a strongly scattered *P*-type hexagonal sub-cell with $a_H \approx 0.603$ nm and $c_H \approx 0.619$ nm. Since the extra spots appear along [001]* direction they can be considered as a superstructural along the c-axis. Therefore the *c* unit-cell parameter has to be multiplied. Accordingly, the real unit-cell of *5L2*-$Ba_6W_{3-x}Nb_xO_{15-x/2}$ (x = 2) is bigger, with dimensions of $a_H \approx 0.603$ nm and $c_H \approx 1.24$ nm. These results are in good agreement with the data obtained from the Le Bail profile fitting (Fig. 17).

As said before, there is a little or no arrangement as to the position of additional reflections (see diffuse intensity distributions in ED patterns). The variable position and even the existence of particular weak reflections is temperature dependent (Fig. 22). Thus the ED

patterns of the sample fired at 1500°C for 15 hours and then quenched to room temperature exhibits more pronounced diffuse intensities with respect to the ED patterns of the sample fired at lower temperature; *i.e.* 1400 °C (Fig. 22). According to Welberry *et al.*, [1994] such diffuse scatterings reflect the short-range ordering of the crystal structure most commonly related to the compositional flexibility of the system [Withers *et al.*, 1998], which is certainly possible in BaO-rich systems such as $Ba_6W_{3-x}Nb_xO_{15-x/2}$ (x = 2) due to water absorption. Hence OH^- ions incorporate into the anion sublattice, which consequently leads to the vacancies on A-sublatice.

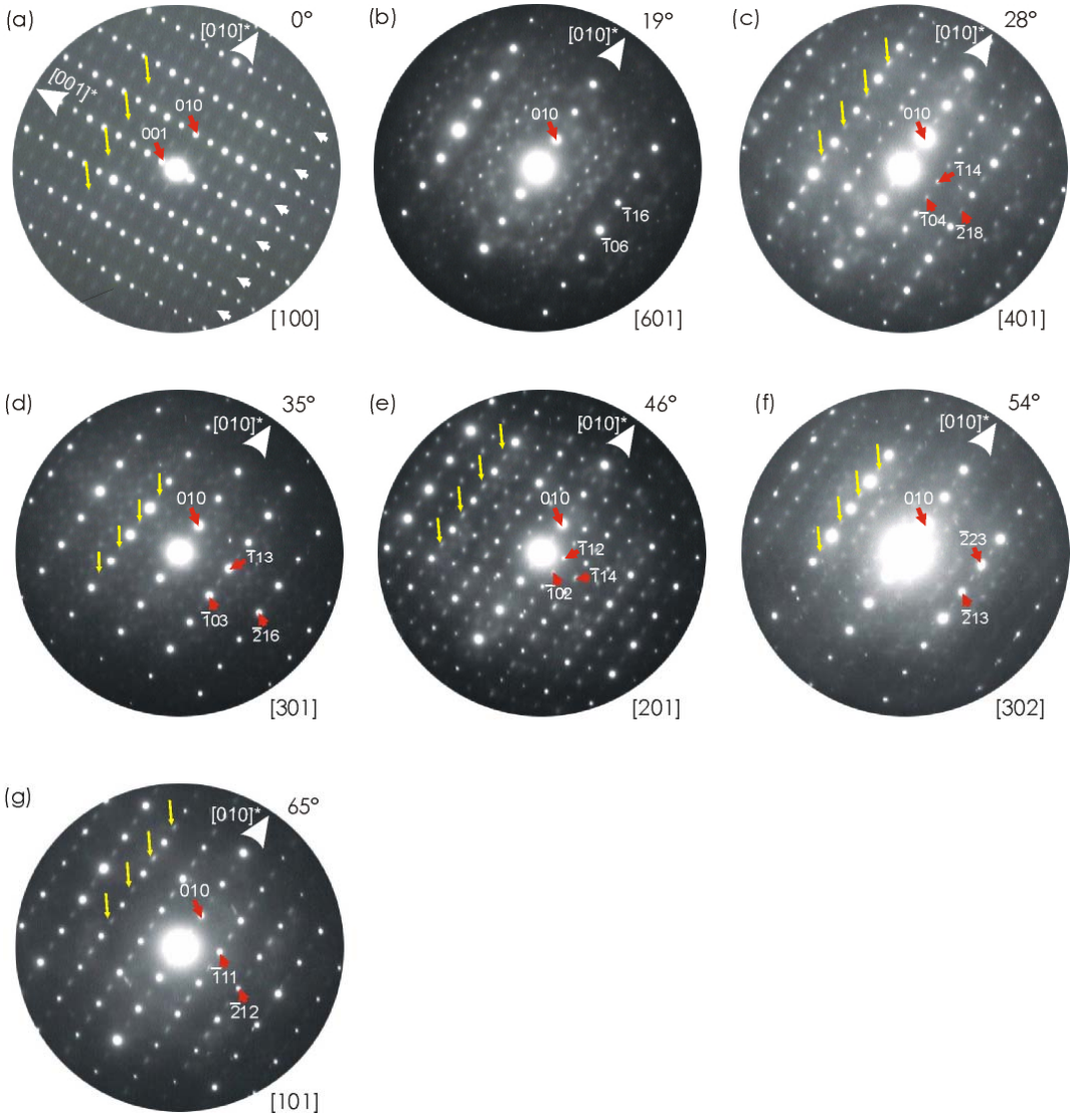

Figure 18: A set of selected-area electron-diffraction patterns from a single *5L2*-$Ba_6W_{3-x}Nb_xO_{15-x/2}$ (x = 2) crystal obtained in a tilting experiment. The fundamental reflections are indexed according to the hexagonal unit-cell with the space group symmetry P-3m1 and with a_H = 0.6030(1) nm and c_H = 1.244(1) nm. The additional reflections are not indexed with respect to the space group P-3m1. Yellow arrows denote the elongated reflections, which probably appear due to the presence of discrete phases related to structural differences on the atomic scale.

Regarding the 6L structural model and the unit-cell parameters a_H = 0.6030(1) nm and c_H = 1.244(1) nm obtained in the Le Bail profile fitting (Fig. 17), the structure has an unusual distance between BaO-layers along c-axis consistent with 0.2073 nm. For the perovskite structures where only octahedrons are set between AO-layers this value should be around 0.24 nm. This fact implies that B-site cations must be in alternative coordination, which consequently affects the distance between BaO-layers similarly as in the case of α-$Ba_4Nb_2O_9$. The interlayer distance consistent with ~ 0.2 nm is known in hexagonal perovskite-derivatives. The main feature of such a structure would be the presence of chains that consist of face-sharing octahedra and face-sharing trigonal prisms lined along the c-axis [Darriet *et al.*, 1995].

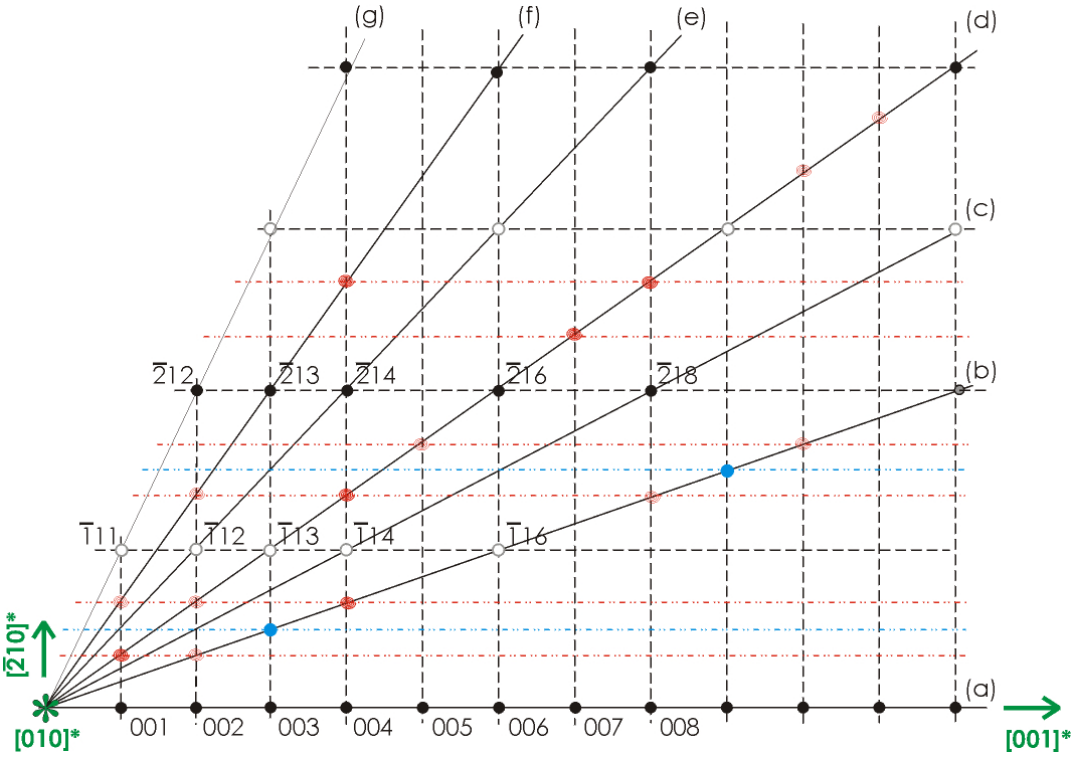

Figure 19: The reconstructed $[120]_H$ ZAP for a single *5L2*-$Ba_6W_{3-x}Nb_xO_{15-x/2}$ (x = 2) crystal normal to the [010]* tilt-axis. Diffuse red points indicate diffuse reflections not compatible with a space group *P-3m1*. The blue spots denote weak reflections evident from ED patterns.

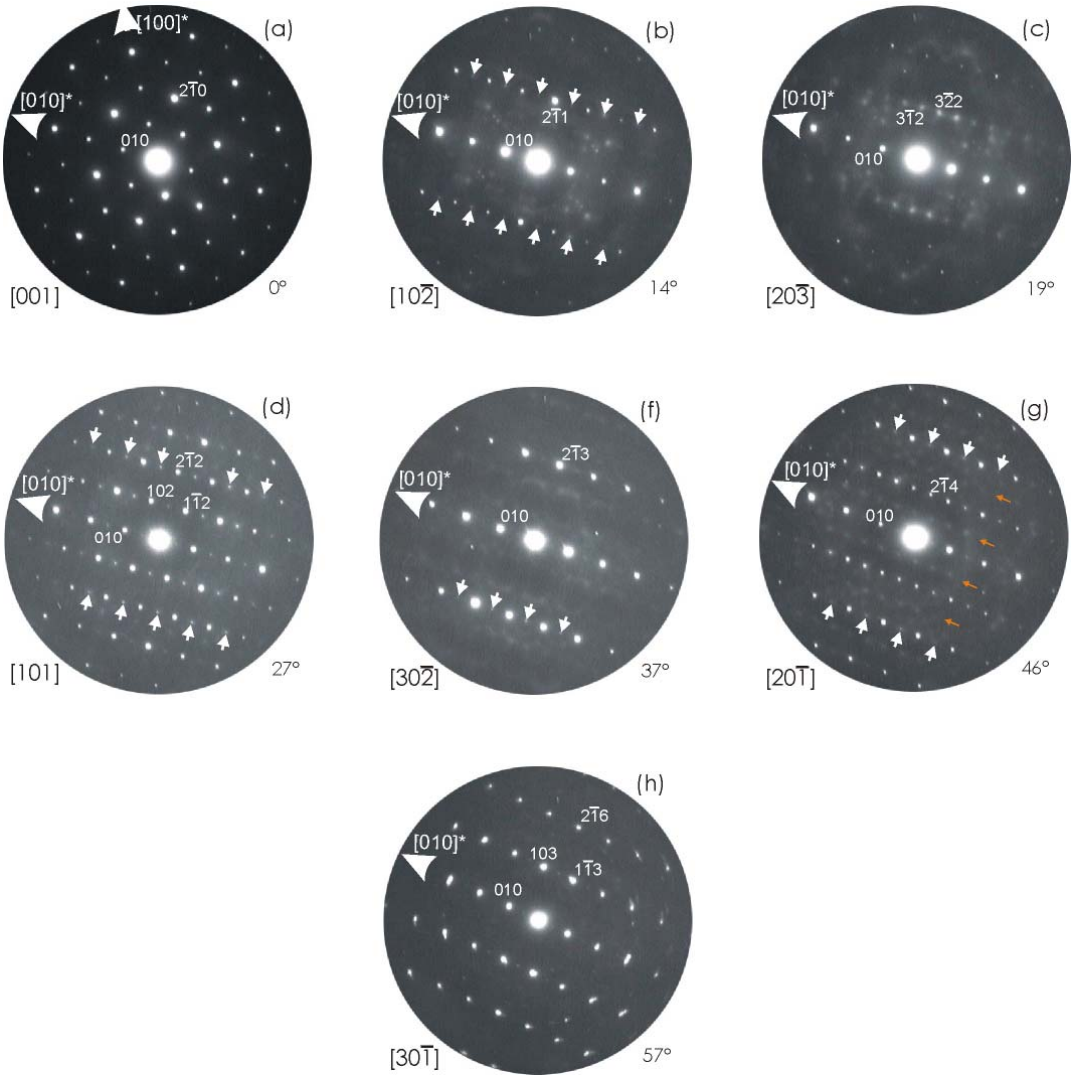

Figure 20: A set of selected-area electron-diffraction patterns from a single *5L2*-$Ba_6W_{3-x}Nb_xO_{15-x/2}$ (x = 2) crystal obtained in the second tilting experiment (Crystal II). The fundamental reflections are indexed according to the hexagonal unit-cell with the space group symmetry *P-3m1* and with a_H = 0.6030(1) nm and c_H = 1.244(1) nm. Extra reflections are not indexed with respect to the space group *P-3m1*. Two sets of additional reflections can be observed. The first one is marked by orange arrows, while the second set having weaker and diffuse intensities is denoted by thick white arrows.

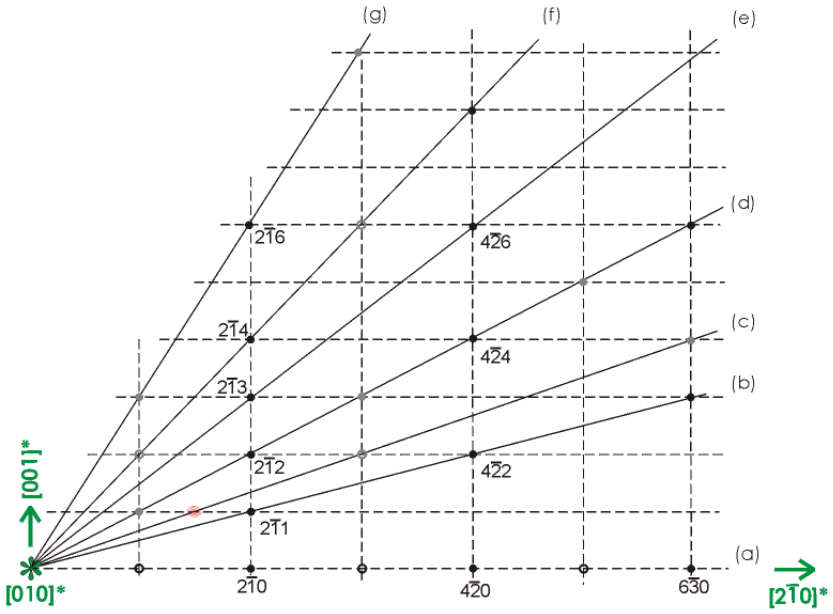

Figure 21: The reconstructed reciprocal layer of *5L2*-$Ba_6Nb_2WO_{14}$ crystal perpendicular to the $[010]_H$* tilt axis. Diffuse red points indicate diffuse reflections not compatible with a space group *P-3m1*.

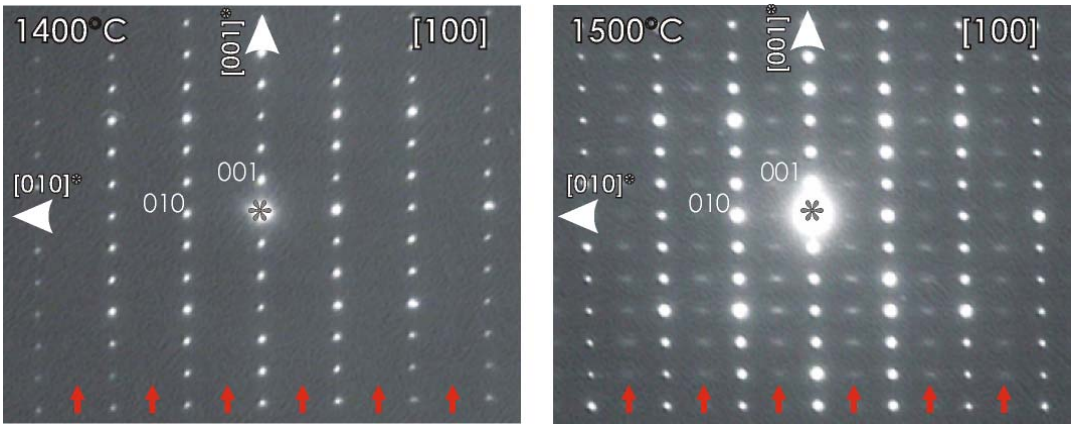

Figure 22: Representative $[100]_H$ zone-axes patterns obtained for *5L2*-$Ba_6W_{3-x}Nb_xO_{15-x/2}$ (x = 2). For the sample quenched to room temperature after annealing at **(a)** 1500 °C for 15h and **(b)** 1400 °C for 10h. Red arrows indicate the presence/absence of additional reflections

6. CONCLUSIONS

6.1. The $BaO–Nb_2O_5$ binary system

The lack of literature data about the polymorphic phase transitions in the $Ba_4Nb_2O_9$ binary system and the crystal structure of the individual polymorph inspired my investigations, which can be divided into two major topics: (i) the phase formation and phase transitions of $Ba_4Nb_2O_9$ and (ii) the crystal structure of α- and γ-$Ba_4Nb_2O_9$.

6.1.1. Phase formation and phase transitions of $Ba_4Nb_2O_9$

In this investigation three $Ba_4Nb_2O_9$ polymorphs were isolated. These included the hexagonal (α) and two orthorhombic (γ, β) modifications. The low-temperature α-modification and the high-temperature γ-modification are the only stable polymorphs in this system. The α-$Ba_4Nb_2O_9$ is observed below 1176 °C, while γ-$Ba_4Nb_2O_9$ is thermodynamically stable above this temperature. The rate of cooling applied to the γ-$Ba_4Nb_2O_9$ sample strongly affects the nature of the phase transitions. The rapid cooling (quenching) of the γ-phase sample down to room temperature results in the γ-modification, while slow cooling leads to the formation of the α-modification. The orthorhombic β-$Ba_4Nb_2O_9$ has been proved to be a distorted γ-modification (γ'). It is metastable and observed after reheating the pre-sintered γ-$Ba_4Nb_2O_9$ in the temperature range 360-585°C. The $\alpha \rightarrow \gamma$ transformation is accompanied by the formation of a 120° domain structure, which is a consequence of the hexagonal → orthorhombic unit-cell reconstruction. However, all the polymorphs of $Ba_4Nb_2O_9$ are structurally closely related, implying that only minor structural perturbations are involved in polymorphic phase transformation processes in this system. In air, the surfaces of the $Ba_4Nb_2O_9$ grains decompose to nanocrystalline $Ba_5Nb_4O_{15}$ and BaO. The latter instantly reacts with atmospheric CO_2 to form $BaCO_3$. Decomposition of the sample is more enhanced in vacuum. This was confirmed by the presence of two barium-deficient secondary phases in the samples, *i.e.*, $Ba_5Nb_4O_{15}$ and $Ba_3Nb_2O_8$. Since no amorphous BaO-rich secondary phase was observed in the TEM samples this may indicate the loss of BaO from the system.

6.1.2. The crystal structure of α- and γ-$Ba_4Nb_2O_9$

In order to characterize the crystal structure of the α- and γ-modifications, both phases were studied in different zone-axis orientations using a transmission electron microscope. The SAED patterns recorded during the tilting experiments and HRTEM images of the crystals in the most relevant zone-axes revealed that α-$Ba_4Nb_2O_9$ has a hexagonal unit-cell with the an average space-group symmetry corresponding to *P-62c* and a cell parameter consistent with a = 1.025 nm and c = 0.848 nm. The atypical distance between the Ba-O layers, *i.e.*, $d_{(001)H}$ = 0.212

nm, indicates that α-$Ba_4Nb_2O_9$ crystallizes as a hexagonal perovskite derivative. Its crystal structure can be described in terms of the hexagonal stacking of the BaO_3 and $BaA'O_6$ layers along the $[001]_H$ crystallographic direction. The alternating of these layers creates columns of two successive face-sharing octahedra followed by one trigonal prism along the three-fold axes of the hexagonal unit cell. Moreover, all the BO_6 polyhedra are linked with each other over the triangular faces. The α-$Ba_4Nb_2O_9$ occurs in two different polytypes. These include the commensurate and incommensurate modulated structures. The α-$Ba_4Nb_2O_9$ can be interpreted as an intergrowth-modulated crystal structure with the general formula $A_{1+x}A'_xB_{1-x}O_3$ for x = 1/3. The γ = 2/3 for the commensurate analogue, but it is slightly different to 2/3 for the incommensurate one. Generally, both varieties are composed of two subsystems, *i.e.*, the $[Ba]_\infty$ and $[(Nb,A')O_3]_\infty$ subsystems. The first subsystem has cell parameters consistent with a_H = 1.025 nm and c_H = 0.2827 nm, while the second subsystem has a_H = 1.025 nm and c_H = 0.424 nm. The symmetry of the compound can be described with the centrosymmetric super-space group *R-3m (00γ)0s*. Nonetheless, the presence of diffuse scattering indicates the strong structural disorder of both the α-$Ba_4Nb_2O_9$ polytypes.

The unit cell of the γ-modification was determined from ED patterns obtained during the tilting experiments. It can be described with the space group *Pnma* and the unit-cell parameters *a* = 1.26, *b* = 2.18 nm and *c* = 2.55 nm. Since the angle between the reciprocal directions is not exactly 90° the unit cell of the γ- $Ba_4Nb_2O_9$ can be considered as at least pseudo-orthorhombic.

6.2. The $BaO–Nb_2O_5–WO_3$ ternary system

Ceramics with the nominal compositions *5L1*- and *5L2*-$Ba_6Nb_xW_{3-x}O_{15-x/2}$ (x = 1, x = 2), *9L*-$Ba_9Nb_2W_4O_{26}$, *12L*-$Ba_4Nb_2WO_{12}$ and *27L*-$Ba_9Nb_6WO_{27}$ were synthesized in order to study their phase relations, crystal structure and dielectric properties in the microwave frequency region. The *5L2*-$Ba_6Nb_xW_{3-x}O_{15-x/2}$ (x = 2) and *9L*-$Ba_9Nb_2W_4O_{26}$ were obtained as single-phase materials under specific synthesis conditions, described in the Experimental part. The *27L*-$Ba_9Nb_6WO_{27}$, *12L*-$Ba_4Nb_2WO_{12}$ and *5L1*-$Ba_6Nb_xW_{3-x}O_{15-x/2}$ (x = 1) contained at least one secondary phase. The formation of these three polytypes began with a reaction between the binary compounds and continues over a series of intermediate, hexagonal, perovskite phases lying on the $Ba_3W_2O_9$–$Ba_5Nb_4O_{15}$ tie-line. The *5L2*-$Ba_6Nb_xW_{3-x}O_{15-x/2}$ (x = 1) appeared over the binary $Ba_4Nb_2O_9$ and other barium-tungsten oxides, while the *5L2*-$Ba_6Nb_xW_{3-x}O_{15-x/2}$ (x = 2) formed through a reaction between $Ba_5Nb_4O_{15}$ and barium-tungsten oxides. The *5L2*-$Ba_6Nb_xW_{3-x}O_{15-x/2}$ (x = 2) appeared in two different polymorphs structurally related to the hexagonal $Ba_6Ta_2WO_{14}$ and to the orthorhombic γ-$Ba_4Nb_2O_9$. The selected-area electron-diffraction studies revealed that the basic crystal structure of the high-temperature modification adopts the *P-3m1* space-group symmetry and the unit-cell dimensions a_H = 0.603 nm and c_H = 1.244

nm. Additional reflections of various intensities and strong diffuse scattering indicate a disorder in the crystalline material – either compositional or displacive. The disorder is strongly related to the firing temperature and can be reduced by optimizing the syntheses conditions. Moreover, the interlayer distances, *i.e.*, $d_{(001)H}$ = 0.2073 nm along the crystallographic c-direction suggest that *5L2*-$Ba_6Nb_xW_{3-x}O_{15-x/2}$ (x = 2) is structurally close to the hexagonal perovskite derivatives composed of the BaO_3 and $Ba_3A'O_6$ layers.

7. Acknowledgements

I wish to express my sincere gratitude to **Prof. Dr. Danilo Suvorov**, our head of department, who warmly welcomed me into the Department for Advanced Materials Research. It was certainly not without risk to accept a geologist who had no prior experience and knowledge of ceramics. Prof. Suvorov, thank you for giving me an opportunity to learn from you! Thank you for giving me a chance to spread my horizons and improve my knowledge by attending many international schools and crystallographic meetings.

I would like to express my gratitude to my supervisor, **Assist. Prof. Dr. Boštjan Jančar**, for his assistance and guidance with my PhD studies, his help with writing papers and his work in finalizing my thesis.

I would like to express my gratitude to my dear friend **Assist. Prof. Dr. Aleksander Rečnik** for sparking my interest in crystal-structure solutions and transmission electron microscopy. I would like to thank you Sandi for believing in me and always pushing me to do my best. Thank you for encouraging me in my studies and inspiring my self-confidence during my study.

Great opportunities for international experience were given to me throughout the cooperation with **Dr. Philippe Boullay** and **Dr. Nicolas Barrier** (CRISMAT Laboratory, Caen, France). Thank you, Philippe, for your patience, understanding, guidance and an introduction into the Tilting Method. Many thanks to you, Nicolas, for helping me with the Rietveld refinement.

Personally, I am very grateful to **Prof. Dr. Artem Abakumov** (University of Antwerp, Belgium) for his interest in my work and many professional discussions.

Finally, I would like to acknowledge my friends at the Jožef Stefan Institute who have spent so many days with me and contributed to my study and my life.

As a Ph.D. Student from January 2005 to June 2009 I had been supported by the Slovenian Research Agency under the Programme No. P2-0091-0106-032 entitled 'Advanced inorganic materials and technologies' and under the Grant No. 3311-04-831835.

8. Publications

The results of the investigations related to the Ph.D. Thesis, are published in the following scientific papers:

Bezjak, J.; Jančar, B.; Rečnik, A. and Suvorov, D. The synthesis and polymorphic phase transitions of $Ba_4Nb_2O_9$ ceramics, *Journal of European Ceramic Society*, Vol. 28, No. 14,pp 2771–2776 (2008).

Accepted for the publication:

Bezjak, J.; Rečnik, A.; Jančar, B.; Boullay, Ph.; Radosavljević Evans, I. and Suvorov, D. High-Temperature Transmission Electron Microscopy and X-Ray Powder Diffraction Studies of Polymorphic Phase Transitions in $Ba_4Nb_2O_9$. *Journal of American Ceramic Society,* (2009).

Bezjak, J.; Jančar, B.; Boullay, Ph., Rečnik, A. and Suvorov, D. Hexagonal perovskite-type phases in the BaO-rich part of the $BaO–WO_3–Nb_2O_5$ system. *Journal of American Ceramic Society*, (2009).

The results of the thesis were presented at the following international conferences and institutes:

Bezjak, J.; Jančar, B.; Meden, A. and Suvorov, D. Crystal structure and microwave dielectric properties of hexagonal perovskites in the ternary system $BaO-WO_3-Nb_2O_5$. In: Proceedings of the *14th Conference on Materials and Technology,* pp. 65 (Institute of metals and technology, Portorož, Slovenia, 2006).

Bezjak, J.; Jančar, B. and Suvorov, D. Synthesis and crystal-structure refinement of $Ba_4Nb_2O_9$, In: Proceedings of the *2007 Annual Meeting of the American Crystallographic Association, Inc, Salt Lake City* (*Program and abstract book*, American Crystallographic Association, Inc., Buffalo, New York, 2007).

Bezjak, J.; Jančar, B. and Suvorov, D. X-ray diffraction analyses of the polymorphic phase transitions of $Ba_4Nb_2O_9$, In *The Seventh Students' Meeting SM-2007, Processing and Application of Ceramics.* pp. 12 *(Program and book of abstracts,*Faculty of Technology, Novi Sad, Serbia, 2007).

Bezjak, J.; Jančar, B.; Rečnik, A. and Suvorov, D. The crystal-structure model of an α-$Ba_4Nb_2O_9$ modification based on the hexagonal stacking of Ba_3O_9 and Ba_3NbO_6 layers, In *WomenInNano winter school: 2008*, Kranjska Gora, pp. 45 *(Book of abstracts*, Jozef Stefan Institute, Ljubljana, Slovenia, 2008).

Bezjak, J.; Jančar, B.; Boullay, Ph.; Rečnik, A. and Suvorov, D. The polymorphic phase transition studies of the compounds with the nominal composition of $Ba_4Nb_2O_9$. In: Proceedings of the *Seventeenth Croatian-Slovenian Crystallographic Meeting*, pp. 68 *(Book of abstracts and program*, University of Ljubljana, Faculty of Chemistry and Chemical Technology, Slovenia, 2008).

Bezjak, J.; Jančar, B.; Boullay, Ph. and Suvorov, D. The synthesis, crystal structural study and microwave dielectric properties of $Ba_6WNb_2O_{14}$, In: Proceedings of the *XXI Congress of the International Union of Crystallography, IUCr2008 (Book of abstracts),* Osaka, Japan, 2008).

Bezjak, J.; Jančar, B.; Boullay, Ph. and Suvorov, D. The crystal structural study and microwave dielectric properties of $Ba_6WNb_2O_{14}$ ceramic. In*: Proceedings of the Slovenski kemijski dnevi 2008, Maribor,* FKKT. pp 54 (*Zbornik povzetkov referatov s posvetovanja*, Maribor, Slovenia, 2008).

Bezjak, J.; Jančar, B.; Rečnik, A.; Boullay, Ph. and Suvorov, D. Visoko-temperaturne raziskave polimorfnih faznih prehodov med $Ba_4Nb_2O_9$ modifikacijami in določitev osnovne celice nizko-temperaturne α-modifikacije, In proceedings of the D*an mladih raziskovalcev kemije, materialov, biokemije in znanosti o okolju,* pp. 1 (Institut "Jožef Stefan", Ljubljana, Slovenia, 2009)

9. References

Abakumov, A.M.; Van Tendeloo, G.; Scheglov, A.A.; Shpanchenko, R.V. and Antipov, E.V. The Crystal Structure of $Ba_8Ta_6NiO_{24}$: Cation Ordering in Hexagonal Perovskites. *Journal of Solid State Chemistry*, Vol. **125**, No. 1, pp 102–107 (1996).

Abraham, F.; Minaud, S. and Renard, C. Preliminary crystal structure of mixed-valency $Sr_4Ni_3O_9$, the actual formula of the so-called $Sr_5Ni_4O_{11}$. *Journal of Material Chemistry*, Vol. **4**, pp 1763–1764 (1994).

James, M. and Attfield, J.P. A new nickel (III) oxide family: MSr_3NiO_6 (M = Sc, In, Tm, Yb and Lu). *Chemistry-A European Journal* Vol. **2**, No. 6, pp 737–741 (2006).

Ali, R. and Yashima, M. Space group and crystal structure of the Perovskite $CaTiO_3$ from 296 to 1720K. *Journal of Solid State Chemistry*, Vol. **178**, pp 2867–2872 (2005).

Aurivillius, B. Mixed bismuth oxides with layer lattices. II. Structure of $Ba_4Ti_3O_{12}$. *Arkiv für Kemi 1*, pp 499–512 (1949).

Bazuev, G.V.; Zaitseva, N.A. and Kellerman, D.G., New complex oxides of the $A_{3n+3m}A'_nB_{3m+n}O_{9m+6n}$ family: $Ba_6A'Mn_4O_{15}$ (A' = Mg, Ni), *Solid State Sciences*, Vol. **5**, pp 1465–1470 (2003).

Barwick, M.; Azough, F. and Freer, R. Structure and dielectric properties of perovskite ceramics in the system $Ba(Ni_{1/3}Nb_{2/3})O_3$–$Ba(Zn_{1/3}Nb_{2/3})O_3$, *Journal of the European Ceramic Society*, Vol. **26**, No. 10-11, pp 1767–1773 (2006).

Battle, P.D.; Blake, G.R.; Sloan, J. and Vente, J.F. Commensurate and Incommensurate Phases in the System $A_4A'Ir_2O_9$ (A = Sr, Ba; A' =Cu, Zn), *Journal of solid state chemistry*, Vol. **136**, pp 103–114 (1998).

Bazuev, G.V.; Zaitseva, N.A. and Kellerman, D.G. New complex oxides of the $A_{3n+3m}A'_nB_{3m+n}O_{9m+6n}$ family: $Ba_6A'Mn_4O_{15}$ (A' = Mg, Ni), *Solid State Sciences*, Vol. **5**, pp 1465–1470 (2003).

Bezjak, J.; Jančar, B.; Rečnik, A. and Suvorov, D. The synthesis and polymorphic phase transitions of $Bar_4Nb_2O_9$ ceramics. *Journal of European Ceramic Society,* Vol. **28**, No. 14, pp 2771–2776 (2008).

Bie, l.; Lin, J.; Wang, Y. and Loong, Ch. K. n = 2 Member of the hexagonal perovskite-intergrowth manganate family $A_{n+1}Mn_nO_{3n+3}(Ca_2O)$. *Inorganic Chemistry Communications*, Vol. **5**, pp 966–970 (2002).

Bieringer, M.; Moussa, S.M.; Noailles, L.D.; Burrows, A.; Kiely, Ch.J.; Rosseinsky, M.J. and Ibbson, R.M. Cation Ordering, Domain Growth, and Zinc Loss in the Microwave Dielectric Oxide $Ba_3ZnTa_2O_{9-\delta}$. *Chemistry of Materials,* Vol. **15**, pp 586–597 (2003).

Bing, Y. Synthesis, structure and properties of high piezo- and ferroelectric complex perovskite systems (Ph.D. thesis, Simon Fraser University, 2005).

BLOSS, F.D. Crystallography and crystal chemistry (Virginia Polytechnic Institute and State University, Rinehart & Winston, Inc, New York, 1971).

Claridge, J.B.; Layland, R.C. and zur Loye, H.-C. Ca_4PtO_6. *Acta Crystallographica,* Vol. **53**, pp 1740–1741(1997).

Claridge, J.B.; Layland, R.C.; Adams, R.D. and zur Loye. H.-C., The Structures and Characterization of Two New Oxides of the Sr_4PtO_6 Type: $NaCa_3IrO_6$ and $NaCa_3RuO_6$. *Zeitschrift für anorganische und allgemeine Chemie*, Vol. **62**, No. 7, pp 1131–1134 (2004).

Campá, J.A.; Gutiérrez-Puebla, E.; Monge, M.A.; Rasines, I. and Ruìz-Valero, C. Nickel Supermixed Valence in Stoichiometric $BaNi_{0.83}O_{2.5}$. *Journal of Solid State Chemistry*, Vol. **108**, No. 2, pp 230–235 (1994).

Clearfield, A. The synthesis and crystal structures of some alkaline earth titanium and zirconium sulfides. *Acta Crystallographica*, Vol. **16**, No. 2, pp 135–142 (1963).

Cussen, E.J.; Sloan, J.; Vente, J.F.; Battle P.D. and Gibb, T.C. 15R $SrMn_{1-x}Fe_xO_{3-\delta}$ ($x \approx 0.1$); A New Perovskite Stacking Sequence, *Inorganic Chemistry*, Vol. **37**, No. 23, pp 6071–6077 (1998).

Colville, A.A. and Geller, S. The crystal structure of brownmillerite, Ca_2FeAlO_5. *Acta Crystallographica*, Vol. **27**, No. 12, pp 2311–2351(1971).

Darriet, J. and Subramanian, M.A. Structural relationship between compounds based on the stacking of mixed layers related to hexagonal perovskite-type structures. *JMC*, Vol. **5**, pp 543–552 (1995).

Davis, M.J.; Smith, M.D.; Stitzer, K.E. and zur Loye, H.-C. High temperature flux growth, structural characterization, and magnetic properties of $Ca_{3.15}Li_{0.85}IrO_6$, Sr_3LiIrO_6, Ca_3LiRuO_6 and Sr_3LiRuO_6. *Journal of Alloys and Compounds*, Vol. **351**, pp 95–100 (2003).

Desu, S.B. and O'Bryan, H.M, Microwave Loss Quality of $BaZn_{1/2}Ta_{2/3}O_3$. Ceramics, Journal of American Ceramic Society, Vol. **68**, No. 10, pp 546–551 (1985).

Donohue, P.C.; Katz, L. and Ward, R. The crystal structure of barium ruthenium oxide and related compounds. *Inorganic Chemistry*, Vol. **4**, pp 306–310 (1965).

Dussarrat, C.; Fompeyrine, J. and Darriet, J. $Ba_5Ru_2O_{10}$: A new structural model resulting from the sacking of [BaO_3] and [Ba_2O] mixed layers. Structural relationship to the hexagonal perovskite-type structures. *European journal of solid state and inorganic chemistry*, Vol. **31**, pp 289–300 (1994).

Dussarrat, C.; Fompeyrine, J. and Darriet, J. $Sr_4Ru_2O_9$: A structural model resulting from the stacking of [Sr_3O_9] and [Sr_3O_6] mixed layers, Structural relationships to related perovskite-type structures. *European journal of solid state and inorganic chemistry*, Vol. **32**, No. 1, pp 3–14 (1995).

Dussarrat, C. Novel series of perovskite-related crystal structures. *Solid State Ionics*, Vol. 108, pp 165–173 (1998).

Evain, M.; Boucher, F.; Gourdon, O.; Petricek, V.; Dusek, M. and Bezdicka, P. Incommensurate versus Commensurate Description of the A_xBX_3 Hexagonal Perovskite-Type Structure, $Sr_{1.2872}NiO_3$ Incommensurate Composite Compound Example. *Chemistry of Materials*, Vol. **10**, pp 3068–3076 (1998).

Fjellvåg, H.; Gulbrandsen, E.; Aasland, S.; Olsen, A. and Hauback, B.C. Crystal Structure and Possible Charge Ordering in One-Dimensional $Ca_3Co_2O_6$. *Journal of solid state chemistry*, Vol. **124**, pp 190–194 (1996).

Floros, N.; Michel, C.; Hervieu, M. and Raveau, B. A New Hexagonal 16L Perovskite-Related Structure: $Ba_4Ca_{1-x}Mn_{3+x}O_{12-\delta}$. Chemistry of Materials, Vol. **12**, pp 3197–3201 (2000).

Gingl, F.; Vogt, T.; Akiba, E. and Yvon, K. Cubic $CsCaH_3$ and hexagonal $RbMgH_3$: new examples of fluoride-related perovskite-type hydrides, *Journal of Alloys and Compounds*, Vol. **282**, No. 1–2, pp 125–129 (1999).

Goldschmidt, V.M. Die Gesetze der Krystallochemie, Die Naturwissenschaften, Oslo, Heft, **21**, pp 477–485 (1926).

Goldschmidt, V.M. Geochemische Verteilungsgesetze VIII. Bau und Eigenschaften von Krystallen. Skrifter utgitt av det Norske Videnskaps-Akademi i Oslo 1: *Matematisk-Naturvidenskapelig Klasse*, Vol. **8**, pp 1–156 (1927).

Gracıa-Gonzalez, E.; Parras, M. and Gonzalez-Calbet, J.M. Electron Microscopy Study of a New Cation Deficient Perovskite-like Oxide: $Ba_3MoNbO_{8.5}$. *Chemistry of Materials*, Vol. **10**, pp 1576–1581 (1998).

Gracía-González, E.; Parras, M. and González-Calbert, J.M. A new structure model for $Ba_3Nb_2O_8$: A HRTEM study. *Chemistry of Materials*, Vol. **12**, pp 2485–2489 (2000).

Grasset, F.; Zakhour, M. and Darriet, J. Synthesis, crystal structure and magnetic properties of $Ba_5Ru_2O_9(O_2)$, $Ba_5Nb_2O_9(O_2)$ and $Ba_5Ru_2O_{10}$ related to the perovskite-type structure, and structural relationships with corresponding sulfides. *Journal of Alloys and Compounds*, Vol. **287**, pp 25–31 (1999).

Haines, P.J., Thermal methods of analyses; principles, applications and problems (Blackie Academic and Professional, an imprint of Chapman & Hall, Glasgow, 1992).

Hegde, M.S.; SATYALAKSHMI, K.M.; RAMESH, S.; VASANTHACHARYA, N.Y. and GOPALAKRISHNAN, J. New defect-perovskite oxides related to the yttrium-barium-copper oxide superconductor. *Materials research bulletin*, Vol. **27**, No. 9, pp 1099–1106 (1992).

Hutchison, J.L. and Jacobson, A.J. Electron microscopy of the perovskite polytypes $Ba_4Ta_3LiO_{12}$ and $Ba_5W_3Li_2O_{15}$. *Acta Crystallographica,* Vol. **31**, No. 5, pp 1442–1444 (1975).

Huvé, M.; Renard, C.; Abraham, F.; Van Tendeloo, G. and Amelinckx, S. Electron Microscopy of a Family of Hexagonal Perovskites: One-Dimensional Structures Related to $Sr_4Ni_3O_9$. *Journal of Solid State Chemistry*, Vol. **135**, pp 1–16 (1998).

International tables for crystallography, *Volume A*: Space-group symmetry (Theo Hahn, Fourth revised edition, Dordrecht, Boston, London, 1996).

Janssen, T.; Jannrt, A.; Looijenga-vos, A. and de Wolff, P.M. Incommensurate and commensurate modulated structures. International tables for crystallography, Vol. **C**, Ch. 9.8., pp. 907-955 (2006).

Jagodzinski, H. Eindimensionale Fehlordnung in Kristallen und ihr Einfluss auf die Röntgeninterferenzen. Berechnung des Fehlordnungsgrades aus den Röntgenintensitäten. *Acta Crystallographica*, Vol. **2**, pp 201–207 (1949).

Jacobson, A.J.; Collins, B.M. and Fender, B.E.F. A powder neutron-diffraction determination of the structure of $Ba_5W_3Li_2O_{15}$. *Acta Crystallographica,* Vol. **30**, No. 3, pp 816–819 (1974).

Jacobson, A.J.; Collins, B.M. and Fender, B.E.F. A powder neutron-diffraction determination of the structure of $Ba_4Sb_3LiO_{12}$: the preparation and structure of the perovskite-related compounds $Ba_4M_3LiO_{12}$ (*M* = Sb, Bi) and $Ba_5M_3LiO_{15-x}$ (*M* = Te, U). *Acta Crystalography,* Vol. **30**, No. 7, pp 1705–1711 (1974).

Jacobson, A.J. A powder neutron diffraction study of the structure of ana oxygen vacancy distribution in 6H $BaFeO_{2.79}$. *Acta Crystallographica*, Vol. **32**, No. 4., pp 1087–1090 (1975).

Jawahar, I.N.; Mohanan, P. and Sebastian, M.T. $A_5B_4O_{15}$ (A = Ba, Sr, Mg, Ca, Zn; B = Nb, Ta) micrawave dielectric ceramics, Materials Letter, Vol. **57**, pp 4043–4048 (2003).

Jendrek, E.F.Jr.; Potoff, A.D. and Katz, L. A single-crystal study of eight-layer barium niobium lithium oxide, $Ba_4Nb_3LiO_{12}$, *Journal of Solid State Chemistry*, Vol. **9**, No. 4, pp 345–379 (1974).

Kamba, S.; Petzelt, J.; Buixaderas, E.; Haubrich, D.; Vanek, P.; Kuzel, P.; Jawahar, I.N.; Sebastian, M.T. and Mohanan, P. High frequency dielectric properties of $A_5B_4O_{15}$ microwave ceramics. *Journal of Applied Physics*, Vol. **89**, No. 7, pp 3900–3906 (2001).

Kan, A.; Ogawa, H.; Yokoi, A. and Ohsato, H. Microwave dielectric properties of perovskite-like structured $Ba_8Ta_6(Ni_{1-x}M_x)O_{24}$ (M = Co, Cu and Zn) solid solutions. *Japanese Journal of Applied Physics*, Vol. **45**, No. 9B, pp 7494–7498 (2006).

Kawashima, S.; Nishida, M.; Ueda, I.; Ouchi, H. and Hayakawa, S. Dielectric Properties of $Ba(Zn_{1/3}Nb_{2/3})O_3$-$Ba(Zn_{1/3}Ta_{2/3})O_3$ Ceramics. *Proc. Ferroelectr. Mater.* Appl., Vol. **1**, pp 293 (1977).

Keith, G.M.; Kirk, C.A.; Sarama, K.; Alford, N.McN.; Cussen, E.J.; Rosseinsky, M.J. and Sinclair, D.C. Synthesis, crystal structure, and characterization of $Ba(Ti_{1/2}Mn_{1/2})O_3$: A High permittivity 12R-type hexagonal perovskite. *Chemistry of Materials*, Vol. **16**, pp 2007–2015 (2004).

Kemmler-Sack, S. Hexagonale 5 L - Stapelvarianten in den Systemen $Ba_5BaW_{3-x}^{VI}M_x^{V}O_{15-x/2}$ mit M^V = Nb, Ta. *Zeitschrift für anorganische und allgemeine Chemie*, Vol. 471, pp 109–114 (1980).

Kemmler-Sack, S. Rhomboedrische 9L-Stapelvarianten in den Systemen $Ba_3W_{2-x}^{VI}M_x^{V}O_{9-x/2x/2}$ mit M^V= Nb, Ta, *Zeitschrift für anorganische und allgemeine Chemie*, Vol. **471**, pp 102–108 (1980).

Kemmler-Sack, S. and Treiber, U., Die Struktur der rhomboedrischen 9L-Stapelvarianten $Ba_3W_{2-x}^{VI}Nb_x^{V}O_{9-x/2x/2}$. *Zeitschrift für anorganische und allgemeine Chemie*, Vol. **478**, pp 198–204 (1981).

Kemmler-Sack, S. Die rhomboedrischen 12 L-Stapelvarianten $Ba_4M_2^{V}WO_{12}$ mit M^V = Nb, Ta, *Zeitschrift für anorganische und allgemeine Chemie*, Vol. **457**, pp 157–160 (1979).

Kemmler-Sack, S. $Ba_9Nb_6W_2O_{27}$ – die erste Perowskit-Stapelvariante vom rhomboedischen 27 L-Typ, *Zeitschrift für anorganische und allgemeine Chemie*, Vol. **461**, pp 146–150 (1980).

Kemmler-Sack, S. and Treiber, U. Structurbestimmung an $Ba_9Nb_6W_2O_{27}$ – der ersten Stapelvariante eines rhombohedrischen 27 L-Typs. *Zeitschrift für anorganische und allgemeine Chemie*, Vol. **462**, pp 166–172 (1980).

Kim, D.W.; Kim, J.R., Yoon S.H. and Hong, K.S., Microwave Dielectric Properties of Low-Fired $Ba_5Nb_4O_{15}$, Journal of American Ceramic Society, Vol. **85**, No. 11, pp 2759–62 (2002).

Kim, D.W.; Youn, H.J.; Hong, K.S. and Kim, C.K. Microwave dielectric properties of (1–X)$Ba_5Nb_4O_{15}$-X$BaNb_2O_6$ mixtures. *Japanese Journal of Applied Physics*, Vol. **41**, No. 6, pp 3812–3816 (2002).

Kuang, X.; Allix, M.M.B.; Claridge, J.B.; Niu, H.; Rosseinsky, M.J.; Ibberson, R.M. and Iddles, D.M. Crystal structure, microwave dielectric properties and AC conductivity of B-cation deficient hexagonal perovskites $La_5M_xTi_{4-x}O_{15}$ (x = 0.5, 1; M = Zn, Mg, Ga, Al). *Journal of Materials Chemistry*, No. 16, pp 1038–1045 (2006).

Layland, R.C.; Kirkland, S.L. and zur Loye, H.-C. Synthesis, Characterization, and Magnetic Properties of New Rh(III) Compounds with the K_4CdCl_6 Structure-Type: Sr_3MRhO_6 (M = Sm, Eu, Tb, Dy, Ho, Er, and Yb). *Journal of Solid State Chemistry*, Vol. **139**, pp 79–84 (1998).

Levin, I.; Chan, J.Y.; Geyer, R.G.; Maslar, J.E. and Vanderah, T.A. Cation Ordering Types and Dielectric Properties in the Complex Perovskite Ca $(Ca_{1/3}Nb_{2/3})O_3$. *Journal of Solid State Chemistry*, Vol. **156**, pp 122–134 (2001).

Levin, I.; Chan, J.Y.; Scott, J.H.; Farber, L.; Vanderah, T.A. and Maslar, J.E. Complex Polymorphic Behavior and Dielectric Properties of Perovskite-Related $Sr(Sr_{1/3}Nb_{2/3})O_3$. *Journal of Solid State Chemistry*, Vol. **166**, pp 24–41 (2002).

Leshchenko, P.P.; Paramova, M.V.; Lykova, L.N. and Kovba, L.M. Polymorphism of the barium niobate $Ba_4Nb_2O_9$. *Vestnik Moskovskogo Universiteta, Seriya 2: Khimiya*, Vol. **34**, No. 2, pp 148–151 (1979).

Leshchenko, P.P.; Lykova, L.N.; Kovba, L.M.; Stefanovich, S.Yu. and Checkin, V.V. Phase transitions in $Ba_4Nb_2O_9$. *Inorganic Materials*, Vol. **21**, No. 2, pp 278–281 (1985).

Lightfoot, P. and Battle, P. D. The crystal and magnetic structures of $Ba_3NiRu_2O_9$, $Ba_3CoRu_2O_9$, and $Ba_3ZnRu_2O_9$. *Journal of Solid State Chemistry*, Vol. **89**, No. 1, pp 174–183 (1990).

Ling, C.D.; Avdeev, M. and Aivazian, K. Synthesis, structure, and stability of the high-temperature 6H-type perovskite phase $Ba_3BaSb_2O_9$, *Acta Crystallographica*, Vol. **63**, pp 584–588 (2007).

Liou, Y.C.; Shiu, W.H. and Shih, C.Y. Microwave ceramics $Ba_5Nb_4O_{15}$ and $Sr_5Nb_4O_{15}$ prepared by a reaction-sintering process. *Materials Science and Engineering B*, Vol. **131**, pp. 142-146 (2006).

Liu, G. and Greedan, J.E. Syntheses, structures, and characterization of 5-layer $BaVO_{3-x}$ (X = 0.2, 0.1, 0). *Journal of Solid State Chemistry*, Vol. **110**, pp 274–289 (1994).

Loye, H.-C.; Stitzer, K.E.; Smith, M.D.; Abed, A.El and Darriet, J. Observation of a Large Magnetic Anisotropy in the New 2H-Perovskite Related Oxide $Ba_8CoRh_6O_{21}$: Magnetic Measurements on Aligned Single Crystals. *Inorganic Chemistry,* Vol. **40**, pp 5152–5156 (2001).

Liu, S.; Merrick, V. and Newman, N. Structural, chemical and dielectric properties of ceramic injection molded $Ba(Zn_{1/3}Ta_{2/3})O_3$ microwave dielectric ceramics. *Journal of European Ceramic Society*, Vol. **26**, No. 15, pp 3273–3278 (2006).

Luana, V., Costales, A. Pendas, A.M., Florez, M. and Fernandez, V.M.G., Structural and chemical stability of halide perovskites, *Solid State Communications*, Vol. **104**, No. 1, pp 47–50 (1997).

Macquart, R.B.; Gemmill, W.R.; Davis, M.J.; Smith, M.D. and zur Loye, H.-C. Megaw, H. D., A simple theory of the off-centre displacement of cations in octahedral environments, *Acta Crystallographica*, Vol. **24**, No. 1, pp149–153 (1968).

Mallinson, P.M.; Allix, M.M.B.; Claridge, J.B.; Ibberson, R.M.; Iddles, D.M.; Rice, T. and Rosseinsky, M.J. $Ba_8CoNb_6O_{24}$: A d^0 Dielectric Oxide Host Containing Ordered d^7 Cation Layers 1.88 nm apart. *Angewandete Chemie International Edition*, Vol. **44**, pp 7733–7736 (2005).

Mallinson, P.; Claridge, J.B.; Iddles, D.; Price, T.; Ibberson, R.M.; Allix, M. and Rosseinsky, M.J. New 10-layer hexagonal perovskites: Relationship between cation and vacancy ordering and microwave dielectric loss, *Chemistry of Materials*, Vol. **1**8, pp 6227–6238 (2006).

Megaw, H. Crystal Structures (W.B. Saunders, London, 1973).

Mössner, B. and Kemmler-Sack, S. 9-R Stapelvarianten von Typ $Ba_3(BB')_2O_{9-y}$ mit B B' = Mo, W, V, Ti, *Journal of the Less-Common Metals*, Vol. **114**, pp 333–341 (1985).

Moussa, S.M.; Claridge, J.B.; Rosseinsky, M.; Clarke, S.; Ibberson, R.; Price, T.; Iddles, D.M. and Sinclair, D.C. $Ba_8ZnTa_6O_{24}$: a high-Q microwave dielectric from a potentially diverse homologous series. *Applied physics letters*, Vol. **82**, No. 25, pp 4537–4539 (2003).

Morniroli, J.P. *The symmetry of microdiffraction patterns* (Ins. Phys. Conf. Ser. No 98; Chapter 3, IOP Publishing Ltd, UK, 1990).

Morniroli, J.P. Microdiffraction as a tool for crystal structure identification and determination. *Ultramicroscopy*, Vol. **45**, pp 219–239 (1992).

Mironov, A.V., Abakumov, A.M. and Antipov, E.V., Powder diffraction of modulated and composite structures, *The Rigaku Journal*, Vol. **19**, No. 2 and Vol. **20**, No. 1 (2003).

Mitchell, H.R. *Perovskites, modern and ancient* (Almaz Press Inc., Ontario, Canada, 2002).

Müller-Buschbaum, H.K. and Abed, M. Ba_2InAlO_5: Ein weiterer Strukturtyp bei Oxometallaten der Formel $A_2M_2O_5$. *Zeitschrift für anorganische und allgemeine Chemie*, Vol. **591**, No. 1, pp 174–180 (1990).

Neubacher, M. and Müller-Buschbaum, H. Ein neues Erdalkalimetall Chlorooxometallat mit Ir^{5+}: $Ba_5IrIn_2Al_2O_{13}Cl$. *Journal of Alloys Compounds*, Vol. **183**, pp 18–23 (1992).

Nguyen, T.N.; Giaquinta, D.M. and zur Loye, H.-C. Synthesis of the New One-Dimensional Compound Sr_3NiPtO_6: Structure and Magnetic Properties. *Chemisty of Materials,* Vol. **6**, pp 1642–1646 (1994).

Núñez, P. Trail, S. and zur Loye, H.-C. Synthesis, Crystal Structure, and Magnetic Properties of Sr_3MgMO_6 (*M* = Pt, Ir, Rh). *Journal of Solid State Chemistry*, Vol. **130**, pp 35–41 (1997).

Paramova, M.V.; Leshchenko, P.P.; Lykova, L.N. and Kovba, M. The polymorphism of barium tantalate $Ba_4Nb_2O_9$. *Vestnik Moskovskogo Universiteta, Seriya 2: Khimiya*, Vol. **31**, No. 4, pp 499–500 (1976).

Parras, M.; Alonso, J.; González-Calbet, J.M. and Vallet-Regí, M. Ordering and Defects in $BaMnO_{3-y}$ ($0.22 \leq y \leq 0.40$). *Journal of Solid State Chemistry*, Vol. **117**, No. 1, pp 21–29 (1995).

Pecharsky, V.K. and Zavalij, P.Y. *Fundamentals of powder diffraction and structural characterization of materials* (Springer Science & Buisness media, Inc., New York, USA, 2005.

Perez-Mato, J.M.; Zakhours-Nakhl, M., Weill, F. and Darriet, J. Structure of composites $A_{1+x}(A'_xB_{1-x})O_3$ related to the 2H hexagonal perovskite: relation between composition and modulation. *Journal of Materials Chemistry*, Vol. **9**, pp 2795–2808 (1999).

Petricek, V.; Dusek, M. and Palatinus, L. *Jana2006; Structure Determination Software Programs*, (Institute of Physics, Prague, Czech Republic, 2006).

Ruddlesden, S.N. and Popper, P., The compound $Sr_3Ti_2O_7$ and its structure. *Acta crystallographica*, Vol. **11**, pp 54–55 (1958).

Powell, A.V. and Battle, P.D. A time-of-flight powder neutron diffraction study of non-stochiometry in barium iridate $BaIrO_{3-\delta}$. *Journal of Alloys and Compounds*, Vol. **232**, No. 1pp 147–153 (1996).

Rath, M. and Muller-Buschbaum, Hk., Ein Beitrag zur Kristallstruktur von Ba_2ScAlO_5 und $Sr_2Sc_{0.5}Al_{1.5}O_5$. *Journal of Alloys and Compounds,* Vol. **189**, No. 1, pp. 127-130 (1992).

Rath, M. and Muller-Buschbaum, Hk., Ein neuer srtukturtyp eines Halogenoxoruthenates mit geordneter Ru(IV)-Ru(V) – Verteilung. *Journal of Alloys and Compounds,* Vol. **209**. No. 1-2, pp 239–243 (1994).

Ratheesh, R.; Sreemoolanadhan, H. and Sebastian, M.T. Vibration analysis of $Ba_{5-x}Sr_xNb_4O_{15}$ microwave dielectric ceramic resonators. *Journal of Solid State Chemistry*, Vol. **131**, pp 2–8 (1997).

Ratheesh, R.; Sebastian, M.T.; Mohanan, P.; Tobar, M.E.; Hartnett, J.; Woode, R. and Blair, D.G. Microwave characterization of $BaCe_2Ti_5O_{15}$ and $Ba_5Nb_4O_{15}$ ceramic dielectric resonators using whispering gallery mode method. *Materials Letters*, Vol. **45**, No. 5, pp 279–285 (2000).

Rawal, R.; Feteira, A., Flore, A.A.; Hyatt, N.C., West, A.R. and Sinclair, D.C. Dielectric properties of the "Twinned" 8H-Hexagonal Perovskite $Ba_8Nb_4Ti_3O_{24}$. *Journal of American Ceramic Society*, Vol. **89**, No. 1, pp 336–339 (2006).

Rother, H.-J.; Kemmler-Sack, S.; Treiber, U. and Cyris, W.-R. Die Struktur von $Ba_4Nb_2WO_{12}$ and $Ba_3LaNb_3O_{12}$. *Zeitschrift für anorganische und allgemeine Chemie*, Vol. **466**, pp 131–138 (1980).

Roy, R., Multiple Ion Substitution in the Perovskite Lattice, *Journal of the American Ceramic Society*, Vol. **37**, No. 12, pp 581–588 (1954).

Quarez, E.; Roussel, P.; Perez, O.; Leligny, H.; Bendraoua, A. and Mentre O. Crystal Structure of the Mixed Mn^{4+}/Mn^{5+} 2H-Perovskite-Type $Ba_4Mn_2NaO_9$ Oxide. *Solid State Sciences*, **6**, pp 931–938 (2004).

Sahner, K., Modeling of p-type semiconducting perovskites for gas sensors applications (Ph.D. thesis, Shaker Verlag Aachen, 2006).

Sasaki, S., Prewitt, C.T., Bass, J.D. and Schultz, W.A. Orthorhombic perovskite $CaTiO_3$ and $CdTiO_3$: structure and space group, *Acta Crystallographica*, Vol. **43**, No. 9, pp 1668–1674 (1987).

Shpanchenko, R.V.; Abakumov, A.M.; Antipov, E.V. and Kovba, L.M., Crystal structure of $Ba_5In_2Al_2ZrO_{13}$. *Journal of Alloys Compd.*, Vol. 206, pp 185–188 (1994).

Shpanchenko, R.V., Nistor, L., Van Tendeloo, G., Amelinckx, S.; Antipov, E.V. and Kovba, L.M. High-resolution electron microscopic study of $Ba_7Sc_6Al_2O_{19}$ and related phases, *Journal of Solid State Chemistry*, Vol. **113**, No. 1, pp 193–204 (1994).

Shpanchenko, R.V.; Nistor, L., Van Tendeloo, G.; Van Landuyt, J., Amelinckx, S.; Abakumov, A.M.; Antipov, E.V. and Kovba, L.M. Structural Studies on New Ternary Oxides $Ba_8Ta_4Ti_3O_{24}$ and $Ba_{10}Ta_{7.04}Ti_{1.2}O_{30}$. *Journal of Solid State Chemistry*, Vol. **114**, No. 2, pp 560–574 (1995).

Smaalen, S. *Symmetry of composite crystals*, *Physical reviews B*, Vol. **43**, No. 13, pp 11330–11341 (1991).

Sreemoolanadhan, H. and Sebastian, M.T. High Permittivity and low loss ceramics in the BaO–SrO–Nb_2O_5 system, *Materials Research Bulletin*, Vol. **30**, No. 6, pp 653–658 (1995).

Stitzer, K.E.; Abed, A.El.; Darriet, J. and zur Loye, H.-C. Growth of $Sr_6Rh_5O_{15}$ Single Crystals from High-Temperature Solutions: Structure Determination Using the Traditional 3-D and the 4-D Superspace Group Methods and Magnetic Measurements on Oriented Single Crystals, *Journal of the American Chemical Society*, Vol. **123***, pp* 8790–8796 (2001).

Stitzer, K.E.; Henley, W.H.; Claridge, J.B.; zur Loye, H.-C. and Layland, R.C. Sr_3NiRhO_6 and Sr_3CuRhO_6 – Two New One-Dimensional Oxides. Magnetic Behavior as a Function of Structure: Commensurate vs Incommensurate. *Journal of Solid State Chemistry*, Vol. **164**, pp 220–229 (2002).

Sinclair, D.C.; Skakle, J.M.S.; Morrison, F.D.; Smith, R.I. and Beales, T.P. Structure and electrical properties of oxygen-deficient hexagonal $BaTiO_3$. *Journal of Material Chemistry,* Vol. **9**, pp 1327–1331 (1999).

Stitzer, K.E.; Darriet, J. and zur Loye, H.-C. Advances in the synthesis and structural description of 2H-hexagonal perovskite-related oxides. *Current Opinion in Solid State and Materials Science*, Vol. **5** pp 535–544 (2001).

Strunk, M. and Müller-Buschbaum, H. Ein weiteres Alkali-Erdalkalimetall-Oxoniccolat mit Perowskitstruktur: $Sr_{12}NaNi_7O_{23}$, *Zeitschrift für anorganische und allgemeine Chemie*, Vol. **620**, No. 9 pp 1565–1568 (1994).

Tancret, N.; Roussel, P. and Abraham, F. Layered perovskite-related ruthenium oxychlorides: crystal structure of two new compounds $Ba_5Ru_2Cl_2O_9$ and $Ba_6Ru_3Cl_2O_{12}$. *Journal of solid state chemistry*, Vol. **177**, No. 3, pp 806–816 (2004).

Thirumal, M. and Davies, P.K. $Ba_8ZnTa_6O_{24}$: A New High Q Dielectric Perovskite. *Journal of American Ceramic Society*, Vol. **88**, No. 8, pp 2126–2128 (2005).

Trolliard, G.; Teneze, N.; Boullay, Ph.; MANIER, M. and Mercurio, D. HRTEM study of cation-deficient perovskite-related $A_nB_{n-\delta}O_{3n}$ ($n \geq 4\delta$) microphases in the $Ba_5Nb_4O_{15}$–$BaTiO_3$ system. *Journal of Solid State Chemistry*, Vol. **173**, No. 1, pp 91–100 (2003).

Trolliard, G.; Teneze, N.; Boullay, Ph. and Mercurio, D. TEM Study of Cation-Deficient-Perovskite Related $A_mB_{(m-1)}O_{3m}$ Compounds: The Twin-Shift Option. *Journal of Solid State Chemistry*, Vol. **177**, pp 1188–1196 (2004).

Trunov, V.K., Velikodnyi, Yu. A. and Makarevich, L.G. The BaO-Nb_2O_5 system, *Journal of Inorganic Chemistry*(Engl. Transl.), Vol. **24**, No. 5, pp 737–739 (1979).

Vanderah, T.A., Talking Ceramics, Materials science, Vol. 298, pp 1182–1184 (2002).

Vanderah, T.A.; Collins, T.R.; Wong-Ng, W.; Roth, R.S. and Farber, L. Phase equilibria and crystal chemistry in the BaO–Al_2O_3–Nb_2O_5 and BaO–Nb_2O_5 systems. *Journal of Alloys and Compounds*, Vol. **346**, pp 116–128 (2002).

Villars, P.; Cenzual, K.; Daams, J.; Gladyshevskii, R.; Shcherban, O., Dubenskyy, V., Melnichenko-Koblyuk, N.; Pavlyuk, O., Savysyuk, I., Stoyko, S. and Sysa, L. Landolt-Börnstein -Numerical Data and Functional Relationships in Science and Technolog Group III: Condensed Matter, Vol. **43**: Crystal structures of Inorganic compounds, subvolume A: Structure types, Part 5, Space groups (173)$P6_3$ – (166) R-3m. *K_4MnCl_6*, Publisher: Springer Berlin Heidelberg, pp 271 (2007).

Vineis, C.; Davies, P.K.; Negas, T. and Bell, S. Microwave dielectric properties of hexagonal perovskites, *Material Research Bulletin*, Vol. **31**, No. 5, pp 431–437 (1996).

Wada, K.; Fukami, Y.; Kakimoto, K. and Ohasato, H. Microwave Dielectric Properties of Textured $BaLa_4Ti_4O_{15}$ Ceramics with Layered Perovskite Structure. *Japanese journal of Applied Physics*, Vol. **44**, No. 9B, pp 7094–7097 (2005).

Welberry, T. R. and Butler, B. D. Interpretation of Diffuse X-ray Scattering via Models of Disorder, *Journal of Applied Crystallography*, Vol. **27**, pp 205–231 (1994).

Whangbo, M.-H.; Dai, D.; Koo, H.J. and Jobic, S. Investigations of the oxidation states and spin distributions in $Ca_3Co_2O_6$ and Ca_3CoRhO_6 by spin-polarized electronic band structure calculations. *Solid State Communications*, Vol. **125**, pp 413–417 (2003).

Wilkens, J. and Müller-Buschbaum, H. Röntgenstrukturanalyse verzwillingter Einkristalle von $Ba_6IrNb_2O_{12}Cl_2$, *Journal of Alloys and Compounds*, Vol. **179**, No. 1-2, pp. 187-193 (1992).

Wilkens, J. and Müller-Buschbaum, H. Single-crystal investigation of a new ruthenium chloride oxide, $Ba_7Ru_4O_{15}Cl_2$. *Acta Chemica Scandinavica*, Vol. **45**, pp 812–815 (1991).

Wilkens, J. and Müller-Buschbaum, H. $Ba_8Ru_3Ta_2O_{18}Br_2$ - Synthesis and Structure Determination of a Novel Oxide Bromide of Ruthenium, *Journal of Alloys and Compounds*, Vol. **182**, No. 2, pp 265–270 (1992).

Wolff, P.M. The Pseudo-Symmetry of Modulated Crystal Structures, *Acta Crystallographica,* Vol. **30**, No. 6, pp 777–785 (1974).

Yamanaka, T.; Hirai, N. and Komatsu, Y. Structure change of Ca_{1-x} Sr_x Ti O_3 perovskite with composition and pressure. *American Mineralogist*, Vol. **87**, pp 1183–1189 (2002).

Yoon, K. H., Kim, D. P. and Kim, E. S. Effect of $BaWO_4$ on the microwave dielectric properties of $Ba(Mg_{1/3}Ta_{2/3})O_3$ ceramic. *Journal of American Ceramic Society*, Vol. **77**, No. 4, pp 1062–1066 (1994).

Zakhour-Nakhla, M.; Darriet, J.; Claridge, J.B., zur Loye, H.-C. and Perez-Mato, J.M. A superspace approach to the composition flexible composite $Ba_{1+x}(Cu_xIr_{1-x})O_3$ (x = 0.2708). *International Journal of Inorganic Materials*, Vol. **2**, pp. 503–512 (2000).

Zakhour-Nakhl, M.; Claridge, J.B.; Darriet, J.; Weill, F.; zur Loye, H.–C. and Perez-Mato, J.M. Structure Determination of Two New Incommensurate Compounds, $Ba_{1+x}[(Cu_xRh_{1-x})O_3]$ with x = 0.1605 and x = 0.1695, Using a General Method Based on the Superspace Group Approach. *Journal of the American Chemical Society*, Vol. **122**, No. 8, pp 1618–1623 (2000).

Zandbergen, H.W. and Ljdo, D. J.W. Barium strontium niobate and barium strontium tantalate, $Ba_3SrNb_2O_9$ and $Ba_3SrTa_2O_9$, a Rietveld refinement of neutron powder diffraction data. *Acta Crystallographica*, Vol. **39**, No. 7, pp 829–832 (1983).

Zhang, W.; Kumada, N., Yonesaki, Y., Takei, T., Kinomura, N.; Hayashi, T., Azuma, M. and Takano, M. Ferroelectric perovskite-type barium copper niobate: $BaCu_{1/3}Nb_{2/3}O_3$. *Journal of Solid State Chemistry*, Vol. **179**, No. 12, pp 4052–4055 (2006).

Zhao, F.; Yeu, Z.; Pei, J.; Gui, Z. and Li, L. Effects of octahedral thickness variance on the temperature coefficient of resonant frequency of the B-site deficient hexagonal perovskites. *Applied Physics Letters*, Vol. **90**, No. 14, pp 142908 (2007).

Zhao, F.; Yue, Z.; Pei, J.; Zhuang, H.; Gui, Z. and Li, L. Improvement on the temperature coefficient of resonant frequency of hexagonal perovskites through intergrowth structures. *Applied Physics Letters*, Vol. **89**, pp 20290 (2006).

Crystallographic data:

ELCORO, L., PEREZ-MATO, J. M., DARRIET, J. AND EL ABED, A., Superspace description of trigonal and orthorhombic $A_{1+x}A_x'B_{1-x}O_3$ compounds as modulated layered structures; application to the refinement of trigonal $Sr_6Rh_5O_{15}$, *Acta Crystallographica, Section B*, Structural Science, 2003, Vol. 59, No. 2, pp. 217-233

Powder-Diffraction-Files are taken from JCPDS-International Center for Diffraction Data:

α-$Ba_4Nb_2O_9$	PDF #35-1154	(1980)
α-$Ba_4Nb_2O_9$	PDF #46-0939	(1979)
β-$Ba_4Nb_2O_9$	PDF #35-1155	(1980)
γ-$Ba_4Nb_2O_9$	PDF #35-1156	(1980)
$Ba_3Nb_2O_8$	PDF #72-0192	(1981)
$Ba_5Nb_4O_{15}$	PDF #87-1247	(1996)
Ba_3WO_6	PDF #77-0624	(1991)
Ba_2WO_5	PDF #78-1335	(1985)
$Ba_3W_2O_9$	PDF #83-1774	(1980)
$BaWO_4$	PDF #72-0746	(1970)
$Ba_6Ta_2WO_{14}$	PDF #35-0187	(1980)
$Ba_3W_{1.33}Nb_{0.66}O_{8.66}$	PDF #72-0191	(1981)
$Ba_4Nb_2WO_{12}$	PDF #73-0913	(1980)
$Ba_9Nb_6W_2O_{27}$	PDF #73-0654	(1980)
$BaCO_3$	PDF #45-1471	(1993)
$Sr_4Ni_3O_9$	ICSD #78515	(1996)
$Sr_4Ru_2O_9$	ICSD #79310	(1996)

List of figures

1. THE PEROVSKITE CRYSTAL STRUCTURES:

3. METHODS:

4. THE BaO-RICH HEXAGONAL PHASES WITHIN THE BaO–Nb_2O_5 BINARY SYSTEM:

5. THE BaO-RICH HEXAGONAL PEROVSKITE LIKE PHASES WITHIN THE $BaO–Nb_2O_5–WO_3$ TERNARY SYSTEM:

List of Tables

3. METHODS:

4. THE BaO-RICH HEXAGONAL PHASES WITHIN THE $BaO–Nb_2O_5$ BINARY SYSTEM:

5. THE BaO-RICH HEXAGONAL PEROVSKITE LIKE PHASES WITHIN THE $BaO–Nb_2O_5–WO_3$ TERNARY SYSTEM:

Appendix I: Standard procedure for the preparation of the ceramic samples by solid-statesynthesis method